Synthesis of Bioinspired Dioxygen Reduction Catalysts Involving Mono and Polynuclear Late Transition Metal Complexes and Spectroscopic Trapping of Reactive Intermediates

Dissertation

zur Erlangung des akademischen Grades

doctor rerum naturalium

(Dr. rer. nat.)

im Fach Chemie

eingereicht an der

Mathematisch-Naturwissenschaftlichen Fakultät
der Humboldt-Universität zu Berlin

von

M.Sc. Anirban Chandra

Präsident der Humboldt-Universität zu Berlin
Prof. Dr.-Ing. Dr. Sabine Kunst

Dekan der Mathematisch-Naturwissenschaftlichen Fakultät
Prof. Dr. Elmar Kulke

Gutachter/in: 1. Prof. Dr. Kallol Ray

2. Dr. Matthias Schwalbe

3. Prof. Dr. Biprajit Sarkar

Tag der mündlichen Prüfung : 26. 01. 2021

Abstract

Metalloenzymes activate dioxygen by employing earth-abundant metals to perform a wide range of key metabolic functions. High-valent metal-oxygen cores of late-transition metals are proposed as reactive intermediates in these processes. Transition metal-mediated dioxygen activation reaction is also industrially important in the context of attaining clean renewable energy sources and also making efficient use of the naturally abundant oxidant (i.e., O_2) in oxidation reactions. Understanding the mechanism of generation of the metal dioxygen intermediates and their reactive properties can provide vital insights into the mechanisms of such enzymatic reactions.

During my doctoral research, I examined the 'structure-activity relationship' of different metal-dioxygen adducts towards various substrates. I have worked with different kinds of metal-dioxygen intermediates, namely dinuclear cobalt-peroxo, and nickel-superoxo, to understand how small changes in the ligand system can influence the behavior of a given reactive system. I have synthesized a unique cobalt-based catalyst for the dioxygen-reduction reaction (ORR). Remarkably, the reaction temperature can be used to change the reaction pathway, from a preferential $4e^-/4H^+$ dioxygen-reduction (PCET-process) to a $2e^-/2H^+$ process (PT-process) by increasing the temperature. Detailed spectroscopic characterization and theoretical studies confirmed the involvement of an end-on-μ-1,2-peroxodicobalt(III) intermediate. The kinetic behavior of the oxidation of a wide range of substrates by end-on-μ-1,2-peroxodicobalt(III) species was also examined leading to new mechanistic insights. For the first time, I observed the amphoteric behavior of an end-on-μ-1,2-peroxodicobalt(III) species in absence of any external additives, which is unprecedented to date. I also revealed the first nickel(II)-superoxo species, which can only behave as a nucleophile by tuning the ligand donation. A two-state reactivity model (TSR) was proposed to explain this unprecedented reactivity of nickel-superoxo species.

To this end, my Ph.D. thesis shows that the reactivity patterns of the high-valent reactive intermediates depend greatly on the subtle electronic changes associated with the ligand, the metal center, and the oxidant employed in the reaction. Using these findings new and temperature controllable mechanistic pathways were revealed, in addition to an enhancement of catalytic efficiency. The deep mechanistic insights into the transition-metal mediated dioxygen reduction process that are obtained from these studies will be helpful for the future design of more efficient bioinspired synthetic catalysts.

Zusammenfassung

Metalloenzyme aktivieren Disauerstoff durch den Einsatz von Metallen, die auf der Erde reichlich vorhanden sind, um eine breite Palette wichtiger Stoffwechselfunktionen zu erfüllen. Hochvalente Metall-Sauerstoff-Zentren später Übergangsmetalle werden als reaktive Intermediate in diesen Prozessen vorgeschlagen. Die übergangsmetallvermittelte Disauerstoffaktivierungsreaktion ist auch von industrieller Bedeutung im Zusammenhang mit der Gewinnung sauberer erneuerbarer Energiequellen und der effizienten Nutzung des natürlich reichlich vorhandenen Oxidationsmittels (d.h. O_2) in Oxidationsreaktionen. Das Verständnis des Entstehungsmechanismus der Metall-Disauerstoff-Intermediaten und ihrer reaktiven Eigenschaften kann wichtige Erkenntnisse über die Mechanismen solcher enzymatischer Reaktionen liefern.

Während meiner Doktorarbeit untersuchte ich die „Struktur-Aktivitäts-Beziehung" verschiedener Metall-Disauerstoff-Addukte zu verschiedenen Substraten. Ich habe mit verschiedenen Arten von Metall-Disauerstoff-Intermediaten gearbeitet, nämlich dinuklearem Kobaltperoxo- und Nickelsuperoxokomplexe, um zu verstehen, wie kleine Veränderungen im Ligandsystem das Verhalten eines bestimmten reaktiven Systems beeinflussen können. Ich habe einen einzigartigen Katalysator auf Kobaltbasis für die Disauerstoffreduktionsreaktion (ORR) synthetisiert. Bemerkenswerterweise kann die Reaktionstemperatur verwendet werden, um den Reaktionsweg von einer bevorzugten $4e^-/4H^+$-Disauerstoffreduktion (PCET) zu einem $2e^-/2H^+$-Prozess (PT) durch Erhöhen der Temperatur zu ändern. Detaillierte spektroskopische Charakterisierung und theoretische Studien bestätigten die Beteiligung eines End-on-μ-1,2-Peroxodikobalt(III)-Intermediats. Das kinetische Verhalten der Oxidation einer Vielzahl von Substraten durch End-on-μ-1,2-Peroxodikobalt(III)-Spezies wurde ebenfalls untersucht, was zu neuen mechanistischen Erkenntnissen führte. Zum ersten Mal beobachtete ich das amphotere Verhalten von End-on-μ-1,2-Peroxodikobalt(III)-Spezies in Abwesenheit jeglicher externer Zusätze, was bis heute beispiellos ist. Ich habe auch die erste Nickel (II) -Superoxo-Spezies entdeckt, die sich nur durch Abstimmung der Ligandenspende als Nucleophil verhalten kann. Ein Zweizustandsreaktivitätsmodell (TSR) wurde vorgeschlagen, um diese beispiellose Reaktivität der Nickel-Superoxo-Spezies zu erklären.

Zu diesem Zweck zeigt meine Doktorarbeit, dass die Reaktivitätsmuster der hochvalenten reaktiven Zwischenprodukte stark von den subtilen elektronischen Änderungen abhängen, die mit dem Liganden, dem Metallzentrum und dem in der Reaktion verwendeten Oxidationsmittel verbunden sind. Mit Hilfe dieser Erkenntnisse wurden neben einer Steigerung der katalytischen

Effizienz auch neue und temperaturkontrollierbare mechanistische Wege aufgezeigt. Die tiefen mechanistischen Einsichten in den übergangsmetallvermittelten Disauerstoffreduktionsprozess, die aus diesen Studien gewonnen werden, werden für das zukünftige Design von effizienteren bioinspirierten synthetischen Katalysatoren hilfreich sein.

This work was performed between January 2016 and May 2020 under the supervision of Prof. Dr. Kallol Ray at the Institut für Chemie, Mathematisch-Naturwissenschaftliche Fakultät at the Humboldt-Universität zü Berlin.

Acknowledgments

First and foremost, I would like to express my sincere gratitude to Prof. Dr. Kallol Ray for his continuous support during my Ph.D. studies. His never-ending passion for science and immense knowledge has always inspired me to perform better. His enthusiastic guidance and active encouragement throughout the course of this work allowed me to grow both professionally and personally. Not only as a professional guide but also, he always takes care of me as his family member. At the same time, I would like to offer my heartfelt gratitude to Dr. Iweta Pryjomska-Ray for her useful advice and tremendous support. Without their strong mental support, this journey would be never possible for me. Words are not enough to express my gratitude for their support during my stay in Berlin. I will forever cherish the valuable time that I have spent with them.

I am indebted to Prof. Dr. Christian Limberg for his valuable suggestions and discussions during the group seminars and also for allowing access to some of his instruments (such as IR, ESI-MS, etc.). During the initial phase, he also permitted me to participate in his research group activities.

I would like to thank Dr. Matthias Schwalbe for his valuable suggestions during the group seminars and for being the second reviewer of my Thesis.

Next, I would like to thank the past and present members of the Ray group for their kind behavior and a countless number of suggestions. Special thanks to the former members of the group: Dr. Subrata Kundu, Dr. Ines M. Perez, and Dr. Teresa Corona from whom I have learned a lot. Thank you also to all the current group members for maintaining the nice atmosphere in the laboratory and for your comradeship. Especially, I would like to thank Katrin Warm and Jennifer Deutscher for measuring my resonance Raman samples, Beatrice Battistella for measuring my EPR samples, Dr. Teresa Corona for her help with measuring my GC-MS samples, and Matthias Jux for taking care of the computer-related issues. I would also like to express my gratitude to Richard Rauchut who always provided me with office utensils and the nice talks we had during lunchtime. I would like to thank Beatrice Battistella, Kuheli Dutta, and Tarali Devi for their support and friendship. Special Thanks to Kuheli Dutta and Katrin Warm for reading and correcting this Thesis. My special thanks go to Katrin Warm who has helped me during the last years with insightful discussions.

Thanks to Dr. Beatrice Braun for her help with the X-ray crystallography.

Thanks to the scientific, technical, and administrative staffs of the Institut für Chemie of the Humboldt Universiät zü Berlin, particularly, to Dr. Andrea Zehl for the elemental analysis and to the NMR department for measuring my samples. Special thanks to Dr. Matthias Karg and Lutz Pospisil for their immense support at the service point.

I would like to acknowledge the contributions of the following individuals and groups who have collaborated in my research projects and have helped in the development of this Thesis.

Thanks to Silvio Künstner at the Institute Nanospectroscopy, Helmholtz Zentrum Berlin (Germany) for his help with the EPR measurements and valuable discussions.

Thanks to Prof. Dr. Peter Hildebrandt and Dr. Uwe Kuhlmann in the Technische-Universität Berlin (Germany) for the access to the rRaman instrument.

Thanks to Prof. Dr. Holger Dau and Dr. Stefan Mebs at Freie Universität Berlin (Germany) for X-ray absorption studies. Special thanks go to Dr. Stefan Mebs for his friendly behavior and useful discussion. I am also thankful to Dr. Erik Farquhar at the Brookhaven National Laboratory (U.S.A.) for X-ray absorption studies.

Thanks to Erik Andris and Prof. Dr. Jana Roithova from the Charles UniversityPrague (Czech-Republic) for the IRPD measurements.

Thanks to Prof. Dr. Matthias Driess and Dr. Chakadola Panda at the Technische-Universität Berlin (Germany) for fruitful collaborations.

Thanks to Bhawana Pandey and Prof. Gopalan Rajaraman at the Indian Institute of Technology Bombay (India) for DFT calculations.

I sincerely acknowledge the financial support from the Cluster of Excellence-Unifying Concepts in Catalysis (UNICAT) and the Cluster of Excellence-Unifying Systems in Catalysis (UniSysCat).

Finally, I am very much indebted to my parents and my wife for their understanding, inspiration, and never-ending support. Especially, I want to thank Animitra, my wife, for always being there for me in good and bad times, no matter how far away we are.

Table of Contents

Chapter 1

General Introduction

1.1. Small molecule activation

Catalytic activation of various small molecules has been in the focus of chemical research in the last decades and there are many fundamental reasons, which captivated this research for future technological development.[1] Environmental crisis, originating from increasing energy demand and excessive use of fossil fuels, has become the main reason behind fostering such research activities. Alternative energy sources and sustainable chemical processes that are economically viable and environmentally benign are needed to address such environmental crisis.[2] In this context, the use of naturally abundant different small molecules such as O_2, H_2, N_2, CO, CO_2 has immense significance.[3] For instance, small molecules such as H_2 and O_2 have the potential to be an alternative energy source in fuel cells. Activation of N_2 and CO_2, as well as the oxidation of hydrocarbons using O_2 can also lead to the generation of different value-added chemical products, which is a lucrative target to achieve. Activation of certain molecules like CO_2, CH_4, and NO_x can significantly improve environmental conditions as they are the potential greenhouse gases.[4]

C-H functionalization, particularly through oxidizing the inert C-H bonds of hydrocarbons, serves the purpose of replacing the current petrochemical feedstocks.[5] Oxidation of CH_4 to methanol is a relevant example. However, kinetic inertness impedes the use of such small molecules in a variety of chemical transformations. Existing methods often use harsh reaction conditions, have low selectivity and turn-over number, and often produce tons of unwanted toxic waste. Current industrial techniques consist of noble, expensive metals such as Pt, Pd, Rh, Ru, Ir, etc as the catalyst.[6] So far, the most efficient known catalyst for methane activation is the platinum-based Periana catalyst[6e]; however, its potential industrial applications are limited by the cost of platinum (a non-abundant metal) as well as by the extreme reaction conditions required. On the other hand, natural enzymes often use cheap 3*d*-transition metals to perform the key metabolic functions such as hydroxylation of methane in methanotrophs, desaturation of fatty acids in plants, DNA and RNA repairs, biosynthesis of β-lactam antibiotics, etc under ambient conditions. Studies revealed that the active centers of different metalloenzymes use either a monometallic or a multimetallic catalytic site to perform various reactions with high efficiency and stereospecificity.[7,8] Thus enzymes have inspired us to develop future generation catalysts using cheap and abundant transition metals. The development of suitable metal-catalysts can make the chemical conversion of small-molecules more feasible by lowering the activation energy and providing an alternative reaction pathway (Figure.1.1.1).

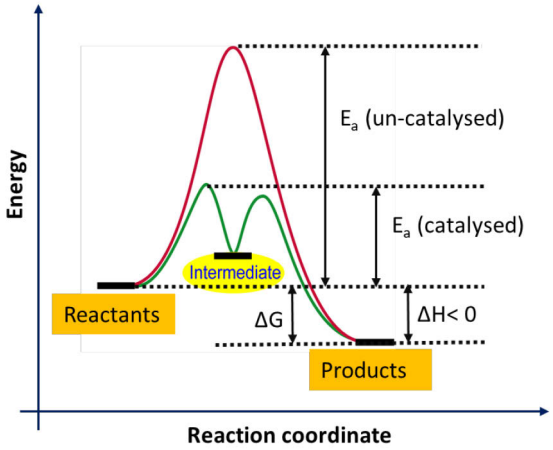

Figure 1.1.1: Reduction in activation energy in catalytic vs non-catalytic reaction pathways.

A biomimetic approach may provide an alternative strategy to address questions related to the metalloenzymes. Understanding the mechanism of biological systems will provide us vital insights into the prerequisites necessary for the design of efficient catalysts in the small molecule activation processes. An accurate understanding of such enzymatic activity may enrich the area of oxidation catalyst development.

1.2. Oxidation reaction

Redox reactions are one of the most fundamental chemical reactions as these are the principal sources of energy, both naturally (photosynthesis and respiration) and artificially (fuel cell) (Scheme 1.2.1).

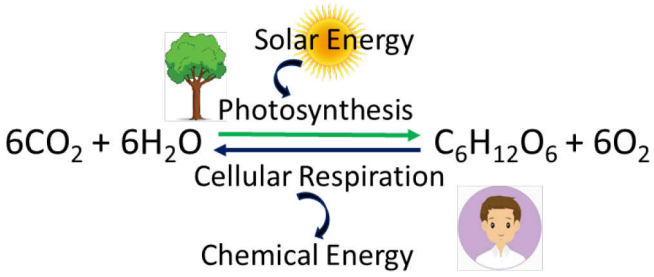

Scheme 1.2.1.: Schematic representation of redox reactions including photosynthesis and respiration in everyday life.

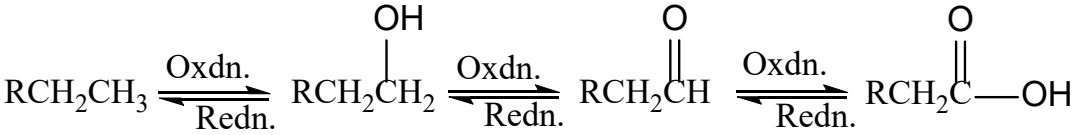

Scheme 1.2.2.: Schematic representation of increasing the oxygen content or decreasing the hydrogen content (oxidation reaction) in an organic molecule.

The term redox involves both oxidation and reduction. According to the IUPAC, the oxidation process can be defined as the complete removal of one or more electron from a molecule or increasing in the oxidation number of an atom within a molecule. However, for organic reactions, the oxidation is defined as the gain of an oxygen atom and/or loss of a hydrogen atom from an organic substrate (Scheme 1.2.2).[9]

1.2.1. Oxidant

The sustainability of any oxidation reaction depends on the choice of the appropriate oxidant.[10] Commonly used industrial oxidants (such as chromate salt, permanganate salt, perchlorate salt, etc.)[11] have a lot of drawbacks as they possess high toxicity, poor selectivity, and produce a lot of toxic waste. An ideal oxidant should be inexpensive, environmentally benign, and must have a high percentage of active oxygen content. In this scenario, scientists are trying to use molecular oxygen and /or hydrogen peroxide as an oxidant. Molecular oxygen is considered to be an 'ideal' and 'green' oxidant due to its higher atom efficiency, natural availability, and lack of toxic byproduct (only water) formation. In biology metalloenzymes often use molecular oxygen in their active sites to perform selective hydrocarbon oxidation reactions under ambient conditions.[12]

1.2.2. Molecular Oxygen

Although molecular oxygen is considered to be an ideal oxidant, it is not straightforward to use molecular O_2 as an oxidant chemically. From a thermodynamic viewpoint, dioxygen is potentially reactive, however direct oxidation of organic molecules with molecular-oxygen is kinetically hindered. The kinetic inertness of molecular oxygen can be explained from its electronic configuration. It contains two unpaired electrons having parallel spins in its anti-bonding molecular orbitals (π_{2px}* and π_{2py}*) with a bond order value of 2. With the spin value S=1, O_2 exists in a triplet ground state (spectroscopic term: $^3\Sigma_g^-$)[13] (Figure 1.2.1). The kinetic inertness of molecular O_2 can be explained by Wigner's spin selection rule.[14,15] Most of the organic substrates are diamagnetic (S=0). Therefore, the reaction of oxygen with the organic substrates (total spin S=1) is spin forbidden as the oxidation products have the spin value of S=0.[16] However, molecular O_2 can react with species that contain unpaired electrons or can undergo single-electron transfer reactions, such as free radicals, photochemically induced excited states, or reduced transition metals.

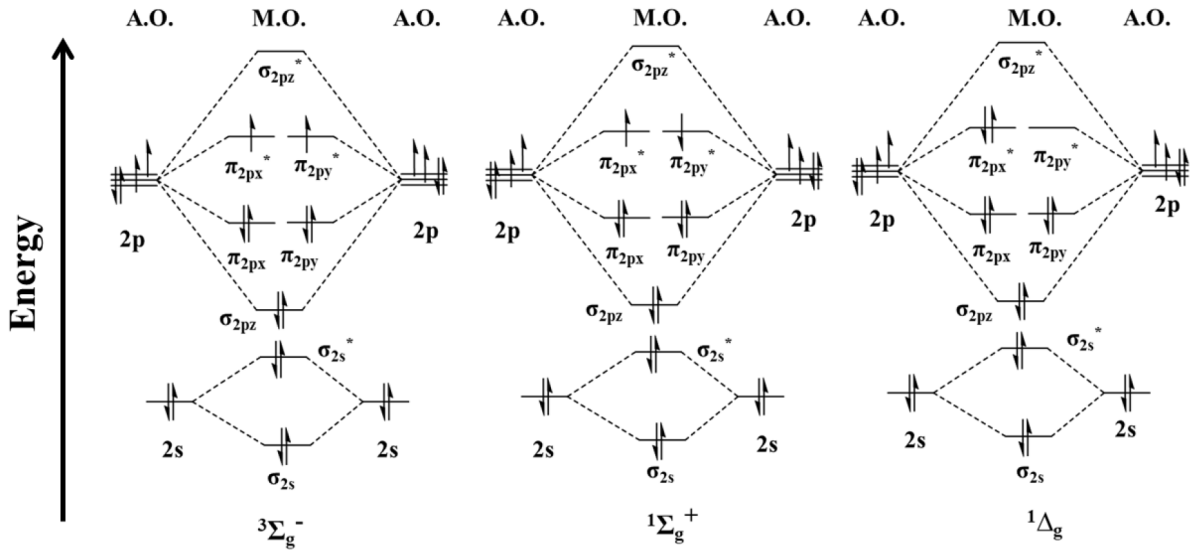

Figure 1.2.1: From left to right, the molecular orbital diagram for triplet oxygen (ground state), singlet oxygen (first excited state), and singlet oxygen (second excited state).

Although molecular oxygen with a triplet ground state is kinetically inert, an electronically excited state of molecular oxygen (termed as 'singlet oxygen') is kinetically active. In singlet oxygen, all the electrons are paired but reside on either the same ($^1\Delta_g$) or different π* orbital(s) ($^1\Sigma_g^+$)[17] (Figure 1.2.1). Reactivity of the singlet oxygen with organic substrates is, therefore, spin allowed in comparison to its triplet counterpart. Despite its higher reactivity, the usage of singlet oxygen as an oxidant is prohibited/ limited because of its poor selectivity and uncontrolled auto-oxidation probability.[18]

1.2.3. Metal mediated oxygen activation

Controlled activation of molecular oxygen takes place in the active sites of metalloenzymes to perform key metabolic functions. Nature often uses cheap and abundant first-row transition metal centers (e.g. Fe, Cu, Mn) in the active site of metalloenzymes.[19] High valent metal-oxygen species, generated upon oxygen activation at mononuclear or dinuclear active sites of metalloenzymes, act as reactive intermediates in the catalytic cycles of a number of enzymatic systems.[20] A significant amount of research has been conducted to establish a common hypothesis about the metal-mediated O_2 activation process (Figure 1.2.2).[21]

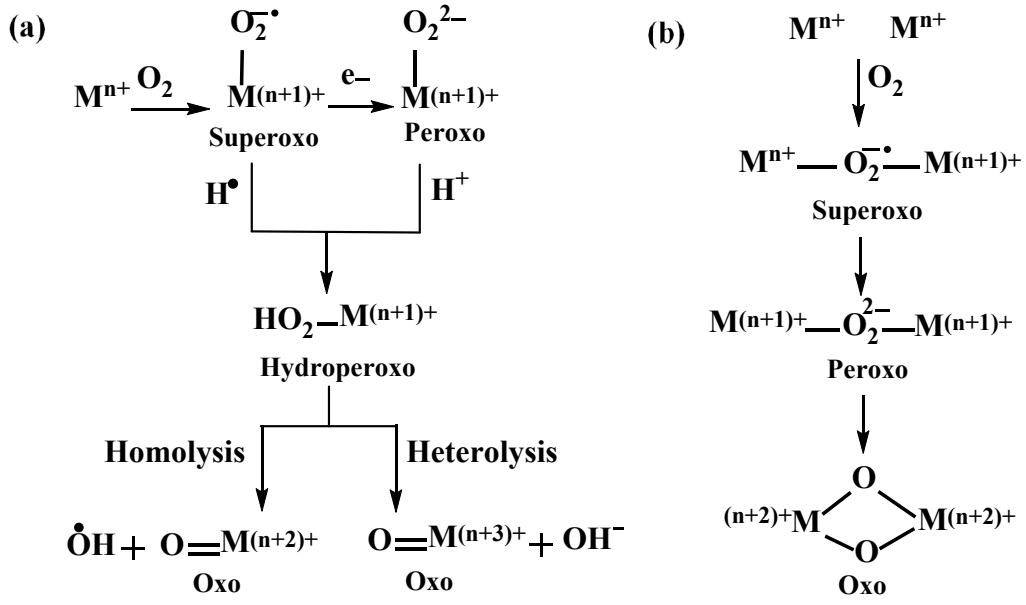

Figure 1.2 2: Proposed mechanisms for the O_2 activation process at (a) mononuclear and (b) dinuclear enzymatic active sites.

According to the proposed mechanism, molecular O_2 first binds to the transition metal center to generate a metal-superoxo species, which has a more reactive doublet state. Subsequent one-electron reduction of the metal-superoxo species takes place to generate a metal-peroxo species, which then takes a proton to form a metal-hydroperoxo species. Metal-superoxo species can also directly abstract a hydrogen atom from the substrate to form the metal-hydroperoxo species. This metal-hydroperoxo species then undergo O-O bond homolysis or heterolysis to form a high valent metal-oxo species (Figure 1.2.2, a). For the dinuclear system metal-superoxo, -peroxo, and -oxo intermediates are known so far (*Figure* 1.2.2, b). Different binding modes of metal-oxygen intermediates are shown in Figure 1.2.3.[22, 23]

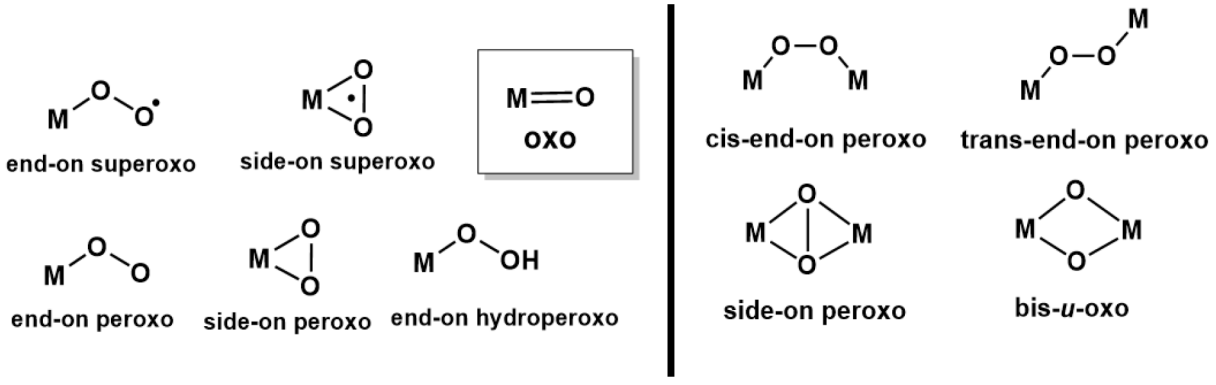

Figure 1.2.3: Different binding modes of metal-oxygen intermediates. Various end-on and side-on binding motifs of molecular dioxygen for mononuclear systems (left) and dinuclear systems (right).

1.3. Relevant enzymes and their intermediates

The O_2 activating enzymes are of two types: (*i*) Oxidase and (*ii*) Oxygenase. Oxidase enzymes are responsible to catalyze the oxidation-reduction reaction using dioxygen as an electron acceptor leading to the formation of water (H_2O) or hydrogen peroxide (H_2O_2) as a by-product, whereas, in oxygenase enzymes an oxygen atom is incorporated into a substrate. In nature, different heme and non-heme metalloenzymes extensively use iron and/ or copper centers in their active sites to catalyze different selective metabolic transformations. The bio-availability and ability to access multiple oxidation states make the iron most common transition metal in enzymatic oxygen activation reactions. Depending upon the ligand environment and the number of metal centers present, three types of high valent iron-oxo active sites are available in iron-containing heme/non-heme metalloenzymes (Figure 1.3.1).[24] The heme-containing enzymes such as catalase, peroxidase, and oxygenases involve mononuclear iron-porphyrin active sites axially coordinated to a cysteine, histidine, or tyrosine residue.[25] The second type of nonheme mononuclear iron enzymes contains two histidines and one carboxylate group such as taurine dioxygenase (TauD) and Rieske dioxygenase.[26] The third type of iron oxo active sites are characterized by dinuclear iron centers associated with two histidines and four carboxylates, such as intermediate Q in soluble MMO.[27]

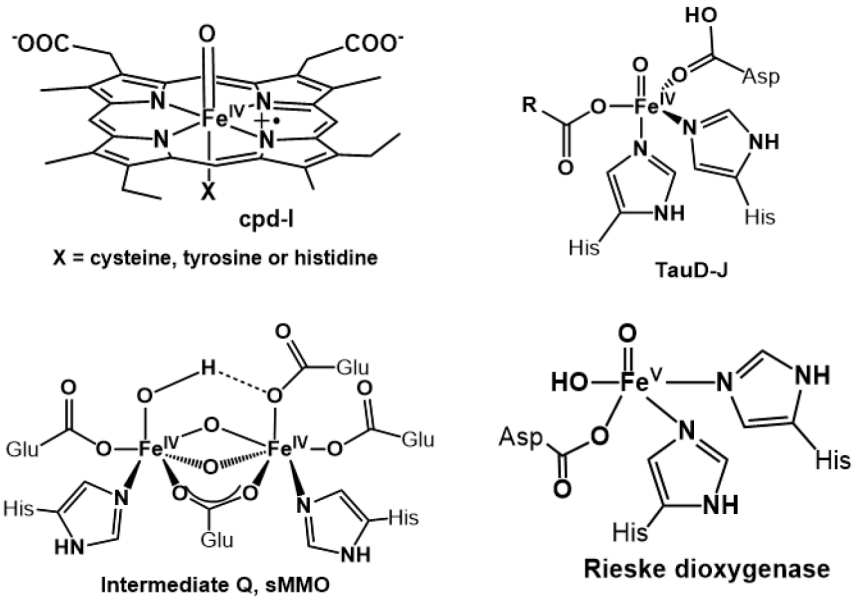

Figure 1.3.1: The structures of the high valent iron-oxo intermediates in the active sites of the respective enzymes.[24]

Enzymatic dioxygen activation generally occurs at the iron (II) center leading to a variety of 2*e*- oxidation reactions; the other two electrons required for complete reduction of dioxygen are then provided by a co-substrate.[27b] The choice of co-substrates can vary depending on the

enzymes. In mononuclear non-heme iron oxygenases, additional co-substrates like 2-oxoacids or tetrahydrobiopterin are used as a co-substrate for the reduction of iron(III)-superoxide to form peroxoiron(III) and oxoiron(IV) species as per the proposed reaction mechanism. In contrast, enzymes such as cytochromes P450 (Cyt-P450), or Rieske dioxygenases employ NADH as a reductant to convert iron(III)-superoxide to iron(III)-peroxide, which upon protonation yields a formally oxoiron(V) species ([(OH)Fe^{V}═O intermediate] in Rieske dioxygenase or an oxoiron(IV) porphyrin π-cation radical ion in P450 (termed as Cpd-I)) via the intermediate formation of hydroperoxoiron(III). In mononuclear copper oxygenases, the initially formed copper(II)-superoxide species undergoes two consecutive hydrogen atom abstraction or proton-coupled electron transfer steps from a suitable substrate (for example ascorbate) to yield a formal oxocopper(III) species. In the polynuclear environment, the additional metal centers provide the necessary electrons required for the conversion of metal-superoxo to metal-oxo in the absence of any additional cosubstrates. In the following sections, the catalytic cycles of some relevant metalloenzymes are discussed, with a special focus on the nature of their key reactive intermediates.

Cytochrome P450 monooxygenases: In Cyt-P450, the resting state is six coordinated having a low spin Fe(III) metal center axially bound to one water and one cysteine moiety.

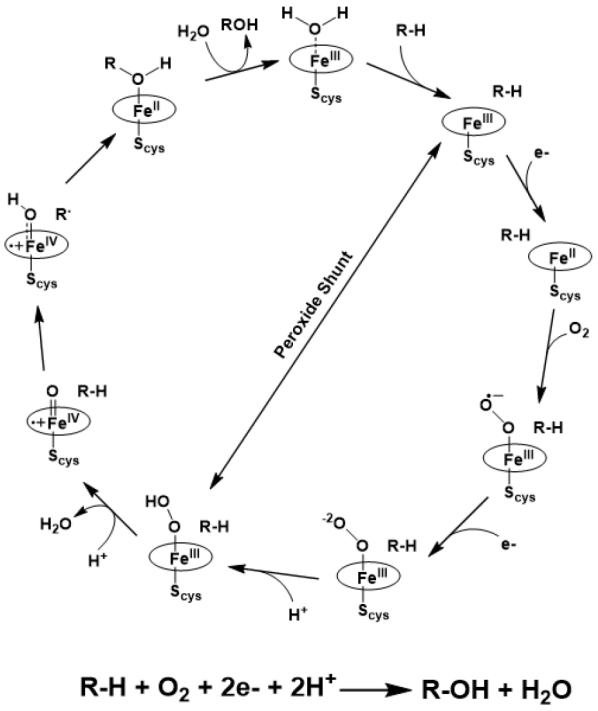

Figure 1.3.2: Mechanism of the hydroxylation reactions catalyzed by Cyt-P450.[28]

Upon binding with an organic substrate it loses the water molecule to form a penta-coordinated high spin Fe(III) complex, which is then reduced to an Fe(II) state. Reduced Fe(II) center binds

with oxygen to form a six coordinated low-spin iron(III) superoxo moiety. The iron(III) superoxo moiety is then reduced by one electron to form an iron(III) peroxo intermediate, which then takes up a proton to form an iron(III) hydroperoxo intermediate (known as Cpd-0). Subsequent protonation of Cpd-0 followed by O-O heterolytic cleavage leads to the generation of a high valent oxoiron(IV) heme cation radical species (known as Cpd-I).[28] Cpd-I is believed to be the most reactive species of the cycle and able to abstract a hydrogen atom from the substrate to generate an iron(IV) hydroxo species and a carbon-centered radical.[29] Then the substrate radical gets hydroxylated to form the corresponding alcohol. The initial state of the enzyme is retained via the 'oxygen-rebound' mechanism (Figure 1.3.2).[30]

Taurine dioxygenase: Taurine Dioxygenase (TauD) is a nonheme iron enzyme that belongs to the family of α-ketoglutarate (α-KG)-dependent dioxygenase enzyme.[31]

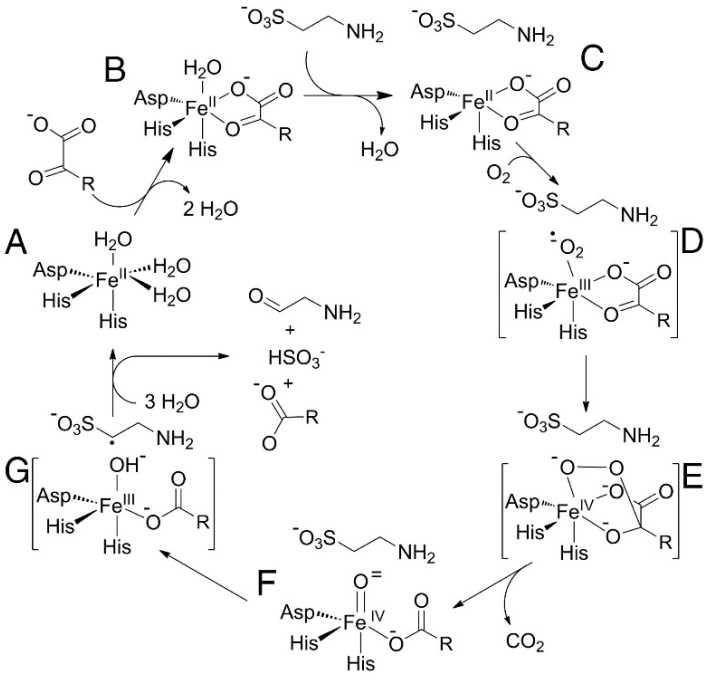

Figure 1.3.3: The proposed catalytic cycle of Taurine Dioxygenase (TauD).[32]

In the resting state, the iron(II) center is coordinated with three water molecules, two histidines, and one aspartate (2-His/ 1-Carboxylate) (state A, Figure 1.3.3). After the addition of α-KG, it releases two water molecules (state B). The third water molecule is released when the substrate (taurine) docks in the active site, leaving a penta-coordinated iron(II) center (state C). An iron(III) superoxo intermediate is generated upon binding of O_2 to the penta-coordinated iron(II) site. The superoxo species then attacks the α-keto position of α-KG, followed by subsequent decarboxylation to generate a high valent iron(IV)-oxo (S = 2) species, which is widely known as Intermediate-J. This intermediate-J is responsible for the hydrogen atom

abstraction from the substrate to give the final hydroxylated product (via an oxygen rebound mechanism).[32] In the case of Rieske dioxygenase, a high valent iron(V)-oxo intermediate (S = 2) is generated using NADH as an electron donor.[33]

Soluble methane monooxygenase: The third type of high valent iron-oxo species found in enzymes contain a dinuclear iron center, such as soluble methane monooxygenase (sMMO) and ribonucleotide reductase (RNR R2). The intermediates present in the active sites are assigned as bis-(μ-oxo)-diiron(IV, IV) and bis-(μ-oxo)-diiron(III, IV), respectively.[34] Because of its emerging capability to oxidize methane to methanol, sMMO has been investigated intensively for a long decade. In the resting state, it contains a diiron(III) cluster. Two-electron reduction of this diiron(III) species produces a diiron(II) species, which then binds with O_2 to give a bridging diiron(III) peroxo moiety. Cleavage of the O-O bond in the peroxo moiety gives a high valent bis-(μ-oxo)-diiron(IV, IV) core known as intermediate-Q (MMO-Q). This diamond core containing high-spin (S = 2) iron(IV) centers is responsible for the oxidation of methane to methanol (Figure 1.3.4).[35]

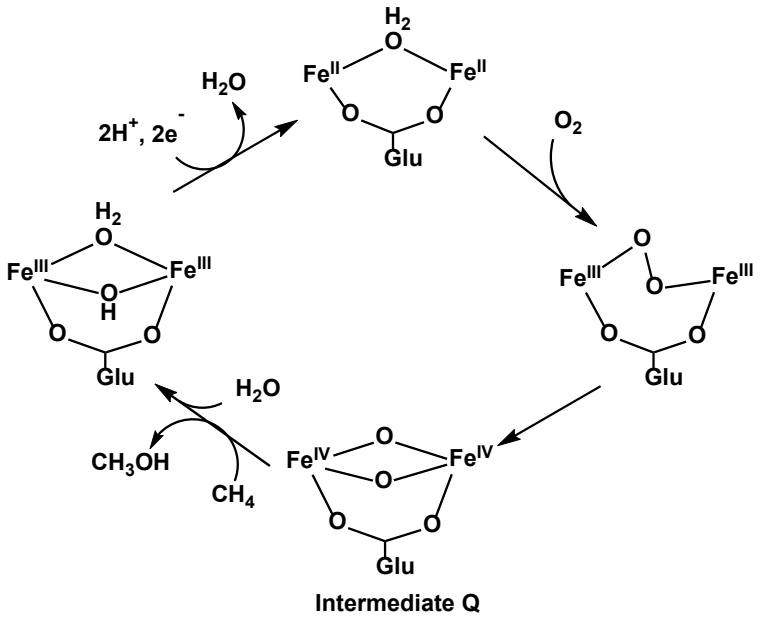

Figure 1.3.4: The proposed Catalytic cycle of sMMO.

Active centers of all these above-mentioned oxygenase enzymes commonly form high-valent iron-oxo core upon oxygen activation, which is the key species to perform different oxygenation reactions such as epoxidation, halogenation, cyclization, decarboxylation, etc (Figure 1.3.5).[26a, 36]

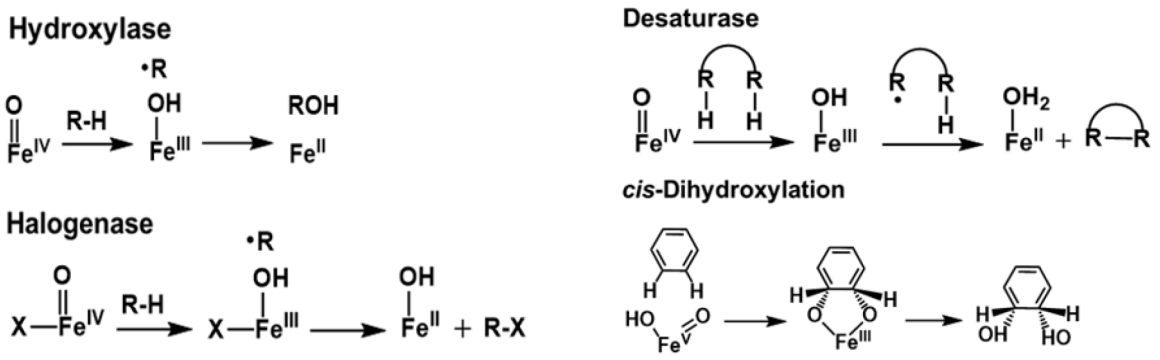

Figure 1.3.5: High Valent iron-oxo mediated transformation reactions by various iron-containing enzymes.[24]

Cytochrome *c* oxidase: Besides oxygenation, metal-oxo core in metalloenzymes are also responsible for the oxidase-like reactivities, like the four-electron reduction of dioxygen to water. In nature, Cytochrome *c* oxidase (C*c*O) and related heme/copper terminal oxidases (Isopenicillin N synthase, ascorbate oxidase) catalyze the selective reduction of O_2 to H_2O without producing any partially reduced intermediates.

C*c*O belongs to the super-family of metalloporphyrin enzymes, which contains heme-porphyrin at its active site. However, C*c*O can be distinguished structurally from other heme-dependent proteins due to the presence of an essential copper metal center proximate to the heme cofactor (heme copper separation is ~5 A °).[37] C*c*O is composed of two heme proteins with iron porphyrin core structures (heme-a, heme-a_3) and two non-heme copper centers (Cu_A, Cu_B).[38] Electron transfer occurs from proteins to their final destination heme-a_3 and Cu_B through the binuclear Cu_A center and heme-a center. The free energy released during oxygen reduction reaction (ORR) is used to pump the protons to the higher potential across the mitochondrial membrane. The active catalytic site of C*c*O is believed to contain bimetallic Fe_B^{II}/Cu_B^{I} centers. Three out of four electrons required for the O_2 reduction process are provided by the Fe_B^{II}/Cu_B^{I} centers, while the fourth electron and one proton are provided either by a tyrosine-244 moiety present in the active site or from the Fe_A/Cu_A redox cofactor. Although the active site of C*c*O is bimetallic, the binding mode of O_2 is very similar to the monomeric heme and nonheme enzymes.[39] Different types of metal-oxygen intermediates (e.g., metal−superoxo, −peroxo, −hydroperoxo, and −oxo) are proposed to involve during the ORR process (Figure 1.3.6).

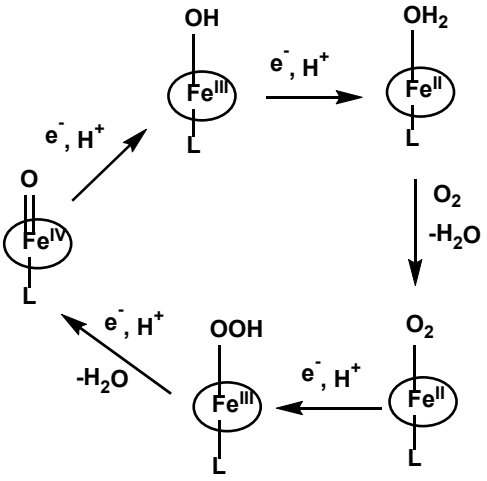

Figure 1.3.6: General mechanism of the catalytic four-electron reduction of dioxygen to water by the active site of CcO.[39c]

Natural enzymes containing coinage metals like copper also play important roles in the biological oxidation processes.[40] One of the well-studied copper-containing oxidase enzymes is galactose oxidase (GAO), which contains a Cu(II)-tyrosyl radical unit in its active site and oxidize alcohol to the corresponding aldehydes.[41] The active species involved in GAO is a Cu(II)-superoxo moiety, which reduces O_2 into H_2O_2 (Figure 1.3.7).

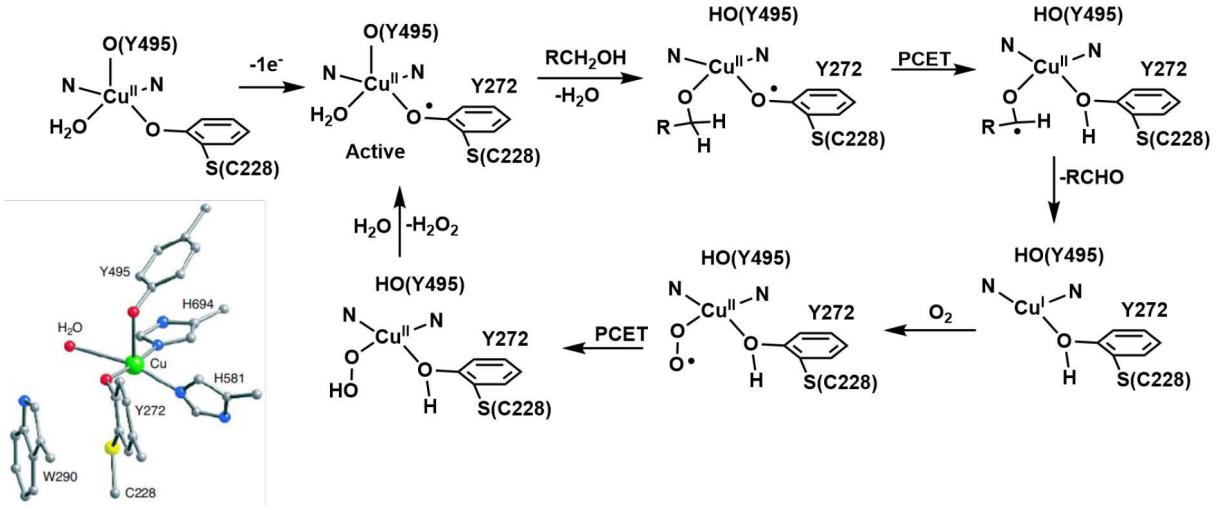

Figure 1.3.7: Crystal structure of the so-called inactive form of GAO and the catalytic cycle of alcohol oxidation.[41a]

Another well-studied copper-containing mono-oxygenase enzyme is tyrosinase which is capable of oxidizing phenols to ortho-catechols and ortho-quinones.[42] The resting state of tyrosinase contains a dinuclear copper(I) site, which binds with oxygen to form a μ-η^2: η^2-peroxo-dicopper(II) species. This dicopper(II) peroxo species then reacts rapidly with the substrate and forms isomeric bis-(μ-oxo)-dicopper(III) species. This bis-μ-oxo core is believed to be responsible for the ortho-hydroxylation reaction *(*Figure 1.3.8*)*.[43] However, it is known

that the interconversion of μ-η^2:η^2-peroxo-dicopper(II) and isomeric bis-(μ-oxo)-dicopper(III) cores are exceedingly rapid, and it is still a subject of considerable interest. Another important dicopper enzyme is particulate methane monooxygenase. It can oxidize methane to methanol.[44]

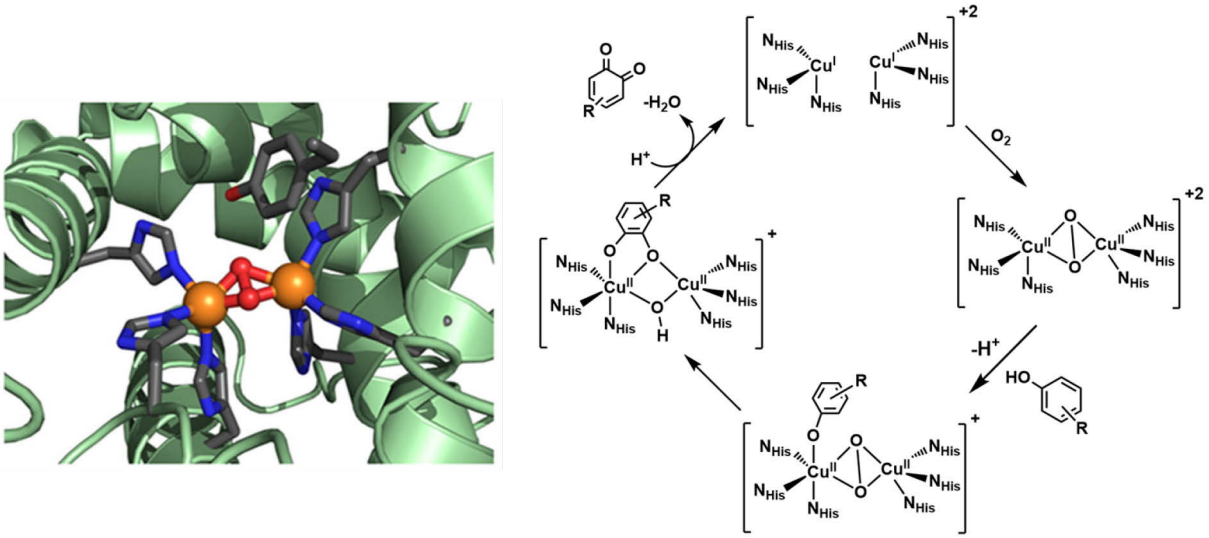

Figure 1.3.8: Crystal structure of substrate-bound tyrosinase and the proposed catalytic cycle of phenol oxidation.[43]

Some other copper-containing monooxygenase enzymes are dopamine-β-monooxygenase (DβM) and peptidylglycine-α-hydroxylating monooxygenase (PHM). The proposed active intermediates involved in both the enzymes are [Cu^{II}-O· or Cu^{III}-O]. These enzymes can hydroxylate a C-H bond using a second reducing equivalent from a distant copper center.[45] An extensive amount of research has been done so far to understand the role of the different copper-oxygen adducts in the oxidation chemistry by natural enzymes[46], however, the search for the terminal high valent copper-oxo core is still missing in the literature.

The above-discussed enzymes are all distinct and perform specific reactions. The nature of the reactivity depends on the stability of the intermediates involved in the reaction mechanism. The metal centers and the ligand environment present in the enzyme play a key role in controlling the stability and reactivity of the different intermediates. Notably, very small changes in the local (ligand) environment of the heme-Fe-O_2 moiety results in absolutely varying chemistry; for example, replacement of the axial cysteine ligand with a histidine residue leads to reversible oxygen activation in hemoglobin that enables its use as an oxygen transfer protein. Similarly, the incorporation of an essential copper metal center proximate to the heme cofactor initiates the oxidase activity in cytochrome C oxidase (C*c*O) that performs the 4e- reduction of O_2 to water. Therefore, a complete understanding of these reactive intermediates is necessary to

develop the synthetic catalysts capable of performing similar reactions. Biomimetic model complexes can provide useful information for a better understanding of known biological intermediates. Furthermore, the ligand environments of the model complexes can be modified both electronically and sterically to get more insights into the enzymatic catalytic mechanisms.

The involvement of high-valent metal oxo core in biological oxidation reactions makes them interesting targets to study. The generated metal-oxo species is subsequently used in a number of two-electron substrate oxidation reactions in oxygenases, or protonated to release water in oxidases. Over the years, a vast number of metal oxo complexes have been synthesized and studied, with a special focus on oxoiron(IV) species. A large number of model iron(IV)-oxo cores have been synthesized in the last two decades; unfortunately, none of them is as reactive as their biological counterparts.[47] The synthetic metal-oxo species have been found to be reactive only toward substrates containing weak C–H bonds. Moreover, in most cases, their reactions are non-catalytic. Furthermore, only in very few cases, the synthetic catalysts are involved in initiating O–O bond formation reactions, and catalytic dioxygen reduction reactions.

In this context, it is important to understand the electronic nature of the metal-oxo species. By increasing the *d*-electron counts on the metal center in tetragonal geometry, the metal-oxo bond order starts decreasing, which increases the nucleophilicity of the oxo group (Figure 1.3.9).[48]

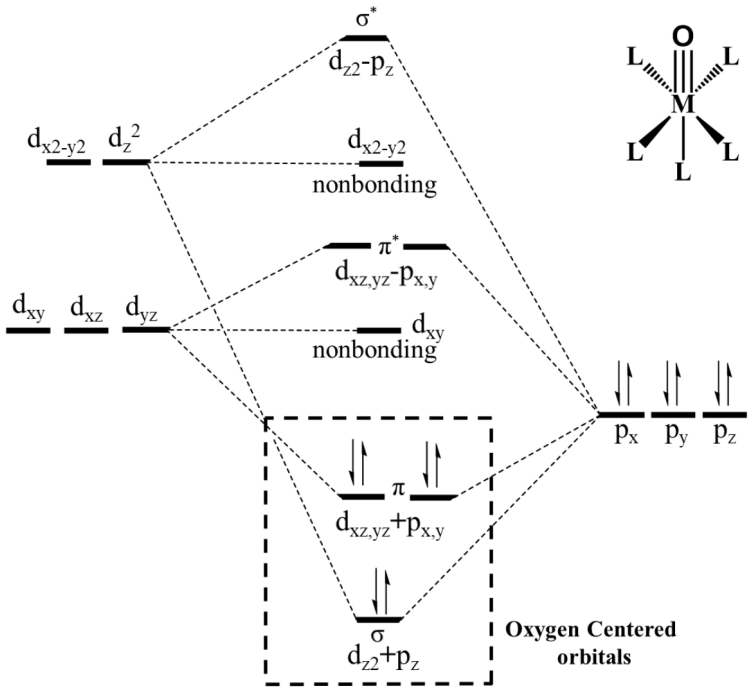

Figure 1.3.9: Schematic representation of the molecular orbital diagram for a $[M(L)_5O]$ complex in a tetragonal symmetry.[48]

A nucleophilic oxo should be amenable for protonation leading to water generation (relevant to the reduction of dioxygen to water). In general, early transition metal complexes that form stable metal-oxo cores, preferably reduce O_2 via a 4*e*- reduction pathway to form water, whereas, the late transition metal complexes typically follow a 2*e*- pathway to yield H_2O_2. However, late transition metal complexes can also reduce O_2 to water catalytically via the formation of binuclear peroxo species followed by homolytic O-O bond cleavage.[49]

As discussed before, the formation of metal-oxo species is the last step of the metal-mediated O-O bond cleavage process. The other metal-dioxygen intermediates involved (such as metal-superoxo, -peroxo, and -hydroperoxo) in the metal-mediated dioxygen activation process are also interesting to study.

1.4. Late transition metal-dioxygen intermediates

Extensive gas-phase studies together with theoretical calculations on methane activation processes mediated by different metal-oxo systems have revealed that the metal-oxo core with metals beyond iron, such as nickel and cobalt, are more reactive towards hydrocarbon functionalization. These studies suggested that on going from left to right across the transition metal series, in the periodic table, the metal-oxygen bond in metal-oxo becomes more naked and weaker. However direct evidence of the late transition metal-oxo cores having *d*-electron count ≥ 5 remains elusive in literature.[50a] Due to the extreme repulsion between the Lewis basic oxo ligand, which is a strong π-donor and the *d*-electrons of the metal center[50b], the terminal M-O bond becomes weaker and unstable, hence more reactive. The ongoing research to isolate the late transition metal-oxo core suffers from its transient nature.[51] Many late transition metal complexes have been synthesized in the last decades, however, their reaction with oxygen or oxidants leads to the formation of metal dioxygen intermediates. Several metal-dioxygen intermediates formed by the late transition metal complexes (e.g. Co, Ni, Cu) with O_2 or H_2O_2 have been isolated and characterized successfully. Recent advances in biomimetic studies have led to the synthesis, characterization, and reactivity studies of a number of metal–superoxo and -peroxo complexes as biomimetic models of the reactive intermediates proposed in biological O_2 reductions.

The initially formed metal-superoxo species can also undergo a C-H bond activation reaction to initiate four-electron oxidation of substrates by a single equivalent of dioxygen in the absence of any reducing cosubstrates.[52] The study of different model complexes shows the electrophilic nature of the metal-superoxo species. Few examples of metal superoxo cores in synthetic models also perform nucleophilic reactivities. In heme enzymes (Cyt P450) and model

complexes, metal-peroxo species act as a nucleophile to attack (among other electrophiles) aldehydes, leading to the production of formate and oxidized coproducts[53] The electrophilic reactions by metal-peroxo cores have also been suggested in biology.[54] However, the synthetic metal-peroxo model complexes with electrophilic nature remain elusive in literature. The details of this exceptional behavior by the newly designed synthetic model complexes (metal-peroxo and superoxo) are discussed in Chapters **2** and **3**.

In addition to the enzymes containing dinuclear active sites such as sMMO, C*c*O, tyrosinase, etc., enzymes containing multi-metal clusters in their active sites are also known. Some examples are nitrogenase that uses a Fe_7MoS_9C cofactor to reduce nitrogen to ammonia, and a Mn_4CaO_5 cluster used by Photosystem-II for water oxidation. Synthetic polynuclear metal complexes can reveal information about the effect of metal nuclearity and the importance of cooperativity for the reactivity of these enzymes and their intermediates.

Different strategies are employed by the biomimetic chemists to stabilize the metal-dioxygen intermediates of the late transition metal and to investigate their reactivity pattern with the exogenous substrates. Some key factors involved are

(*a*) Choice of ligand architecture

(*b*) Steric bulk of the ancillary ligand

(*c*) The electronic nature of the ligand used

(*d*) Non-covalent interaction provided by the ligand

(*e*) Effect of Lewis acids such as Sc^{3+}, Y^{3+}, Ce^{3+}, Zn^{2+}, Ca^{2+}, etc.

1.5. Aim of this thesis work

From the above discussion, the importance of the isolation and detailed characterization of reactive metal-dioxygen intermediates is established. Late-transition metal-oxygen species have extreme significance in the design and discovery of versatile catalysts involving biologically innocuous and inexpensive elements. Moreover, detailed mechanistic investigations are needed to understand their role in different organic transformations. During my doctoral research, my efforts were focused on stabilizing and characterizing different metal-dioxygen intermediates and to study their reactivity towards exogenous substrates. I aimed to examine the effect of the '*structure-activity relationship'* of different metal-dioxygen adducts towards exogenous substrates. In my present thesis, I investigated, how a minor change in ligand systems can drastically change the behavior of a given metal-oxygen reactive system.

In the first project (Chapter 2), a new tetranuclear cobalt complex (**Co_4L1)** involving a nonheme ligand system, **L1**, supported on a stannoxane core (Sn_4O_2) was synthesized. This complex acts as a unique catalyst for dioxygen reduction, whose selectivity can be changed from a preferential $4e^-/4H^+$ dioxygen-reduction (to water) to a $2e^-/2H^+$ process (to hydrogen peroxide) only by increasing the temperature from −50 to 30°C. Detailed experimental and theoretical studies confirmed the involvement of an end-on μ-1,2-peroxodicobalt(III) intermediate, whose stability and subsequent reactivity are found to be the controlling factors in the two- vs four-electron reductions of O_2.

In the second project (Chapter 3), a new nickel (II) dibromide complex (**M**) was synthesized from a new dianionic biuret ligand (**L**). Complex **M**, reacts with excess hydrogen peroxide in the presence of a base to generate a nickel(II)-superoxo intermediate (**2a**). The intermediate was characterized by different spectroscopic techniques. The newly synthesized metal-superoxo intermediate showed unprecedented nucleophilic reactivity in oxidation reactions. For the first time, it was possible to isolate a nucleophilic Ni(II)-superoxo species.

1.6. References

(1) W. B. Tolman, Ed., *Activation of Small Molecules*, Wiley-VCH Verlag GmbH & Co. KGaA, Weinheim, Germany, **2006**.

(2) (a) P. Tang, Q. Zhu, Z. Wu, D. Ma, *Energy Environ. Sci.* **2014**, *7*, 2580. (b) R. E. Blankenship, D. M. Tiede, J. Barber, G. W. Brudvig, G. Fleming, M. Ghirardi, M. R. Gunner, W. Junge, D. M. Kramer, A. Melis, *et al*., *Science*. **2011**, *332*, 805.

(3) (a) F. Meyer and W. B. Tolman, *Inorg. Chem.* **2015**, *54*, 5039. (b) B. Milani, G. Licini, E. Clot and M. Albrecht, *Dalton Trans*. **2016**, *45*, 14419.

(4) S. A. Montzka, E. J. Dlugokencky & J. H. Butler, *Nature.* **2011**, *476*, 43.

(5) (a) R. G. Bergman, *Nature*, **2007**, *446*, 391. (b) Editorial, *Nature* **2013**, *495*, 281.

(6) (a) A. E. Shilov and G. B. Shul'pin, *Chem. Rev*. **1997**, *97*, 2879. (b) Editorial, *Chem. Rev.* **2017**, *117*, 8481. (c) J. A. Labinger, *Chem. Rev.* **2017**, *117,* 8483. (d) J. A. Labinger & J. E. Bercaw. *Nature.* **2002,** *407*, 507. (e) R. A. Periana, D. J. Taube, S. Gamble, H. Taube, T. Satoh, H. Fujii, *Science* **1998**, *280*, 560.

(7) (a) H. Arakawa, *et al*., *Chem. Rev*. **2001**, *101*, 953. (b) T. Punniyamurthy, S. Velusamy, & J. Iqbal, *Chem. Rev*. **2005**, *105*, 2329.

(8) B. L. Conley, *et al.,* in *Activation of Small Molecules: Organometallic and Bioinorganic Perspectives* (ed. Tolman, W. B.) 235–285 (Wiley-VCH, **2006**).

(9) P. Muller, *Pure Appl. Chem.* **1994,** *66*, 1077.

(10) (a) K. Godula, D. Sames, *Science,* **2006**, *312*, 67. (b) A. E. Shilov, G. B. Shulpin, *Chem. Rev.,* **1997**, *97*, 2879. (c) J. A. Labinger, J. E. Bercaw, *Nature,* **2002**, *417*, 507.

(11) (a) J. C. Collins, W. M. Hess, F. J. Frank, *Tetrahedron Lett.* **1968**, 3363. (b) D. G. Lee, S. E. Lamb, V. S. Chang, *Org. Synth.,* **1981**, *60*, 11. (c) J.-E. Bäckvall, *Modern Oxidation Methods*; Wiley-VCH Verlag, **2010**.

(12) (a) M. L. Pegis, C. F. Wise, D. J. Martin, and J. M. Mayer., *Chem. Rev.* **2018**, *118*, 2340. (b) W. Zhang, W. Lai, and R. Cao., *Chem. Rev.* **2017,** *117*, 3717.

(13) R. Prabhakar, P. E. M. Siegbahn, B. F. Minaev and H. Ågren*, J. Phys. Chem. B*, **2002**, *106*, 3742.

(14) C. Carbogno, J. Behler, A. Groß and K. Reuter, *Phys. Rev. Lett.*, **2008**, *101*, 096104.

(15). H. Winter, *Phys. Scr.,* **1983**, T3, 159.

(16) (a) R. L. Whetten, D. M. Cox, D. J. Trevor and A. Kaldor*, J. Phys. Chem.,* **1985**, *89*, 566. (b) Xi. Liu, Y. Ryabenkova and M. Conte., *Phys. Chem. Chem. Phys.,* **2015**, *17*, 715-731.

(17) (a) M. Kristiansen, R. D. Scurlock, K.-K. Iu and P. R. Ogilby, *J. Phys. Chem*., **1991**, *95*, 5190. (b) M. A. J. Rodgers, *J. Am. Chem. Soc*., **1983**, *105*, 6201.

(18) W. T. Borden, R. Hoffmann, T. Stuyver, and B. Chen., *J. Am. Chem. Soc.,* **2017**, *139*, 9010.

(19) (a) M. Sono, M. P. Roach, E. D. Coulter, J. H. Dawson, *Chem. Rev.* **1996**, *96*, 2841. (b) T. L. Poulos, *Chem. Rev*. **2014**, *114,* 3919.

(20) (a) E. I. Solomon, T. C. Brunold, M. I. Davis, J. N. Kemsley, S.-K. Lee, N. Lehnert, F. Neese, A. J. Skulan, Y.-S. J. Zhou, *Chem. Rev*. **2000**, *100*, 235. (b) M. Costas, M. P. Mehn, M. P. Jensen, L. Que, Jr., *Chem. Rev*. **2004**, *104*, 939. (c) R. P. Hausinger, Crit. Rev. *Biochem. Mol. Biol*. **2004**, *39*, 21. (e) E. G. Kovaleva, J. D. Lipscomb, *Nat. Chem. Biol*. **2008**, *4*, 186. (f) C. Loenarz, C. J. Schofield, *Nat. Chem. Biol*., **2008**, *4*, 152.

(21) K. Ray, F. Felix, B. Wang, W. Nam, *J. Am. Chem. Soc.,* **2014**, *136*, 13942.

(22) L, Vaska. *Acc. Chem. Res.*, **1976**, *9*, 175.

(23) (a) L. Que. Jr, W. B. Tolman., *Nature.,* **2008**, *455*, 333. (b) M. Sono, M. P. Roach, E. D. Coulter, J. H. Dawson, *Chem. Rev*., **1996**, *96*, 2841. (c) W. Nam, Y. O. Ryu, W. J. Song, *J. Biol. Inorg. Chem*., **2004**, *9*, 654. (d) R. M. Burger, *Struct. Bonding* **2000**, *97*, 287. (e) I. G. Denisov, T. M. Makris, S. G. Sligar, I. Schlichting, *Chem. Rev*., **2005**, *105*, 2253.

(24) J. Hohenberger, K. Ray, K. Meyer, *Nat. Commun*. **2012**, *3*, 720.

(25) W. Nam, Guest editorial: dioxygen activation by metalloenzymes and models. *Acc. Chem. Res.* **2007***, 40*, 465.

(26)(a) C. Krebs, D. G. Fujimori, C. T. Walsh, & J. M. Bollinger, Jr., *Acc. Chem. Res.* **2007**, *40***,** 484. (b) M. Costas, M. P. Mehn, M. P. Jensen, & L. Que, Jr., *Chem. Rev.* **2004**, *104***,** 939–986.

(27) (a) C. E. Tinberg, & S. J. Lippard, *Acc. Chem. Res.* **2011**, *44,* 280. (b) S. Friedle, E. Reisner, & S. J. Lippard, *Chem. Soc. Rev.* **2010**, *39***,** 2768.

(28) J. Rittle, M. T. Green, *Science.* **2010**, *330*, 933.

(29) M. J. Cryle, J. J. De Voss, *Angew. Chem. Int. Ed.* **2006**, *45*, 8221.

(30) (a) J. T. Groves, G. A. McClusky, *J. Am. Chem. Soc.* **1976**, *98*, 859. (b) F. Ogliaro, N. Harris, S. Cohen, M. Filatov, S. P. de Visser, S. Shaik, *J. Am. Chem. Soc.* **2000**, *122*, 8977.

(31) S. P. de Visser, *Coord. Chem. Rev.* **2009**, *253*, 754–768.

(32) P. K. Grzyska, E. H. Appelman, R. P. Hausinger, and D. A. Proshlyakov*, Proc. Natl. Acad. Sci. U.S.A*. **2010**, *107*, 3982-3987.

(33) (a) D. J. Ferraro, L. Gakhar, S. Ramaswamy, *Biochem. Biophys. Res. Commun*., **2005**, *338*, 175. (b) M. B. Neibergall, A. Stubna, Y. Mekmouche, E. Münck, J. D. Lipscomb, *Biochemistry*, **2007**, *46*, 8004.

(34) L. Que, Jr., Y. Dong, *Acc. Chem. Res.* **1996**, *29*, 190.

(35) (a) M. Merkx, D. A. Kopp, M. H. Sazinsky, J. L. Blazyk, J. Müller, S. J. Lippard, *Angew. Chem. Int. Ed.* **2001**, *40*, 2782. (b) T. C. Brunold, *Proc. Nat. Acad. Sci. USA,* **2007**, *104*, 20641.

(36) W. Nam, *Acc. Chem. Res.,* **2007**, *40*, 522.

(37) Yoshikawa S, Shinzawa-Itoh K, Nakashima R, Yaono R, Yamashita E, Inoue N, Yao M, Fei MJ, Libeu CP, Mizushima T et al., *Science* **1998**, *280,* 1723-1729.

(38) (a) Iwata, S.; Ostermeier, C.; Ludwig, B.; Michel, H. *Nature* **1995**, *376*, 660. (b) Tsukihara, T.; Aoyama, H.; Yamashita, E.; Tomizaki, T.; Yamaguchi, H.; Shinzawa-Itoh, K.; Nakashima, R.; Yaono, R.; Yoshikawa, S. *Science* **1995***, 269*, 1069. (c) Tsukihara, T.; Aoyama, H.; Yamashita, E.; Tomizaki, T.; Yamaguchi, H.; Shinzawa-Itoh, K.; Nakashima, R.; Yaono, R.; Yoshikawa, S. *Science* **1996**, *272*, 1136.

(39) (a) Nam W. *Acc. Chem. Res.* **2007**, 40, 465, and references therein. (b) Proshlyakov, D. A.; Pressler, M. A.; Babcock, G. T. *Proc. Natl. Acad. Sci. U. S. A.* **1998**, *95*, 8020. (c) K. Sengupta, S. Chatterjee, S. Samanta, A. Dey. *Proc. Natl. Acad. Sci. U. S. A.* **2013**, *110*, 8431.

(40) (a) R. H. Holm, P. Kennepohl, E. I. Solomon, *Chem. Rev.* **1996**, *96*, 2239. (b) A. C. Rosenzweig, M. H. Sazinsky, *Curr. Opin. Struc. Biol.* **2006**, *16*, 729.

(41) (a) L. Que. Jr., W. B. Tolman, *Nature*. **2008**, *455*, 333. (b) S.E.V. Phillips et al. *Proc. Natl. Acad. Sci*. **2001**, *98*, 23, 12932.

(42) R. H. Holm, P. Kennepohl, E. I. Solomon, *Chem. Rev.* **1996**, *96*, 2239.

(43) J. S. Plana, I. G. Bosch, A. Company, M. Costas, *Acc. Chem. Res*. **2015**, *48*, 2397.

(44) S. Sirajuddin, A. C. Rosenzweig, *Biochemistry*. **2015**, *54*, 2283.

(45) (a) K. Yoshizawa, N. Kihara, T. Kamachi, Y. Shiota, *Inorg. Chem.* **2006**, *45*, 3034. (b) A. Crespo, M. A. Marti, A. E. Roitberg, L. M. Amzel, D. A. Estrin, *J. Am. Chem. Soc.* **2006**, *128*, 12817. (c) S. Hong, S. M. Huber, L. Gagliardi, C. C. Cramer, W. B. Tolman, *J. Am. Chem. Soc.* **2007**, *129*, 14190. (d) M. Rolff, F. Tuczek, *Angew. Chem. Int. Ed.* **2008**, *47*, 2344. (e) J. P. Klinman, *Chem. Rev.* **1996***, 96,* 2541. (f) S. T. Prigge, B. A. Eipper, R. E. Mains, L. M. Amzel, *Science.* **2004***, 304,* 864. (g) P. Chen, E. I. Solomon, *J. Am. Chem. Soc.* **2004***, 126,* 4991.

(46) (a) E. A. Lewis, W. B. Tolman, *Chem. Rev*., **2004**,*104*, 1047. (b) L. M. Mirica, X. Ottenwaelder, T. D. P. Stack, *Chem. Rev*. **2004**, *104*, 1013. (c) W. B. Tolman, *et al*., *Chem. Rev.* **2017,** *117*, 3, 2059**.**

(47) (a) J.-U. Rohde, J.-H. In, M. H. Lim, W. W. Brennessel, M. R. Bukowski, A. Stubna, E. Münck, W. Nam, L. Que, Jr., *Science* **2003**, *299*, 1037. (b) J. Kaizer, E. J. Klinker, N. Y. Oh, J.-U. Rohde, W. J. Song, A. Stubna, J. Kim, E. Münck, W. Nam, L. Que, Jr., *J. Am.Chem. Soc.* **2004**, *126*, 472. (c) J. England, M. Martinho, E. R. Farquhar, J. R. Frisch, E. L. Bominaar, E. Münck, L. Que, Jr., *Angew. Chem. Int. Ed*. **2009**, *48*, 3622. (d) J. England, Y. Guo, E. R. Farquhar, V. G. Young. Jr., E. Münck, L. Que. Jr., *J. Am. Chem.Soc.* **2010**, *132*, 8635. (e) J. England, Y. Guo, K. M. van Heuvelen, M. A. Cranswick, G. T. Rohde, E. L. Bominaar, E. Münck, L. Que, Jr., *J. Am. Chem. Soc.* **2011**, *133*, 11880. (f) A. R. McDonald, Y. Guo, V.-V. Vu, E. L. Bominaar, E. Münck, L. Que. Jr., *Chem. Sci.* **2012**, *3*, 1680. (g) A. R. McDonald, L. Que. Jr., *Coord. Chem. Rev.* **2013**, *257*, 414. (h) X. Engelmann, I. Monte-Pérez, K. Ray, *Angew. Chem. Int. Ed.* **2016**, *55*, 7632.

(48) (a) K. Ray, F. Heims, F. F. Pfaff, *Eur. J. Inorg. Chem.* **2013,** *2013*, 3784. (b) K. Ray, F. Heims, M. Schwalbe, W. Nam, *Current Opinion in Chemical Biology,* **2015**, *25,* 159.

(49) (a) S. Fukuzumi, H. Kotani, H. R. Lucas, K. Doi, T. Suenobu, R. L. Peterson, K. D. Karlin, *J. Am. Chem. Soc*. **2010**, *132*, 6874. (b) S. Fukuzumi, K. Okamoto, C. P. Gros, R. Guilard, *J. Am. Chem. Soc*. **2004**, *126*, 10441. (c) S. Fukuzumi, S. Mandal, K. Mase, K. Ohkubo, H. Park, J. BenetBuchholz, W. Nam, A. Llobet, *J. Am. Chem. Soc*. **2012**, *134*, 9906. (d) D. Das, Y.-M. Lee, K. Ohkubo, W. Nam, K. D. Karlin, S. Fukuzumi, *J. Am. Chem. Soc.* **2013,** *135*, 4018.

(50) (a) M. K. Goetz, E. A. Hill, A. S. Filatov, J. S. Anderson, *J. Am. Chem. Soc.* **2018**, *140*, 13176. (b) C. Limberg, *Angew. Chem. Int. Ed.* **2009**, *48*, 2270.
(51) (a) S. Hong, F. F. Pfaff, E. Kwon, Y. Wang, M. S. Seo, E. Bill, K. Ray, W. Nam, *Angew. Chem. Int. Ed.* **2014**, *53*, 10403. (b) F. F. Pfaff, S. Kundu, M. Risch, S. Pandian, F. Heims, I. Pryjomska-Ray, P. Haack, R. Metzinger, E. Bill, H. Dau, P. Comba, K. Ray, *Angew. Chem. Int. Ed.* **2011**, *50*, 1711. (c) B. Wang, Y. Lee, Tcho, W., et al., *Nat Commun*. **2017**, *8*, 14839.

(52). (a) S. Fukuzumi, Y.-M. Lee, W. Nam, *Dalton Trans*. **2019**, *48*, 9469. (b) G. Xing, L. M. Hoffart, Y. Diao, K. S. Prabhu, R. J. Arner, C. C. Reddy, C. Krebs, J. M. Bollinger, Jr., *Biochemistry* **2006**, *45*, 5393. (c) G. Xing, Y. Diao, L. M. Hoffart, E. W. Barr, K. S. Prabhu, R. J. Arner, C. C. Reddy, C. Krebs, J. M. Bollinger, Jr., *Proc. Natl. Acad. Sci. U.S.A.* **2006**, *103*, 6130.

(53) (a) D. D. LeCloux, A. M. Barrios, S. J. Lippard, *Bioorg. Med. Chem*.**1999***, 7*, 763. (b) D. L. Wertz, J. S. Valentine, *Struct. Bonding.* **2000**, *97*, 37. (c) J. Annaraj, Y. Suh, M. S. Seo, S. O. Kim, W. Nam, *Chem. Commun.* **2005**, 4529. (d) J. Cho, R. Sarangi, J. Annaraj, S. Y. Kim, M. Kubo, T. Ogura, E. I. Solomon, W. Nam, *Nat. Chem*. **2009**, *1*, 568. (e) M. Selke, J. S. Valentine, *J. Am. Chem. Soc*. **1998**, *120*, 2652. (f) J. Cho, R. Sarangi, H. Y. Kang, J. Y. Lee, M. Kubo, T. Ogura, E. I. Solomon, W. Nam, *J. Am. Chem. Soc.* **2010**, *132*, 16977.
(54) (a) A. M. Valentine, S. S. Stahl, S. J. Lippard, *J. Am. Chem. Soc*. **1999**, *121*, 3876. (b) L. G. Beauvais, S. J. Lippard, *J. Am. Chem. Soc*. **2005**, *127*, 7370.

(55) I. M. Pérez, S. Kundu, A. Chandra, K. E. Craigo, P. Chernev, U. Kuhlmann, H. Dau, P. Hildebrandt, C. Greco, C. Van Stappen, N. Lehnert and K. Ray, *J. Am. Chem. Soc*. **2017**, *139*, 15033.

Chapter 2

Synthesis and Characterization of a Tetranuclear Cobalt Complex Supported on a Stannoxane Core with Temperature-Dependent Catalytic Dioxygen Reduction Ability and Unprecedented Amphoteric Reactivity.

A part of this work has been published in

Dalton Trans. **2020**, *49*, 6065–6073

A. Chandra, S. Mebs, S. Kundu, U. Kuhlmann, P. Hildebrandt, H. Dau, K Ray*.

2.1. Introduction

At present, humankind faces critical energy and environmental crises due to the rapid depletion of fossil fuels. Based on the current scenario (reserve levels/ consumption levels) fossil fuels can provide the global energy demand for the next one or two centuries. [1-2] Therefore, the supply of clean and sustainable energy sources is one of the most important scientific challenges in the 21st century. The effective conversion and storage of solar energy are of great interest in these regards. In nature, green plants can successfully convert and store solar energy in chemical form. By using solar energy, water is oxidized at the oxygen-evolving center (OEC) of photosystem II (PSII) to release O_2, which is essential for aerobic life. Meanwhile, generated protons and electrons are eventually used to convert carbon dioxide into carbohydrates. The generated protons help to create a proton gradient, which is used by ATP synthase to generate ATP. The electrons are used to reduce the $NADP^+$ to NADPH. Upon excitation with light, chlorophyll P680 in PSII generates a cation radical $P680^{\bullet+}$, which acts as an electron acceptor to abstract an electron from the adjacent Mn_4CaO_x cluster in OEC. After four successive electron transfer processes, four oxidizing equivalents are stored at the Mn_4CaO_x cluster for water oxidation.[2c] A better understanding of the key step, which is the O-O bond formation reaction leading to the oxidation of water to dioxygen, is needed to increase the effectiveness of the solar-driven fuel cells. Similarly, the O-O bond cleavage reaction of dioxygen to water is also important as it is the common cathodic reaction that is involved in all types of fuel cells. In the fuel-cell, the combustion of hydrogen produces free energy with water as the only byproduct.[3] Commonly used hydrogen fuel cells involve oxidation of hydrogen to protons at the anode and 4*e*- reduction of O_2 to water at the cathode by platinum impregnated in carbon.[4] High loading of the precious metal (such as Pt) is required to get the maximum reactivity, which increases the overall cost for production.[5] Therefore, the development of novel catalysts based on non-precious metals with high efficiency and selectivity for dioxygen reduction reaction (ORR) is highly desirable.

In this context, the oxidase enzymes that can perform the O-O bond cleavage reactions are of particular interest. Catalytic 4*e*- reduction of oxygen to water (Scheme 2.1.1) is not only essential to maintain biological activities but it also has tremendous technological significance.[6] In nature cytochrome *c* oxidase (C*c*O) and multi-copper terminal oxidases such as laccase, catalyze the selective $4e^-$ reduction of dioxygen without producing any partially reduced peroxide or superoxide species (Figure 2.1.1).[7] Therefore, cheap and readily available non-precious transition-metal complexes of Fe, Co, Ni, and Cu have the potential to replace the expensive Pt metal in the fuel cell.

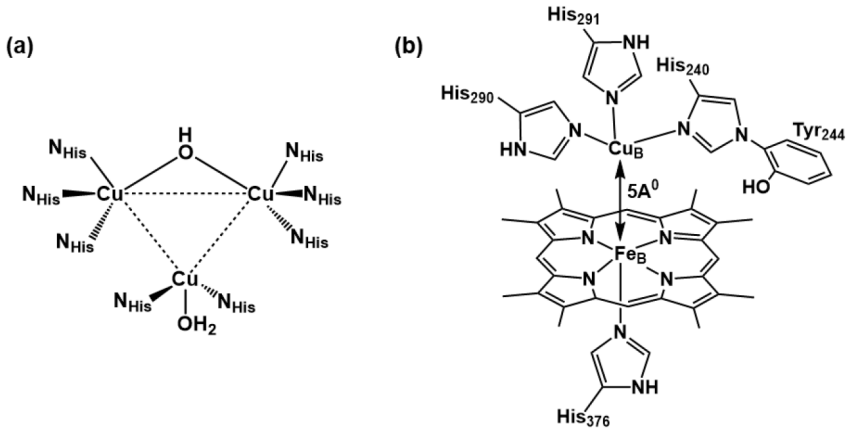

Figure 2.1.1: (a) The tri-nuclear copper cluster of laccases and (b) The active site structure of Cyt-c-oxidase.

The structural feature of C*c*O has already been discussed in Chapter **1**. The X-ray structure of C*c*O has revealed that the catalytic site consists of a bimetallic center of heme a_3 and a tris-histidine- coordinated Cu (Cu_B) (Figure 2.1.1). The distance between the Fe and Cu center is about 5.0 Å. A significant amount of research was done to mimic the coordination environment of the Fe/ Cu core as well as the catalytic function of the four-electron reduction of O_2. So far, the precise role of copper metal center (Cu_B) in the O_2 reduction reaction was not clearly understood. Karlin and coworkers have synthesized a number of model complexes to understand the role of Cu-center (Cu_B) in C*c*O. Dioxygen reactivity on mononuclear heme and its Cu analog suggests the formation of Fe^{III}-peroxo-Cu^{II} species.[7e] The key question is how the C*c*O can reduce O_2 to only water without releasing any trace of H_2O_2. Over the past decades, several heme and non-heme model complexes were synthesized and their reactivity towards O_2 activation was tested. A limited number of heterobimetallic (porphyrin)Fe^{III}-O_2-Cu^{II} complexes are known to date and all feature short Fe-Cu distances of 3.5-4.0 Å. Therefore, the formation of the proposed Fe^{III}-O_2-Cu^{II} core with a significantly shorter Fe-Cu distance (from 5 Å in the reduced form to 3.5-4.0 Å in the oxidized form) may warrant a significant structural distortion relative to the resting state of the enzyme, which may be extremely energy demanding.

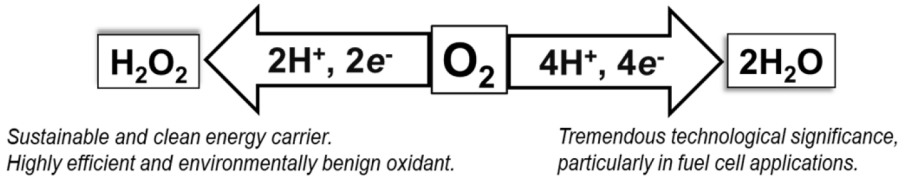

Scheme 2.1.1: Schematic representation of the dioxygen reduction reactions to H_2O_2 and H_2O.

The catalytic $2e^-$ reduction of O_2 to H_2O_2 (Scheme 2.1.1) has also got significant attention. H_2O_2 is considered as a promising candidate for a sustainable and clean energy carrier because of its

high energy density at ambient temperature.[8] H_2O_2 acts as a highly efficient and environmentally benign oxidant in terms of delignification efficiency and the reduction of negative ecological impacts.[9] Industrial production of hydrogen peroxide (the anthraquinone process, Scheme 2.1.2) needs hydrogen as a reducing agent and palladium to regenerate the anthrahydroquinone, which increases the production cost significantly.[9d] However, nature uses relatively cheaper copper metal centers in copper oxidase enzymes such as galactose oxidases (GAO), and copper amine oxidases (CAO) for selectively reducing O_2 to H_2O_2 via a 2*e*-reduction process during substrate oxidation reactions.[10]

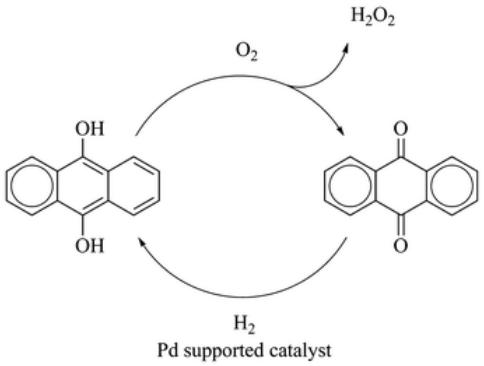

Scheme 2.1.2: Catalytic hydrogen peroxide production through the anthraquinone process.[9d]

Catalytic O_2 reduction by metal complexes in homogeneous systems can provide deeper mechanistic insights about the controlling factors of the O_2 reduction process. The stability of the metal dioxygen species, involved during dioxygen reduction reaction, plays a key role in controlling the $2e^-$ vs $4e^-$ reduction process of O_2. Several factors control the stability of the M-O_2 adducts such as metal nuclearity, ligand environment, the distance between the metal centers, etc. Change in ligand environments or in the distance between the metal centers, which are involved in the formation of the metal dioxygen intermediates can vary the stability of the metal-dioxygen intermediates.

An extensive amount of research has been carried out for decades to develop efficient catalysts based on cheap transition metals, which can reduce O_2 selectively. Unfortunately, the model complexes reported to date suffer from poor selectivity and non-catalytic activity. The activities exhibited by the previously synthesized model complexes are found to be falling far short of the activity of the biological catalysts in many cases, which have prevented their technological applications. Thus, new and innovative synthetic strategies are still needed to seek out the problem and for a better understanding of the enzymatic mechanisms. Recently multinuclear transition metal catalysts have been under investigation for small molecule activation processes because of their higher catalytic efficiency. In this respect, transition metal-based dendrimer

ligand structures are of special interest because they can provide synergistic interactions between the multiple metal centers.[11] Transition metal complexes with dendrimer structures have potential applications in various fields, as they can provide a closed framework, where the extensive cooperative effect between the individual metal centers can be observed towards small molecule activation.[12] However, the synthetic challenges related to the generation of such suitable multinuclear ligands have restricted this research field. The organo-stannoxane approach, first proposed by Chandrasekhar and coworkers in 2005, is an efficient methodology for dendrimer ligand synthesis containing multiple pockets for binding metal centers.[12b]

The same strategy was taken by our group to explore the cooperativity and synergistic effects between the transition metal centers towards dioxygen activation. In 2012, Ray and coworkers reported the synthesis of a non-heme hexanuclear ligand (**L2**) supported on a stannoxane core (Sn_6O_6) and its iron(II) complex $\{[Fe_6L2]^{12+}\}$. This iron(II) complex performed an intramolecular O−O bond formation reaction when it reacted with 2-(tert-butylsulfonyl)-iodosylbenzene (^{s}PhIO) in CH_2Cl_2 at 25 °C. Theoretical calculations suggested that the reaction occurred via the formation of a bridged diiron(III)-peroxo (Fe^{III}-O-O-Fe^{III}) intermediate.[13] The M-O-O-M peroxo cores (where M= metal center) are also proposed intermediates in metal-mediated O_2 reduction reactions. Based on the efficiency of the ligand architecture in performing the O-O bond formation reaction by the iron complex $\{[Fe_6L2]^{12+}\}$, it can also be predicted that the same ligand architecture can support the O-O bond cleavage reaction. Following this idea, in 2017, Ray and co-workers reported the synthesis and characterization of a novel hexanuclear cobalt(II) complex $\{[Co_6L2]^{12+}\}$ (or **Co_6L2)** based on the same drum-shaped hexanuclear ligand having a stannoxane (Sn_6O_6) core.[14] The hexanuclear cobalt(II) complex $\{[Co_6\ L2]^{12+}\}$ reacted with dioxygen reversibly in the temperature range from -50 ºC to +25 ºC. The replacement of the metal centers from iron to cobalt increased the stability of the M^{III}-O-O-M^{III} core, which is evident from the isolation of the corresponding $\{[L2(Co^{III}\text{-}O\text{-}O\text{-}Co^{III})_3]^{12+}\}$ (*S=0*) complex upon dioxygen activation. The hexa-cobalt(II) complex $\{[L2Co_6]^{12+}\}$ showed unprecedented catalytic reactivity towards dioxygen reduction reaction, whose selectivity can be changed from a preferential $4e^-/4H^+$ dioxygen-reduction (to water) to a $2e^-/2H^+$ process (to hydrogen peroxide) only by increasing the temperature from −50°C to 25 °C (Scheme 2.1.3). A variety of spectroscopic techniques with advanced theoretical calculations were applied to explore the geometric and electronic structure of **Co_6L2** and the corresponding peroxo intermediate. The change in selectivity of the catalyst **Co_6L2**, towards dioxygen reduction with temperature, can be explained by the constraint provided by the stannoxane core that makes the dioxygen binding to **Co_6L2** an entropically unfavorable process.

The end-on peroxodicobalt(III) intermediate was unstable at 25 °C leading to the generation of H_2O_2 via the $2e^-/2H^+$ process. In contrast, at −50 °C, the higher thermodynamic stability of the bridging peroxo intermediate led to the cleavage of the O−O bond to complete the O_2 reduction to H_2O via the overall $4e^-/4H^+$ pathway.

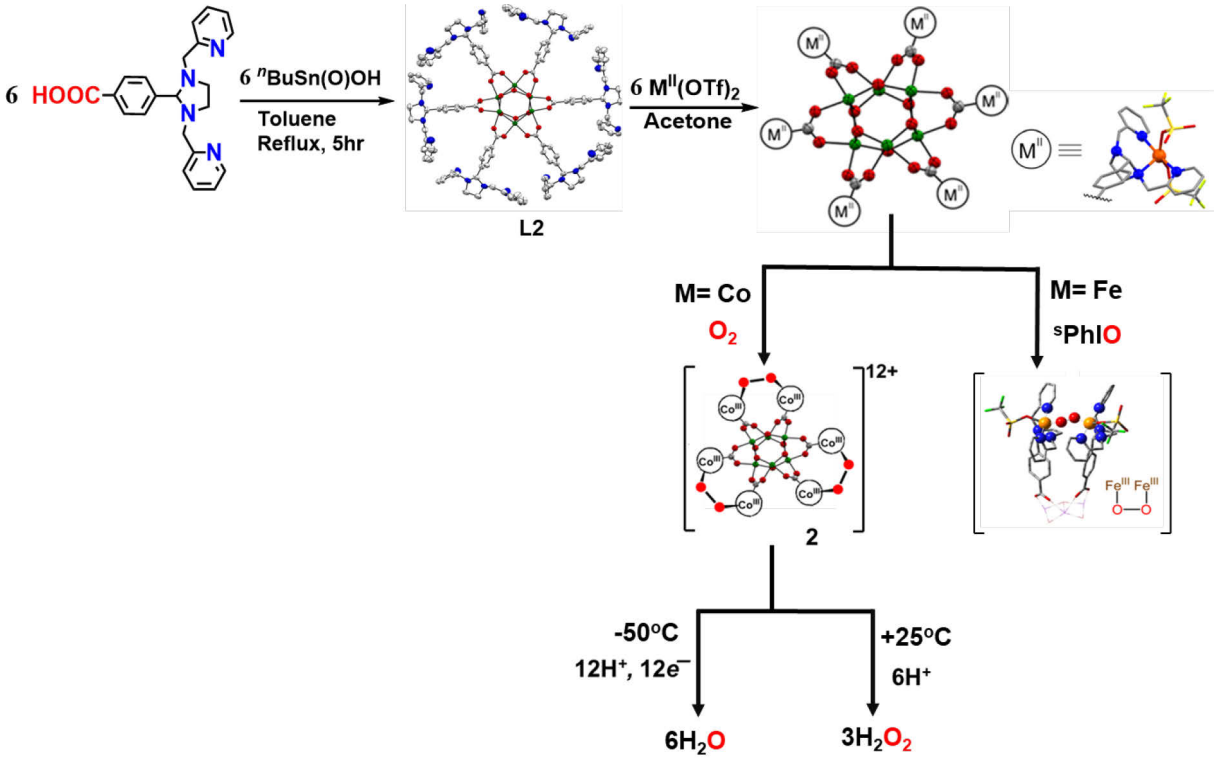

Scheme 2.1.3: Schematic representation of the preparation of a hexanuclear nonheme ligand and its corresponding metal complexes. The reactivities of the iron(II) and cobalt(II) complexes towards dioxygen activation are also shown.[13,14]

The important lessons that we learned from the above discussion are (*a*) the metal peroxo intermediate plays a key role in the dioxygen reduction reaction and it is the stability of the metal-peroxo species which governed the O_2 reduction pathways; (*b*) the stability of the metal peroxo species significantly depends on the nature of the central metal ion; (*c*) for dinuclear metal peroxo species the stability depends on the distance between the metal centers before O_2 binding, which depends on the constraint provided by the ligand architecture.

These findings inspired us to investigate more about the involvement/ role of the supporting dendrimer stannoxane ligand structures towards dioxygen reduction reaction as the organooxotin clusters are known to form a diverse arrangement of structures.[15] The present work shows how the change in ligand architecture (leading to the variation of metal-metal distance in the polynuclear metal complex) affects the catalytic oxygen reduction reaction.

2.2. Results and Discussion:

2.2.1. Syntheses and Characterization of a Tetranuclear Ligand (L1)

The condensation reaction of equimolar amounts of di-*n*-butyltin oxide ($^{n}Bu_2SnO$) and 4-(1,3-bis(2-pyridylmethyl)-2-imidazolidinyl)benzoic acid (**L0**) in dry toluene afforded the tetranuclear ligand (**L1**) as a yellow solid (Scheme 2.2.1). **L0** was synthesized from the condensation of N,N'-Bis(pyridin-2-ylmethyl)-ethane-1,2-diamine (bispicen) with 4-carboxybenzaldehyde in anhydrous ether. Bispicen ligand was prepared according to the reported method.[16]

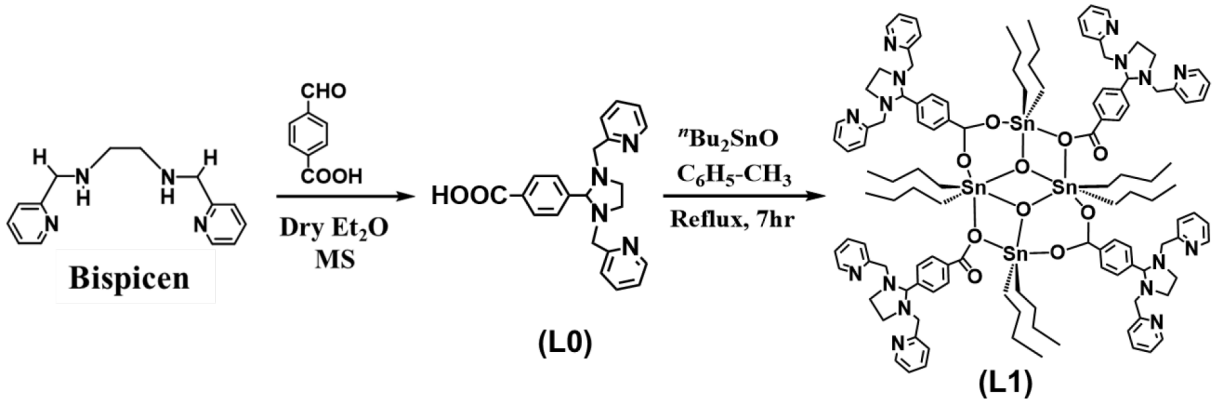

Scheme 2.2.1: Synthesis of the tetranuclear stannoxane ligand.

The ligand **L1** is characterized by various spectroscopic techniques. ^{119}Sn-NMR spectrum of **L1** shows two sharp singlets of equal intensity at −210.82 ppm and −213.81 ppm (Figure 2.2.1a), which is the characteristic signature for a planar Sn_4O_2 core.[17] The infrared spectrum shows four vibrations at 1622 cm^{-1}, 1591 cm^{-1}, 1569 cm^{-1}, and 1545 cm^{-1} for the carboxyl absorptions (ν_{COO}), and one strong band at 682 cm^{-1} assigned to ν_{Sn-O} for the Sn_4O_2 core (Figure 2.2.1 b).

Unlike the previously reported drum-shaped hexanuclear ligand, the tetranuclear ligand has a ladder shaped geometry having four tin atoms and two oxygen atoms at the center and four metal-binding sites consisting of one imidazole and two pyridine units. From the crystal structures of the tetranuclear ligand (**L1**), it is evident that out of four only two metal-binding sites are in close proximity to each other (Figure 2.2.2).

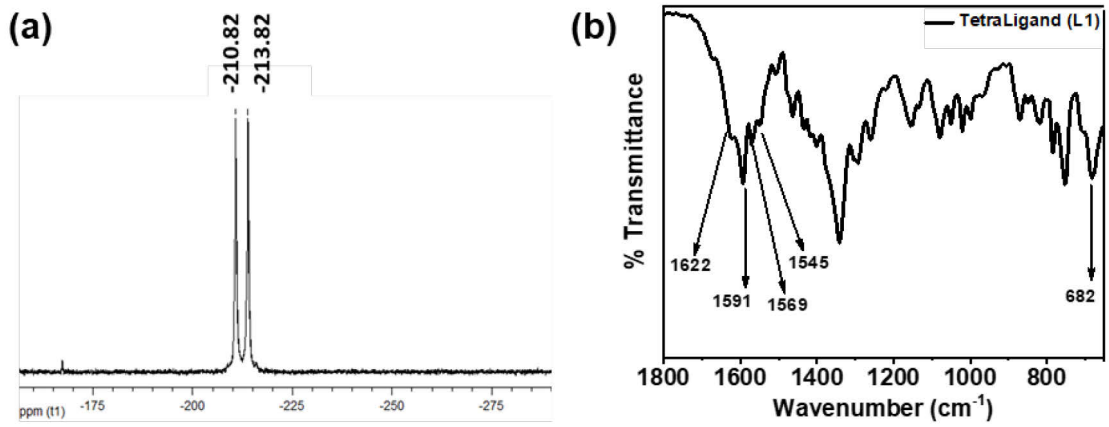

Figure 2.2.1: (a) ^{119}Sn NMR spectrum of **L1** in $CDCl_3$ at 25 °C. (b) The FTIR spectra of the tetrameric stannoxane ligand (**L1**).

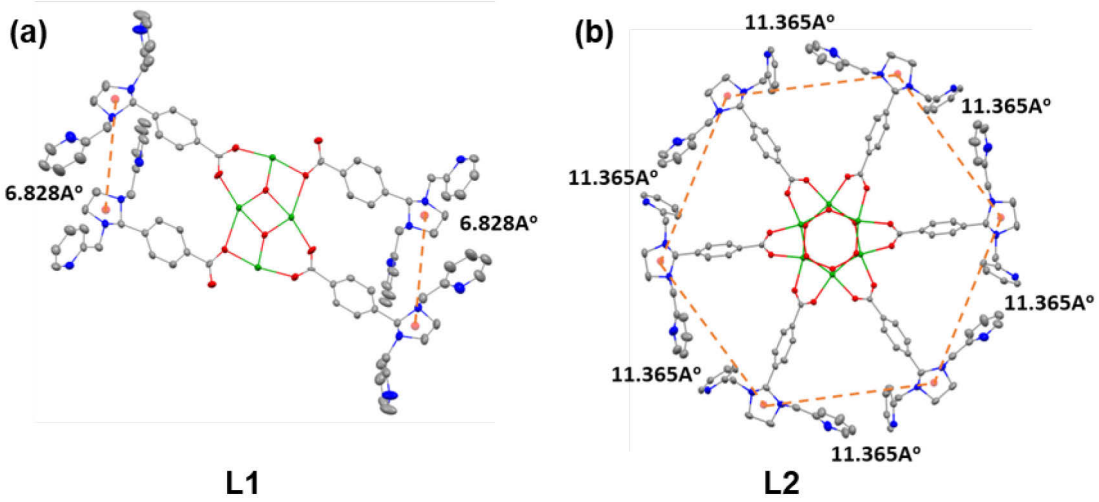

Figure 2.2.2: Distances between the metal-binding sites in the tetranuclear ligand **L1**(left) and the hexanuclear ligand **L2** (right). X-ray crystal structures of **L1** and **L2** are shown with the 30% ellipsoid probability of the atoms. Hydrogen atoms and the n-butyl (^{n}Bu-) groups on the tin atoms have been omitted for clarity. Color code: nitrogen-blue; carbon-grey; oxygen-red; tin-green.

2.2.2. Syntheses and Characterization of an Extended Ligand (L3)

To investigate more about the structure-activity relationship of the 'bispicen' derivatives of the different stannoxane cores towards catalytic O_2 reduction reaction we planned to synthesize the previously reported hexaligand (**L2**) with an extended arm-length attached to the stannoxane core. Our idea was that the extended arm of the stannoxane ligand core may provide extra flexibility to the metal centers towards oxygen binding and will change the catalytic behavior significantly. The extended ligand (**L3**) was synthesized using the ligand precursor '**LE**' with *n*-butylstannoic acid [*n*BuSn(O)(OH)] (Scheme 2.2.2 d*)*. The synthesis of the ligand precursor '**LE**' (Scheme 2.2.2 c) was carried out by following the same procedure as stated before. The

formation of the‘**LE**’ and its purity were corroborated by proton magnetic nuclear resonance (^{1}H-NMR) and ESI-MS measurements (Figure 2.2.3 and Figure 2.2.4).

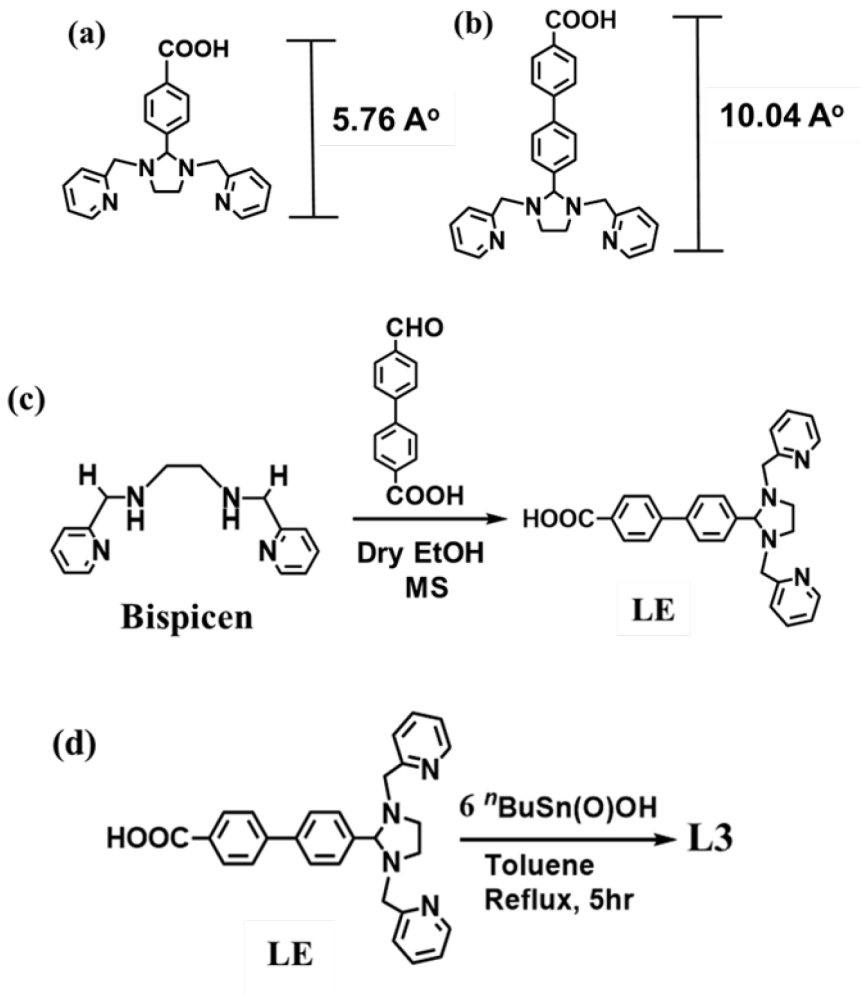

Scheme 2.2.2: (a) The ligand precursor used for the synthesis of the tetranuclear ligand (**L1**) and the previously reported hexanuclear ligand(**L2**). (b) The ligand precursor **LE** with an extended arm length for the synthesis of **L3.** (c) Schematic representation for the synthesis of the ligand precursor **LE.** (d) Synthesis of the extended ligand (**L3)** from the ligand precursor **‘LE’.**

The ligand precursor (**LE)** has been synthesized and characterized successfully. However, the condensation reaction of the ligand **LE** with *n*-butylstannoic acid [*n*BuSn(O)(OH)] (1:1 ratio) in dry toluene (5 hrs reflux) didn’t give the desired result. Analysis of the reaction product confirmed that no hexameric stannoxane core was formed in the reaction. Structurally diverse polynuclear compounds that involve tin centers in different environments show distinct resonances in ^{119}Sn-NMR based on their nuclearity.[17] ^{119}Sn-NMR spectra of the product (**L3**) gives three signals at -281.76 ppm, -456.54 ppm, -482.64 ppm (Figure 2.2.5), which may correspond to a ‘football cage’ structural motif as reported previously in the literature. [17e, 15a] Unfortunately, several attempts to crystallize the new product are not successful so far.

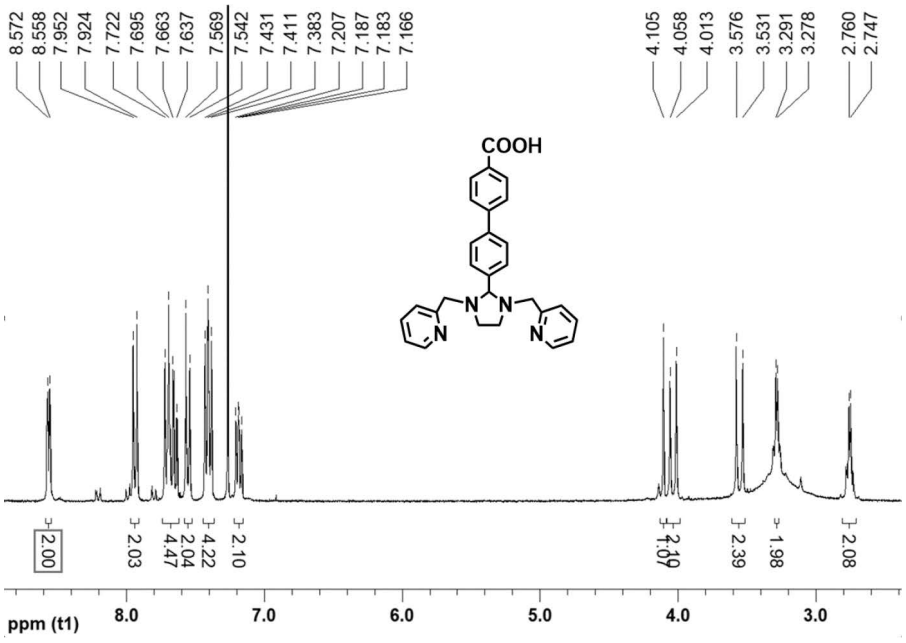

Figure 2.2.3: ^{1}H-NMR spectra of the ligand precursor **LE** in $CDCl_3$.

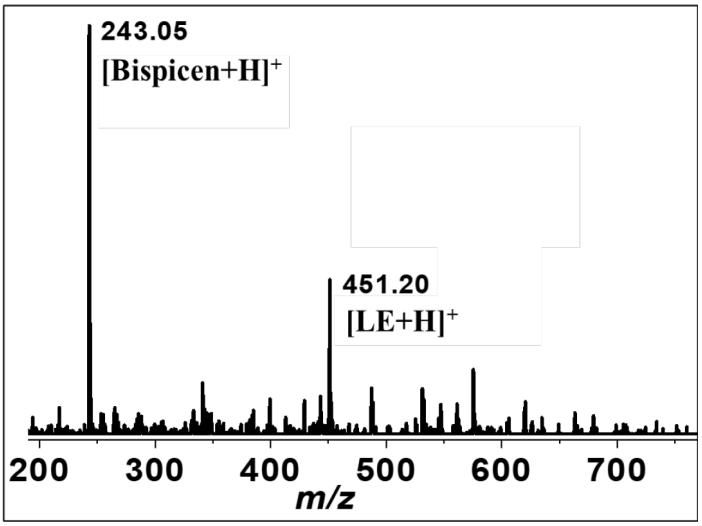

Figure 2.2.4: ESI-MS(+) spectra of the ligand precursor '**LE**'.

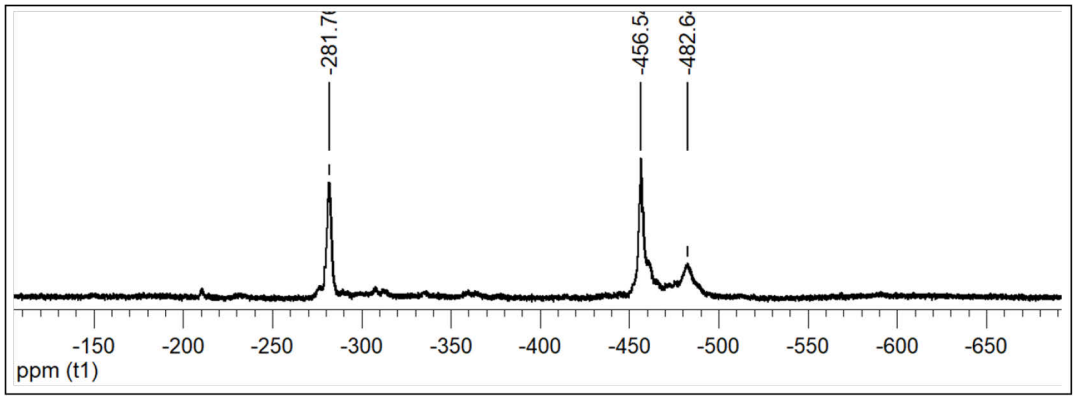

Figure 2.2.5: ^{119}Sn NMR spectra of the reaction product between the ligand precursor **LE** and n-butylstannoic acid in $CDCl_3$ at 25 °C.

Therefore, the exact structure of the ligand **L3** is still unknown to us. In the absence of a proper knowledge of the structure of **L3** no further metallation and dioxygen reduction studies were performed with **L3**.

2.2.3. Syntheses and Characterization of the Tetranuclear Cobalt(II) Complex (Co_4L1)

Metallation reaction of the ligand **L1** with 4.0 equivalent of $Co^{II}(CF_3SO_3)_2$ in acetone yields the metallated species **Co_4L1** as a dark-yellow powder in 75% yield (Scheme 2.2.3). The elemental analysis (EA) data confirmed the presence of four cobalt centers per tetra ligand, each associated with two triflates. The infrared spectrum of **Co_4L1** shows the characteristic vibration bands of the Sn_4O_2 core at 1625 cm^{-1}, 1593 cm^{-1}, 1572 cm^{-1}, and 1549 cm^{-1} for the carboxylates, and 682 cm^{-1} for Sn-O vibration. The vibrations for **L1** and **Co_4L1** are only very slightly shifted, which reveals that the tetranuclear arrangement of the stannoxane core is always maintained in **L1** and **Co_4L1**. Notably, small alternations in structural symmetry of the organostannoxane core is expected to result in large shifts of the ν_{COO} and ν_{Sn-O} vibrations (Figure 2.2.6*a*).[18]

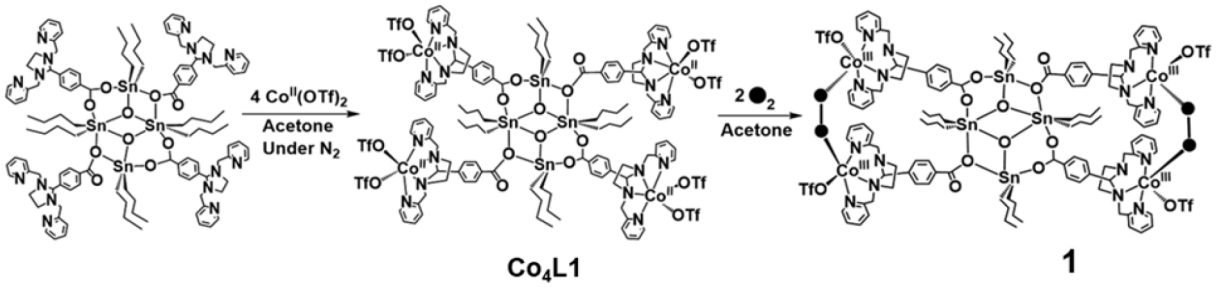

Scheme 2.2.3: Synthesis of the tetra-nuclear cobalt(II) complex (**Co_4L1**) from the tetra-nuclear stannoxane ligand (**L1**) and the formation of the end-on μ-1,2-peroxo-dicobalt(III) species (**1**) after reaction of **Co_4L1** with dioxygen.

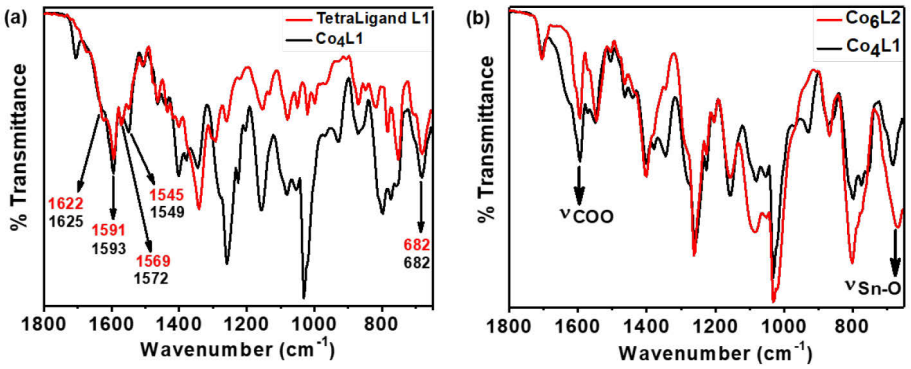

Figure 2.2.6: (a) FTIR spectra of the stannoxane ligand **L1** and **Co_4L1**: vibration frequencies are shown for **L1** (red color) and **Co_4L1** (black color). (b) Comparison between the FTIR spectra of the cobalt complexes containing the hexameric (black line) and tetrameric stannoxane ligands (red line).

Overlap of the infrared spectra of the complexes **Co4L1** and the previously reported **Co6L2** is shown in figure 2.2.6*b*. Both the ν_{COO} and ν_{Sn-O} vibrations are lying in the same region for the complexes **Co4L1** and **Co6L2**.

2.2.3a. EPR spectroscopy: X-band EPR spectrum of **Co4L1** in acetone at 13 K (Figure 2.2.7) exhibits a slightly rhombic signal with *g* values ($g^{\perp} \approx 4.01$ and $g^{\parallel} \approx 2.10$), which is characteristic of a high-spin ($S = 3/2$) cobalt(II) center.[19] Isolation of well-formed $S = 3/2$ signal suggests a lack of interaction between the individual cobalt(II) center within the complex.

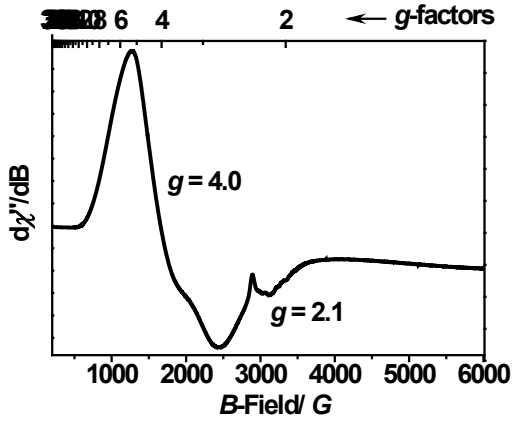

Figure 2.2.7: EPR spectra of complex **Co4L1 (**2 mM**)** in acetone. This spectrum was acquired at 13.5 K, microwave-frequency 9.354355 GHz, using a power of 2.00 mW and a field modulation amplitude of 5.002 G.

2.2.4. Generation and Characterization of the intermediate 1

The reaction of **Co4L1** with O_2 saturated acetone at -50ºC under an inert condition leads to the formation of a deep orange intermediate **1** (Scheme 2.2.4). The formation of **1** was monitored by following the growth of the intense absorption band at 464 nm (ε_{max} = 12,232 $M^{-1}cm^{-1}$, at -50 °C) in the UV-vis spectrum. This process is reversible in the temperature range −50 to 30 °C (Figure 2.2.8).

Formation of **1** is found to be complete within 400 s following first-order kinetics with a rate constant (k_{obs}) of 2.94×10^{-3} s^{-1} at −50 °C. The rate of the reaction is found to be independent of the starting concentration of **Co4L1** (0.015−0.07 mM), thereby suggesting an intramolecular mechanism for the dioxygen activation reaction (Figure 2.2.9).

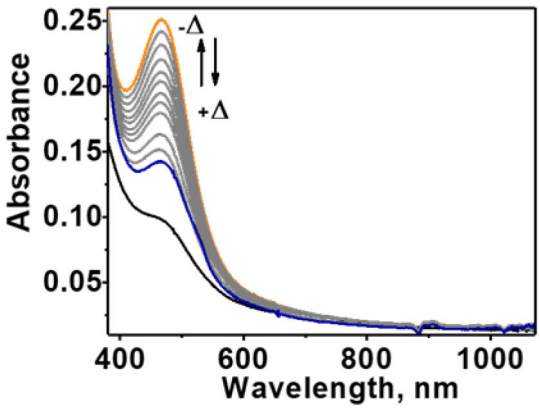

Figure 2.2.8: Absorption spectra showing the reversibility of dioxygen binding to **Co4L1**. The addition of O_2 saturated acetone solution into an acetone solution of **Co4L1** (0.02 mM) produces **1** (in high yield) at −50 °C (orange, solid line). Increasing the temperature up to 25 °C produces the blue solid spectrum. After recooling to −50 °C the orange solid spectrum can be regenerated.

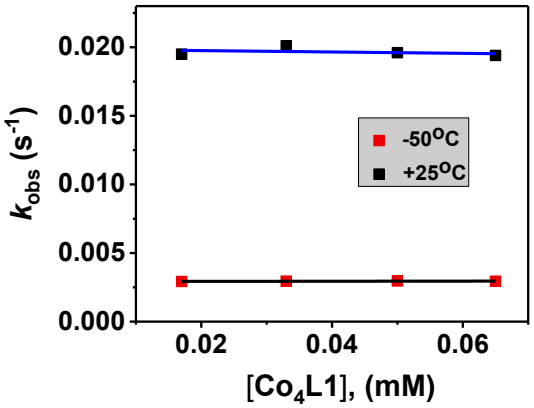

Figure 2.2.9: Plot of the rate of formation of **1** (k_{obs}) vs concentration of **Co4L1** (0.015-0.07 mM) at different temperatures. In each experiment, the amount of oxygen used was constant with respect to the initial concentration of **Co4L1** taken.

2.2.4a. EPR spectroscopy: X-band EPR spectra of the intermediate **1** is silent at 12K, indicating either *S=0* ground state or *S*=2 (an integer spin state).

2.2.4b. Resonance Raman (rR) Spectroscopy: To explore the nature of the intermediate **1,** generated after dioxygen binding to **Co4L1**, resonance Raman (*r*R) spectroscopic experiments were performed using oxygen ($^{16}O_2$ and $^{18}O_2$). The *r*Raman spectrum of **1** (Figure 2.2.10) was measured in acetone-d_6 at −40 °C using a 514 nm laser excitation. Two $^{16}O/^{18}O$ isotopically sensitive vibrational bands were observed at 862 and 595 cm^{-1}, which were downshifted to 808 and 561 cm^{-1} respectively, in the $^{18}O_2$ prepared samples. The 862 cm^{-1} band with an isotopic shift of 54 cm^{-1} is assigned to the O−O stretching mode of a μ-1,2-peroxo-dicobalt(III) core, and the 595 cm^{-1} band with an isotopic shift of 34 cm^{-1} is assigned to the Co−O stretching mode.

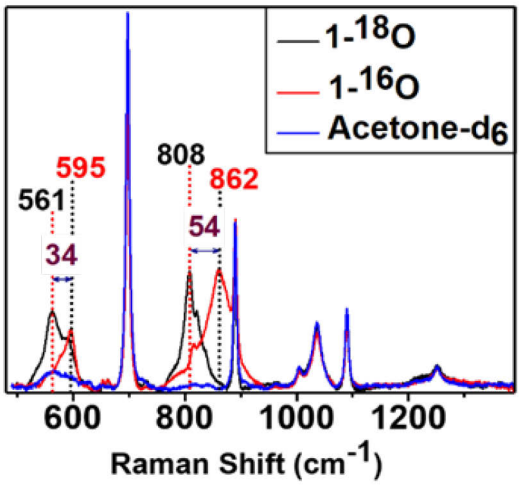

Figure 2.2.10: Resonance Raman spectra of **1** (red trace with $^{16}O_2$ and black trace with $^{18}O_2$) with 514 nm laser excitation in acetone-d_6 at −40 °C. Solvent bands are marked by "blue color".

2.2.4*c.* Electronic and Geometric Structures of Co4L1 and 1:

X-ray absorption spectroscopy (XAS) in conjunction with density functional theory (DFT) calculations were applied to get more insights into the electronic and geometric structures of **Co4L1** and **1**. The oxidation states of the cobalt center in **Co4L1** and **1** were determined by the near edge structure (XANES) and the extended fine structure (EXAFS) explored the local site geometries around the Co atoms in **Co4L1** and **1**. The spectra are displayed in Figure 2.2.11; the corresponding fit values are collected in Table 2.2.1.

The XANES spectrum of the complex **Co4L1 (**the blue one**)** is shown in Figure 2.2.11a. This spectrum is displayed together with spectra from Co reference compounds of known oxidation states (Co^{2+}, $Co^{2.66+}$, Co^{3+}). From the above figure, it is clear that the cobalt center in **Co4L1** is consistent with a Co^{2+} oxidation state (Figure 2.2.11b). The EXAFS of **Co4L1** could be well fitted by four shells (Figure 2.2.11c, d), with one shorter N-shell with coordination number (*N*) of 5, a longer N/O-shell with $N = 1$, and two C-shells with $N = 3$ and 2. There are up to nine C-atoms within a radius of 3.5 Å around the Co-atom, however, due to the pronounced inhomogeneity of the Co–C distances, these shells may partially cancel each other out. The average Co–O/N distance is found to be 2.17 Å.

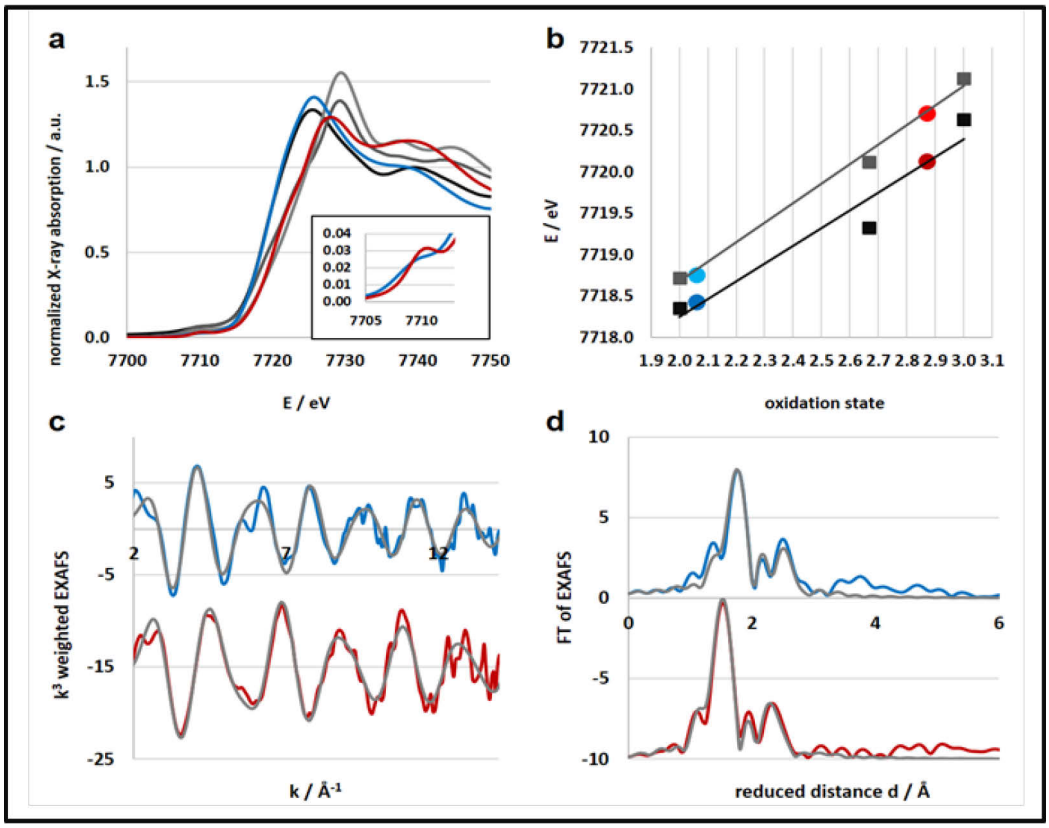

Figure 2.2.11: (a) Co K-edge XANES spectra of reference compounds (black: $Co(OH_2)_6(NO_3)_2$, dark grey: Co_3O_4 spinel, grey: CoOOH) and samples (blue: **Co₄L1**, red: **1**). The horizontal line at 0.5 is used for the determination of the oxidation states. (b) Oxidation states of samples **Co₄L1** and **1** derived from linear fit lines extracted from the 0.5 edge-rise positions of reference compounds (black line and squares) and derived from the integral method (grey line and squares). Both methods result in equal oxidation state assignments. (c) k-space EXAFS spectra (k^3 weighted, colored) and respective fits (grey) (blue: **Co₄L1**, red: **1**). (d) Fourier transform of the EXAFS spectra (colored) and fits (grey) (blue: **Co₄L1**, red: **1**).

Table 2.2.1: EXAFS fit parameters for **Co₄L1** and **1**. [a] Value kept constant in the final refinement. Amplitude reduction factor $S_{02} = 0.95$. 'N' represents the EXAFS coordination number, 'R' the absorber-backscatter distance, and 'σ' the Debye-Waller parameter.

Model	Shell	*N*[a]	*R* (A⁰)	Err	σ (A⁰)	Err
Co_4L1	Co-N	5	2.14	0.01	0.056	0.007
R_f = 18.4	Co-N	1	2.34	0.05	0.056	
E_0 = 0.74	Co-C	3	2.94	0.03	0.056	
d_{av} = 2.17 Å	Co-C	2	3.06	0.05	0.056	
1	Co-N	4	1.91	0.01	0.036	0.009
R_f = 15.0	Co-O	1	2.02	0.03	0.036	
E_0 = 2.82	Co-C	3	2.78	0.03	0.036	
d_{av} = 1.93 Å	Co-C	2	2.92	0.05	0.036	

In the absence of any X-ray diffraction (XRD) structure of **Co₄L1**, there is a possibility that the EXAFS fits may suffer from non-uniqueness and misinterpretations, as the Co atoms are mainly surrounded by O, N, and C atoms with similar scattering properties. To reduce this problem a

computational study was performed utilizing a simplified model involving a single arm of the stannoxane core. DFT calculations were conducted in the experimentally observed (from EPR) $S = 3/2$ spin state for a series of potential structural variants of the monomeric subsection of the organic ligands. As triflate was the only counter anion present during the synthesis, the calculations were also directed to elucidate whether the complex is truly bound by triflate and if so, by how many. This approach is justified as there are no intra-molecular electronic interactions detectable between adjacent Co(II) sites, as evident from the X-band EPR spectrum of **Co$_4$L1**. Different models (*Models 1-6*) were used to verify the best structural model including triflate (OTf) and/or solvent acetone molecules in *cis*- or *trans*-orientations, and with or without inherent molecular symmetry (Figure 2.2.12).

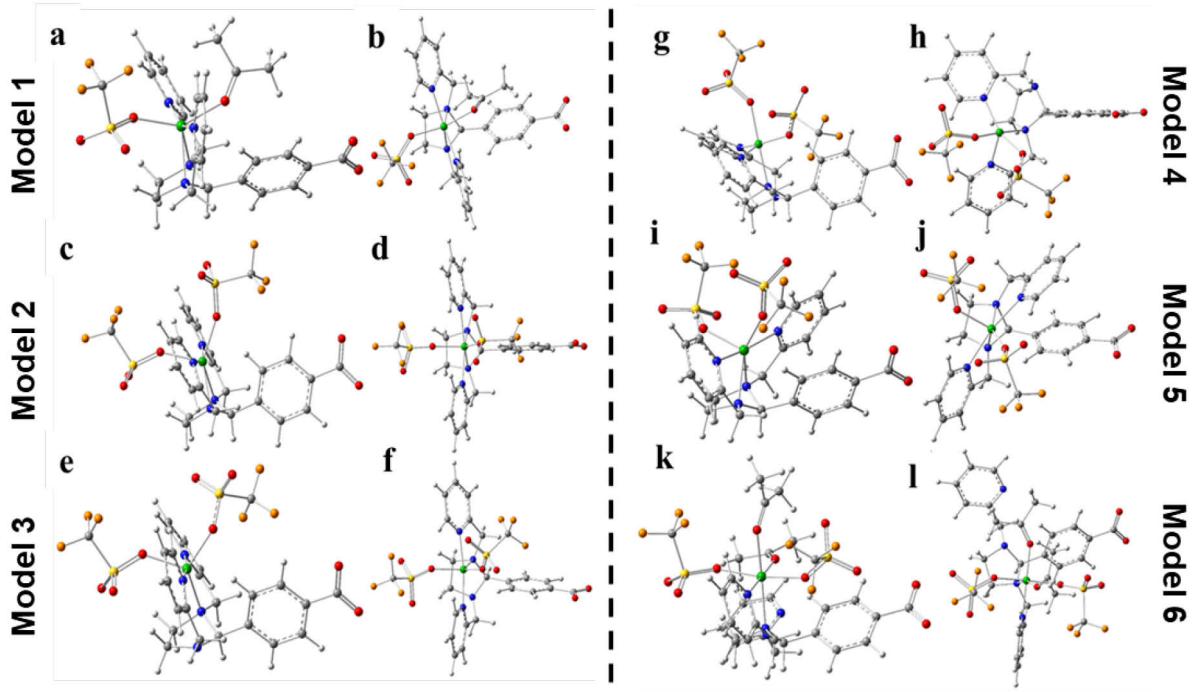

Figure 2.2.12: Left: Side view (left column) and top view (right column) of the DFT optimized models **1-3**. Model **1** (a, b) comprises one triflate anion and one acetone solvent molecule in a trans-like arrangement as coordinating ligands; model **2** (c, d) has two triflate anions under the restriction of Cs-symmetry; model **3** (e, f) is equal to model **2**, but without symmetry restriction.
Right: Side view (left column) and top view (right column) of DFT models **4-6**. Model **4** (g, h) has two triflate anions in a cis-like arrangement; model **5** (i, j) is related to model **3**, but shows less symmetric ligand binding; model **6** (k, l) considers the potential coordination of two triflate anions and two acetone solvent molecules.

Out of the six DFT models, four models show hexa-coordinated Co(II) structures (no. 1, 2, 5, and 6), and the other two show penta-coordination (model no. 3 and 4). All these DFT calculations were done considering both the unprotonated (COO–) and protonated (COOH) DFT models 1-6 (resembling of **Co$_4$L1**) to see the effect of protonation of the carboxylate

group**.** The calculated Co-X (X = N, O) bond distances are listed in table 2.2.2, which suggests that the protonation of the carboxylate group doesn't affect the average Co-X (X = N, O) bond distances.

Table 2.2.2: Calculated Co–X (X = N, O) distances of the unprotonated (COO–) and the protonated (COOH) DFT models **1-6** (in Å) resembling **Co_4L1**, and the dimer model resembling **1**. The effect of protonation of the carboxylate group is negligible. Color code is included to guide the eye. Model **6** has four O-atom and two N-atom ligands. For the 5-coordinate models **3** and **4,** the long Co–N distance was not included in the averaging. O and O` represents the distance (in Å) between the cobalt center and the O-atoms of the coordinated ligand molecules (triflate and/ or acetone) present in the DFT models **1-6.** $N^p$ and $N^{p`}$ represent the distance (in Å) between the cobalt center and the N-atoms of the pyridine moiety in the DFT models **1-6**. N^i and $N^{i`}$ represents the distance (in Å) between the cobalt center and the other two N-atoms present in the coordinated ligand molecules in the DFT models **1-6**. For the dimer model of **1**, **Co1** and **Co2** represent the two cobalt centers present in **1**.

COO-	O	O'	N^i	$N^{i'}$	N^p	$N^{p'}$	d(av)
1	2.14	2.11	2.25	2.17	2.11	2.16	2.16
2	2.15	2.13	2.24	2.24	2.19	2.19	2.19
3	2.04	2.07	3.30	2.10	2.11	2.14	2.09
4	2.16	2.03	3.60	2.18	2.07	2.03	2.09
5	2.15	2.07	2.23	2.27	2.25	2.19	2.19
6	2.12	2.13	2.14	2.05	2.22	2.09	2.13

COOH	O	O'	N^i	$N^{i'}$	N^p	$N^{p'}$	d(av)
1	2.15	2.10	2.25	2.18	2.12	2.16	2.16
2	2.14	2.12	2.25	2.25	2.19	2.19	2.19
3	2.04	2.07	3.31	2.10	2.12	2.14	2.09
4	2.16	2.03	3.56	2.16	2.08	2.04	2.09
5	2.14	2.07	2.21	2.29	2.25	2.19	2.19
6	2.12	2.12	2.13	2.06	2.24	2.09	2.12

1	Otf	OO	N^i	$N^{i'}$	N^p	$N^{p'}$	d(av)
Co1	1.97	1.81	1.92	3.37	1.95	1.92	1.92
Co2	1.97	1.80	1.95	3.27	1.96	1.91	1.92

Since unrestrained EXAFS fits of **Co_4L1** indicate the hexa-coordination, the corresponding DFT models are considered to be closer to the actual structure of **Co_4L1.** The hexa-coordinated model **5** has the lowest molecular energy (Table 2.2.3). Fine structural details are available in the EXAFS wave, which promises more insight into the real structure than geometric and energetic considerations alone. The EXAFS was calculated for all the six DFT models (*Models 1-6*) and compared to the experimental spectra of **Co_4L1** (Figure 2.2.13).

Table 2.2.3: Absolute and relative molecular energies of DFT models **1-6** (unprotonated). Energy differences are referenced to model **5** (highlighted), which has the minimum energy.

model	energy	delta	kJ/mol
1	-2520.475		
2	-3288.748	0.012	31.4
3	-3288.758	0.002	5.2
4	-3288.741	0.019	51.2
5	*-3288.760*	*0.000*	*0.0*
6	-3674.991		

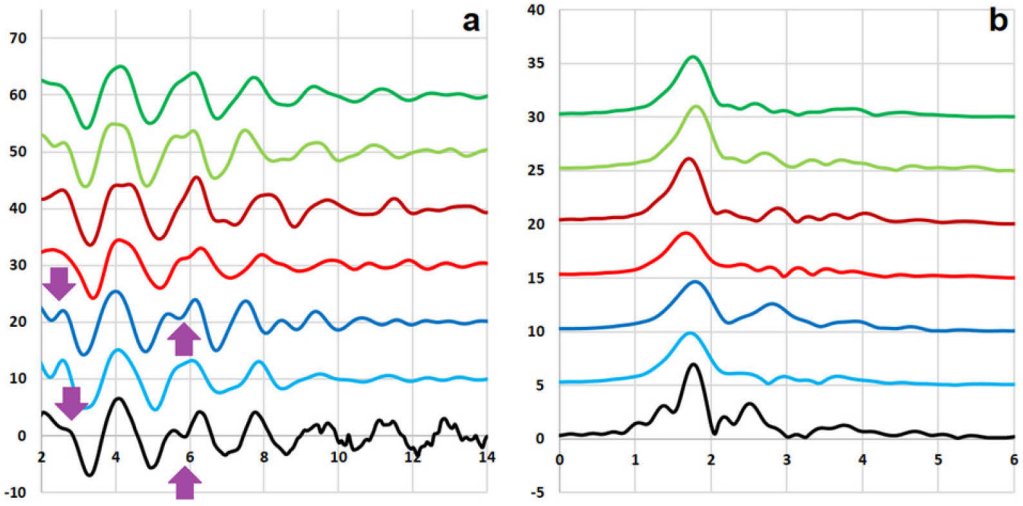

Figure 2.2.13: (a) k^3 weighted EXAFS and (b) FT of EXAFS of DFT models **1** (dark green), **2** (light green), **3** (dark red), **4** (light red), **5** (dark blue), **6** (light blue), and experimental data of compound **Co4L1** (black). The purple arrows are included to guide the eye towards similarities between the DFT spectrum of model 5 and the experimental data of **Co4L1**.

The experimental data and theoretical calculations suggest that model **5** seems to be the closest representative for the structure of **Co4L1**. In this model, the six O and N-atoms bound to the central Co-atom are aligned in a low symmetrical fashion, which might be described as quadratic-pyramidal (O_2N_3) with one (extra) N-atom below (see Figure 2.2.14).

From the viewpoint of the XANES spectrum of **Co4L1**, it looks like typical octahedral or trigonal–bipyramidal (*i.e.* high local coordination symmetry) compounds, very much similar to the hexa–aqua Co(II) compound used for reference (black line in Fig. 2.2.11). The high symmetrical coordination environment around the Co-center in **Co4L1** can be explained from the electronic and steric effects of the agostic proton in the DFT structure (model **5**), which is part of the carboxylated phenyl group, (see Figure 2.2.14). Due to the limited flexibility of the organic ligand, all the six coordinated atoms can't provide the high symmetrical environment

around the cobalt center. However, an unoccupied coordination site can be filled by a C–H···Co contact, which can provide the coordination geometry is an N-capped O_2N_3H–octahedron, (green lines in Fig. 2.2.14).

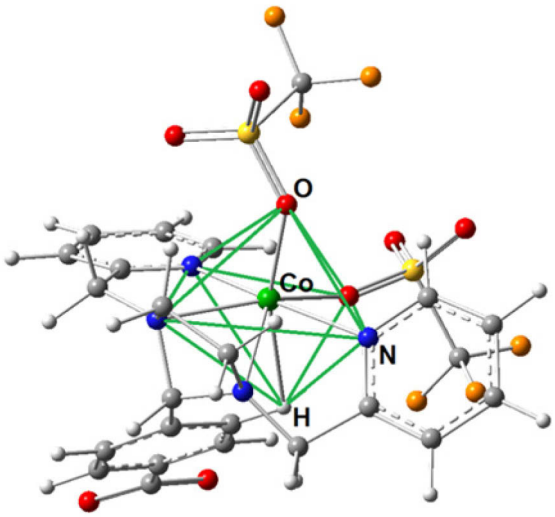

Figure 2.2.14: Energy optimized DFT calculated coordination environment of the individual Co-centers in **Co$_4$L1**(model **5**), which matches best with the experimental data. The straight green lines reveal the N-capped O_2N_3H–octahedron environment of the central Co(II) center, by taking into account the agostic C–H···Co interaction. Color code: nitrogen, blue; carbon, gray; oxygen, red; sulfur, yellow; fluorine, dark yellow; and cobalt, green.

XAS study on 1: The oxidation state and the coordination environment of the Co center in **1** are also examined by XAS study. The XANES spectrum of **1** (Figure 2.2.11*a, b*) suggests almost complete oxidation from Co^{2+} to Co^{3+} during the transformation of **Co$_4$L1** to **1**. The edge shape of **1** shows minor change compared to **Co$_4$L1**. The rise of the pre-edge peak shifts (Figure 2.2.11*a* inset) indicates an increased ligand field strength in **1** compared to **Co$_4$L1**. Lower steepness of the edge rise and formation of a shoulder in the edge indicates a slightly lower coordination number and symmetry in **1**. The EXAFS of **1** reveals a 5-coordinate geometry at Co with 4 short Co–N/O distances at 1.91 Å, and one long Co–N/O distance at 2.02 Å. The average Co–O/N distances of 2.17 Å for **Co$_4$L1** and 1.93 Å for **1**, is a consequence of the different oxidation states and the lower steric requirements of five versus six ligands attached to the Co-atom (Table 2.2.1). The optimized structure (Figure 2.2.15) reveals the presence of a Co^{III}–O–O–Co^{III} unit in **1**. The calculated Co-X (X = N, O) bond distances of the unprotonated (COO–) and protonated (COOH) DFT models resembling the intermediate **1** are listed in table 2.2.2, which suggests that the effect of protonation of the carboxylate group is negligible.

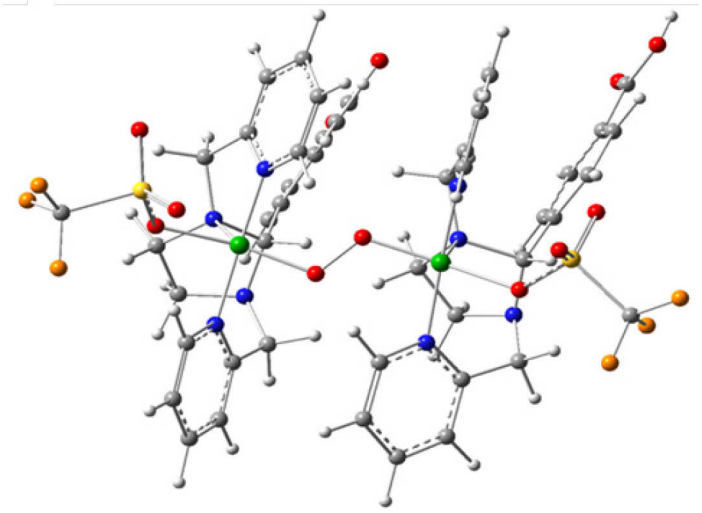

Figure 2.2.15: DFT optimized model of **1** with fixed carboxylate C···C atom distance of 6.43123 Å according to the XRD structure of the free ligand. In **1**, **L1** acts as a tetradentate ligand with one of the nitrogen atoms staying away from the coordination environment of the cobalt center. Color code: nitrogen, blue; carbon, gray; oxygen, red; sulfur, yellow; fluorine, dark yellow; and cobalt, green.

Intermediate **1** is expected to have an $S = 0$ ground state based upon the absence of any EPR signal and DFT calculations as the DFT calculated metrical parameters for the $S = 0$ ground state very well match with the experiments. Previously reported end-on μ-1,2-peroxo-dicobalt(III) complexes[22] are all characterized by the presence of an intense absorption band around 300−500 nm with molar extinction coefficients (ε) > 5000 M^{-1} cm^{-1} whereas the side-on Co(III) peroxo complexes display absorption features with much lower molar extinction coefficients (ε) < 1000 M^{-1} cm^{-1}.[23] Spectroscopic characterization together with theoretical studies of **1** confirms the presence of antiferromagnetically coupled μ-1,2-peroxodicobalt(III) cores in **1** with an $S = 0$ ground state.

2.2.5. Co_4L1 catalyzed dioxygen reduction reaction (ORR)

To date, electrocatalytic method has been mostly applied to study the catalytic activity of synthetic catalysts in the oxygen reduction reaction. However, the electrocatalytic procedure suffers from the difficulties in the detection of active intermediates, which makes mechanistic studies difficult.[24] To overcome this limitation, in 2004, Fukuzumi, Guiliard, and coworkers reported an innovative way of testing the homogeneous catalytic reduction of O_2.[24a] This technique can provide deep mechanistic insights into the oxygen reduction reaction (ORR) employed by homogeneous catalysts. The evaluation of the catalytic activity of **Co_4L1** towards dioxygen reduction was carried out using Fukuzumi and Guilard's method, where ferrocene derivatives were employed as one electron donors, trifluoroacetic acid (TFA) or perchloric acid ($HClO_4$) were used as proton sources, and, in their presence, O_2 was set to react with a catalytic amount of **Co_4L1** in acetone. The occurrence of the oxygen reduction reaction was proved by

the formation of ferrocenium ions with characteristic absorption bands (ferrocenium: λ_{max} = 620 nm, ε = 430 $M^{-1}cm^{-1}$; dimethylferrocenium: λ_{max} = 650 nm, ε = 360 $M^{-1}cm^{-1}$; decamethylferrocenium: λ_{max} = 780 nm, ε = 520 $M^{-1}cm^{-1}$ in acetone).[25]

When **Co_4L1** (0.04 mM) was employed as a catalyst (at 30 ºC, 25 ºC, and -50 ºC) in presence of ferrocene (3 mM) as a reductant and trifluoroacetic acid (TFA) or triflic acid (TfOH) or fluoroboric acid (HBF_4) (10 mM) as proton source in O_2 saturated acetone solution (0.18 mM), no oxygen reduction took place, as evidenced by the absence of any ferrocenium ions in the solution. The same thing happened when 1,1′-Dimethylferrocene (Me_2Fc) was used as the reductant under the same condition. However, when decamethylferrocene ($Me_{10}Fc$ or Fc*) was employed as the reductant under the same condition, O_2 reduction reaction took place, which was proved by the formation of decamethylferrocenium ion (Fc^{*+}) with a characteristic absorption band at 780 nm (Figure. 2.2.16a; $\varepsilon_{780\ nm}$ = 520 M^{-1} cm^{-1}). This phenomenon can be explained by comparing the oxidation potential values of different ferrocene derivatives (Table 2.2.4).

Table 2.2.4: Oxidation potential values of different ferrocene derivatives referred against the saturated calomel electrode (SCE)[26].

Ferrocene derivatives	**Fc**	**Me_2Fc**	**$Me_{10}Fc$**
E_{ox} vs SCE (V)	0.37	0.26	-0.08

Since Fc* is a good electron donor (the strongest reductant listed) and is easily oxidized in the presence of an acid, this reaction also occurs in the absence of the catalyst (**Co_4L1**) but at a significantly slower rate; therefore, the control experiments were always taken into consideration to determine the catalytic capacity of **Co_4L1** towards O_2 reduction reaction.

The dioxygen reduction reaction can occur via two processes: (*a*) two-electron reduction process to form hydrogen peroxide (equation 1) and (*b*) four-electron reduction to water (equation 2).

$O_2 + 2\ Me_{10}Fc + 2\ H^+ \rightarrow 2\ Me_{10}Fc^+ + H_2O_2$ …….(1)

$O_2 + 4\ Me_{10}Fc + 4\ H^+ \rightarrow 4\ Me_{10}Fc^+ + 2\ H_2O$ …….(2)

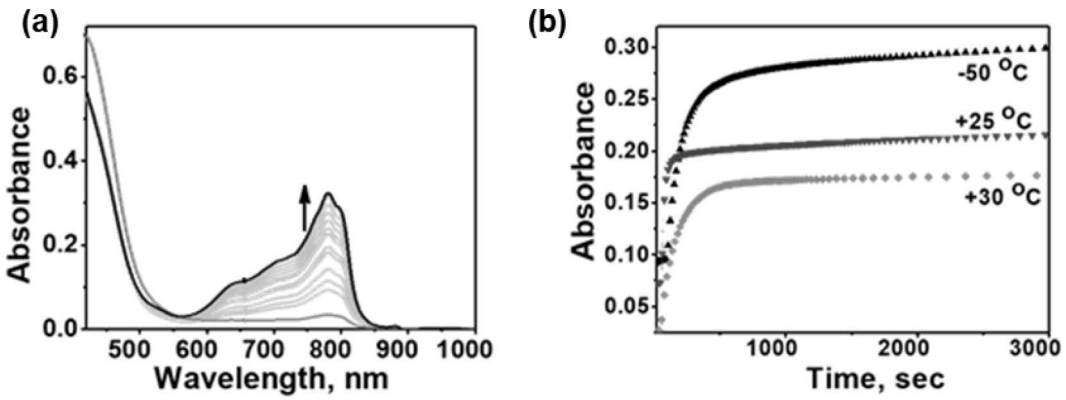

Figure 2.2.3: (a) Spectral changes associated with the catalytic reduction of dioxygen by **Co4L1** (0.04 mM) in the presence of Fc* (3 mM) and TFA (10 mM), at −50 °C (b) Time profiles of the formation of Fc^{*+} monitored at 780 nm during the reduction of O_2 (0.18 mM) by Fc* (3 mM) and **Co4L1** (0.04 mM) in the presence of TFA (10 mM) in acetone at 30 °C, 25 °C as well as at −50 °C.

The concentration of Fc^{*+} formed in the **Co4L1**-catalyzed reduction of O_2 by Fc* depends on the temperature at which the reactions were performed (Figure. 2.2.16b). To understand the detailed mechanistic aspects of the O_2 reduction process, **Co4L1** was employed as a catalyst, and O_2 was used as the limiting reagent. To 2 mL of a dry and oxygen-free acetone solution containing Fc* (3mM), TFA (10 mM) and **Co4L1** (0.04 mM), 0.03 mL of an oxygen saturated acetone solution (11 mM) was added (final concentration 0.18 mM) at -50 °C. The reduction of O_2 was monitored by a rise in the absorbance band at 780 nm which is attributable to the decamethylferrocenium cation (Fc^{*+}) (Figure. 2.2.16a). The formation of Fc^{*+} ion was monitored until the complete conversion of O_2 was achieved and the increase in the 780 nm band was no longer observed. At −50 °C, the amount of Fc^{*+} formed is 0.62 mM, which is 3.45 times relative to the initial concentration of O_2 (0.18 mM). At 30 °C, the amount of Fc^{*+} ion that is generated is 0.35 mM, which corresponds to approximately twice that of the O_2 concentration (0.18 mM). Thus, the two-electron reduction of O_2 predominates at 30 °C. At 25 °C, the amount of Fc^{*+} formed is 0.44 mM, which is 2.5 times higher than the initial O_2 concentration (0.18 mM). The identity of the product formed in the O_2 reduction reaction was confirmed by iodometric and ^{1}H-NMR measurements (Figure. 2.2.17). NaI reacts with H_2O_2 in an acidic media to form the anion I_3^- (equation 3), which has a strong absorbance band at λ_{max}= 360 nm (ε = 28000 $M^{-1}cm^{-1}$) and can be easily detected (Figure. 2.2.17a).[27]

$$3\ I^- + H_2O_2 + 2\ H^+ \rightarrow I_3^- + 2\ H_2O \quad \text{…….. (3)}$$

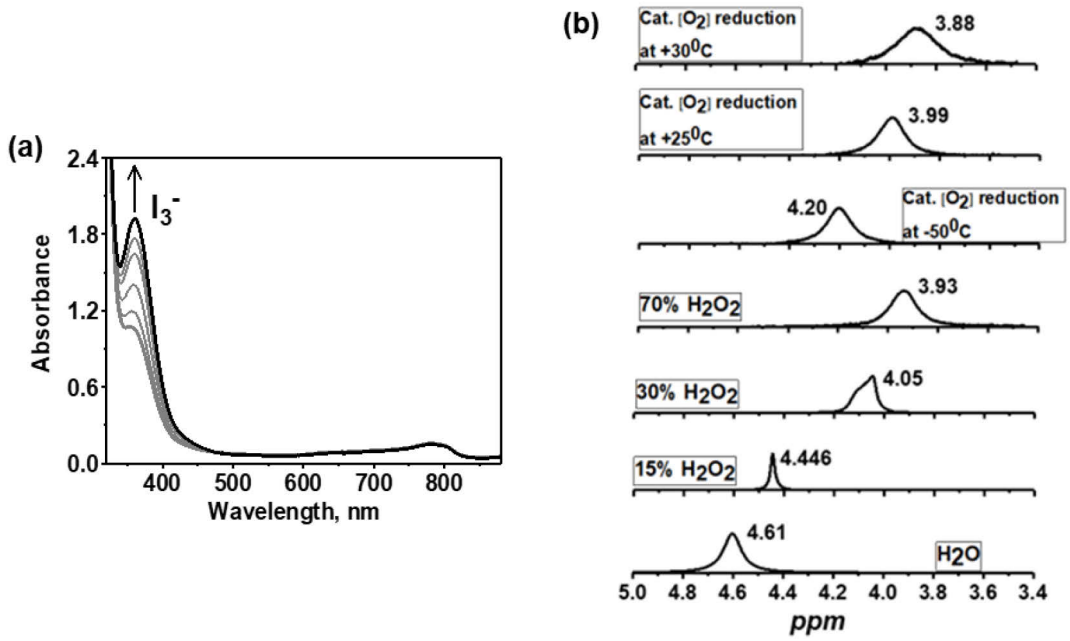

Figure 2.2.17: (a) Spectral changes in the reaction of NaI (50 mM) and 20% diluted (by acetone) reaction mixture of **Co$_4$L1** (0.04 mM), Fc* (3 mM), TFA (10 mM) and O_2 (0.18 mM) in acetone at 30 °C. Formation of I_3^- confirms the presence of H_2O_2 in the resultant reaction mixture. (b) ^{1}H-NMR spectra of the products formed during the complex **Co$_4$L1** catalyzed dioxygen reduction reactions at 25 °C, 30 °C and −50 °C [**Co$_4$L1** (0.04 mM), Fc* (3 mM), TFA (10 mM) and O_2 (0.18 mM)] in acetone-d_6 and comparison with authentic samples containing 70%, 30%, 15% and 0% (weight percent H_2O_2 basis) H_2O_2/H_2O mixtures. All the ^{1}H-NMR measurements were performed at 25 °C. The results obtained for **Co$_4$L1** are then compared with that for **Co$_6$L2** [14] in Table 2.2.5.

With decreasing the temperature, the amount of Fc^{*+} generated from O_2 reduction reaction (ORR) by **Co$_4$L1** increases (Figure. 2.2.16b). This result indicates that the contribution of the four-electron reduction of O_2 increases with decreasing the temperature. Iodometry titration performed at −50 °C after ORR does not give any characteristic absorbance band corresponding to I_3^-, which confirms that no H_2O_2 was formed at −50 °C after the reaction was complete.

Table 2.2.5: Comparison between the temperature dependence catalytic ORR activity mediated by **Co$_4$L1** and **Co$_6$L2** at different temperatures.

Temp.	Catalyst used	mM	Equiv of O_2 Reduced	% of H_2O_2 formed (from NMR)
-50 ^{0}C	Co_4L1	0.01	3.46	20 %
+25 ^{0}C		0.01	2.5	62 %
+30 ^{0}C		0.01	1.92	74 %
-50 ^{0}C	Co_6L2	0.01	3.80	0
+25 ^{0}C		0.01	1.88	70 %

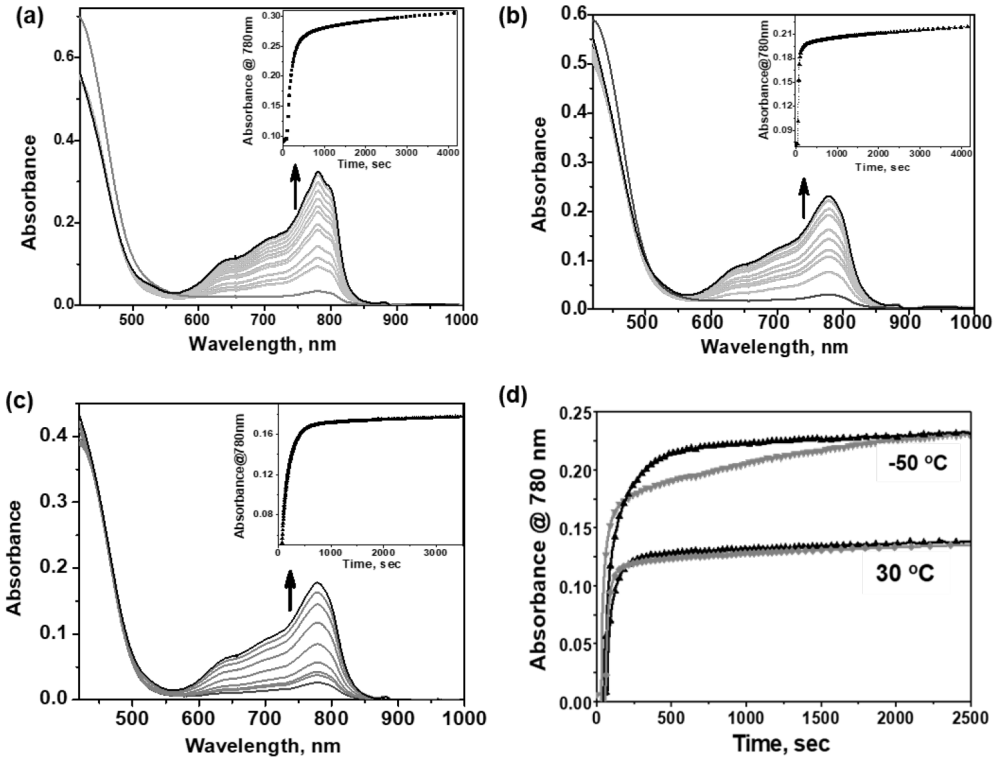

Figure 2.2.18: Spectral changes associated with the reduction of dioxygen by Fc* (3.0 mM) catalyzed by **Co_4L1** (0.04 mM) in the presence of TFA (10.0 mM) in O_2-saturated acetone (0.18mM) at -50 °C (a), +25 °C (b), +30 °C (c); Inset: Time trace of the absorption band at 780 nm due to the formation of Fc^{*+}.; (d) Time profiles of the formation of Fc^{*+} monitored at 780 nm during the reduction of O_2 (0.13 mM) by Fc* (3 mM) and Co_4L1 (0.04 mM) in the presence of Triflic acid (10 mM, black line) and HBF_4 (10 mM, gray line) in acetone at 30 °C as well as at −50 °C.

The change in ORR mechanism from 2*e*- reduction to 4*e*- reduction by **Co_4L1** with decreasing the temperature was further confirmed by the ^{1}H-NMR spectra of the reaction mixture of **Co_4L1** (0.01 mM), Fc* (3 mM), TFA (10 mM), and O_2 (0.18 mM) at various temperatures in d_6-acetone (Figure 2.2.17b). The solution after the **Co_4L1** catalyzed ORR at 30 °C shows a signal at 3.88 ppm. This value is upshifted relative to the signal at 3.93 ppm obtained for an authentic H_2O_2/H_2O mixture (70 weight % H_2O_2 basis) in d_6-acetone at 25 °C. Therefore at 30 °C, >70% H_2O_2 concentration in the product can be identified. The ^{1}H-NMR signal corresponding to an H_2O_2/H_2O mixture undergoes a downshift with increasing amounts of water in the mixture. Notably, pure water shows a signal at 4.61 ppm under the same condition. The ORR process catalyzed by **Co_4L1** at 25 °C shows a signal at 3.99 ppm, which suggests an increasing amount of water in the product mixture relative to the catalytic ORR reaction at 30 °C. Authentic 15% and 30% H_2O_2/H_2O mixtures (15 and 30 weight % H_2O_2 basis) show signals at 4.44 ppm and 4.05 ppm respectively under the same condition. The resultant solution after ORR catalysis at -50 °C shows a signal at 4.20 ppm, thereby confirming the presence of a higher amount of water as the 4e^- reduction product. Such a temperature-dependent product selectivity of the catalytic

ORR was also observed for the previously reported hexanuclear catalyst **Co6L2.**[14] However, the relative amounts of the products formed (H_2O vs H_2O_2) depends on the nature of the catalyst used under the same reaction condition (Table 2.2.5).

The rate of formation and yield of Fc^{*+} are not significantly affected by the nature of the proton source used (Triflic acid or HBF_4) in the ORR catalysis process. Our findings suggest that the conjugate bases ($CF_3SO_3^-$ or BF_4^-) play no major role in controlling the efficiency of the O_2 reduction reactions (Figure 2.2.18*d*).

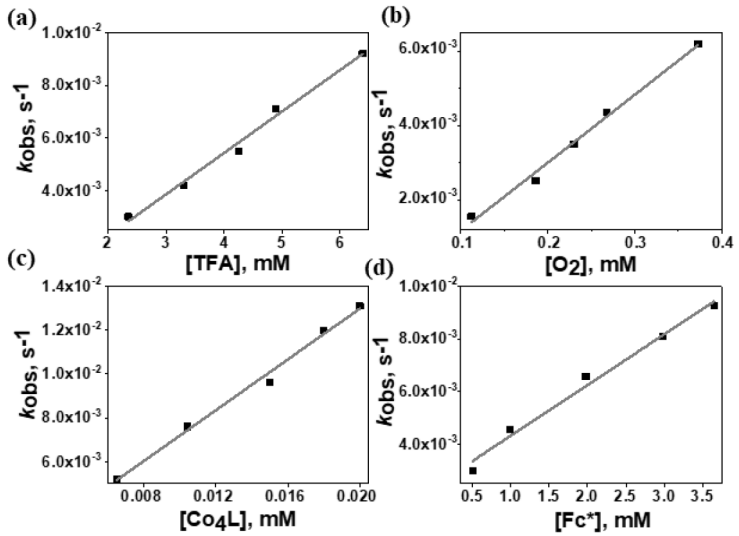

Figure 2.2.19: Studies of the four-electron reduction of O_2 in acetone at -50 °C catalyzed by **Co4L1**: (a) Plot of k_{obs} vs TFA concentration for the O_2 reduction reaction in O_2 saturated acetone with Fc* (3 mM) catalyzed by **Co4L1** (0.04 mM) with TFA (2−6.5 mM). (b) The plot of k_{obs} vs [O_2] for the reduction of O_2 (0.1−0.4 mM) with Fc* (3 mM) catalyzed by **Co4L1** (0.04 mM) with TFA (10 mM). (c)The plot of k_{obs} vs [**Co4L1**] for the O_2 reduction reaction in O_2 saturated acetone (11 mM) with Fc* (3 mM) catalyzed by **Co4L1** (0.0005− 0.02 mM) with TFA (10 mM). (d) Plot of k_{obs} vs [Fc*] for the O_2 reduction reaction in O_2 saturated acetone with Fc* (0.5−3.5 mM) catalyzed by **Co4L1** (0.05 mM) with TFA (10 mM).

To get more information about the mechanism of ORR by **Co4L1** kinetic studies were performed under different conditions at -50 °C and +25 °C. The rate of formation of Fc^{*+} (k_{obs}) obeys pseudo-first-order kinetics under the condition [**Co4L1**] << [Fc*] < [TFA]. The pseudo-first-order rate constant (k_{obs}) increased linearly with increasing concentration of **Co4L1** at -50 °C and +25 °C. The k_{obs} values are also found to be proportional to the concentration of Fc*, TFA, and O_2 at -50 °C and +25 °C. Therefore, the rate equation of **Co4L1** is:

$d[Fc^*]/dt = k_{obs}$ [**Co4L1**] ; where k_{obs} is the pseudo-first-order rate constant

$k_{obs} = k_{cat}$ [Fc*][O_2][TFA] ; where k_{cat} is the apparent rate constant for catalytic ORR.

Experimental details confirm that the 'k_{cat}' is the apparent fourth-order rate constant for both the catalytic two-electron and four-electron reduction processes of O_2 by **Co$_4$L1** at -50 °C and 25 °C respectively (Figure 2.2.19 and 2.2.20). Notably, in the case of **Co$_6$L2** at -50 °C, k_{cat} was reported to be independent on O_2 concentration create a third-order kinetics, although, at +25 °C, the rate constant is of fourth-order for **Co$_6$L2** catalyzed oxygen reduction reaction.[14]

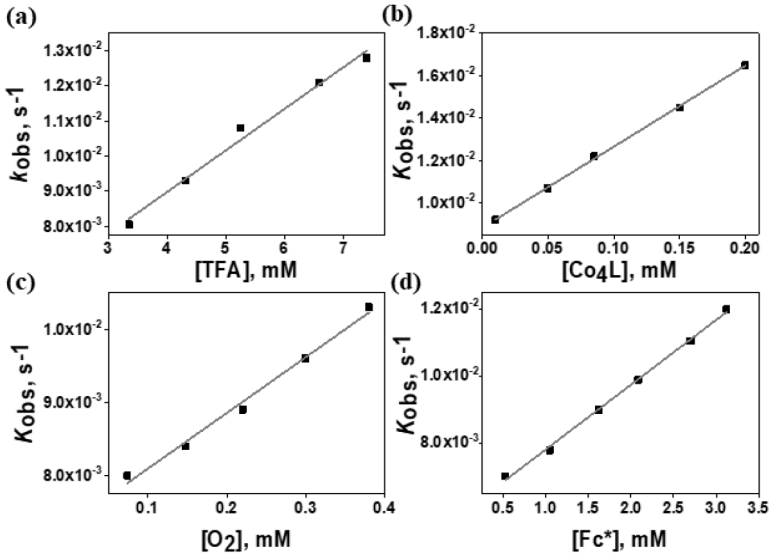

Figure 2.2.20: Studies of the two-electron reduction of O_2 in acetone at 25 °C catalyzed by **Co$_4$L1**: (a) Plot of k_{obs} vs TFA concentration for the O_2 reduction reaction in O_2 saturated acetone with Fc* (3 mM) catalyzed by **Co$_4$L1** (0.04 mM) with TFA (3−7.5 mM). (b) Plot of k_{obs} vs [**Co$_4$L1**] for the O_2- reduction reaction in O_2- saturated acetone (11 mM) with Fc* (3 mM) catalyzed by **Co$_4$L1** (0.01− 0.2 mM) with TFA (10 mM). (c) The plot of k_{obs} vs [O_2] for the reduction of O_2 (0.05−0.4 mM) with Fc* (3 mM) catalyzed by **Co$_4$L1** (0.01 mM) with TFA (10 mM). (d) A plot of k_{obs} vs [Fc*] for the O_2-reduction reaction in O_2- saturated acetone with Fc* (0.5−3.2 mM) catalyzed by **Co$_4$L1** (0.01 mM) with TFA (10 mM).

2.2.5*a.* TON calculation during ORR by Co$_4$L1:

The turnover number (TON) was calculated from the moles of the product formed in the O_2 reduction reaction (calculated from the moles of Fc^{*+} formed) divided by the initial moles of the catalyst (**Co$_4$L1**) used in the reaction. Since, from our experimental findings, we knew that the acid used in the ORR can also reduce Fc* to Fc^{*+}, control reactions were always performed in the absence of the catalyst (**Co$_4$L1**). The amount of Fc^{*+} formed in the control reaction was subtracted from that obtained in the catalytic reaction to determine the TON value. TON was calculated from a reaction mixture containing **Co$_4$L1**, $Me_{10}Fc$, and TFA with concentrations of 0.01 mM, 3.0 mM, and 10 mM, respectively, in 2 mL of O_2-saturated acetone at different temperatures (Figure 2.2.21). Experimental results obtained at various temperatures show that the turnover number decreases linearly with increasing the temperature (from -50 ^oC to +30 ^oC) for the **Co$_4$L1** catalyzed O_2 reduction reaction (Figure 2.2.22 and Table 2.2.6).

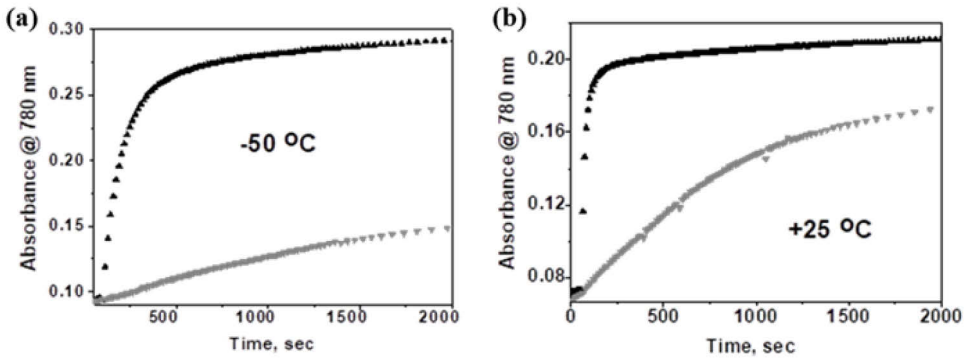

Figure 2.2.21: Time profiles of the formation of Fc^{*+} monitored at 780 nm during the reaction of (a) Fc* (3 mM) with O_2 (saturated acetone solution, 11 mM) in the presence of TFA (10 mM) in acetone at -50 °C catalyzed by **Co_4L1** (0.01 mM) (black squares) and without a catalyst (gray circles); and (b) Fc* (3 mM) with O_2 (saturated acetone solution, 11 mM) in the presence of TFA (10 mM) in acetone at +25 °C catalyzed by **Co_4L1** (0.01 mM) (black squares) and without a catalyst (gray circles).

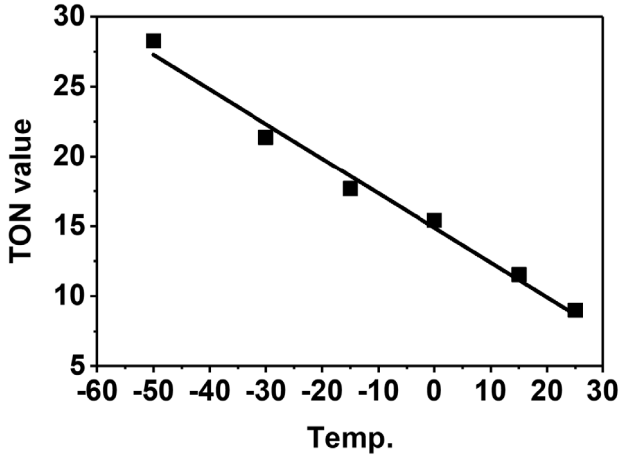

Figure 2.2.22: TON vs temperature plot for the **Co_4L1** catalyzed O_2 reduction reaction.

Table 2.2.6: Variation of TON as a function of temperature for the **Co_4L1** catalyzed O_2 reduction reaction.

Temp.	[Co_4L1]	TON
-50 °C	0.01 mM	28.7
-30 °C	0.01 mM	21.4
-15 °C	0.01 mM	17.7
0 °C	0.01 mM	15.4
+15 °C	0.01 mM	11.5
+25 °C	0.01 mM	9

2.2.6. Reactivity of the intermediate 1 with protons and electrons:

The ability of the complex **Co$_4$L1** to be an effective catalyst towards oxygen reduction depends on the stability of the end-on μ-1,2-peroxo-dicobalt(III) species (**1**). We observed that species **1** exhibited different reactivities with proton and electron donors depending on the reaction temperature. At −50 °C, complex **1** does not react with either TFA or Fc* alone. However, absorption maxima of **1** decay in the presence of both TFA and Fc* at −50 °C, which suggests a proton-coupled electron transfer (PCET) process. At 25 °C in the absence of TFA, Fc* alone can't reduce the complex **1**. Whereas at 25 ºC in the absence of Fc*, TFA alone can decay **1,** which clearly supports a proton transfer (PT) mechanism to form H_2O_2 as the major product. These initial observations influenced us to investigate further and explore the reaction mechanism. Therefore, a series of experiments were performed to determine the temperature dependence of the PT and PCET processes. PCET rates were determined at −50 °C, −40 °C, −30 °C and −20 °C under the condition [**1**] ≪ [Fc*] ≪ [TFA] to ensure pseudo-first-order kinetics (at these temperatures PT rates are negligible). Similarly, PT rates were determined at 20 °C, 22 °C, 25 °C, 30 °C and 32 °C under the condition [**1**] ≪ [TFA].

2.2.6*a*. Determination of k_{PCET} at low temperatures:

A solution of **Co$_4$L1** (0.015 mM) in anhydrous acetone (2 mL) was prepared in a glove box and taken in a cuvette with a path length of 1 cm. The cuvette was then placed in a Unisoku cryostat connected to the UV-vis spectrometer and the temperature of the cryostat was maintained at -50 °C. After attaining the thermal equilibrium, 0.1 mL of an oxygen saturated acetone solution (11 mM; final concentration 0.55 mM) was injected into the cuvette at -50 °C. **1** starts forming immediately after the addition of O_2 into the solution of **Co$_4$L1**; approximately 2000 seconds were necessary for the complete formation of **1**. To remove the excess O_2 from the solution completely, argon was then bubbled into the solution (through the septum) with an outlet for 2-3 mins. Fc* (varying concentrations 0.13- 0.38 mM) and TFA (3 mM) were then added to the resultant solution. The absorption spectra of **1** start to decay immediately and was monitored by UV-vis spectroscopy. A pseudo-first-order decay of the characteristic absorption band of **1** at 464 nm was observed (Figure 2.2.23 inset). The second-order rate constant (k_2') at -50 °C was determined from the linear dependence of the pseudo-first-order rate constants (k_{obs}) on Fc* concentrations (Figure 2.2.23). The same experiment was performed for four different concentrations of TFA (2 mM, 4 mM, 5 mM, and 6 mM). The k_{PCET} value was then determined from the slope of the k_2' vs [TFA] plot. The k_{PCET} values were also determined by using the same procedure at -50 ºC, -40 ºC, -30 ºC, and -20 ºC (Figure 2.2.25, Left).

For PCET rates: -d[**1**]/dt = k_{PCET} [TFA][Fc*][**1**] ;……..when **[1]** ≪ [Fc*] ≪ [TFA];

-d[**1**]/dt = k_{obs} [**1**] ;…… where $k_{obs} = k_{PCET}$ [TFA][Fc*];

for [Fc*] ≪ [TFA]; $k_{obs} = k_2$'[Fc*] ;…….. where $k_2' = k_{PCET}$ [TFA];

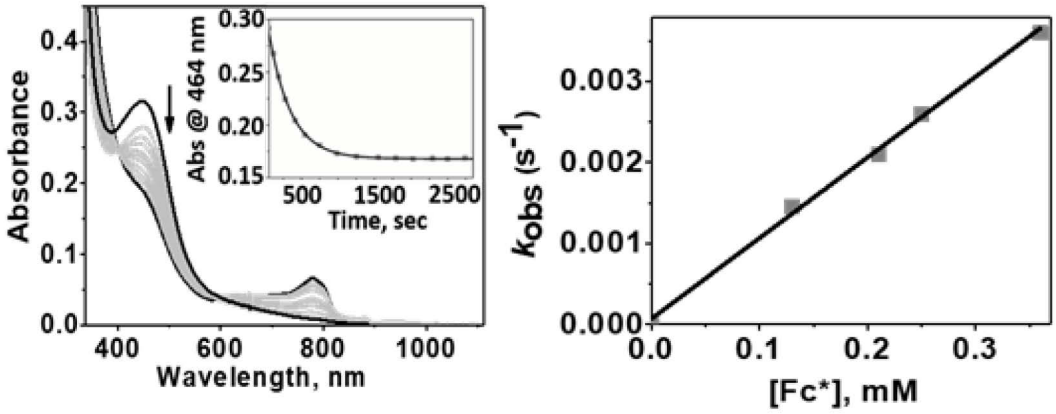

Figure 2.2.23: Changes in the absorption band associated with the reaction of **1** (0.015 mM) with TFA (3 mM) and Fc* (0.15 mM) at −50 °C; Inset: The pseudo-first-order decay of the absorption band at 464 nm as a function of time (left) and the linear dependence (right) of the pseudo-first-order rate constants (k_{obs}) on Fc* concentrations (0.13–0.38 mM) that led us to determine the second-order rate constant value, k'_2.

2.2.6b. Determination of k_{PT} at high temperatures:

As mentioned earlier, the end-on μ-1,2-peroxo-dicobalt(III) complex (**1**) can react with TFA alone at 25°C, in the absence of Fc*. The rate of the PT process was determined at different temperatures (20 ºC, 22 ºC, 25 ºC, 30 ºC, and 32 ºC) by varying the TFA concentrations. The experimental methodology used here is the same as mentioned before for the PCET process except that the temperature is different. A solution of **1** (0.015 mM) in anhydrous acetone (2 mL) was prepared in a glove box and placed in a Unisoku cryostat connected to the UV-vis spectrometer at -50 °C. After attaining the thermal equilibrium, 0.1 mL of an oxygen-saturated acetone solution (11 mM; final concentration 0.55 mM) was injected into the cuvette. **1** starts forming immediately after the addition of O_2; approximately 2000 seconds were necessary for the complete formation of **1**. Argon was then bubbled into the solution (through the septum) with an outlet for 3-4 mins, to remove the excess O_2 from the solution completely. The temperature was then raised to 25 ºC. An acetone solution of TFA (0.75 mM) was then injected into the solution of **1** and the course of the reaction was monitored by UV-vis. The disappearance of the characteristic absorption band at 464 nm with a pseudo-first-order decay profile was observed (Figure 2.2.24 inset). The k_{obs} value increased with increasing concentrations of TFA (0.75-2.70 mM). The PT rate was determined from the slope of the k_{obs} vs [TFA] plot (Figure 2.2.24). The same process was repeated at 20 ºC, 22 ºC, 30 ºC, and 32 ºC (Figure 2.2.25, Right).

For PT rates: -d[**1**]/dt = k_{PT} [TFA][**1**];

For [**1**] ≪ [TFA]; -d[**1**]/dt= k_{obs} [**1**], where k_{obs} = k_{PT} [TFA].

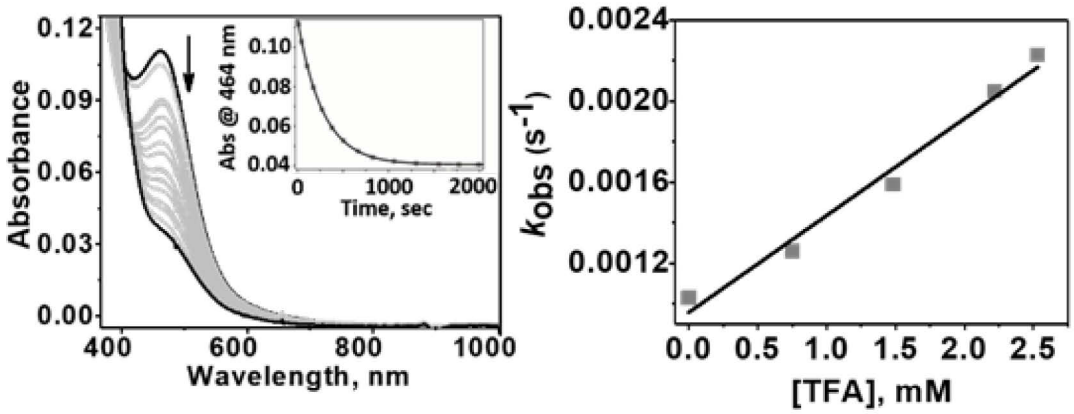

Figure 2.2.24: Changes in the absorption band associated with the reaction of **1** (0.015 mM) with TFA (0.75 mM) at +25 °C; inset: the pseudo-first-order decay of the absorption band at 464 nm as a function of time (left) and the linear dependence (right) of the pseudo-first-order rate constants (k_{obs}) on TFA concentrations (0.75–2.7 mM) led us to determine the second-order rate constant value, k'_2.

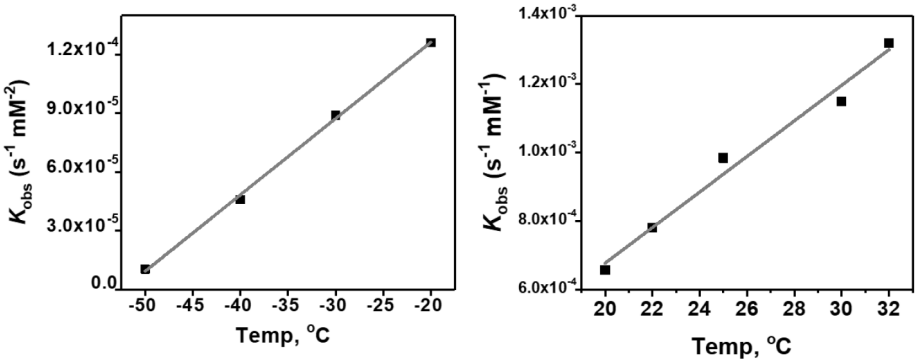

Figure 2.2.25: Variation of the PCET (left) and PT (right) rates as a function of temperature for **Co$_4$L1**.

A comparison between the temperature-dependent PCET and PT processes of **Co$_4$L1** and **Co$_6$L2** [14] is shown in figure 2.2.26. From the above figure, it is evident that in both cases the rate of the PT process varies much faster with temperature relative to the PCET process. The transition temperature from a predominantly PCET to a PT mechanism is 11 °C for **Co$_4$L1**, which is significantly lower than the 19.5 °C determined previously for **Co$_6$L2.**

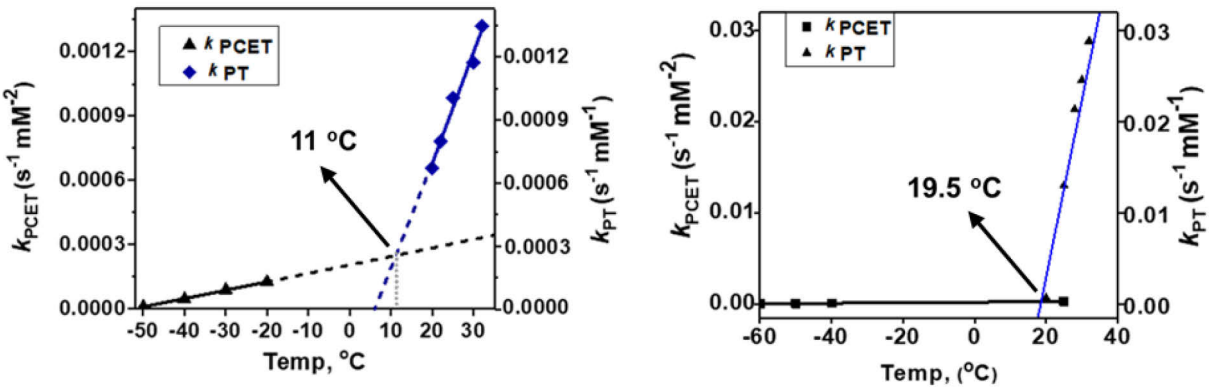

Figure 2.2.26: Comparison between the temperature-dependence of the PCET vs. PT rate constants for **1** (present work, left) and **2** (previous work[14], right).

2.2.7. Hydrogen atom transfer and oxygen atom transfer capabilities of 1 and 2

As previously discussed in Chapter 1, reductive activation of dioxygen at reduced metal centers results in a variety of metal-oxygen intermediates such as metal-superoxo, -peroxo, -hydroperoxo, and -oxo. Among all the different metal-oxygen intermediates, metal-oxo species have been generally considered as the key oxidants responsible for the oxygenation reactions in different enzymes. However, in recent biomimetic studies, investigations of the kinetics of formation of the metal-dioxygen intermediates and their reactivity have raised the question, whether the key oxidants in metalloenzymes should rather be described as metal-superoxo,-peroxo, or -hydroperoxo species.[28,29] For example, bioinspired metal-superoxo intermediates are found to be capable of performing a variety of two-electron oxidation processes leading to hydroxylation or epoxidation products.[30-41] High valent metal-oxo and -superoxo species are typically considered as electrophilic oxidants leading to hydrogen-atom abstraction (HAT) from a C-H bond and oxygen-atom transfer (OAT) to alkenes, phosphines, or sulfides.[42-44]

Metal-superoxo species can also be converted to the metal-peroxo unit upon one-electron reduction, either by an exogenous reductant or by a second reduced metal center. Metal-peroxo species are also discussed as active oxidants performing a variety of nucleophilic and electrophilic enzymatic reactions. The nucleophilic nature of metal-peroxo species is known in enzymes like ADO (aldehyde-deformylating oxygenases), Cyt P_{450}, etc, where the metal-peroxides can attack aldehydes leading to the production of formate and oxidized products (Figure 2.2.27*a*).[44b-c,23] Electrophilic oxidation reactions by metal-peroxo units are also discussed in biology. One example is the diiron(III)-peroxo species termed as H_{Peroxo}, which is generated upon dioxygen activation at the reduced diiron(II) center of sMMO.[45a,b] Proton-promoted O−O bond scission and rearrangement of the diiron core in H_{Peroxo} leads to a bis(μ-oxo)diiron(IV) unit, which is called intermediate Q. This intermediate Q is directly responsible

for the oxidation of methane to methanol.[45c,d] Relative reactivity studies with various substrates have revealed that H_{Peroxo} is a more electrophilic oxidant than the intermediate Q, preferring to react with substrates either by a two-electron or by a hydride abstraction pathway. Another example is $T_{201}S_{peroxo}$, a diiron(III)-peroxo species responsible for aromatic hydroxylation reactions in toluene monooxygenase.[45e] Possible involvement of mononuclear metal-peroxo species in electrophilic oxidation reactions are also considered in biology. The crystal structure of a dioxygen bound naphthalene dioxygenase (NDO) in the presence of substrate revealed that both the oxygen atoms attack on the double bond of the electron-rich aromatic substrate (Figure 2.2.27*b, Rieske Dioxygenase*).[45f,g] However, the electrophilic reactivity of synthetic dinuclear metal-peroxo species has not been observed to date.

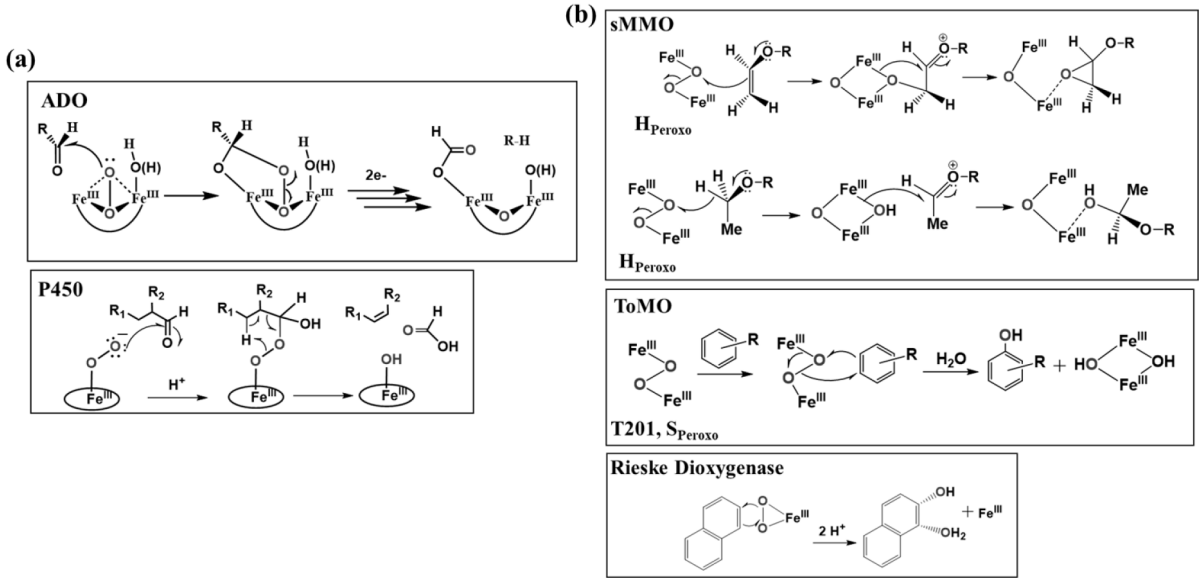

Figure 2.2.27: Proposed (a) nucleophilic vs (b) electrophilic oxidation reactions mediated by metal-peroxo intermediates in biology.[35]

Metal-oxygen intermediates showing both the electrophilic and nucleophilic reactivities are rare in literature. Recent studies have revealed that some of the oxygenated metal species can show the amphoteric reactivities. Goldberg and coworkers have reported that the high valent manganese(V)-oxo complex [Mn^{V}(O)(TBP_8Cz) (TBP_8Cz = octakis(p-tert-butylphenyl)corrolazinato^{3-})] can act as both an electrophile and a nucleophile.[46a,47] The nucleophilic reactivity of a superoxido-iron species (containing a nonheme hexanuclear ligand unit with a drum-shaped stannoxane (Sn_6O_6) core) with aldehydes has also been reported from our group, which supports the role of superoxido–iron species as both an electrophile and a nucleophile in biology.[13,49,50] Also, the amphoteric reactivity of the copper-superoxo species is reported in the literature.[24] Similarly, metal hydroperoxo[52] and metal alkylperoxo[53] cores are also well known to exhibit both electrophilic and nucleophilic reactivities. Very recently,

Nam and Fukuzumi have shown that a mononuclear iron(III) peroxo complex $\{(TMC)Fe^{III}(O_2)]^+$ (TMC=1,4,8,11-tetramethyl-1,4,8,11-tetraazacyclotetradecane)} can show amphoteric reactivity upon binding with redox inactive metal ions acting as Lewis acids.[54] Homo and hetero-dinuclear bis(μ-oxo) complexes also show both electrophilic and nucleophilic reactivities.[55-58]

With this background, one of our research goals is to emphasize the reactivity of homodinuclear metal-peroxo species. In our effort to uncover the structure–reactivity relationships of mono and multinuclear metal-dioxygen intermediates, we investigate the detailed reactivity studies of the intermediates **1** and **2** supported by a non-heme ligand with the stannoxane cores Sn_4O_2 and Sn_6O_6, respectively (*Scheme 2.2.4*).[14, 59] Both the intermediates **1** and **2** contain end-on μ-1,2-peroxodicobalt(III) units with different ligand scaffolds, hence can be distinguished from their absorption maxima and molar extinction coefficient values (Figure 2.2.28). The absorption maxima (λ_{max}) for intermediate **1** is 464 nm whereas for **2** it is 470 nm.

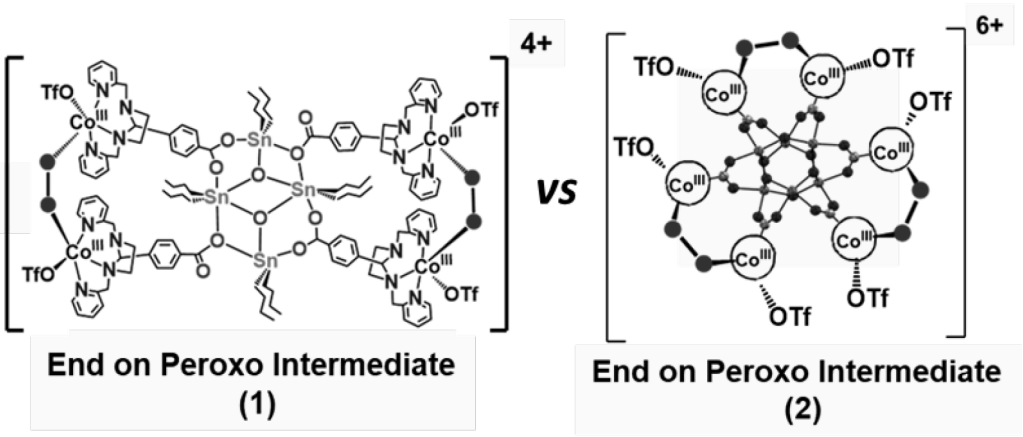

Scheme 2.2.4: Schematic representation of the end-on μ-1,2-peroxodicobalt (III) intermediates **1** and **2** supported by a non-heme ligand with the stannoxane cores Sn_4O_2 and Sn_6O_6, respectively.

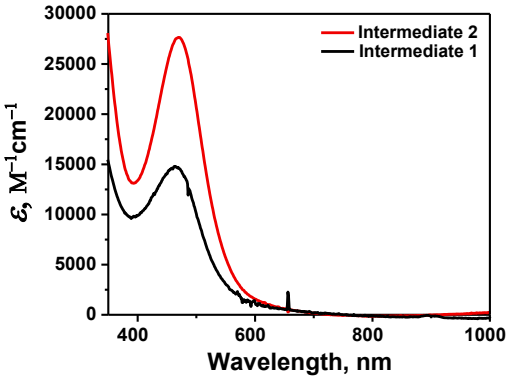

Figure 2.2.28: Comparison of the absorption spectra between the end-on μ-1,2-peroxodicobalt (III) intermediates **1** (black line, Absorption maximum 464 nm) and the previously reported **2** (red line, Absorption maximum 470 nm) at 25 °C in acetone.

2.2.7*a.* The reaction of intermediates 1 and 2 with substrates:

The oxidative reactivities of **1** and **2** were researched with various substrates at 25 ºC. For every test reaction, intermediates **1** and **2** were generated in situ by reacting with oxygen in a dichloromethane solutions of $\mathbf{Co_4L_1}$ and $\mathbf{Co_6L_2}$, respectively, at -50 ºC. The formation of the intermediate was monitored by following the rise in the respective absorbance band in the UV-vis spectra. After the complete formation of the intermediate, excess oxygen was removed by bubbling argon into the solution. An excess amount of substrate (in 0.1 ml DCM or acetone solution) was then injected into the reaction mixture and the temperature was quickly raised to +25 ºC. The decay of the band at 464 nm for **1** and 470 nm for **2** was monitored and fitted to a pseudo-first-order process, from which k_{obs} was determined. The series of k_{obs} thus obtained increased linearly with the amount of added substrates. The slope of the rate constant (k_{obs}) vs substrate concentration fitting plot provided the second-order rate constants (k_2). These kinetic behaviors indicate that the reactions between the substrates and the intermediates are simple bimolecular processes. Here its worth to mention that every plot does not cross the "y" axis at the origin (x,y = 0,0) but has a positive intercept due to the self-decay of the intermediate species **1** and **2** (self-decay rate = 8.6×10^{-4} s^{-1} for **1** vs. 2.5×10^{-4} s^{-1} for **2** at 25 °C).

2.2.7*b.* Nucleophilic oxidative reactivity of 1 and 2

In biomimetic studies, several metal-peroxo model complexes have been characterized and their reactivities have been intensely investigated.[60,61,62] The nucleophilic oxidative reactivities of the intermediates **1** and **2** were tested by using different substrates, e.g. 2-Phenylpropionaldehyde (2-PPA) and different para-substituted benzaldehydes at +25ºC. The series of k_{obs} obtained increased linearly upon increasing the amount of the added substrates, and the slope of the linear fit of k_{obs} vs. the substrate concentration represents the second-order rate constant (k_2) of the reaction. The reactions of **1** and **2** with 2-PPA are shown in figure 2.2.29. From the experimental results, we can see that **2** is a better oxidant than **1** for 2-PPA (Table 2.2.7).

To get further insights into the nucleophilic character of **1** and **2**, different benzaldehydes with a series of electron-donating and withdrawing substituents at the para-position of the phenyl group were employed as substrates, namely para-*X*-PhCHO where *X*= OMe, Me, H, and Cl. The reactions of **1** and **2** with PhCHO are shown in Figure 2.2.30 The respective k_2 values are listed in table 2.2.8. An analysis of the reaction mixture showed the formation of benzoic acid as the product of the reaction.

Table 2.2.7: Second-order rate constants (k_2) for the nucleophilic oxidative reactions of **1** and **2** with 2-PPA.

Intermediate Complex	Substrate	k_2 ($M^{-1}s^{-1}$)
1	2-PPA	0.0433
2	2-PPA	0.321

Table 2.1.8: Second-order rate constants (k_2) for the nucleophilic oxidative reactions of **1** and **2** with para-substituted benzaldehydes.

Substrate (*p*-*X*-PhCHO)	Hammett Cont. (σ_p^+)	k_2 ($M^{-1}s^{-1}$) For **1**	k_2 ($M^{-1}s^{-1}$) For **2**
X = Cl	0.1	0.071	0.335
X = H	0	0.057	0.296
X = Me	-0.3	0.038	0.221
X = OMe	-0.75	0.026	0.138

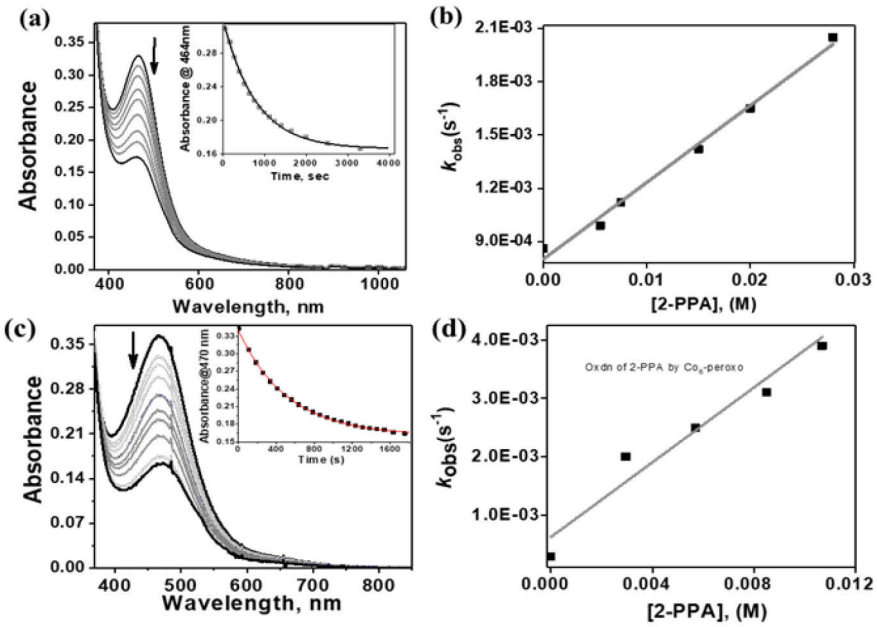

Figure 2.2.29: (a) Changes in the absorption spectra associated with the reaction of **1** (in CH_2Cl_2) with 2-PPA (100 equiv.) at +25 °C. The inset shows the time trace of the decay of the 464 nm band upon the addition of 2-PPA, which can be fitted to a pseudo-first-order kinetic model to obtain a first-order rate constant (k_{obs}). (b) A linear dependence of k_{obs} on the concentration of 2-PPA as determined for the reaction of **1** with the 2-PPA in CH_2Cl_2 at 25 °C. (c) Changes in the absorption spectra associated with the reaction of **2** (in CH_2Cl_2) with 2-PPA (100 equiv.) at +25 °C. The inset shows the time trace of the decay of the 470 nm band upon the addition of 2-PPA, which can be fitted to a pseudo-first-order kinetic model to obtain a first-order rate constant (k_{obs}). (d) The linear dependence of k_{obs} on the concentration of 2-PPA as determined for the reaction of **2** with the 2-PPA in CH_2Cl_2 at 25 °C.

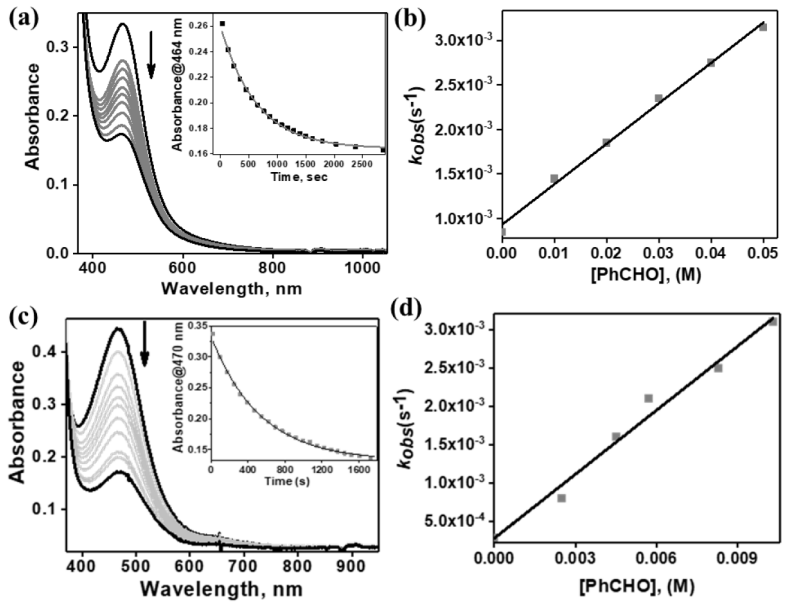

Figure 2.2.30: (a) Changes in the absorption spectra associated with the reaction of **1** (in CH_2Cl_2) with PhCHO (80 equiv.) at +25 °C. The inset shows the time trace of the decay of the 464 nm band upon the addition of PhCHO, which can be fitted to a pseudo-first-order kinetic model to obtain a first-order rate constant (k_{obs}). (b) The linear dependence of k_{obs} on the concentration of PhCHO as determined for the reaction of **1** with the PhCHO in CH_2Cl_2 at 25 °C. (c) Changes in the absorption spectra associated with the reaction of **2** (in CH_2Cl_2) with PhCHO (80 equiv.) at +25 °C. The inset shows the time trace of the decay of the 470 nm band upon the addition of PhCHO, which can be fitted to a pseudo-first-order kinetic model to obtain a first-order rate constant (k_{obs}). (d) A linear dependence of k_{obs} on the concentration of PhCHO as determined for the reaction of **2** with the PhCHO in CH_2Cl_2 at 25 °C.

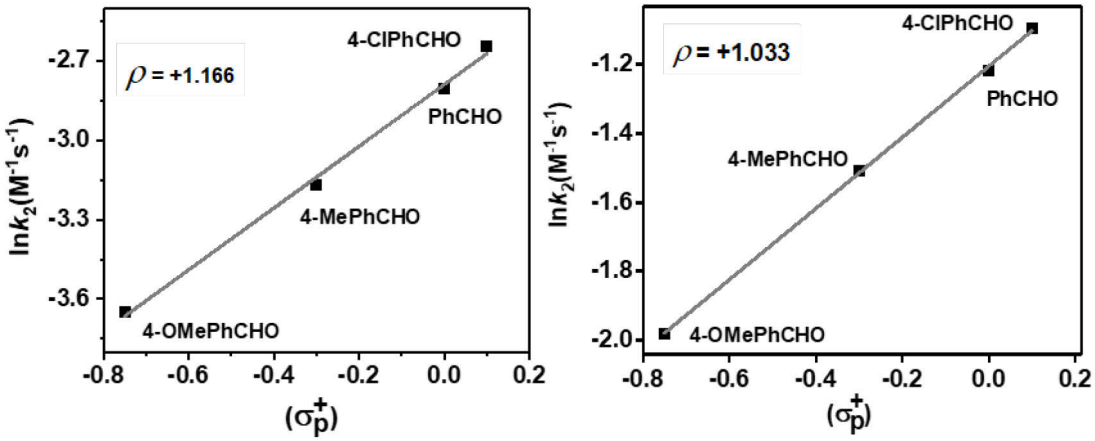

Figure 2.2.31: (a) Hammett plot of ln k_2 against σ_p^+ for the reaction of **1** with para-substituted benzaldehydes (para-*X*-PhCHO; *X*= OMe, Me, H, Cl) in CH_2Cl_2 at 25 °C. (b) Hammett plot of ln k_2 against σ_p^+ for the reaction of **2** with para-substituted benzaldehydes (para-*X*-PhCHO; *X*= OMe, Me, H, Cl) in CH_2Cl_2 at 25 °C.

The Hammett analysis shows that the second-order rate constants increase linearly with increasing the electron-withdrawing capability of the para-substituents benzaldehydes. Experimentally determined Hammett reaction constant (ρ) values are +1.166 and +1.033 for

intermediates **1** and **2,** respectively. The positive Hammett ρ value corroborates the nucleophilic character of **1** and **2** (Figure 2.2.31), which can be related to the bridging μ-1,2-peroxo-dicobalt(III) units since metal-peroxides are known to have a nucleophilic character.[23b,63,64]

2.2.7*c*. Electrophilic oxidative reactivity of 1 and 2

Transition metal-peroxo species are generally associated with oxidative nucleophilic reactions (*e.g*. aldehyde deformylation), whereas metal-oxo and metal-superoxo species are typically considered as electrophilic oxidants leading to hydrogen-atom abstraction (HAT) from a C-H bond and oxygen-atom transfer (OAT) to alkenes, phosphines, or sulfides.[65-69] Lessons learned from synthetic model complexes can be useful to uncover structure-reactivity relationships of the respective metalloproteins. The electrophilic reactivities of the intermediates **1** and **2**, were tested in three different kinds of reactions: (*a*) C−H bond activation, (*b*) oxygen atom transfer, and (*c*) O−H bond activation reactions. For the C−H bond activation reaction by the intermediates **1** and **2**, five substrates were employed, namely 1-benzyl-1,4-dihydronicotinamide (BNAH), xanthene, dihydroanthracene (DHA), 1,4-cyclohexadiene (CHD), and fluorine (Figure 2.2.32). The oxo-group transfer reactivity, on the other hand, was tested using triphenylphosphine (PPh_3) as a substrate (Figure 2.2.33 and Table 2.2.9).

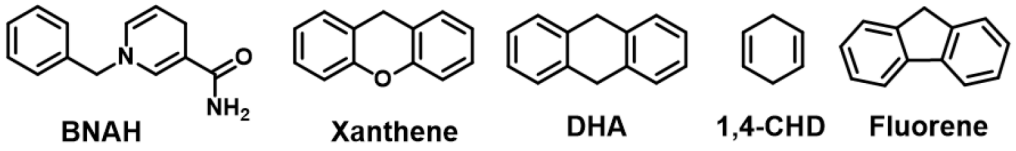

Figure 2.2.32: Structures of the substrates used to test the C−H bond activation capacity of intermediates **1** and **2.**

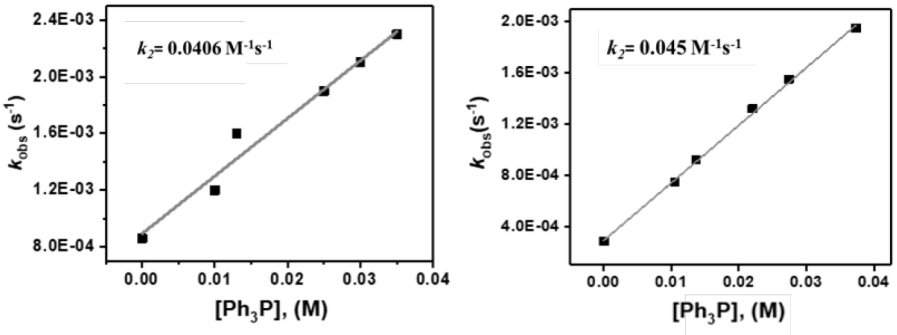

Figure 2.2.33: Linear dependence of k_{obs} on the concentration of Ph_3P determined in CH_2Cl_2 at 25 °C by **1**(left) and **2**(right).

Table 2.2.9: Second-order rate constants (k_2) for the oxo transfer reactions of **1** and **2** with Ph_3P.

Intermediate Complex	Substrate	k_2 ($M^{-1}s^{-1}$)
1	PPh_3	0.0406
2	PPh_3	0.0455

The procedure followed for the evaluation of the reactivity of intermediates **1** and **2** against these substrates was similar as described before. The decay of the band at 464 nm for **1** and 470 nm for **2** was then recorded and fitted to a pseudo-first-order decay to obtain k_{obs}, which was then plotted against the substrate concentration to obtain the second-order rate constant k_2. The obtained second-order rate constants are listed in table 2.2.10 below, together with the bond dissociation energies (BDE)[70] of each substrate. A trend can be observed in which the reaction rate decreases as the BDE of the substrates increases (Figure 2.2.34). From the experimental results, we find out that intermediate **2** can react with substrate containing stronger C-H bonds such as fluorene whereas **1** is not that efficient. Therefore intermediate **2** is a stronger electrophilic oxidant than **1**.

The key question that arises from these experimental observations is how the end-on μ-1,2-peroxodicobalt(III) intermediates can perform electrophilic oxidation reactions. Enzymatic studies have revealed that metal-peroxo intermediates can perform electrophilic oxidation reactions via two possible ways (Scheme 2.2.5). Either a metal-peroxo species can be converted to a high valent metal-oxo species which is then responsible for the electrophilic oxidation reaction, or the metal-peroxo species itself can act as an electrophilic oxidant.

Table 2.2.10: Second-order rate constants (k_2) for the electrophilic oxidative reactions of **1** and **2** with different substrates.

Substrate	BDE (kcal/mol)	k_2 ($M^{-1}s^{-1}$) For **1**	k_2 ($M^{-1}s^{-1}$) For **2**
BNAH	67.9	0.065	0.0933
Xanthene	74	0.048	0.0635
DHA	76.3	0.042	0.0576
1,4-CHD	76.9	0.039	0.0534
Fluorene	81.2	No Reaction	0.0395

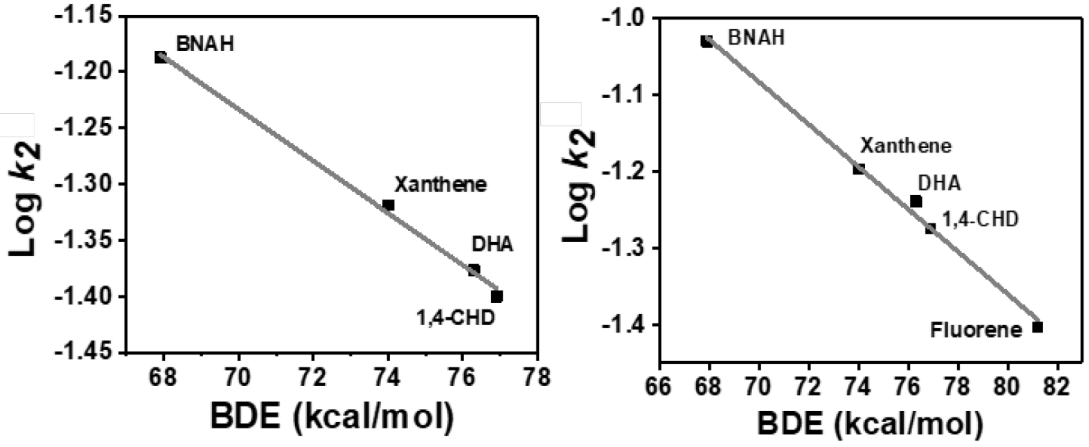

Figure 2.2.34: Plot of the Log k_2 vs BDE for the reactions of **1** (left) and **2** (right) with different substrates in CH_2Cl_2 at 25 °C.

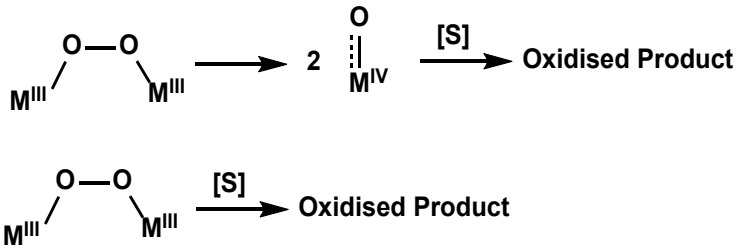

Scheme 2.2.5: Proposed reaction pathways for the electrophilic oxidation reaction mediated by a metal-peroxo species.

To elucidate the possible reaction pathways and further corroborate that the C−H bond activation reactions proceeded via a rate-determining hydrogen atom abstraction step in solution, deuterium kinetic isotope effect (KIE) was determined for the reactions of **1** and **2** with xanthene and d_2-xanthene. KIE value (k_H/k_D) of 2.33 and 3.02 were determined for **1** and **2,** respectively (Figure 2.2.35).

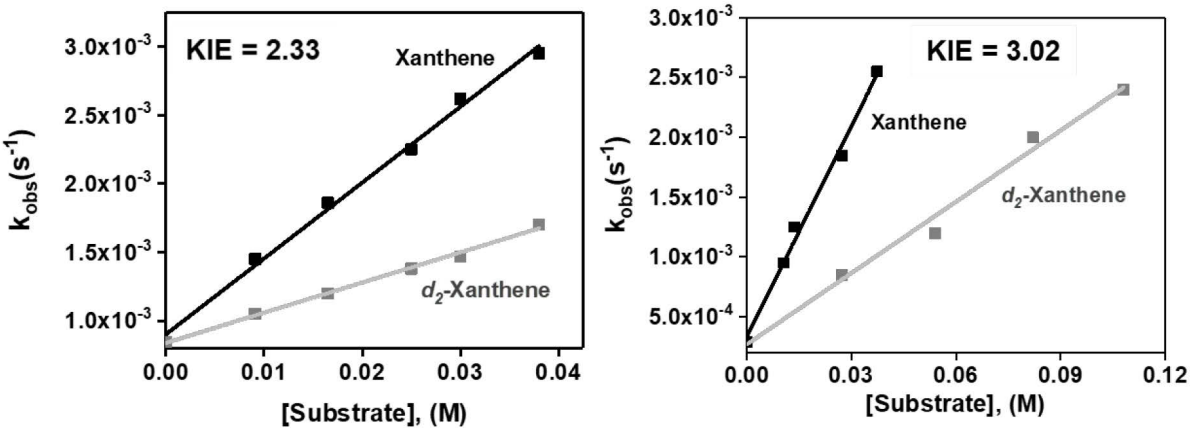

Figure 2.2.35: Linear dependence of k_{obs} with the concentration of the substrate for the reaction of **1**(left) and **2** (right) with Xanthene and d_2-Xanthene.

These KIE values are rather small in comparison with the KIE values reported for the other metal-oxo species (KIE = 4-25).[69,71,72] High KIE values for the metal-oxo mediated H-atom abstraction reactions arise due to the hydrogen tunneling effects, as has been proposed for other metal-oxo intermediates of non-heme enzymes and models. Therefore the interpretation of such small KIE values in the reactions mediated by intermediates **1** and **2** are not straightforward, it might indicate that it is not the oxocobalt species that is responsible for the electrophilic behavior, but rather the bridging μ-1,2-peroxodicobalt(III) species. One indirect method frequently used to prove the presence of a metal-oxo species in solution is to carry out the catalytic oxidation reactions in the presence of ^{18}O-labeled water ($H_2{}^{18}O$) since metal-oxo species can exchange their O-atom with ^{18}O-labeled water prior to the O-atom transfer to organic substrates.[73-75] To determine whether or not an oxocobalt(IV) species was forming in solution and responsible for the electrophilic reactivity in this system, both **1** and **2** were set to react with PPh_3 in acetone in the presence of 0.01 mL of $H_2{}^{18}O$. The analysis of the reaction mixture after the reaction was completed showed no presence of ^{18}O incorporation in the triphenylphosphine oxide. This indicates that there is probably no oxocobalt(IV) species in solution, but rather the end-on μ-1,2-peroxo-dicobalt(III) unit is responsible for both the nucleophilic and the electrophilic reactivities of **1** and **2**. This is an exciting finding since bridging peroxo species are not typically reported to perform electrophilic oxidation reactions.[76]

2.2.7*d*. Phenol Oxidation Reactivity by 2

This unprecedented amphoteric behavior of the intermediates **1** and **2** towards different exogenous substrates influenced us to investigate more about their reactivity pattern towards the O-H bond activation process. Therefore we tried to explore the mechanistic insight of the end-on μ-1,2-peroxo-dicobalt(III) species in phenol oxidation reactions. The conversion of phenols to phenoxyl radicals plays a vital role in a number of biological systems; photosystem II is the most prominent example.[77-79] Phenoxyl radical intermediates play an important role in various other enzymes such as ribonucleotide reductases, cytochrome *c* oxidase, and prostaglandin H synthase.[80] In these respective enzymes, the phenoxyl radical was derived from the active site of tyrosine via the oxidation of transition metal-oxo species.[81] Phenoxyl radicals are not only important for their antioxidant/radical scavengers properties, but they are also important in many synthetic applications e.g. to create new magnetic materials or molecules with various characteristics.[82,83] It is believed that phenoxyl radical derivatives will be an important key component in organic radical batteries (ORBs), to make metal-free, environmentally benign ORBs.[84-86] Herein we report the first systematic study on the oxidation

of neutral phenols(ArOH) by the end-on μ-1,2-peroxo-dicobalt(III) species **2** and provide deeper insights into the O-H bond activation mechanism by applying the Brønsted/Tafel analogy published by Ram and Hupp.[87] The mechanism of phenol oxidation is concluded from several kinetic and physical measurements including (*a*) Kinetic isotope effect (KIE) determination (*b*) Correlation of the activation parameters determined from the reaction kinetics with their oxidation potential value (*c*) Spectroscopic evidence for the formation of phenoxyl radicals and (*d*) Product analysis using both $^{16}O_2$ and $^{18}O_2$.

The kinetic deuterium isotope labeling experiment was done with two phenol substrates namely 2,6-Di-tert-butyl-4-methoxyphenol (*p*-OMe-2,6-DTBP), Phenol(PhOH), and their deuterated versions at 25°C. The KIE values (k_H/k_D) obtained are 3.09 and 2.93, respectively, for the O−H bond activation reactions mediated by the end-on μ-1,2-dicobalt(III)-peroxo intermediate **2** (Figure 2.2.36). Positive KIE values confirm that the oxidation of phenol derivatives occurs via a rate-limiting O-H bond activation process, *i.e.* proton transfer is involved in the rate-determining step of the reaction. However, the obtained values are smaller than the KIE values reported for most metal-oxo mediated HAT reactions (4-25).[88-90]

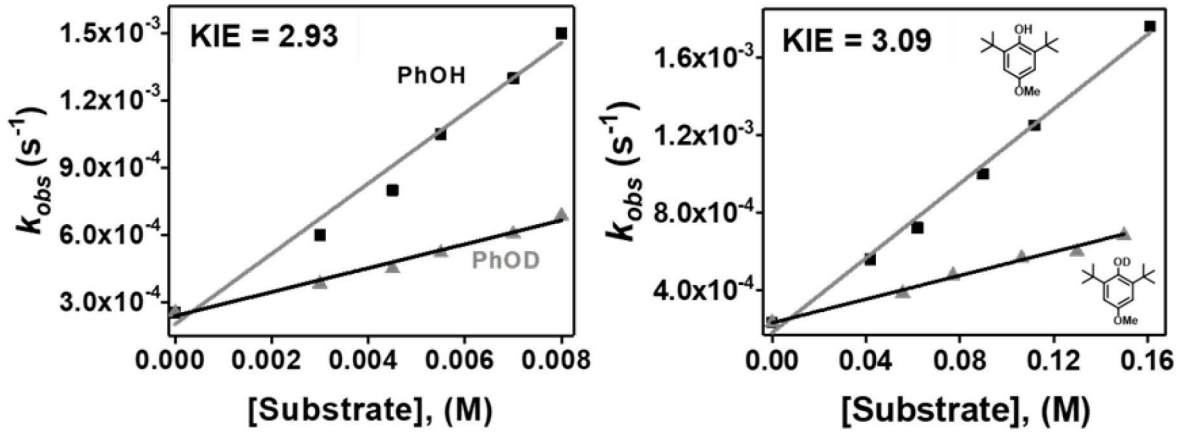

Figure 2.2.36: Linear dependence of k_{obs} with the concentration of substrate for the reaction of **2** with (a) PhOH and PhOD (b) 2,6-di-tert-4-methoxyphenol and 2,6-di-tert-4-methoxy-d-phenol in CH_2Cl_2 at 25 °C.

Notably, Karlin and coworkers reported the KIE values of 11 and 4.2 for the reactions of *p*-OMe-DTBP and 2,6-Di-tert-butyl-4-methylphenol (*p*-Me-DTBP) with the copper(II)-superoxo complex $[(DMM\text{-}tmpa)Cu^{II}(O_2^{\bullet-})]^+$ {DMMtmpa = tris((4-methoxy-3,5-dimethylpyridin-2-yl)methyl)-amine}.[91,92] These values are larger than the KIE of 1.21-1.56 reported by Fukuzumi and co-workers in the reaction of a (μ-η^2:η^2-peroxo)dicopper(II) complex with different phenol derivatives.[93] In that same communication, Fukuzumi also reported a KIE of

1.23-1.48 for the corresponding bis(μ-oxo)dicopper(III) complex. These observations suggest two things:

(a) The KIE value for the metal-superoxo species will be much higher compared to the metal-peroxo species.

(b) If there is an equilibrium operating between the metal-peroxo and metal-oxo unit then that can't be distinguishable from only KIE values.

To find out whether any equilibrium is operating or not, phenol oxidation reaction by the intermediate **2** was carried out in the presence of ^{18}O-labeled water. No ^{18}O incorporated product was obtained after the oxidation reaction was done, which suggests that there is probably no metal-oxo unit involved in the phenol oxidation reaction.

There are three possible ways (Scheme 2.2.6) to transfer the hydrogen atom (or Proton) from neutral phenol to end-on μ-1,2-peroxo-dicobalt(III) unit: (*a*) Electron transfer (ET) followed by proton transfer (PT) (*b*) Proton transfer (PT) followed by electron transfer (ET) or (*c*) a concerted electron and proton transfer pathway (HAT or PCET). The formation of phenoxyl radical via the HAT or PCET process involves homolytic cleavage of the O-H bond at the rate-determining step of the reaction.

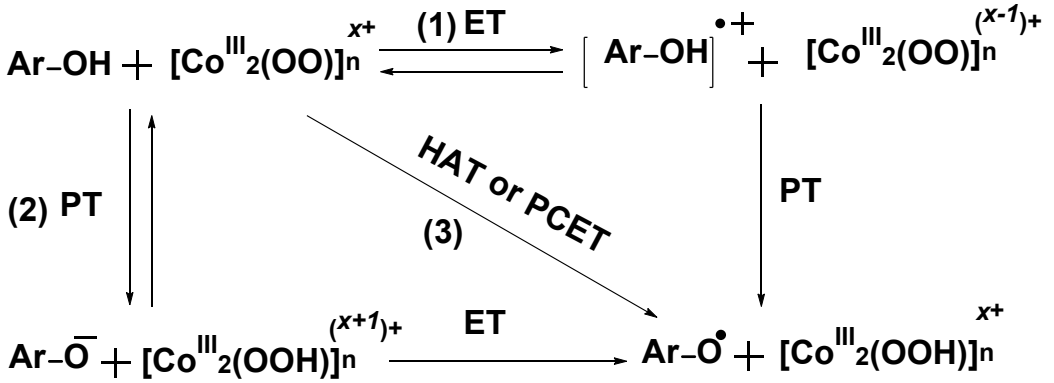

Scheme 2.2.6: Possible reaction pathways for the oxidation of phenols by cobalt(III) peroxo complex.

In the HAT process, both the proton and electron of the hydrogen radical come from the same orbital. For the PCET process both the proton and electron come from the different orbitals in a concerted process at the rate-determining step.[94] Proton and electron transfer can also be uncoupled with either PT or ET being the rate-determining step. A HAT mechanism has been established for phenol oxidation by high valent metal-oxo, metal superoxo complexes.[95-96] In contrast, the PCET mechanism was established for homodinuclear dicopper-dioxygen complexes having (μ-oxo)dicopper(III) and (μ-η^2:η^2-peroxo)dicopper(II) cores.[97] Metal

mediated oxidation of phenols by uncoupled PT-ET mechanism is still unknown in literature, although this mechanism is known for phenol oxidation by organic radicals.[98]

The phenol oxidation mechanism can be predicted from the observed KIE values. The KIE (k_H/k_D) values reported for the hydrogen atom transfer (HAT) reaction from toluene and DHA to permanganate are 6±1 and 3±0.6, respectively.[99] A large KIE (9.0) was also reported for the cumylperoxyl radical mediated oxidation of *p*-OMe-DTBP.[91] Cumylperoxyl radical is known to react with phenols via a pure HAT process.[100,101] Experimentally observed KIE values (3.09 and 2.93) for phenol oxidation reactions mediated by **2** are much smaller (Figure 2.2.36). Low KIE was also observed for the PCET reaction between guanidine and $Ru(bpy)_3^{3+}$ (k_H/k_D = 1.4),[102] as well as those of 4-substituted phenols and dicopper–dioxygen (Cu_2/O_2) complexes.[97] Thus from the experimentally observed KIE values, we can clearly say that the reaction of phenols with intermediate **2** is not a pure HAT process; it rather points towards a PCET process.

Deeper insights into the O–H bond activation mechanism towards substituted phenols by **2** was obtained by applying the Brønsted/Tafel analogy published by Ram and Hupp[87] for electron transfer processes. Treatment of a preformed solution of **2** with excess phenol derivatives at 25ºC leads to pseudo-first-order decay of the characteristic 470 nm band (Figure 2.2.37 and 2.2.38).

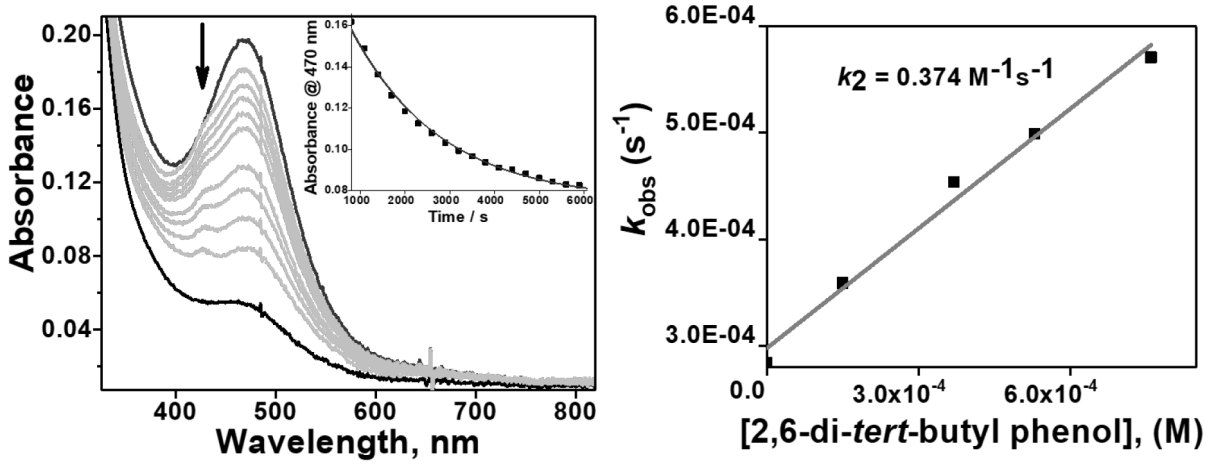

Figure 2.2.37: Left: Absorption spectra showing the decay of **2,** formed in situ from the reaction of a dichloromethane solution of **1** (0.010 mM) with O_2, after the addition of 40 equivalents of 2,6-DTBP in CH_2Cl_2 at 25 °C. Inset: Time trace of the decay of **2** monitored at 470 nm and pseudo-first-order fitting (red line). Right: Linear dependence of k_{obs} on the concentration of 2,6-DTBP determined in CH_2Cl_2 at 25 °C.

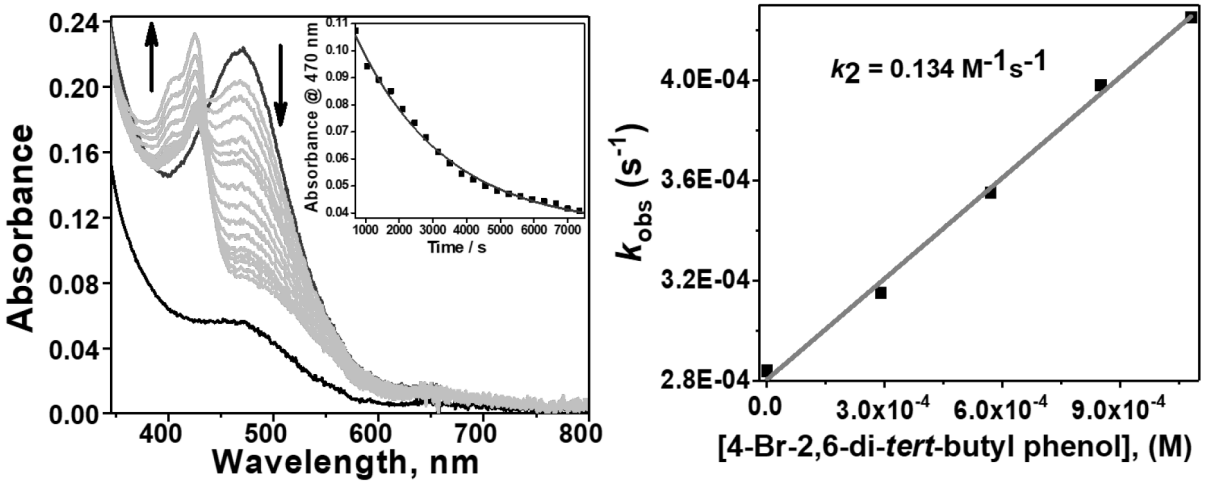

Figure 2.2.38: Left: Absorption spectra showing the decay of **2,** formed in situ from the reaction of a dichloromethane solution of **1** (0.011 mM) with O_2, after the addition of 50 equivalents of 4-Br-2,6-DTBP in CH_2Cl_2 at 25 °C. Inset: Time trace of the decay of **2** monitored at 470 nm and pseudo-first-order fitting (red line). Right: Linear dependence of k_{obs} on the concentration of 4-Br-2,6-DTBP determined in CH_2Cl_2 at 25 °C.

Table 2.2.11: The oxidation potential (E_{ox}^0) of ArOH[103] and the k_2 values for the oxidation of ArOH by the μ-1,2-peroxodicobalt(III) complex(**2**) determined at 25 °C.

Substrate (ArOH)	E^0_{Ox} / V (+25°C)	k_2 ($M^{-1}s^{-1}$)
4-OMe-Phenol	1.43	0.9510
2,4-DTBP	1.46	0.7189
4-Ph-Phenol	1.52	0.3773
4-Me-Phenol	1.54	0.3446
2,4,6-TTBP	1.58	0.2272
Phenol	1.59	0.1539
4-F-Phenol	1.61	0.1250
2,6-DTBP	1.62	0.8901
4-Chloro Phenol	1.63	0.0904
4-Br-2,6-DTBP	1.64	0.1246

The pseudo-first-order rate constant increases with increasing the substrate concentration giving a second-order rate constant (k_2) at 25°C. The same method was used for the oxidation of various other substituted phenol derivatives by **2** to determine the respective k_2 values. These kinetic behaviors indicate that the reaction between phenols and **2** is a simple bimolecular process. The k_2 values for the oxidation of various substituted phenol derivatives were listed with the E^0_{ox} values (reported in the literature) of the phenols (Table 2.2.11).[103] The k_2 values of different phenol derivatives increase with decreasing E^0_{ox} values of the substrates. The plot of (RT/F)ln k_2 vs E^0_{ox} affords good linear correlations as expected for the electron transfer reactions (Figure 2.2.39).

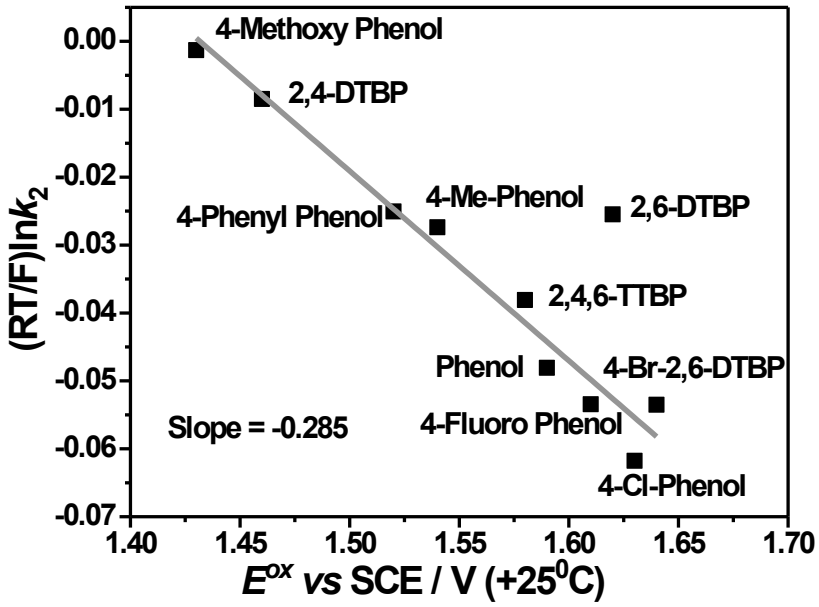

Figure 2.2.39: Plot of (RT/F)lnk_2 against the oxidation potential ($E_{ox}{}^0$) of ArOH for the reaction of substituted ArOH with **2** in CH_2Cl_2 at 25 ºC.

The slope obtained from the plot of (RT/F)lnk_2 *vs* the oxidation potential ($E_{ox}{}^0$) of substituted phenols is -0.285(±0.05). According to the Brønsted/Tafel analogy published by Rum and Hupp[87] if electron transfer (ET) is the rate-determining step of the reaction followed by fast proton transfer (PT) then the slope of the (RT/F)ln k_2 vs $E^0{}_{ox}$ plot should be -0.5, as expected from Marcus theory.[104] On the other hand, if the proton transfer is the rate-determining step followed by electron transfer then the slope should be -1.0. If the rates of ET and PT are comparable and thereby coupled to each other (PCET mechanism), a value between -0.5 and -1.0 would be obtained.[87,92,101] In contrast, for the HAT process the k_2 values for phenol oxidation are independent on their $E^0{}_{ox}$ values, so the k_2 values would be constant irrespective of their $E^0{}_{ox}$ values.[105] Thus the observed negative slope -0.285(±0.05) indicates a concerted ET/PT pathway. Such a smaller slope value has already been reported previously for the reaction of $[(DMM\text{-}tmpa)Cu^{II}(O_2^{\bullet-})]^+$ with different substituted phenols by Karlin, Fukuzumi, and coworkers.[91] The smaller slope than expected for transfer of a full unit of charge has been reported to result from only partial transfer of charge in hydrogen atom transfer reactions from hydrogen donors to the triplet excited state of benzophenone.[106] Thus, it is most likely that hydrogen transfer from *p*-*X*-DTBP to cobalt(III)-peroxo proceeds via a partial transfer of charge rather than an ET/PT pathway in which a full unit of charge is transferred.

Analysis of the reaction mixture shows the formation of benzoquinone as a major product (yield = ~30-40%) (Scheme 2.2.7). The product analysis was performed for 2,6-DTBP, 4-OMe-2,6-DTBP, and 2,4,6-tri-tert-butylphenol. To obtain more mechanistic details of the phenol

oxidation reactions, the X-band EPR spectrum of a reaction mixture of **2** and 2,4,6-tri-tert-butylphenol was carried out at 77K. The EPR spectrum shows a characteristic $S = ½$ single isotropic signal at a *g* value of 2.015, which confirms the formation of phenoxyl radicals (~27% yield) in the reaction mixture (Figure 2.2.40). The lower yield of the phenoxyl radical can be corroborated by its transient nature and tendency to convert instantly into the corresponding product(s) at the reaction condition.

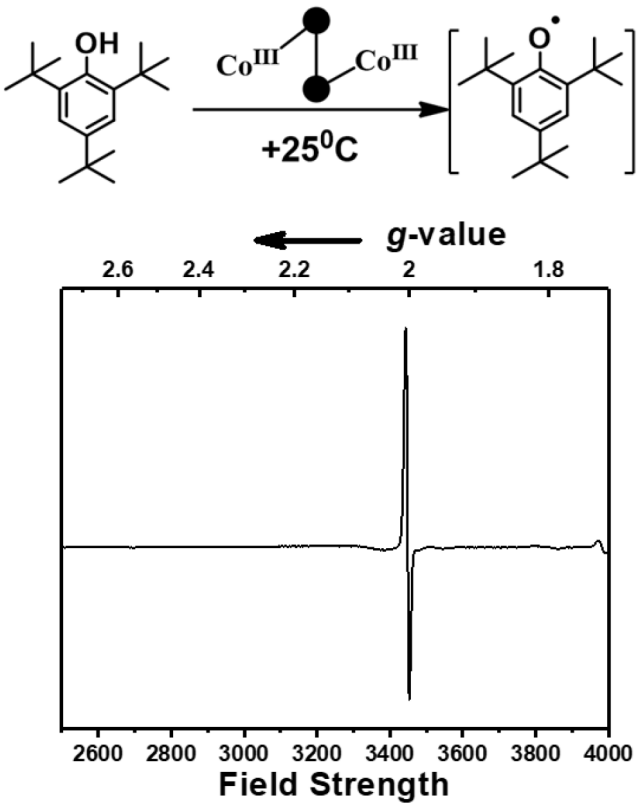

Figure 2.2.40: EPR spectrum of the crude reaction mixture of **2** and 2,4,6-tri-tert-butylphenol in dichloromethane at 77 k.

Qualitative and quantitative product analyses were carried out to understand the mechanism of the phenol oxidation reaction (Scheme 2.2.8). The detection of the formaldehyde was accomplished spectrophotometrically via an aqueous-based Nash assay (see Chapter 5 for details). [91, 107] The reaction mixture obtained from the reaction of intermediate **2** with 2,6-Di-tert-butyl-4-methoxy-phenol (4-OMe-2,6-DTBP) at 25 ºC, was added to a vial charged with 2 mL of the Nash reagent cocktail. The reaction mixture was then heated to 70 °C for 15 min at which time the absorbance at 413 nm was appeared, which confirmed the presence of formaldehyde in the reaction mixture (Figure 2.2.41).

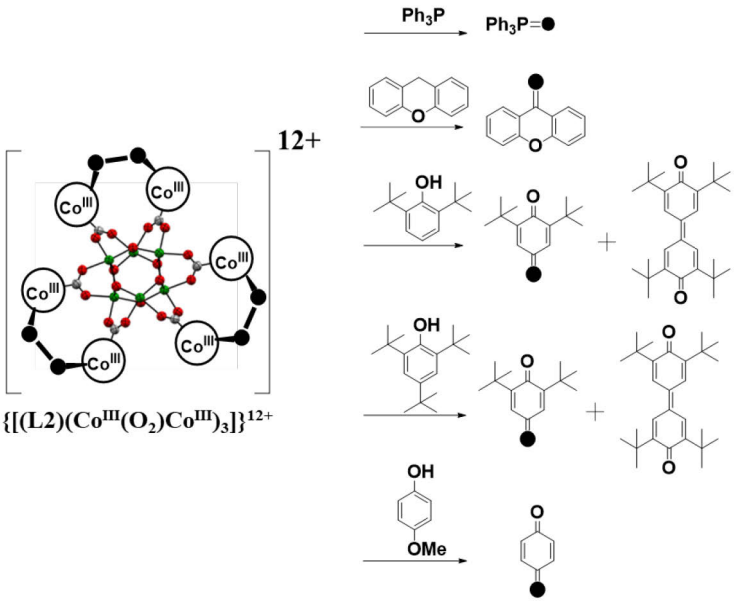

Scheme 2.2.7: Products obtained in the oxidation reaction of various of substrates by **2**. Products were identified using GC-MS.

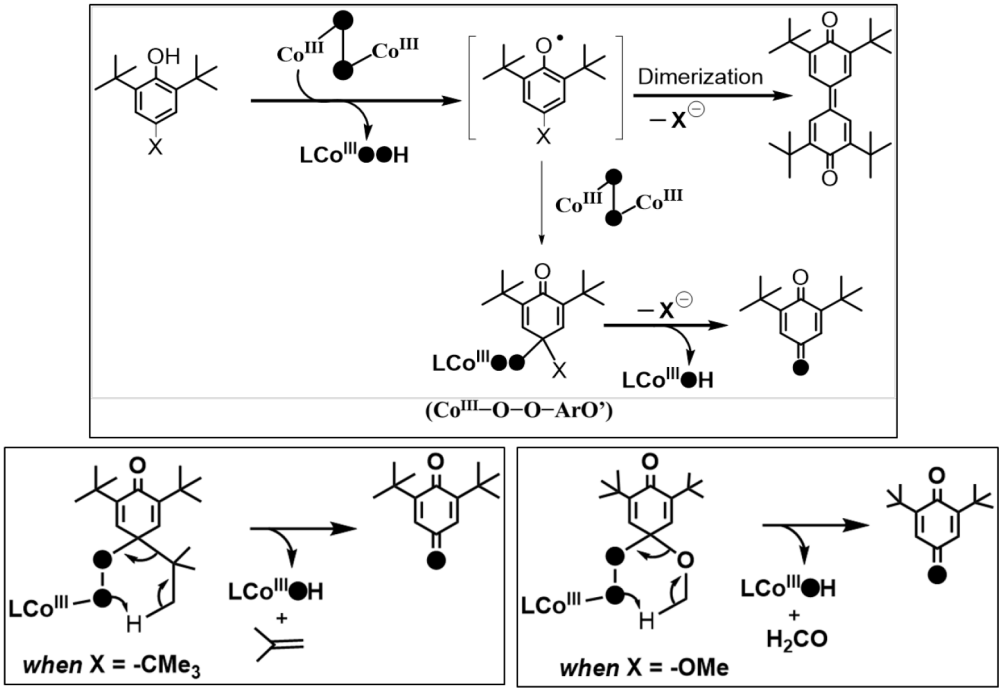

Scheme 2.2.8: Proposed mechanistic pathways for the reaction of dicobalt(III)-peroxo species (**2**) with phenol derivatives.

In fact, for all phenolic substrates, 1,4-benzoquinones are produced. An ^{18}O-labeling experiment with 2,4,6-tri-tert-butylphenol (see the experimental details in chapter 5) where intermediate **2** was generated using $^{18}O_2$ gas revealed that ^{18}O was incorporated into the product 2,6-Di-tert-butyl-1,4-benzoquinone (DTBQ) (Scheme 2.2.7). These experiments confirm that the oxygenation of phenol occurs from the cobalt(III)-peroxo species. In 1981, Nishinaga and co-workers reported the reactions of a cobalt-superoxo species $[Co^{III}(O_2^{\bullet-})]^+$ (formed from Co^{II}

and O_2) with phenol substrates.[108] Nishinaga also obtained a cobalt peroxy species (Co^{III}–O–O–ArO'), and its crystal structure for a para-^{t}Bu phenol substrate. In 2014, Karlin and coworkers reported the phenol oxidation reactions by a cupric–superoxo complex [(DMM-tmpa)$Cu^{II}(O_2^{\bullet-})]^+$ (DMMtmpa = tris((4-methoxy-3,5-dimethylpyridin-2-yl)methyl)-amine).[91] Their works provide a precedent to us for the proposed phenol oxidation mechanism by bridging μ-1,2-peroxo-dicobalt(III) species (Scheme 2.2.8). Moreover, Driess and co-workers recently reported the phenol oxidation reactions by a new nickel(II) superoxo complex $[Ni^{II}(O_2^{\bullet-})]^+$,[109] where they also proposed an intermediate analogous to our proposed one, to explain the products formed from *p*-R-DTBP (R = H, Me, ^{t}Bu) substrates.

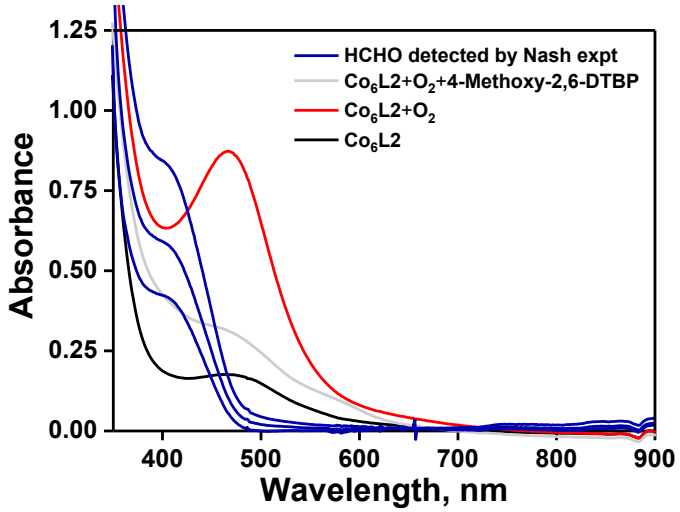

Figure 2.2.41: UV-vis absorption spectra for the detection of HCHO with Nash reagent. Blue lines with an absorption maximum at 413 nm confirms the formation of HCHO during the reaction of the intermediate **2** with 4-OMe-2,6-DTBP. Black-line corresponds to the absorption spectra of the starting Co_6L2 complex. The red line corresponds to the absorption maxima of intermediate **2** and the gray-line corresponds to the absorption spectra after the reaction of intermediate **2** with 4-OMe-2,6-DTBP completed.

2.3. Conclusions and Remarks

In conclusion, this chapter has demonstrated the synthesis and characterization of a novel tetranuclear cobalt complex (**Co_4L1**), supported on a stannoxane core (Sn_4O_2), and its catalytic dioxygen reduction ability. The complex **Co_4L1** acts as a unique catalyst for dioxygen reduction reaction (ORR), whose selectivity can be changed from a preferential $4e^-/4H^+$ dioxygen-reduction (to water) to a $2e^-/2H^+$ process (to hydrogen peroxide) only by increasing the temperature from −50 to 30°C. Detailed spectroscopic evidence together with advanced theoretical calculations confirm the presence of an end-on μ-1,2-peroxo-dicobalt(III) complex (**1**) as the active intermediate, which is reduced to H_2O by a PCET mechanism at low temperature, or to H_2O_2 by a proton transfer (PT) mechanism at elevated temperatures. The

stability of the $Co^{III}–O_2–Co^{III}$ core in **1**, together with its temperature-dependent reactivity in the presence of protons and electrons, makes the **Co4L1** complex a unique catalyst for dioxygen reduction reaction (Figure 2.2.42).

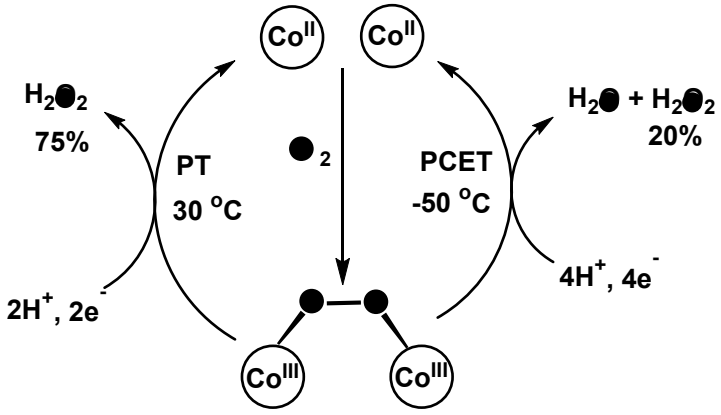

Figure 2.2.42: Proposed mechanism of the temperature-dependent ORR, mediated by the dicobalt(II) units of **Co4L1**.

In our previous work[14], we reported a novel hexanuclear ligand **L2** (Scheme 2.1.3) and its hexanuclear cobalt complex **Co6L2**, supported on a Sn_6O_6 stannoxane core. That was the first time we found out that the complex **Co6L2** has the unique catalytic ability to reduce dioxygen depending on temperature. The mechanism of ORR was explained by the constraint provided by the stannoxane core that makes the O_2-binding to complex **Co6L2** an entropically unfavorable process. This makes the end-on μ-1,2-peroxodicobalt(III) intermediate **2** unstable against a preferential proton-transfer step at 25 °C leading to the generation of H_2O_2. In contrast, at −50 °C the higher thermodynamic stability of **2** leads to the cleavage of the O−O bond via the PCET process. In the present work, we change the core structure of the ligand, from hexanuclear to a tetranuclear one to understand how it will affect the ORR capabilities. **L2** has a more symmetric structure than **L1**. In **L2** all the six plausible metal-binding sites are equidistant from each other at 11.365 Å, whereas, in **L1**, only two of the four metal-binding sites are close to each other. Therefore, complex **Co6L2** ensures more efficient cooperative dioxygen binding than **Co4L1**. This reflects in the lower stability of the μ-1,2-peroxodicobalt(III) intermediate originating from complex **Co4L1** than that from complex **Co6L2**. The lower stability is evident from the faster self-decay rate (~1×10^{-4} s^{-1} for **2** vs. ~1×10^{-3} for **1** at 25 °C), as well as the 16 $cm^{-1,}$ downshift in the Co–O vibration energy ($\nu_{Co–O}$ for **1** is 595 cm^{-1} and 611 cm^{-1} for **2**) in **1** relative to **2**. The constraints imposed by the stannoxane core ensure the entropic instability of both **1** and **2** due to the large reduction in the Co–Co distances that are associated with their formation. Approximate shortening of ~2.4 Å (from a distance of 6.82 Å in **L1** to the DFT calculated distance of 4.48 Å in **1**) and ~7 Å (from a

distance of 11.36 Å in **L2** to the DFT calculated distance of 4.48 Å in **2**) can be predicted for dioxygen binding at **Co_4L1** and **Co_6L2** complexes, respectively, which impose a large strain on the μ-1,2-peroxo-dicobalt(III) cores in **1** and **2.** For both **1** and **2**, the PT rates are found to vary drastically with temperature relative to the PCET rates, and PT becomes the predominant mechanism at 11 °C for **1** and at 19.5 °C for **2**. The ∼10 °C reduction in the transition temperature for **1** can be attributed to its reduced stability relative to **2**, as also evident from the faster self-decay rate and lower ν_{Co-O} vibration energy in **1** relative to **2**. Thus we demonstrate the importance of subtle electronic and steric changes in the reactivity of the biologically relevant metal–dioxygen intermediates, and their product selectivity in catalytic dioxygen reductions.

We also revealed that these end-on μ-1,2-peroxodicobalt(III) complexes **1** and **2** are very unique in behavior. These peroxo species are not only able to show nucleophilic reactivity but also they show electrophilic oxidative reactivity and group transfer reactivity. From the experimental observations, we found out that **2** is a better electrophilic oxidant than **1**. Better cooperativity and higher constrain provided by the stannoxane core in **2** make it a better oxidant than **1**. Detailed kinetic experiments were carried out to obtain mechanistic insights. The electrophilic nature of the intermediates **1** and **2** could be assigned to the bridging-μ-1,2-peroxo-dicobalt(III) species based on small KIE values and the lack of any ^{18}O-incorporation to the oxidized products in the presence of $H_2{}^{18}O$. Based on the correlations obtained between second-order rate-constant (k_2) and the BDEs of the substrates and the KIE values, we confirm that the H-atom abstraction is the rate-determining step for both C-H and O-H activation processes. In the case of phenol oxidation, the hydrogen atom transfer from *p-X*-DTBP proceeds via a partial transfer of charge rather than a complete transfer of charge in a concerted ET/PT pathway. The incorporation of 18-O, in the product obtained, confirms that the peroxyl oxygen of the cobalt(III) peroxo is involved in the oxidative reactions with the substrates.

This is an exciting finding since synthetic bridging homodinuclear metal-peroxo species are not typically reported to perform electrophilic oxidation reactions. This is in contrast to nature, where the dinuclear non-heme iron enzymes (*such as* AurF: 4-aminobenzoate N-oxygenase)[110] are known to activate dioxygen for oxygenation of organic substrates and hydrogen atom abstraction reactions via the formation of peroxo-bridged diferric intermediates. During the last decades, many efforts have been dedicated to elucidate the electrophilic behavior of homo dinuclear metal-peroxo species. Recently Solomon and coworkers have reported that the end-on μ-1,2-peroxo-bridged $Fe(III)_2$ intermediate in AurF needs to be protonated to perform

electrophilic/single-electron-transfer reactivity.[111] In this context, our present work is extremely important because here we never add any proton source or any Lewis acids to activate the peroxo species for electrophilic reactivity. It is the constrain provided by the stannoxane core which plays the key role in determining the unprecedented electrophilic reactivity. The reactivity studies also show how modulation of the ligand architecture in the metal complex can significantly change the behavior of the corresponding metal-oxygen intermediate towards exogenous substrates. Therefore, more intensive research about the metal-oxygen complex with appropriate ligand architecture will help us to develop more efficient catalysts for amphoteric reactivity in the future.

2.4. References

(1) (a) R. E. Blankenship, D. M. Tiede, J. Barber, G. W. Brudvig, G. Fleming, M. Ghirardi, M. R. Gunner, W. Junge, D. M. Kramer, A. Melis, T. A. Moore, C. C. Moser, D. G. Nocera, A. J. Nozik, D. R. Ort, W. W. Parson, R. C. Prince, R. T. Sayre, *Science.* **2011**, *332*, 805. (b) D. Gust, T. A. Moore, A. L. Moore, *Acc. Chem. Res.* **2009***, 42,* 1890.

(2) (a) V. Balzani, A. Credi, M. Venturi, *Chem. Sus. Chem.* **2008**, *1*, 26. (b) J. Barber, *Chem. Soc. Rev*. **2009**, *38*, 185. (c) B. Loll, J. Kern, W. Saenger, A. Zouni, J. Biesiadka *Nature.* **2005**, 438, 1040.

(3) (a) G. L. Soloveichik, *Beilstein J. Nanotechnol.* **2014,** *5,* 1399. (b) J. A. Cracknell, K. A. Vincent, F. A. Armstrong, *Chem. Rev.* **2008**, *108*, 2439. (c) I. Willner, Y.-M. Yan, B. Willner, R. Tel-Vered, *Fuel Cells* **2009**, *9*, 7.

(4) B. C. H. Steele, A. Heinzel, *Nature.* **2001**, *414,* 345.

(5) (a) F. C. Anson, C. Shi, B. Steiger, *Acc. Chem. Res*. **1997**, *30*, 437. (b) P. Peljo, T. Rauhala, L. Murtomäki, T. Kallio, K. Kontturi, *Int. J. Hydrogen Energy.* **2011**, *36*, 10033. (c) J. P. Collman, N. K. Devaraj, R. A. Decréau, Y. Yang, Y.-L. Yan, W. Ebina, T. A. Eberspacher, C. E. D. Chidsey, *Science.* **2007**, *315*, 1565. (d) J. P. Collman, R. A. Decréau, H. Lin, A. Hosseini, Y. Yang, A. Dey, T. A. Eberspacher, *Proc. Natl. Acad. Sci. U. S. A.* **2009**, *106*, 7320. (e) J. P. Collman, S. Ghosh, A. Dey, R. A. Decréau, Y. Yang, *J. Am. Chem. Soc.* **2009**, *131*, 5034.

(6) (a) N. S. Lewis, D. G. Nocera, *Proc. Natl. Acad. Sci. U. S. A.* **2007**, *104*, 15729. (b) A. B. Stambouli, E. Traversa, *Renew. Sustain. Energy Rev.* **2002**, *6*, 297.

(7) (a) E. I. Solomon, P. Chen, M. Metz, S.-K. Lee, A. E. Palmer, *Angew. Chem. Int. Ed.* **2001**, *40*, 4570. (b) T. Tsukihara, H. Aoyama, E. Yamashita, T. Tomizaki, H. Yamaguchi, K.

Shinzawa-Itoh, R. Nakashima, R. Yaono, S. Yoshikawa, *Science.* **1995**, *269*, 1069. (c) C. F. Blanford, R. S. Heath, F. A. Armstrong, *Chem. Commun.* **2007**, 1710. (d) Z. Halime, K.D. Karlin, *Copper oxygen chemistry: In Wiley Series on Reactive Intermediates in Chemistry and Biology.* Edited by Rokita SE. Wiley; **2011**, 283. (e) R. A. Ghiladi, K. R. Hatwell, K. D. Karlin, H.-W. Huang, P.Moe¨nne-Loccoz, C. Krebs, L. A. Marzilli, R. J. Cotter, S.Kaderli, A. D. Zuberbühler, *J. Am. Chem. Soc.* **2001**, *123*,6183.

(8) (a) S. Fukuzumi, Y. Yamada, K. D. Karlin, *Electrochim. Acta.* **2012**, *82*, 493. (b) R. S. Disselkamp, *Energy Fuels.* **2008,** *22*, 2771. (c) R. S. Disselkamp, *Int. J. Hydrogen Energy.* **2010**, *35*, 1049.

(9) (a) S. Abrantes, E. Amaral, A. P. Costa, A. A. Shatalov, A. P. Duarte, *Ind. Crop. Prod.* **2007**, *25*, 288. (b) S. H. Zeronian, M. K. Inglesby, *Cellulose.* **1995**, *2*, 265. (c) L. Li, S. Lee, H. L. Lee, H. J. Youn, *BioResources.* **2011**, *6*, 721. (d) N. Montoya Sánchez, A. de Klerk, *Appl Petrochem Res*. **2018**, *8*, 55.

(10) (a) K. J. Humphreys, L. M. Mirica, Y. Wang, J. P. Klinman, *J. Am. Chem. Soc*. **2009**, *131*, 4657. (b) A. Mukherjee, V. V. Smirnov, M. P. Lanci, D. E. Brown, E. M. Shepard, D. M. Dooley, J. P. Roth, *J. Am. Chem. Soc*. **2008**, *130,* 9459.

(11) (a) J. Klingele, S. Dechert, F. Meyer, *Coord. Chem. Rev.* **2009**, *253*, 2698. (b) A. L. Gavrilova, B. Bosnich, *Chem. Rev.* **2004**, *104*, 349. (c) A. McAuley, S. Subramanian, *Coord. Chem. Rev.* **2000**, *200–202*, 75.

(12) (a) H. P. Dijkstra, P. Steenwinkel, D. M. Grove, M. Lutz, A. L. Spek, G. Van Koten, *Angew.Chem. Int. Ed.* **1999**, *38*, 2185. (b) V. Chandrasekhar, S. Nagendran, R. Azhakar, M. R. Kumar, A. Srinivasan, K. Ray, T. K. Chandrashekar, C. Madhavaiah, S. Verma, U. D. Priyakumar, G. N. Sastri, *J. Am. Chem. Soc.* **2005**, *127*, 2410.

(13) S. Kundu, E. Matito, S. Walleck, F. F. Pfaff, F. Heims, B. Rábay, J. M. Luis, A. Company, B. Braun, T. Glaser, K. Ray., *Chem.- Eur. J.* **2012**, *18*, 2787.

(14) I. M. Pérez, S. Kundu, A. Chandra, K. E. Craigo, P. Chernev, U. Kuhlmann, H. Dau, P. Hildebrandt, C. Greco, C. Van Stappen, N. Lehnert and K. Ray, *J. Am. Chem. Soc*. **2017**, *139*, 15033.

(15) (a) V. Chandrasekhar, S. Nagendran and V. Baskar, *Coord. Chem. Rev.* **2002**, *235*, 1. (b) R. R. Holmes, *Acc. Chem. Res.* **1989**, *22*, 190.

(16) (a) S. Kundu, *PhD Thesis: Synthesis, Spectroscopic Characterization and Reactivity of the High-Valent Metal-Oxo/Imido Cores of the Late Transition Metals*, Humboldt-Universität Zu Berlin, Berlin, **2013**. (b) P. Mialane, A. Nivorojkine, G. Pratviel, L. Az8ma, M. Slany, F.

Godde, A. Simaan, F. Banse, T. Kargar-Grisel, G. Bouchoux, et al., *Inorg. Chem*. **1999**, *38*, 1085.

(17) (a) T. S. Basu Baul, W. Rynjah, E. Rivarola, C. Pettinari, M. Holčapek, R. Jirásko, U. Englert, A. Linden, *J. Organomet. Chem.* **2007**, *692*, 3625. (b) R. R. Holmes, C. G. Schmid, V. Chandrasekhar, R. O. Day, J. M. Holmes, *J. Am.Chem. Soc.* **1987**, *109*, 1408. (c) V. Chandrasekhar, S. Nagendran, S. Bansal, M. A. Kozee, D. R. Powell, *Angew. Chem. Int. Ed.* **2000**, 3*9*, 1833. (d) V. Chandrasekhar, S. Nagendran, S. Bansal, A. W. Cordes, A. Vij, *Organometallics* **2002**, 3297. (e) C. E. Baron, F. Ribot, N. Steunou, C. Sanchez, F. Fayon, M. Biesemans, J. C. Martins, R. Willem, *Organometallics* **2000**, *19*, 1940.

(18) (a) V. Chandrasekhar, S. Nagendran, S. Bansal, M. A. Kozee, D. R. Powell, *Angew. Chem., Int. Ed.* **2000**, *39*, 1833. (b) R. R. Holmes, C. G. Schmid, V. Chandrasekhar, R. O. Day, J. M. Holmes, *J. Am. Chem. Soc*. **1987**, *109*, 1408.

(19) (a) C. Benelli, D. Gatteschi, *Inorg. Chem.* **1982**, *21*, 1788. (b) K. Fukui, H. Ohya-Nishiguchi, N. Hirota, K. Aoyagi, H. Ogoshi, *Chem. Phys. Lett.* **1987**, *140*, 15. (c) F. F. Pfaff, S. Kundu, M. Risch, S. Pandian, F. Heims, I. Pryjomska-Ray, P. Haack, R. Metzinger, E. Bill, H. Dau, P. Comba, K. Ray, *Angew. Chem., Int. Ed.* **2011**, *50*, 1711.

(20) R. W. F. Bader, *Atoms in Molecules. A Quantum Theory*, Cambridge University Press, Oxford U.K., **1991.**

(21) E. R. Johnson, S. Keinan, P. Mori-Sanchez, J. Contreras-García, A. J. Cohen, W. Yang, *J. Am. Chem. Soc*. **2010**, *132*, 6498.

(22) (a) G. Givaja, M. Volpe, M. A. Edwards, A. J. Blake, C. Wilson, M. Schröder, J. B. Love, *Angew. Chem., Int. Ed*. **2007**, *46*, 584. (b) T. Tanase, T. Onaka, M. Nakagoshi, I. Kinoshita, K. Shibata, M. Doe, J. Fujii, S. Yano, *Chem. Commun*. **1997**, 2115. (c) E. Askarizadeh, S. B. Yaghoob, D. M. Boghaei, A. M. Z. Slawin, J. B. Love, *Chem. Commun*. **2010**, *46*, 710.

(23) (a) J. Cho, R. Sarangi, H. Y. Kang, J. Y. Lee, M. Kubo, T. Ogura, E. I. Solomon, W. Nam, *J. Am. Chem. Soc*. **2010**, *132*, 16977. (b) X. Hu, I. Castro-Rodriguez, K. Meyer, *J. Am. Chem. Soc.* **2004**, *126*, 13464. (c) J. Cho, R. Sarangi, W. Nam, *Acc. Chem. Res.* **2012***, 45*, 1321.

(24) (a) S. Fukuzumi, K. Okamoto, C. P. Gros, R. Guilard, *J. Am. Chem. Soc.* **2004**, *126*, 10441. (b) S. Fukuzumi, L. Tahsini, Y. Lee, K. Ohkubo, W. Nam, *J. Am. Chem. Soc.* **2012**, *134*, 7025.

(25) (a) Z. Halime, H. Kotani, Y. Li, S. Fukuzumi, K. D. Karlin, *Proc. Natl. Acad. Sci. U.S.A.* **2011**, *108*, 13990. (b) D. Das, Y.-M. Lee, K. Ohkubo, W. Nam, K. D. Karlin, S. Fukuzumi, *J. Am. Chem. Soc.* **2013**, *135*, 2825.

(26) S. Fukuzumi, H. Kotani, K. A. Prokop, D. P. Goldberg, *J. Am. Chem. Soc.* **2011**, *133*, 1859.

(27) K. Mase, K. Ohkubo, S. Fukuzumi, *Inorg. Chem.* **2015**, *54*, 1808.

(28) (a) S. Fukuzumi, *Biochim. Biophys. Acta*. **2016,** *1857*, 5, 604. (b) L. Que, Jr., *J. Biol. Inorg. Chem*. **2004**, *9*, 684. (c) I. G. Denisov, T. M. Makris, S. G. Sligar, I. Schlichting, *Chem. Rev.* **2005**, *105*, 2253. (d) M. Sono, M. P. Roach, E. D. Coulter, J. H. Dawson, *Chem. Rev.* **1996**, *96*, 2841.

(29) (a) W. Nam, *Acc. Chem. Res*. **2015**, *48*, 2415. (b) G. Xing, L. M. Hoffart, Y. Diao, K. S. Prabhu, R. J. Arner, C. C. Reddy, C. Krebs, J. M. Bollinger, Jr., *Biochemistry*, **2006**, *45*, 5393. (c) G. Xing, Y. Diao, L. M. Hoffart, E. W. Barr, K. S. Prabhu, R. J. Arner, C. C. Reddy, C. Krebs, J. M. Bollinger, Jr., *Proc. Natl. Acad. Sci. U.S.A*. **2006**, *103*, 6130.

(30) H. M. Neu, R. A. Baglia, D. P. Goldberg, *Acc. Chem. Res.* **2015**, *48*, 2754.

(31) W. Nam, Y.-M. Lee, S. Fukuzumi, *Acc. Chem. Res.* **2014**, *47*, 1146.

(32) R. A. Baglia, J. P. T. Zaragoza, D. P. Goldberg, *Chem. Rev.* **2017**, *117*, 13320.

(33) S. Sahu, D. P. Goldberg, *J. Am. Chem. Soc.* **2016,** *138*, 11410.

(34) T. A. Betley, Q. Wu, T. Van Voorhis, D. G. Nocera, *Inorg. Chem.* **2008**, *47*, 1849.

(35) K. Ray, F. F. Pfaff, B. Wang, W. Nam, *J. Am. Chem. Soc.* **2014**, 136, 13942.

(36) S. Hong, Y.-M. Lee, K. Ray, W. Nam, *Coord. Chem. Rev.* **2017**, 334, 25.

(37) C. E. Elwell, N. L. Gagnon, B. D. Neisen, D. Dhar, A. D. Spaeth, G. M. Yee, W. B. Tolman, *Chem. Rev.* **2017**, *117*, 2059.

(38) B. L. Conley, W. J. Tenn, K. J. H. Young, S. Ganesh, S. Meier, V. Ziatdinov, O. Mironov, J. Oxgaard, J. Gonzales, W. A. Goddard, R. A. Periana, W. B. Tolman, Ed.; *In Activation of Small Molecules: Organometallic and Bioinorganic Perspectives; Wiley-VCH: Weinheim*, *Germany*, **2006**; pp 235.

(39) (a) M. Costas, M. P. Mehn, M. P. Jensen, L. Que, Jr., *Chem. Rev.* **2004**, 104, 939. (b) W. Nam, *Acc. Chem. Res*. **2007***, 40*, 465.

(40) A. E. Shilov, G. B. Shul, G. B. Shul'pin, *Chem. Rev.* **1997,** *97*, 2879.

(41) Z. Halime, K. D. Karlin, In Copper-Oxygen Chemistry; K. D. Karlin, S. Itoh, Eds*.; Wiley Series of Reactive Intermediates in Chemistry and Biology; John Wiley & Sons: New York,* **2011**; pp 283.

(42) S. Itoh, *Acc. Chem. Res***. 2015**, 48, 2066.

(43) A. Gunay, K. H. Theopold, *Chem. Rev.* **2010**, 110, 1060.

(44) (a) K. Ray, F. Heims, M. Schwalbe, W. Nam, *Curr. Opin. Chem. Biol*. **2015**, 25, 159. (b) J. Cho, R. Sarangi, J. Annaraj, S. Y. Kim, M. Kubo, T. Ogura, E. I. Solomon, W. Nam, *Nat. Chem.* **2009,** *1*, 568. (c) M. Selke, J. S. Valentine, *J. Am. Chem. Soc*. **1998**, *120*, 2652.

(45) (a) K. E. Liu, D. Wang, B. H. Huynh, D. E. Edmondson, A. Salifoglou, S. J. Lippard, J. *Am. Chem. Soc.* **1994**, *116*, 7465. (b) A. M. Valentine, S. S. Stahl, S. J. Lippard, *J. Am. Chem. Soc.* **1999**, *121*, 3876. (c) L. Shu, J. C. Nesheim, K. Kauffmann, E. Münck, J. D. Lipscomb, L. Que, Jr., *Science* **1997**, *275*, 515. (d) S.-K. Lee, B. G. Fox, W. A. Froland, J. D. Lipscomb, E. Münck, *J. Am. Chem. Soc*. **1993**, *115*, 6450. (e) W. J. Song, R. K. Behan, S. G. Naik, B. H. Huynh, S. J. Lippard, *J. Am. Chem. Soc*. **2009**, *131*, 6074. (f) A. Karlsson, J. V. Parales, R. E. Parales, D. T. Gibson, H. Eklund, S. Ramaswamy, *Science* **2003**, *299*, 1039. (g) D. T. Gibson, R. E. Parales, *Curr. Opin. Biotechnol***. 2000**, *11*, 236.

(46) H. M. Neu, R. A. Baglia, D. P. Goldberg, *Acc. Chem. Res.* **2015**, *48*, 2754.

(47) H. M. Neu, T. Yang, R. A. Baglia, T. H. Yosca, M. T. Green, M. G. Quesne, S. P. de Visser, D. P. Goldberg, *J. Am. Chem. Soc.* **2014**, 136, 13845.

(48) J. P. Klinman, *J. Biol. Chem*. **2006**, 281, 3013-3016.

(49) (a) S. C. Peck, W. A. van der Donk, *Curr. Opin. Chem. Biol*. **2013**, *17*, 580. (b) L. M. Mirica, J. P. Klinman, *Proc. Natl. Acad. Sci. USA* **2008**, 105, 1814.

(50) J. M. Bollinger, J. C. Price, L. M. Hoffart, E. W. Barr, C. Krebs, *Eur. J. Inorg. Chem*. **2005**, *2005*, 4245.

(51) P. Pirovano, A. M. Magherusan, C. McGlynn, A. Ure, A. Lynes, A. R. McDonald, *Angew. Chem. Int. Ed*. **2014**, *53*, 5946.

(52) (a) S. Kim, J. W. Ginsbach, J. Y. Lee, R. L. Peterson, J. J. Liu, M. A. Siegler, A. A. Sarjeant, E. I. Solomon, K. D. Karlin, *J. Am. Chem. Soc*. **2015**, 137, 2867. (b) C.-C. Wang, H.-C. Chang, Y.-C. Lai, H. Fang, C.-C. Li, H.-K. Hsu, Z.-Y. Li, T.-S. Lin, T.-S. Kuo, F. Neese, S. Ye, Y.-W. Chiang, M.-L. Tsai, W.-F. Liaw, W.-Z. Lee, *J. Am. Chem. Soc.* **2016**, *138*, 14186.

(53) S. Hikichi, H. Okuda, Y. Ohzu, M. Akita, *Angew. Chem. Int. Ed*. **2009**, *48*, 188.

(54) S. H. Bae, Y.-M. Lee, S. Fukuzumi, W. Nam, *Angew. Chem. Int. Ed*. **2017**, *56*, 801.

(55) M. Sankaralingam, S. H. Jeon, Y.-M. Lee, M. S. Seo, K. Ohkubo, S. Fukuzumi, W. Nam, *Dalton Trans.* **2016**, 45, 376.

(56) S. Kundu, F. F. Pfaff, E. Miceli, I. Zaharieva, C. Herwig, S. Yao, E. R. Farquhar, U. Kuhlmann, E. Bill, P. Hildebrandt, H. Dau, M. Driess, C. Limberg, K. Ray, *Angew. Chem. Int. Ed*. **2013**, 52, 5622.

(57) M.-C. Kafentzi, M. Orio, M. Réglier, S. Yao, U. Kuhlmann, P. Hildebrandt, M. Driess, A. J. Simaan, K. Ray, *Dalton Trans.* **2016**, 45, 15994.

(58) X. Engelmann, S. Yao, E. R. Farquhar, T. Szilvási, U. Kuhlmann, P. Hildebrandt, M. Driess, K. Ray, *Angew. Chem. Int. Ed.* **2017**, 56, 297.

(59) A. Chandra, S. Mebs, S. Kundu, U. Kuhlmann, P. Hildebrandt, H. Dau, K Ray, *Dalton Trans.* **2020**, *49*, 6065.

(60) M. Sankaralingam, Y. M. Lee, S. H. Jeon, M. S. Seo, K. B. Cho, W. Nam, *Chem. Commun.* **2018**, *54*, 1209.

(61) B. Shin, K. D. Sutherlin, T. Ohta, T. Ogura, E. I. Solomon, J. Cho, *Inorg. Chem*. **2016**, *55*, 12391.

(62) W. Adam, W. Malisch, K. J. Roschmann, C. R. SahaMo¨ller, W. A. Schenk, *J. Organometallic Chem*. **2002,** *661,* 3.

(63) J. Kim, B. Shin, H. Kim, J. Lee, J. Kang, S. Yanagisawa, T. Ogura, H. Masuda, T. Ozawa, and J. Cho, *Inorg. Chem*. **2015**, 54, 6176.

(64) Y. Jo, J. Annaraj, M. S. Seo, Y. M. Lee, S. Y. Kim, J. Cho, W. Nam, *J. Inorg. Biochem.* **2008,** *102*, 2155.

(65) M. Sankaralingam, Y.-Min Lee, W. Nam, S. Fukuzumi, *Coord. Chem. Rev.* **2018,** *365*, 41.

(66) (a) D. L. Wertz, J. S. Valentine, *Struct. Bonding.* **2000**, *97*, 37. (b) W. Nam, *Acc. Chem. Res.* **2015**, *48*, 2415.

(67) F. F. Pfaff, S. Kundu, M. Risch, S. Pandian, F. Heims, I. Pryjomska-Ray, P. Haack, R. Metzinger, E. Bill, H. Dau, P. Comba, K. Ray, *Angew. Chem. Int. Ed*. **2011**, *50*, 1711.

(68) J. England, Y. Guo, H. K. M. Van, M. A. Cranswick, G. T. Rohde, E. L. Bominaar, E. Munck, Que, L. Jr., *J. Am. Chem. Soc.* **2011**, *133*, 11880.

(69) S. Hong, F. F. Pfaff, E. Kwon, Y. Wang, M.-S. Seo, E. Bill, K. Ray, W. Nam, *Angew. Chem. Int. Ed.* **2014**, *53*, 10403.

(70) Y.-R. Luo, *Comprehensive Handbook of Chemical Bond Energies, CRC Press, Boca Raton, Florida,* **2007**.

(71) A. Gunay, K. H. Theopold, *Chem. Rev*. **2010**, *110*, 1060.

(72) X. Engelmann, I. Monte-Pérez, K. Ray, *Angew. Chem. Int. Ed.* **2016**, *55*, 7632.

(73) W. Nam, Y.-M. Lee, S. Fukuzumi, *Acc. Chem. Res.* **2014**, *47*, 1146.

(74) M. S. Seo, J.-H. In, S. O. Kim, N. Y. Oh, J. Hong, J. Kim, L. Que. Jr., W. Nam, *Angew. Chem.Int. Ed.* **2004**, *43*, 2417.

(75) I. Prat, A. Company, V. Postils, X. Ribas, L. Que. Jr., J. M. Luis, M. Costas, *Chem. Eur. J.* **2013**, *19*, 6724.

(76) I. M. Pérez, *Ph.D. Thesis: Bioinspired oxidation reactions involving mono- and poly-nuclear transition metal complexes: hydrogen atom abstraction and group transfer reactions*, Humboldt-Universität Zu Berlin, Berlin, **2017**.

(77) (a) J. Stubbe, W. A. van der Donk, *Chem. Rev.* **1998**, *98*, 705. (b) C. Tommos, G. T. Babcock, *Biochim. Biophys. Acta*, **2000**, *1458*, 199.

(78) G. Renger, *Biochim. Biophys. Acta*, **2004**, *1655*, 195.

(79) T. J. Meyer, M. H. V. Huynh and H. H. Thorp, *Angew. Chem., Int. Ed*., **2007**, *46*, 5284.

(80) J. Stubbe, W. A. van der Donk, *Chem. Rev.* **1998**, *98*, 705.

(81) A.-F. Miller, *Acc. Chem. Res*., **2008**, *41*, 501.

(82) C. Xie, P. M. Lahti, C. George, *Org. Lett*., **2000**, *2*, 3417.

(83) M. Miyasaka, T. Yamazaki, E. Tsuchida and H. Nishide, *Polyhedron.* **2001**, *20*, 1157.

(84) Y. Yonekuta, K. Susuki, K. Oyaizu, K. Honda and H. Nishide, *J. Am. Chem. Soc.* **2007**, *129*, 14128.

(85) H. Nishide, T. Suga, *J. Electrochem. Soc.,* **2005**, *14*, 32.

(86) T. Suga, H. Oshiro, S. Sugita, K. Oyaizu, H. Nishide, *Adv. Mater*. **2009**, *21*, 1627.

(87) M. S. Ram, J. T. Hupp, *J. Phys. Chem*. **1990**, *94*, 2378.

(88) D. E. Lansky, D. P. Goldberg, *Inorg. Chem*. **2006**, *45*, 5119.

(89) J. Cho, J. Woo, J. Eun Han, M. Kubo, T. Ogura and W. Nam, *Chem. Sci*. **2011**, *2*, 2057.

(90) (a) L. Que, Jr., *Acc. Chem. Res*. **2007**, *40*, 493. (b) W. Nam, *Acc. Chem. Res*. **2007**, *40*, 522. (c) J. Hohenberger, K. Ray and K. Meyer, *Nat. Commun*. **2012**, *3*, 720.

(91) J. Y. Lee, R. L. Peterson, K. Ohkubo, I. Garcia-Bosch, R. A. Himes, J. Woertink, C. D. Moore, E. I. Solomon, S. Fukuzumi, K. D. Karlin, *J. Am. Chem. Soc*. **2014**, *136*, 9925.

(92) R. L. Peterson, R. A. Himes, H. Kotani, T. Suenobu, L. Tian, M. A. Siegler, E. I. Solomon, S. Fukuzumi, K. D. Karlin, *J. Am. Chem.Soc.* **2011**, *133*, 1702.

(93) S. Itoh, H. Kumei, M. Taki, S. Nagatomo, T. Kitagawa, S. Fukuzumi, *J. Am. Chem. Soc.* **2001**, *123*, 6708.

(94) M. H. V. Huynh, T. J. Meyer, *Chem. Rev*. **2007**, *107*, 5004.

(95) D. E. Lansky, D. P. Goldberg, *Inorg. Chem*. **2006**, *45*, 5119.

(96) J. Cho, J. Woo, J. Eun Han, M. Kubo, T. Ogura, W. Nam, *Chem. Sci*. **2011**, *2*, 2057.

(97) T. Osako, K. Ohkubo, M. Taki, Y. Tachi, S. Fukuzumi, S. Itoh, *J. Am. Chem. Soc*., **2003**, *125*, 11027.

(98) (a) G. Litwinienko, K. U. Ingold*, J. Org. Chem.* **2003**, *68*, 3433. (b) G. Litwinienko, K. U. Ingold, *J. Org. Chem*. **2004**, *69*, 5888. (c) M. C. Foti, C. Daquino, C. Geraci, *J. Org. Chem.* **2004**, *69*, 2309.

(99) K. A. Gardner, L. L. Kuehnert, J. M. Mayer, *Inorg. Chem*. **1997**, *36*, 2069.

(100) T. Osako, K. Ohkubo, M. Taki, Y. Tachi, S. Fukuzumi, S. Itoh, *J. Am. Chem. Soc.* **2003**, *125*, 11027.

(101) S. Fukuzumi, K. Shimoosako, T. Suenobu, Y. Watanabe, *J. Am.Chem. Soc.* **2003**, *125*, 9074.

(102) S. C. Weatherly, I. V. Yang, H. H. Thorp, *J. Am. Chem. Soc*. **2001**, *123*, 1236.

(103) (a) M. Patz, H. Mayr, J. Maruta, S. Fukuzumi, *Angew. Chem., Int. Ed*. **1995**, *34*, 1225. (b) T. Osako, K. Ohkubo, M. Taki, Y. Tachi, S. Fukuzumi, S. Itoh*, J. Am. Chem. Soc*. **2003**, *125*, 11027. (c) J. Shearer, C. X. Zhang, L. N. Zakharov, A. L. Rheingold, K. D. Karlin, *J. Am. Chem. Soc*. **2005**, *127*, 5469.

(104) R. A. Marcus and N. Sutin, *Biochim. Biophys. Acta*, **1985**, *811*, 265.

(105) S. Fukuzumi, K. Shimoosako, T. Suenobu, Y. Watanabe, *J. Am. Chem. Soc*., **2003**, *125*, 9074.

(106) (a) J. B. Guttenplan, S. G. Cohen, *J. Am. Chem. Soc*. **1972**, *94*, 4040. (b) P. J. Wagner, H. M. H. Lam, *J. Am. Chem. Soc.* **1980**, *102*, 4167.

(107) T. Nash, *Biochem. J*. **1953**, *55*, 416.

(108) (a) A. Nishinaga, H. Tomita, T. Matsuura, *Tetrahedron Lett*. **1980**, *21*, 3407. (b) A. Nishinaga, H. Tomita, K. Nishizawa, T. Matsuura, S. Ooi, K. Hirotsu, *J. Chem. Soc. Dalton Trans.* **1981**, 1504.

(109) A. Company, S. Yao, K. Ray, M. Driess, *Chem. Eur. J.* **2010**, *16*, 9669.

(110) (a) V. K. Korboukh, N. Li, E. W. Barr, J. M. Bollinger., Jr., C. Krebs, *J. Am. Chem. Soc.* **2009,** *131,* 13608. (b) N. Li, V. K. Korboukh, C. Krebs, J. M. Bollinger., Jr., *Proc. Natl. Acad. Sci. U. S. A*. **2010**, *107*, 15722.

(111) K. Park, N. Li, Y. Kwak, M. Srnec, C. B. Bell, L. V. Liu, S. D. Wong, Y. Yoda, S. Kitao, M. Seto, M. Hu, J. Zhao, C. Krebs, J. M. Bollinger, Jr., E. I. Solomon, *J. Am. Chem. Soc.* **2017**, *139*, 7062.

Chapter 3

Synthesis and Characterization of a Nickel(II)-Superoxo Species Supported by an Anionic Biuret Ligand with Nucleophilic Oxidative Reactivity.

A part of this work has been published in

Angew. Chem. Int. Ed. **2018**, *57*, 14883 –14887

C. Panda[+], A. Chandra[+], T. Corona, E. Andris, B. Pandey, S. Garai, N. Lindenmaier, S. Kgnstner, E. R. Farquhar, J. Roithov,* G. Rajaraman,* M. Driess,* and K. Ray*

[+] These authors contributed equally to this work

3.1. Introduction:

Metalloenzymes activate dioxygen to carry out a variety of biological reactions. Controlled oxidation of the organic substrates by the metal-mediated activation of dioxygen is responsible for controlling the key metabolic functions in biology.[1,2] Therefore one of the primary goals of biomimetic research is to understand the structure of the active sites and the mechanistic insights of the metal-mediated dioxygen activation reactions. Metalloenzymes use diverse active sites to reductively activate dioxygen into various metal-oxygen adducts, such as metal-superoxo, -peroxo, -hydroperoxo, -alkylperoxo, and -oxo species. Over the years the active site structures of many oxygenases and oxidase enzymes were uncovered. Among them, iron, copper, and manganese are found to be the predominant metals, present in metalloenzymes that can perform highly efficient and selective oxidation reactions. As a result, scientists were more focused to explore the synthetic model complexes of the above-mentioned metals. In contrast, the artificial oxidation catalysts based on late-transition metals such as nickel are much rarer in literature. However, the discovery of a few nickel-based enzymes involved in oxidation processes in the last decades have changed the storyline.[3] Another important reason is the industrial demand of the palladium-analogs as catalysts.[4] Many of the metal-mediated oxidation catalysts used in industry are based on palladium metals, which increase the overall cost of the process. Therefore, it's a long-time demand to replace the novel Pd-metal by the cheaper analogous nickel reagents.

Concerning nickel-based enzymes (Figure 3.1.1), nickel superoxide dismutase catalyzes the disproportionation of superoxide in a process in which a superoxonickel(II) and superoxonickel(III) species play the key role.[5] For quercetin 2,4-dioxygenase, during the oxidative cleavage of the flavonol quercetin, a nickel–dioxygen adduct has been crystallographically detected.[6] However, the identification of high valent nickel-oxo species in the catalytic cycle is still missing. In 2012, Ray and co-workers have postulated the formation of an oxo/hydroxo-nickel(III) species by the reaction of $[Ni^{II}(CF_3SO_3)_2(TMG_3tren)]$ with *m*CPBA at -30 °C.[7] Very recently Anna Company and coworkers have reported the formation of a metastable oxyl-nickel(III) species in the reaction of a nickel(II)-bis(amidate) complex with *m*CPBA at low temperature(-30 °C).[8] Several nickel-dioxygen adducts, such as nickel-superoxo and -peroxo species, have been reported so far and the binding modes of the O_2 unit (end-on: η^1 vs side-on: η^2) and their electronic nature was thoroughly investigated using different spectroscopic techniques.[9] The reactivities of the metal-dioxygen intermediates in electrophilic and nucleophilic reactions have always been under investigation. In general, mononuclear non-heme metal peroxo species show oxidative nucleophilic reactivity (such as

aldehyde deformylation), whereas metal superoxo species are associated with electrophilic oxidation reactions such as abstraction of H-atom from a C-H bond and oxygen-atom transfer (OAT) to alkenes, phosphines, or sulfides. However, this general consideration is not always true and detail biomimetic studies have shown us the exceptional behavior of the metal superoxide complexes. For example Fe^{III}–superoxide intermediates can involve in both electrophilic and nucleophilic reactions.[10] In isopenicillin N synthase (IPNS), 2-hydroxyethylphosphonate dioxygenase (HEPD), 2-hydroxypropylphosphonic acid epoxidase (HppE), and 1-aminocyclopropane-1-carboxylic acid oxidase (ACCO), the Fe^{III}–superoxide unit is proposed to perform HAA during the O_2 activation process. Whereas in the *α*-ketoglutarate (*α*-KG) dependent oxygenases and the pterin-dependent hydroxylases, the Fe^{III}–superoxide intermediate is proposed to be responsible for the nucleophilic attack.[11] Very recently from our group, the nucleophilic reactivity of the iron-superoxide species containing a hexanuclear non-heme ligand with the aldehydes has been reported.[12] McDonald and co-workers have reported that the [N,N′-bis(2,6-diisoproylphenyl)-2,6-pyridinedicarboxamido]-superoxo-copper(II) species can show both electrophilic and nucleophilic reactivities.[13]

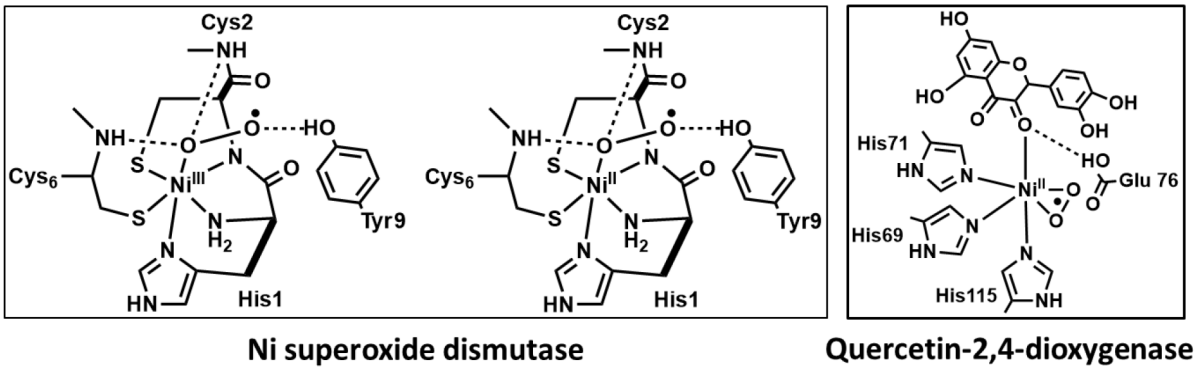

Ni superoxide dismutase **Quercetin-2,4-dioxygenase**

Figure 3.1.1: Biologically relevant terminal nickel–oxygen species in nickel superoxide dismutase and quercetin 2,4-dioxygenase.[3e]

The reactivity of nickel- superoxo species has also gained an attractive interest in biomimetic research. So far, the synthetic nickel-superoxido model complexes reported in the literature are only capable of performing electrophilic oxidation reactions.[14] Among all these nickel superoxo species reported so far the side-on superoxido-nickel(II) complex [$L'Ni^{II}O_2^{\bullet-}$] (**1a**; Figure 3.1.2), involving the monoanionic *β*-diketiminate ligand **L'**, exhibited a dioxygenase-like reactivity when exposed to para-substituted di-tert-butylphenols where the oxidation product involved both the oxygen atoms from a single Ni-O_2 subunit.[15]

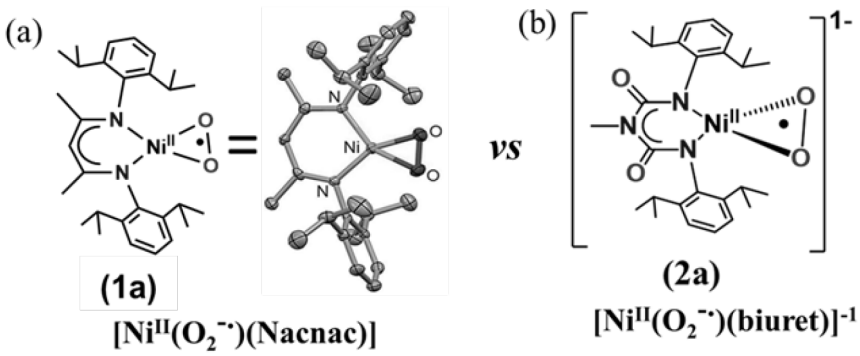

Figure 3.1.2: (a) Side-on nickel(II)-superoxo species (**1a**) and its molecular structure, as reported by Driess and co-workers.[14c] (b) Newly synthesized monoanionic nickel(II)-superoxo species (**2a**).

The recently demonstrated nucleophilic ability of the copper-superoxo and iron-superoxo species raised the question whether or not such nucleophilic reactivity could be found with superoxido-nickel species as well. To the best of our knowledge, no direct evidence for a synthetic nickel(II) superoxide species that reacts as a nucleophile has been reported to date. In this present work, we put our efforts to uncover structure–reactivity relationships of mononuclear metal–dioxygen intermediates. Although the neutral nickel-superoxo species (**1a**) is shown to exhibit electrophilic reactivities, the newly synthesized monoanionic nickel-superoxo species(**2a**) is demonstrated to act as a nucleophile (Figure 3.1.2). In this chapter, we show how the electronic nature and the reactivity of the nickel–O_2 core varies depending on the nature of the supporting ligands of the nickel complexes.

3.2. Results and Discussions:

3.2.1: Syntheses and Characterization of the biuret ligand LH_2

The ligand was synthesized by coupling of the dichloformyl methylamine with two molar equivalent of the 2,6-diisopropylaniline in the presence of triethylamine (Scheme 3.2.1). The new ligand was characterized by ^{1}H-NMR (Figure 3.2.1), IR, and elemental analysis. ESI-MS spectrum showed the *m/z* ratio, calculated for $[M+H]^+$ ($C_{27}H_{40}N_3O_2$): 438.3121, found: 438.3117. Although the biuret ligand is structurally similar to its Nacnac analog (Scheme 3.2.2), the electronic nature of these two ligands is different. Nacnac can behave as a monoanionic ligand whereas the biuret ligand (LH_2) has a dianionic character.

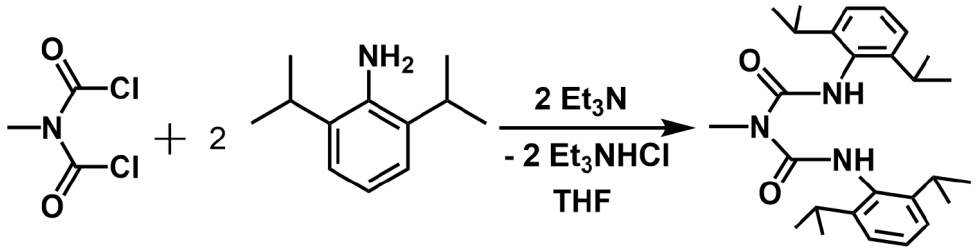

Scheme 3.2.1: Synthesis of the biuret ligand (**LH_2**).

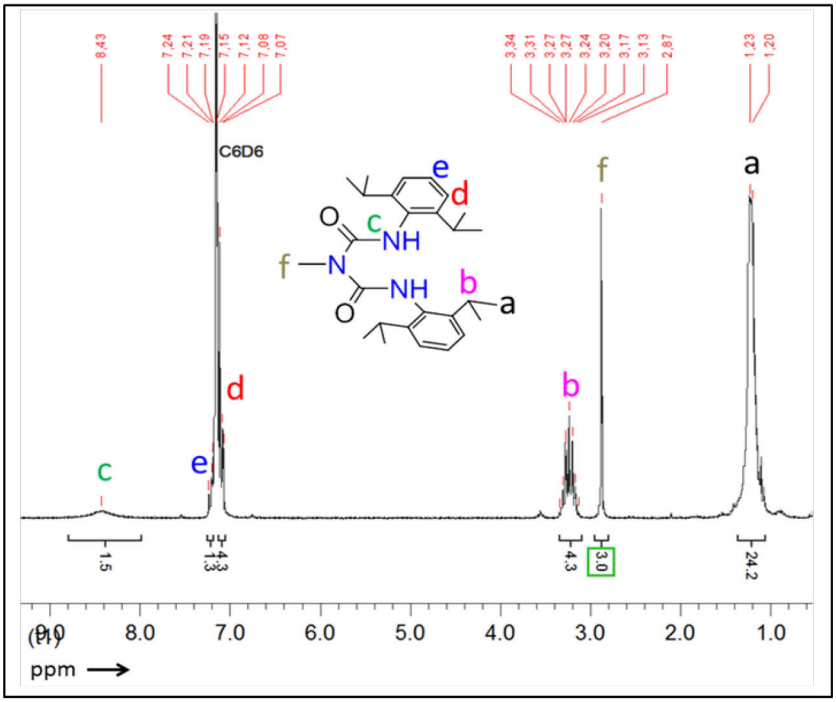

Figure 3.2.1: ^{1}H NMR spectra of the ligand **LH_2** in C_6D_6

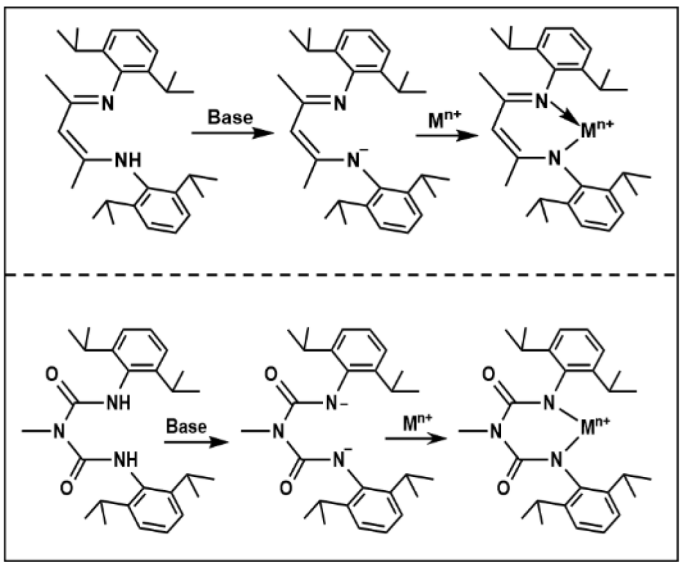

Scheme 3.2.2: A comparison of the coordination abilities of reported monoanionic '*nacnac*' ligand (top) and the newly synthesized biuret ligand (below).

3.2.2: Synthesis of the Nickel(II)Br_2 complex (M)

The nickel(II) complex of the ligand **LH_2** was synthesized according to Scheme 3.2.3. Anhydrous nickel(II) bromide salt was added to the previously deprotonated solution of **LH_2** in THF at -20 ºC under an argon atmosphere. The reaction mixture was then stirred overnight at RT, which gave a dark blue colored solution. The complex was then recrystallized (yield; 62%) from dry THF as dark blue crystals of **M**. Complex **M** was characterized by different spectroscopic techniques. The crystal structure of the complex **M** (Figure 3.2.2) was obtained as the dilithium salt $[Li(thf)_3]_2.[LNi^{II}Br_2]$ (**M**; CCDC 1832378). Single-crystal X-ray diffraction analysis revealed that complex **M** consists of a tetracoordinated Ni^{II} atom. Elemental analysis data matched perfectly with the formula $C_{39}H_{61}Br_2N_3NiO_5$ which corresponds to (**M**- 3×THF-2×Li) composition. UV-vis spectra of **M** (1 mM) in CH_3CN showed λ_{max}: 356 nm (ε = 7770 $M^{-1}cm^{-1}$), 480 nm (ε = 680 $M^{-1}cm^{-1}$), 558 nm (ε = 755 $M^{-1}cm^{-1}$) and 830 nm (ε = 70 $M^{-1}cm^{-1}$). ^{1}H-NMR spectrum (Figure 3.2.3) of **M** measured in CD_3CN at room temperature displays the distribution of the signals in the range of 40 ppm to −30 ppm, corroborates the presence of a paramagnetic Ni(II) center in **M**. Complex **M** is EPR silent. The FTIR spectra of the biuret ligand (**LH_2**) and complex **M** showed a distinct shift in carbonyl stretching frequencies (Figure 3.2.4). The infrared spectrum of **LH_2** showed two intense vibrations at 1687 cm^{-1} and 1643 cm^{-1} for the carbonyl absorptions (ν_{CO}), whereas, for complex **M** carbonyl vibrations appear at 1600 cm^{-1} and 1576 cm^{-1}.

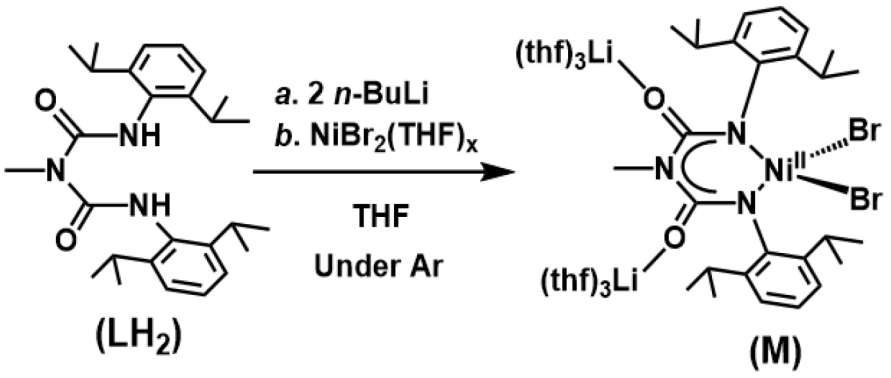

Scheme 3.2.3: Synthesis of the nickel (II) complex (**M**) from the biuret ligand (**LH_2**).

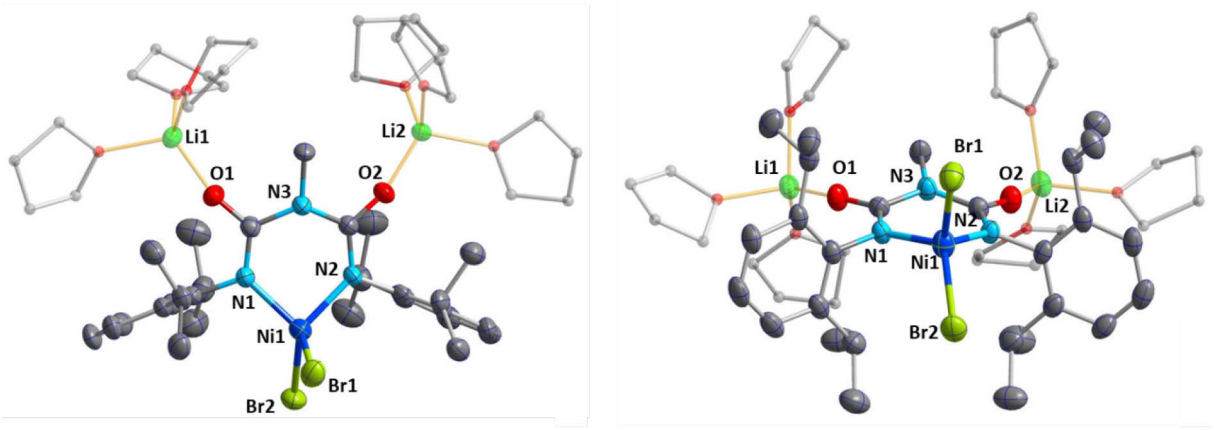

Figure 3.2.2: The molecular structure of the complex **M** as determined by X-ray diffraction analysis. The thermal ellipsoids are shown at the 50% probability level. All hydrogen atoms are omitted for clarity. View from Top(left), and view from Side(right).

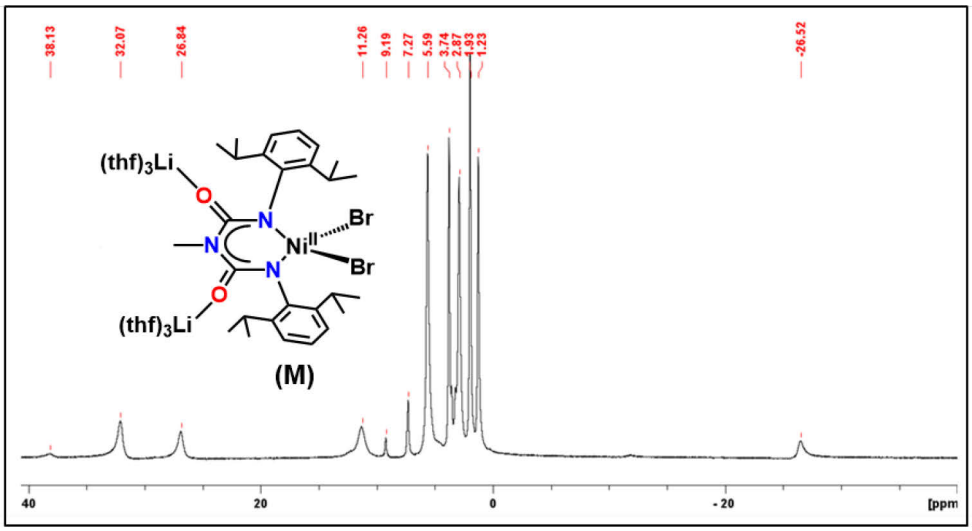

Figure 3.2.3: ^{1}H NMR spectrum of the nickel (II) complex (**M**)in CD_3CN.

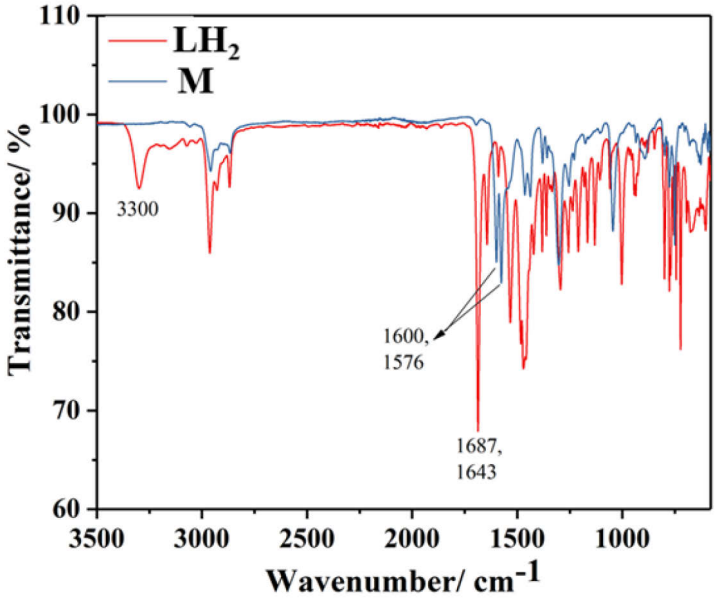

Figure 3.2.4: FTIR spectra of the ligand $\mathbf{LH_2}$ (red line) and the complex **M** (blue line).

3.2.3. Generation and Characterization of the Superoxido-Nickel (II) intermediate (2a)

Nickel(II) complexes are generally inert towards molecular oxygen. The most common approach to generate the metal-dioxygen intermediate involves either the reaction of chemically reduced nickel centers (Ni^{I} or Ni^{0}) with dioxygen[14a,c,d] or the reaction of Ni^{II} complexes with hydrogen peroxide (H_2O_2) in presence of a base.[14b] The newly synthesized Ni(II)-biuret complex (**M**) did not react with molecular oxygen, but it immediately reacts with excess H_2O_2 in presence of excess Et_3N (TEA) in acetonitrile at 25 ºC to form the metastable yellow-orange species **2a** with a half-life ($t_{1/2}$) of 30 minutes at 25 ºC (Scheme 3.2.4). The formation of a new band at λ_{max} = 455 nm (ε = 5900 M^{-1} cm^{-1}) was observed with a shoulder at 300 nm (Figure 3.2.5). The formation of **2a** reached its maximum within 800 sec.

The nature of the yellow-orange intermediate **2a** was established by a variety of spectroscopic techniques such as ESI-MS, EPR, infrared photodissociation (IRPD), and XAS study.

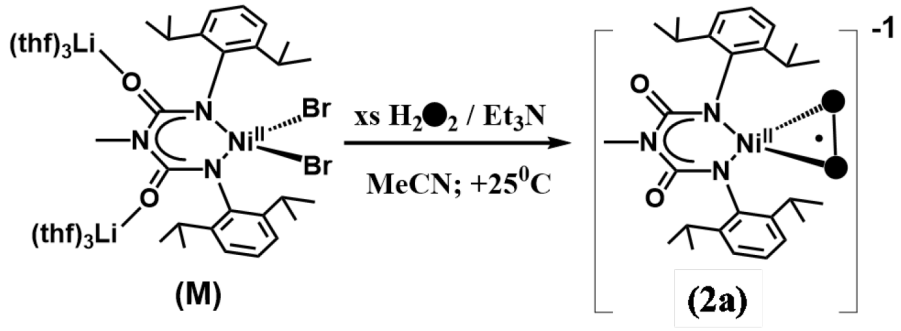

Scheme 3.2.4: Formation of the intermediate **2a** via the reaction of the complex **M** with an excess of hydrogen peroxide (5 equivalent) and Et_3N (2 equivalent).

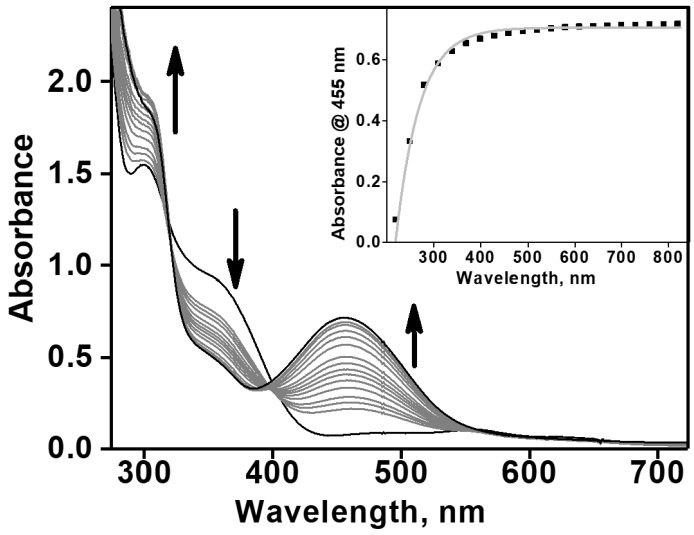

Figure 3.2.5: UV/Vis spectral changes associated with the reaction of $[LNi^{II}Br_2]^{2-}$ with excess H_2O_2 and Et_3N to form **2a** in CH_3CN at 25 ºC. Inset: The rate of the formation of **2a** with time.

3.2.3a. ESI-MS spectral analysis of 2a: To identify the nature of the newly generated species **2a**, the low-temperature ESI-MS experiment was done using 16-O and 18-O labeled H_2O_2. Since **2a** is thermally not stable, freshly prepared solutions of **2a** was used for each experiment. ESI-MS spectra (Figure 3.2.6) of **2a** showed the existence of an intense peak at a mass-to-charge ratio (*m/z*) value of 539.25 whose mass and isotope distribution patterns correspond to $\{Li_2[LNi^{16}O_2]\}^+$. When $H_2{}^{18}O_2$ was used to form **2a** (Figure 3.2.7), then the ESI-MS spectra clearly show the four-unit mass shift from 539.25 to 543.26. This proves that the two oxygen atoms which are incorporated into **2a**, are coming from H_2O_2.

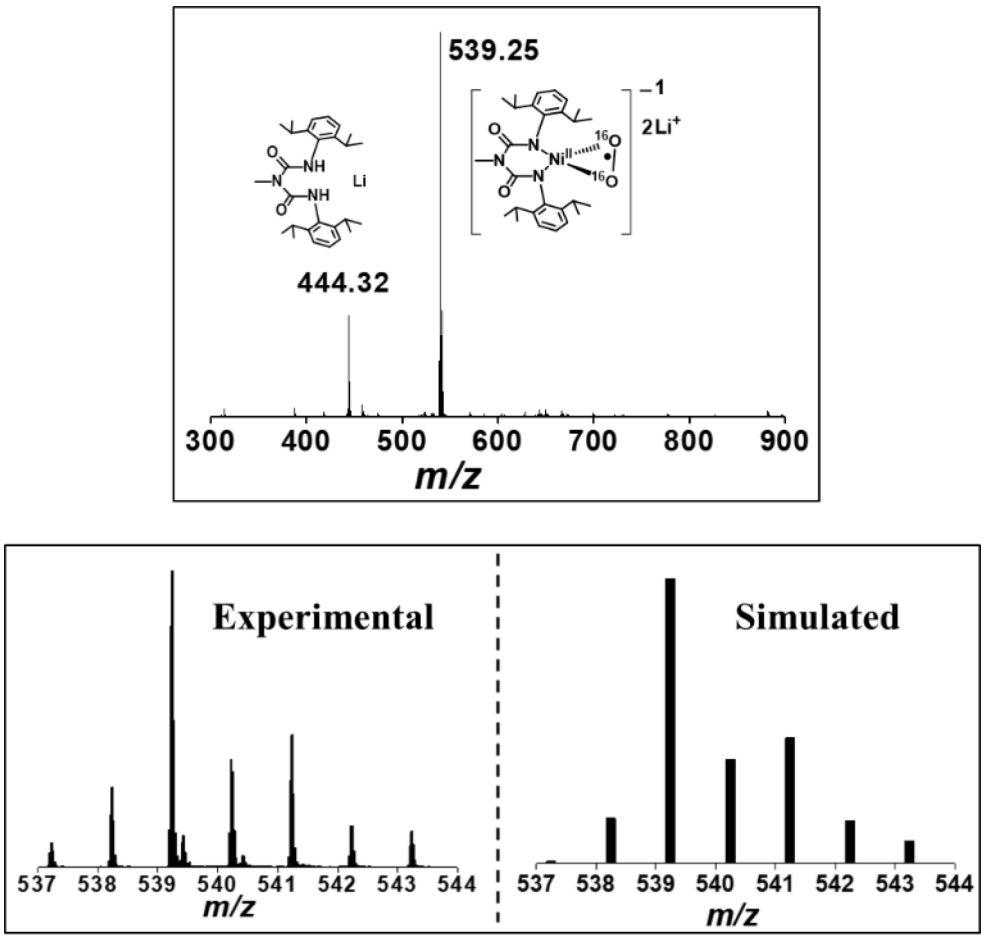

Figure 3.2 6: ESI-MS(+) of **2a** in CH_3CN at 25ºC formed by the reaction of $[Li(thf)_3]_2[LNi^{II}Br_2]$ with 5 equiv of H_2O_2 (16-O) in presence of 2 equiv TEA. The spectrum shows a major peak at m/z 539.25 whose isotopic distribution pattern is consistent with a $\{Li_2[(biuret)Ni^{16}O_2\}^+$ assignment.

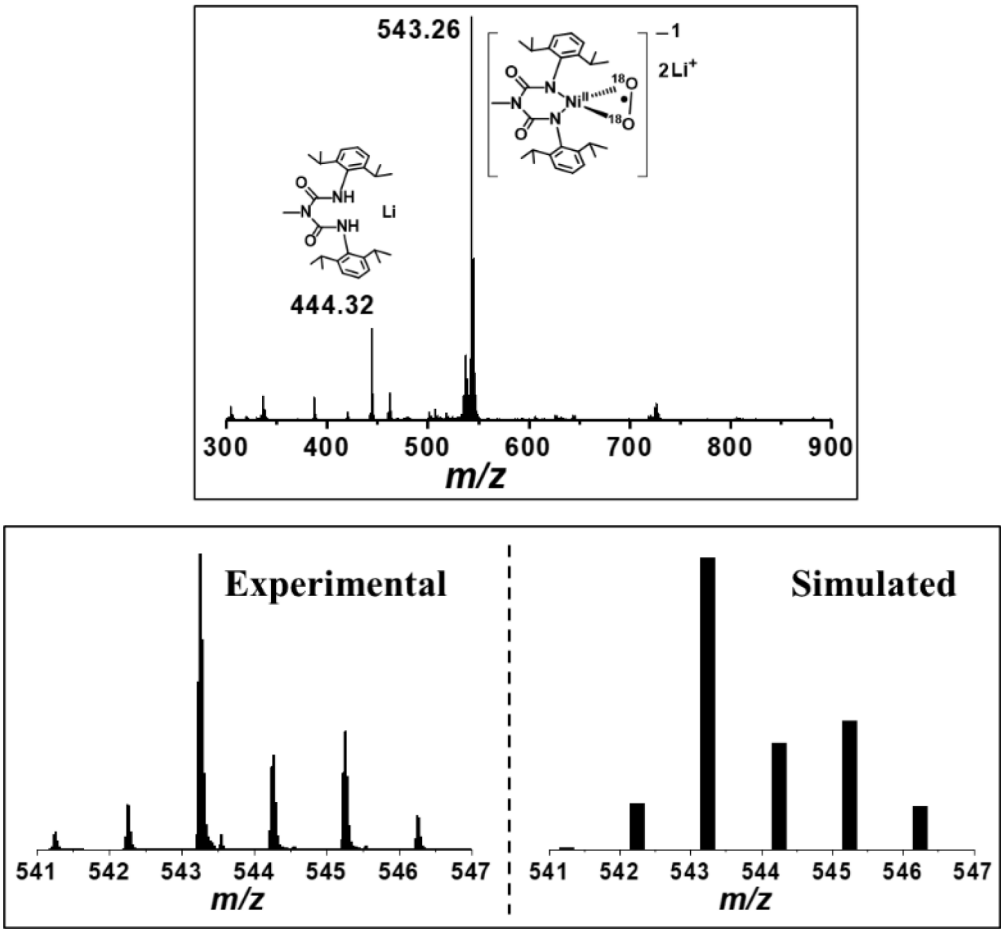

Figure 3.2.7: ESI-MS(+) of ^{18}O-labeled **2a** in CH_3CN at 25ºC formed by the reaction of $[Li(thf)_3]_2[LNi^{II}Br_2]$ with 5 equiv of $H_2{}^{18}O_2$ in the presence of 2 equiv TEA. The spectrum shows a major peak at m/z 543.26 whose isotopic distribution pattern is consistent with a $\{Li_2[(biuret)Ni^{18}O_2\}^+$ assignment.

3.2.3*b*. EPR analysis of 2a: In contrast to the complex **M** ($[LNi^{II}Br_2]^{2-}$) which is EPR silent, intermediate **2a** is EPR active. A freshly prepared solution of intermediate **2a** was transferred into a Young quartz EPR tube and sealed. The solution in the tube was frozen in liquid nitrogen, and EPR measurements were performed at 10K. A slightly rhombic signal was observed at g_x=2.21, g_y=2.17, and g_z=2.06 (Figure 3.2.8). For spin quantification, the EPR signal was double integrated to obtain the area under the signal. It confirms the presence of more than 85% of the total nickel spins in solutions. This value confirmed that **2a** is the major product present in the solution.

The observed *g*-anisotropy ($\Delta_g = g_z - g_x$) of 0.15 resembles quite closely the Δ_g value of 0.12 determined for "free" $O_2^{\cdot-}$ in water with *g*=[2.10, 2.00, 1.98].[16] A similar rhombic EPR spectrum was observed for Riordan's "side-on" nickel superoxo compound **1B,**[17b] $[PhTt^{Ad}]Ni(O_2)$ ($PhTt^{Ad}$ = Phenyltris((1-adamantylthio)methyl)borate), with *g* = [2.24, 2.19, 2.01] (Figure 3.2.9). Notably, **1B** has a higher *g*-anisotropy value (Δ_g =0.23)[17] which can be attributed to a five-coordinate Ni^{II} center, which results in the unpaired electron being

predominantly located in the d_z^2 orbital of the Ni center. A rhombic EPR signal with Δ_g= 0.07 was also reported for complex **1a,** [$Ni^{II}(O_2^{\cdot-})$(Nacnac)], with principal *g* values of 2.138, 2.116, and 2.067.[14c]

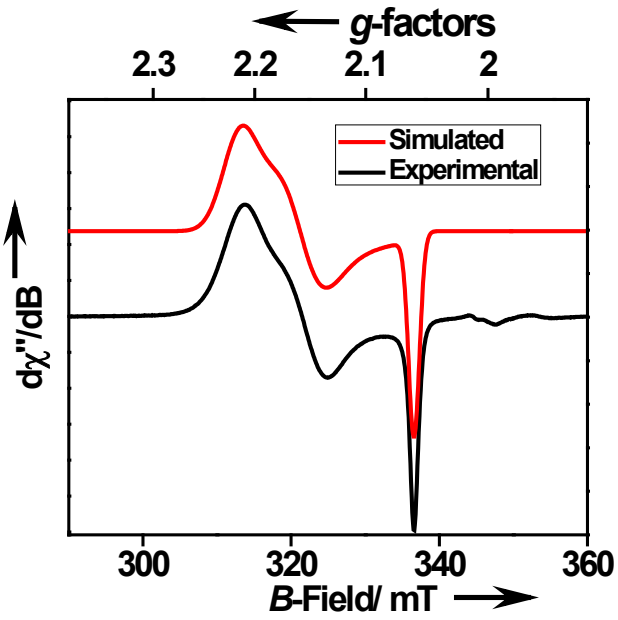

Figure 3.2.8: X-band EPR spectrum of a 2mM solution of **2a** in CH_3CN at 10 K. The spectra were measured with the following parameters: Temperature 10 K, frequency 9.701858 GHz, modulation amplitude 1.0 mT, microwave power 0.015 mW, modulation frequency 100 kHz, the time constant 20.48 ms.

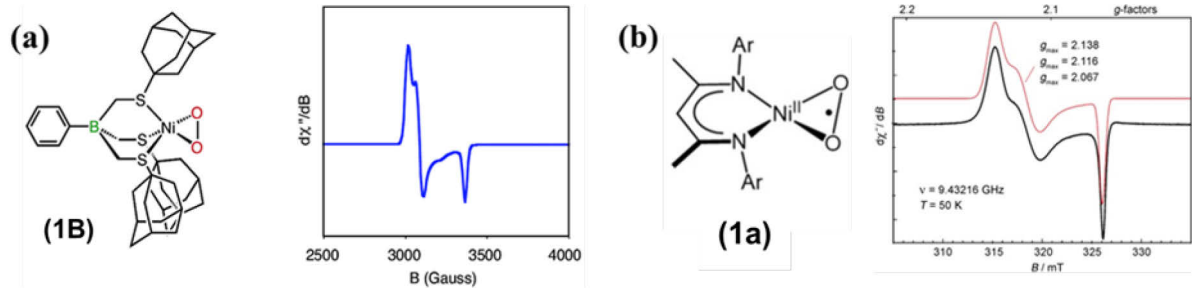

Figure 3.2.9: (a) Riordan and coworkers have reported "side-on" nickel(II) superoxo compound **1B** and its EPR spectrum [17b]; (b) Driess and coworkers reported "side-on" nickel(II) superoxo compound **1a** and its EPR spectrum.[14c]

So, we can conclude that the electronic structure of **2a**, contains a predominantly superoxide-centered radical (*S* = 1/2) coupled to a square-planar (*SqP*) low-spin d^8-Ni^{II} center. The same electronic structure was reported before for complex **1a** [14c], however, the *g*-anisotropy value for **1a** is much lower (Δ_g =0.06).

3.2.3c. IRPD analysis of 2a: The infrared photodissociation (IRPD) spectrum of the deuterium-tagged anionic complex, **2a,** was acquired with the ISORI instrument. [18] The IRPD spectrum showed an oxygen-sensitive band at 980 cm^{-1}, which shifts to 932 cm^{-1} upon ^{18}O labeling

(Figure 3.2.10). The experimental isotopic shift of 48cm^{-1} agrees well with the calculated shift of 57 cm^{-1} for a diatomic O–O bond stretching vibrational mode. The O–O vibration in **2a** (980 cm^{-1}) appears at similar energy to that of the side-on nickel(II)-superoxo complex **1a** (971 cm^{-1}) as reported by Driess and coworkers previously.[14c] Isotope sensitive (^{18}O) vibrational spectroscopic data of different known Ni-superoxo species are shown in table 3.2.1.

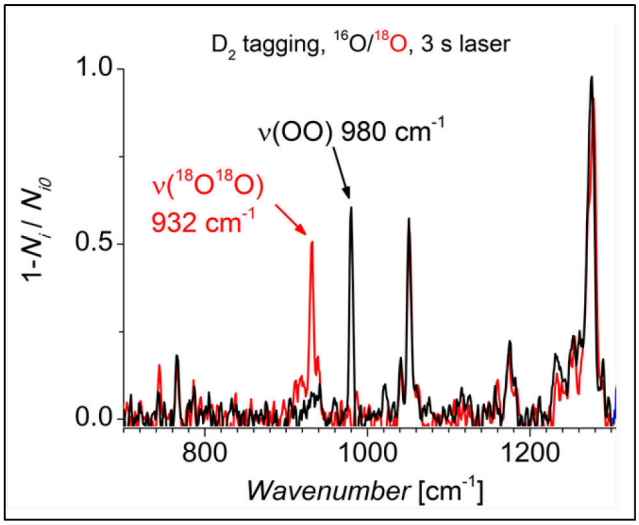

Figure 3.2.10: D_2-tagging IRPD spectra of the $[LNi^{II}O_2]^-$complex anion (m/z 525, black trace) and ^{18}O-labeled $[LNi^{II}O_2]^-$ complex (m/z 529, red trace) measured with the ISORI instrument.

Table 3.2.1: Isotope sensitive (^{16}O vs ^{18}O) vibrational spectroscopic data of different synthetic mononuclear Ni-superoxo species.

Ni(II)-superoxo compounds	**Binding mode**	**ν (^{16}O-^{16}O) /cm^{-1}**	**ν (^{18}O-^{18}O) /cm^{-1}**	**Δν /cm^{-1}**	**Ref.**
$[PhTt^{Ad}]Ni(O_2)$	Side-on	No data available			17b
$[Ni(tmc)(O_2)](OTf)$	End-on	1131	1067	64	14b
$[Ni^{II}(13\text{-}TMC)(O_2)]^+$	End-on	1130	1070	60	14d
$[(nacnac)Ni^{II}O_2]$ (**1a**)	Side-on	971	919	52	14c
$[(L)Ni^{II}O_2]^{-1}$ (**2a**)	Side-on	980	932	48	This Work

3.2.4. XAS (X-ray Absorption Spectroscopy) study:

To probe the metal oxidation states and the geometry in **2a,** X-ray absorption spectroscopic studies were performed for **M**, **2a,** and **1a** at Ni *K*-edges at 15 K. The experimental extended X-ray absorption fine structure (EXAFS) spectra of **M** and **2a** were compared to EXAFS simulations based on the simple model DFT structures. Ni *K*-edge XANES spectra (Figure 3.2.11) shows a comparison of the Ni *K*-edge spectrum of **2a** with its precursor **M**, as well as **1a**.

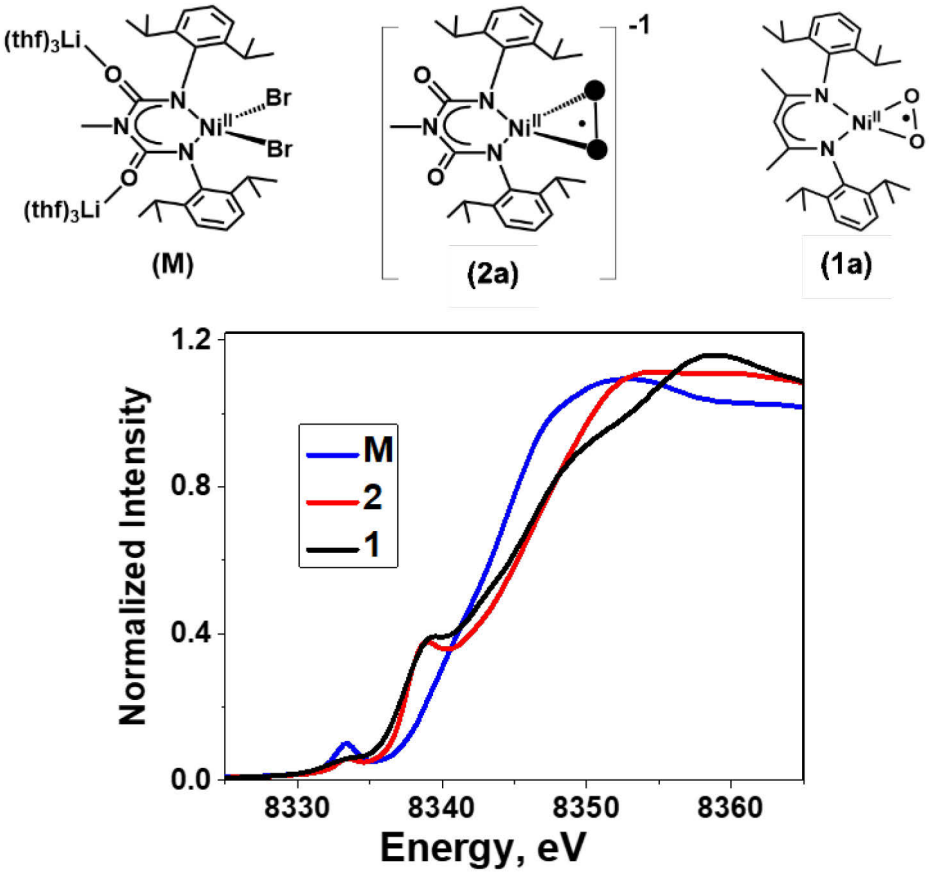

Figure 3.2.11: Ni K-edge XANES spectra of **M** (Blue line), **2a** (Red line), and **1a** (black line) in frozen CH_3CN solutions at 15 K.

From the XANES data plot, we can see that both the complexes **1a** and **2a** show an intense *1s*-to-$4p^+$ shakedown transition along the edge at about 8338.5 eV, which is absent in complex **M**. The *1s*-to-*3d* pre-edges in **1a** and **2a**, found at 8333.2 eV, are significantly weaker than that of **M** ($E_{\text{pre-edge}}$ = 8333.25 eV). These two experimental results strongly indicate a *SqP* coordination geometry of Ni in **1a** and **2a** versus the T_d symmetry of **M.**[19] The Ni^{II} assignment for both complexes **1a** and **2a** have been confirmed from the absence of any pre-edge shift in **1a** and **2a** compared with **M.**

The retention of the four coordinated XRD structure of **M** in solution with two Ni-N/O scatterers @ 1.93 Å and two Ni-Br scatterers @ 2.40 Å was confirmed from extended X-ray absorption fine structure (EXAFS) analysis (Figure 3.2.12 and Table A3.2.1 in appendices). The Fourier transform of the EXAFS of **2a** shows loss of the dominant Ni-Br scattering seen in **M** at *r'* = 2.1 Å along with a shift to lower *r* for the putative Ni-N/O shell around *r'* = 1.5 Å (Figure 3.2.12). This data is consistent with the near-stoichiometric conversion of **M** into **2a** upon reaction with H_2O_2 in the presence of TEA. Analysis of the EXAFS data of **2a** (Table

A3.2.2 in appendices) shows the best fit of four N/O scatterers at 1.85 Å and is comparable to the average Ni-N/O distance of 1.838 (2) Å of **1a**.

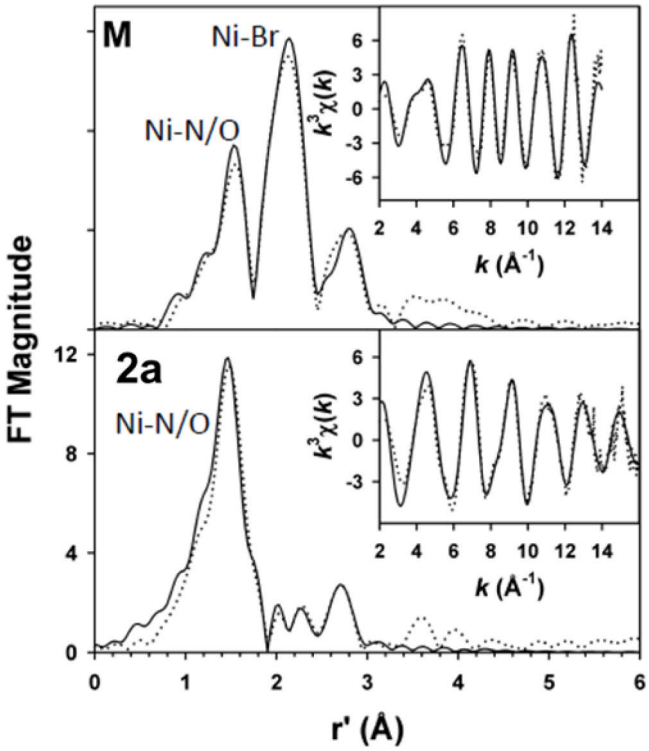

Figure 3.2.12: The Fourier-transformed Ni K-edge EXAFS spectra of **M** (top) and **2a** (bottom) and the respective k^3-weighted EXAFS spectra are in the insets. Experimental data are shown as dotted lines, while the best fits are shown as solid lines.

3.2.5. Reactivity studies of the complex 2a:

As discussed before, mononuclear non-heme metal-superoxo species are typically strong electrophiles. According to our best knowledge, only two examples are available in the literature to date, where iron and copper superoxo complexes showed nucleophilic oxidative reactivity. In general, the superoxido-nickel (II) complexes are strong electrophiles and typically unreactive towards other electrophiles. According to the literature report, although **1a** can oxidize alcohols and amines in various exogenous organic substrates, it did not react with any aldehydes (Figure 3.2.13). The addition of benzaldehyde to **1a** did not result in any change in its UV/Vis spectra.[15]

In contrast to complex **1a**, complex **2a** didn't participate in any electrophilic HAT reactivity towards the C-H bonds of dihydroanthracene or the O-H bonds of para-substituted di-tertbutyl phenols (Figure 3.2.14). However, a pseudo-first-order decay of the absorption band at 455 nm

was observed upon addition of excess 2-PPA or substituted aldehydes to a preformed solution of complex **2a** at 25 ºC.

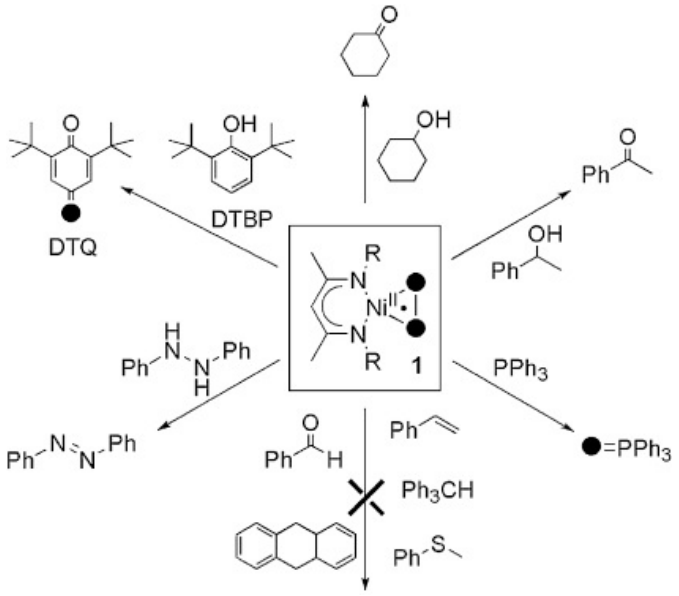

Figure 3.2.13: Reactivity of **1a** towards selected exogenous substrates. R=2,6-*i*$Pr_2C_6H_3$.[15]

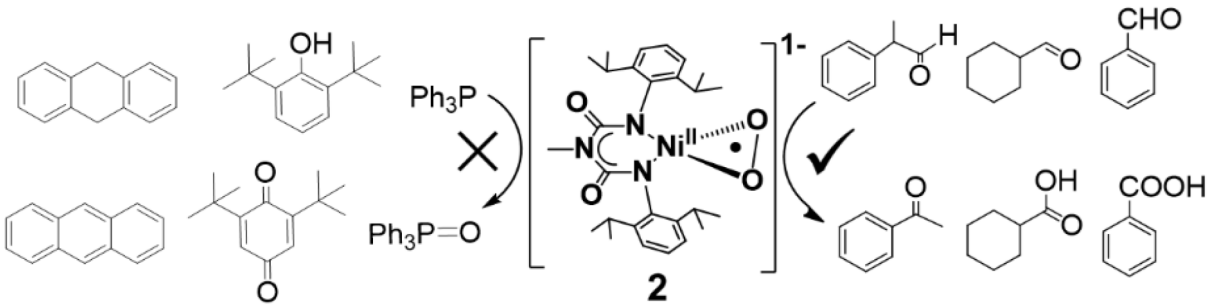

Figure 3.2.14: Reactivity of the complex **2a** towards different substrates.

Reactivity studies were done at 25°C under an inert atmosphere, by injecting the CH_3CN solutions of the substrates to a preformed solution of **2a** in CH_3CN. The pseudo-first-order decay of the 455 nm band was then monitored. The pseudo-first-order fitting of the decay curves gave the rate constant (k_{obs}), which increases linearly with the substrate concentrations. The slope of the rate constant (k_{obs}) *vs* substrate concentration plot provided the second-order rate constant (k_2) values (Figure 3.2.15).

The addition of 2-phenylpropionaldehyde (2-PPA) into the solution of complex **2a** at 25°C, results in the formation of acetophenone with ~74% yield (Figure 3.2.16). The rate constant increases proportionally with the substrate concentration (Figure 3.2.15), affording a second-order rate constant, k_2, of 0.00012 M^{-1} s^{-1} at 25 ºC.

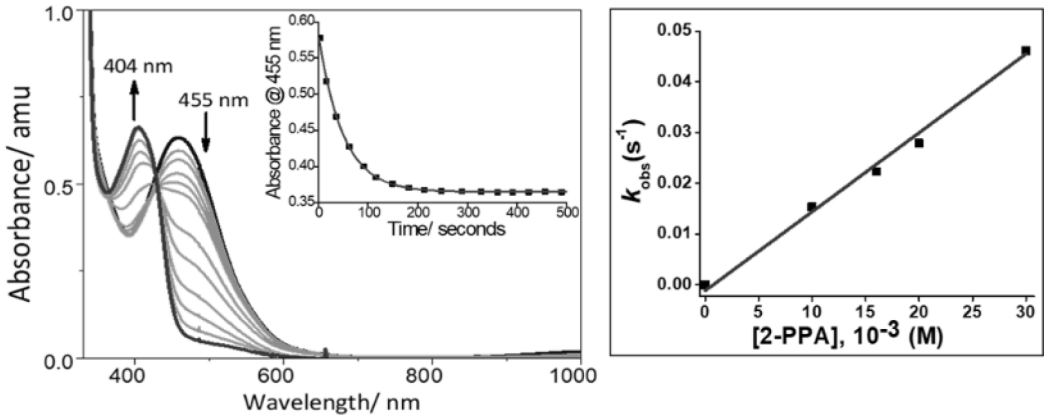

Figure 3.2.15: Left: Absorption spectral changes associated with the reaction of a 1mM solution of **2a** in CH_3CN with 2-PPA (25 mm) at 25 ºC. The inset shows the time trace of the decay of the 455 nm band (black squares) corresponding to **2a** and the pseudo-first-order fitting (solid line). Right: Plot of k_{obs} vs substrate concentration for the reaction of **2a** with 2-phenylpropionaldehyde (2-PPA) in CH_3CN at 25ºC.

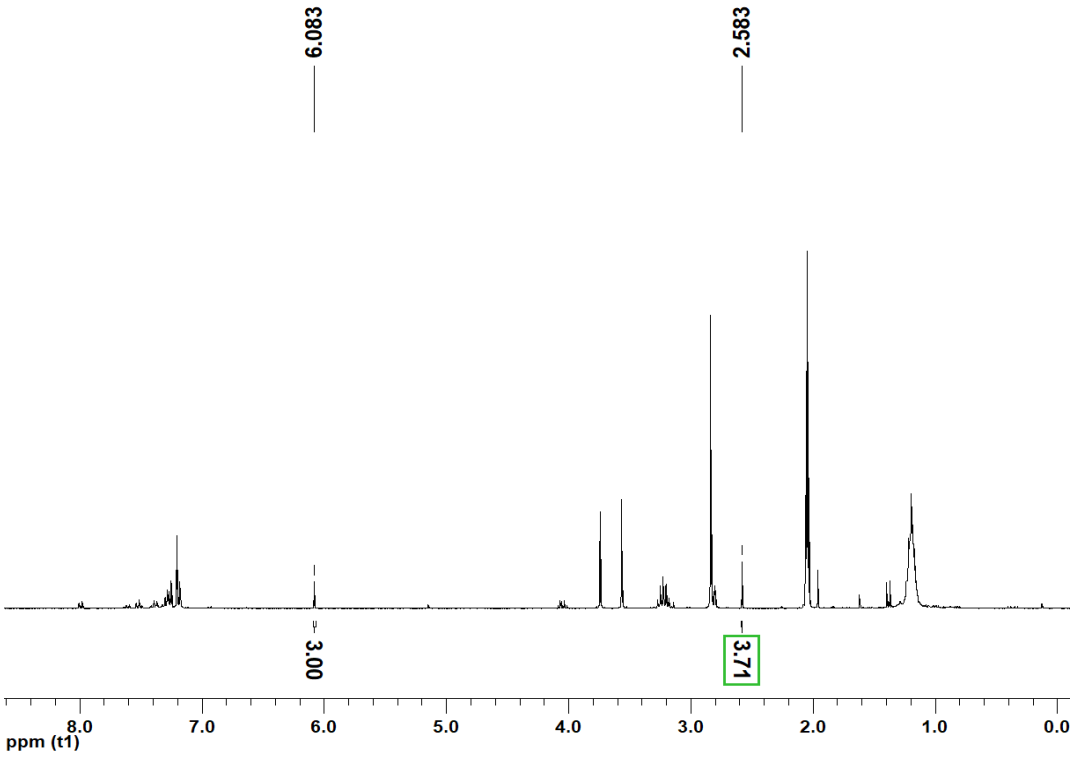

Figure 3.2.16: ^{1}H NMR spectrum of the reaction of **2a** with 2-phenylpropionaldehyde (2-PPA) in CD_3COCD_3 at 25ºC using 1,3,5-trimethoxybenzene as an internal standard (0.2 equiv, signal at 6.084 ppm). The product was identified to be acetophenone based on the appearance of a characteristic signal at 2.58 ppm for the –C(O)CH_3 group. Blank reactions of 2-PPA, with H_2O_2 and Et_3N in the presence and absence of the deprotonated biuret (L^{2-}) ligand did not show any formation of acetophenone product.

The nucleophilicity of **2a** is also demonstrated by its ability to undergo reaction with cyclohexane carboxaldehyde (CCA) to afford cyclohexane carboxylic acid in ~54% yields. The product was identified to be cyclohexane-carboxylic acid based on the appearance of a characteristic signal at 11.15 ppm for the –C(O)OH group (Figure 3.2.17). To investigate more about the nucleophilicity of the complex **2a,** different substituted aldehydes were used and their

reactions with **2a** were monitored by UV/Vis experiment. The reaction of the complex **2a** with different para-substituted benzaldehydes (*para*-*X*-C_7H_5O; X= *t*Bu, Me, H, Cl,) gave a good linear correlation of the rate to the σ_p^+ values of the para substituents (Figure 3.2.18). The plot of ln(k_2) versus the σ_p^+ values for the reaction of **2a,** at 25ºC, with para-*X*-benzaldehydes (*X* = *t*Bu, Me, H and Cl) gives a positive Hammett (ρ) constant of +0.44. The positive Hammett constant value confirms the nucleophilic behavior of complex **2a** with substituted benzaldehydes. This is the first time when any nickel(II)-superoxo species shows nucleophilic reactivity with para-substituted benzaldehydes.

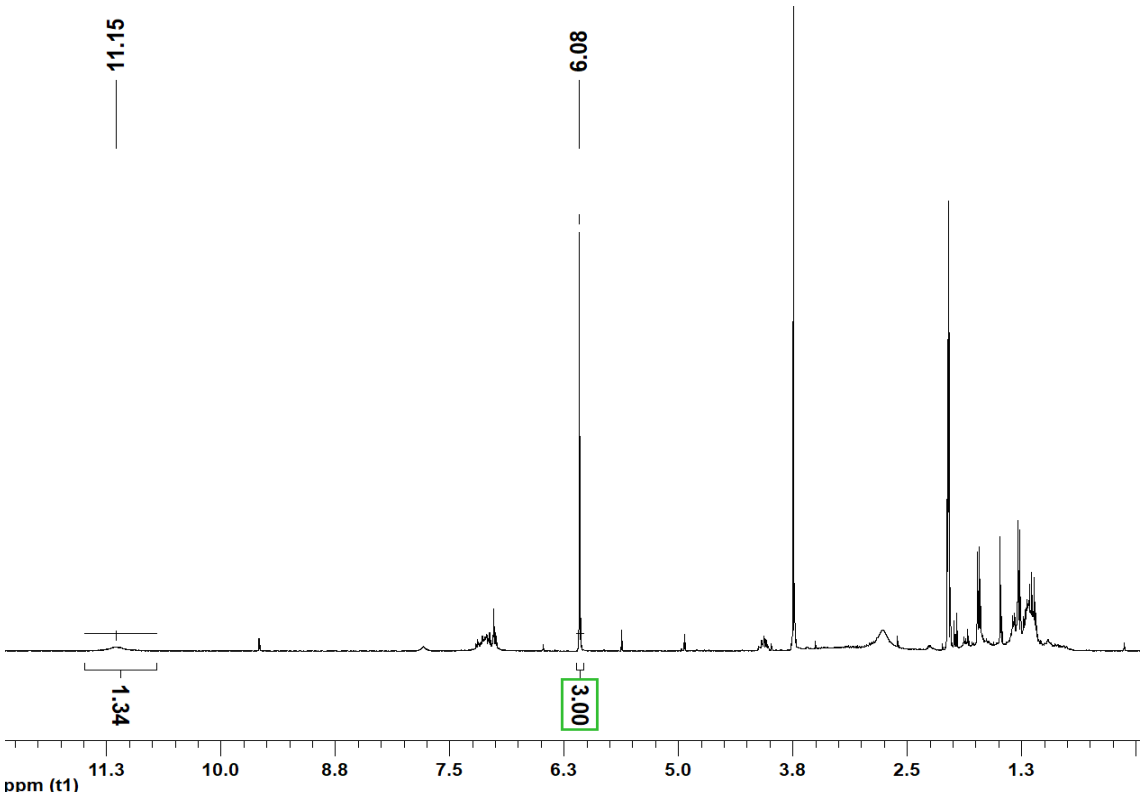

Figure 3.2.17: ^{1}H NMR spectrum of the reaction of **2a** with cyclohexane carboxaldehyde (CCA) in CD_3COCD_3 at 25ºC using 1,3,5-trimethoxybenzene as an internal standard (0.4 equiv, signal at 6.084 ppm). The product was identified to be cyclohexane-carboxylic acid based on the appearance of a characteristic signal at 9.55 ppm for the –C(O)OH group. Blank reactions of CCA, with H_2O_2 and Et_3N in the presence and absence of the deprotonated biuret (L^{2-}) ligand did not show any formation of acetophenone product.

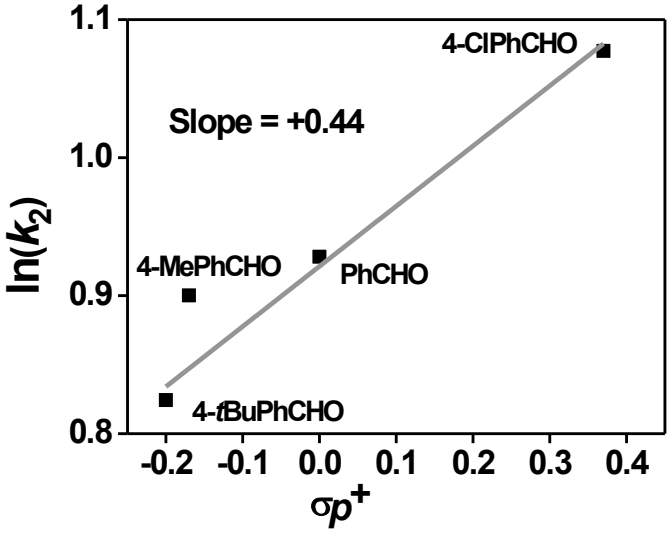

Figure 3.2.18: The plot of ln(k_2) versus the Hammett parameter σ_p+ for the reaction of **2a** with para-X-benzaldehydes (X = tBu, Me, H and Cl) in acetonitrile at 25ºC.

Analysis of the reaction mixture after the reaction of **2a** with 2-PPA shows the formation of Ni^{II} bis-hydroxo product, which is EPR silent (Figure 3.2.19). The ESI-MS spectrum exhibits one prominent peak at *m/z* 592.27 whose mass and isotope distribution corresponds to $\{[(biuret)Ni^{II}(OH)_2(Na)(CH_3CN)]\}^-$ (calculated *m/z* = 592.25).

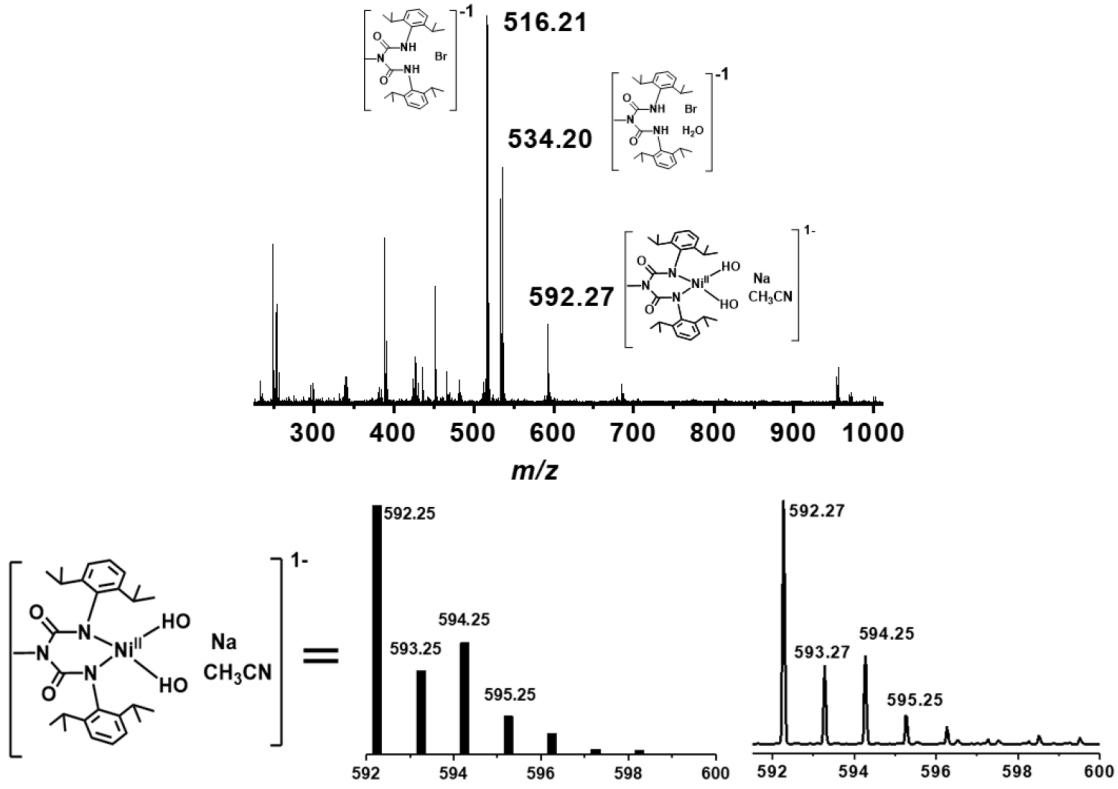

Figure 3.2.19: ESI-MS spectrum of the reaction mixture of **2a** with 2-phenylpropionaldehyde (2-PPA) in CH_3CN at 25ºC. A peak at m/z = 592.27 is obtained, whose isotopic distribution pattern is consistent with a $\{[(biuret)Ni^{II}(OH)_2(Na)(CH_3CN)]\}^-$ assignment.

3.2.6. DFT Calculations:

To understand the contrasting reactivity behavior of nickel superoxo complexes (neutral **1a** and monoanionic **2a**) towards external substrates, detailed DFT calculations were done. The molecular structures and spin densities of the complexes **1a** and **2a** were optimized by DFT (Figure 3.2.20). The neutral complex **1a** has two low lying S =1/2 states (Figure 3.2.21). The ground state (GS), ^{2}**1a**$_{ls}$, contains a low-spin Ni^{II} center and the unpaired electron is mostly localized on the O_2 ligand. There are two excited states (ES) for complex **1a** (Figure 3.2.21). Ferromagnetic coupling between the S =1 high spin hs-Ni^{II} and the S =1/2 $O_2^{-\cdot}$ centers gives the first excited state ^{4}**1a**$_{hs}$, and antiferromagnetic coupling between the hs-Ni^{II} and the S = 1/2 $O_2^{-\cdot}$ centers results in the second ES ^{2}**1a**$_{hs}$ (S=1/2). The excited states (^{4}**1a**$_{hs}$ and ^{2}**1a**$_{hs}$ states) are 25.1 and 36.3 kJmol^{-1} higher in energy relative to the ground state (^{2}**1a**$_{ls}$) respectively.

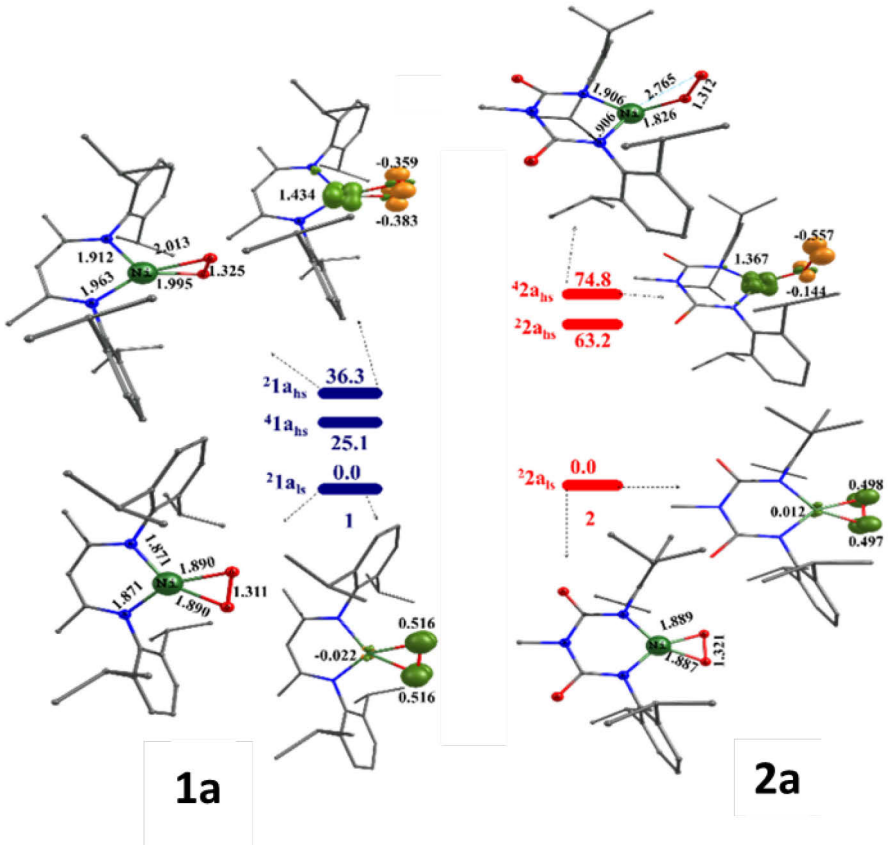

Figure 3.2.20: Relative energies (kJ mol^{-1}) of the DFT-derived ground- and excited-states of **1a** and **2a**, respectively, along with the optimized geometries and spin-density (positive: green, negative: yellow) plots of ^{2}**1a**$_{ls}$ (^{2}**1a**$_{hs}$) and ^{2}**2a**$_{ls}$ (^{2}**2a**$_{hs}$) states. H atoms are removed for clarity.

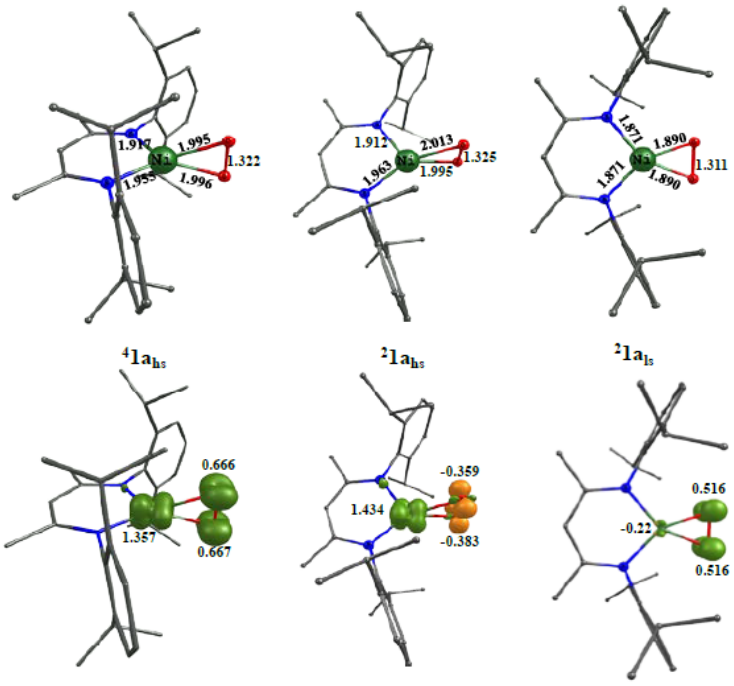

Figure 3.2.21: DFT optimized structures and spin densities of the complex [L'Ni^{II}O$_2$] (**1a**) in the ground state and the excited state. Positive spin density is shown by green color and negative spin density is shown by yellow color.

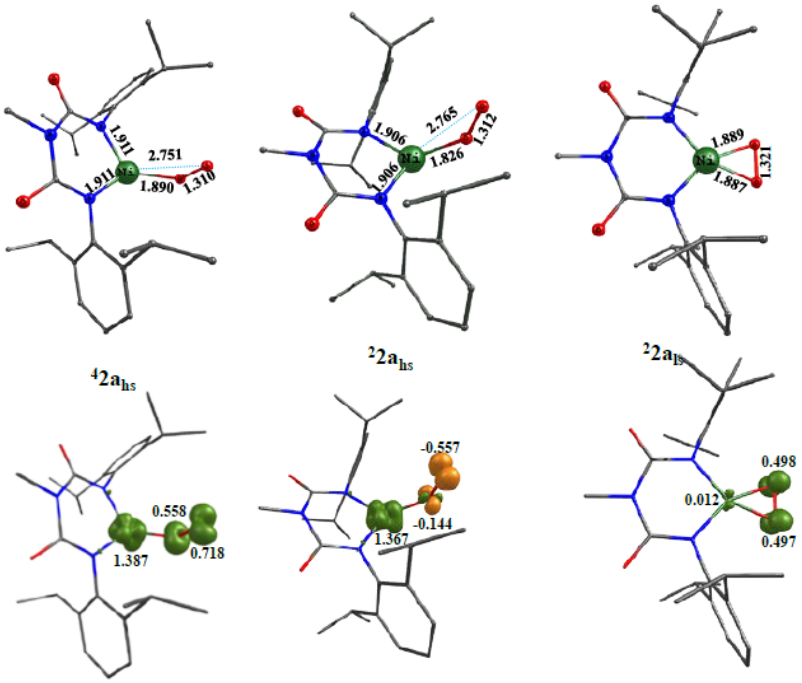

Figure 3.2.22: DFT optimized structures and spin densities of **2a** in the ground state and the excited state. Positive spin density is shown by green color and negative spin density is shown by yellow color.

From the crystal structure[14c] of the complex **1a**, we can see that the Ni-O and Ni-N bond distances in complex **1a** are significantly shorter than those observed in related nickel complexes.[14] Shorter Ni-O (1.89 Å) and Ni-N (1.87 Å) bond distances in complex **1a** match well with the DFT optimized structural parameters for the ^{2}**1a**$_{ls}$ state (Table 3.2.3). In contrast, for the ^{2}**1a**$_{hs}$ state Ni-O bond distances are relatively longer. This can be explained by the

presence of the unpaired electrons in the d_{x2-y2} and d_{z2} orbitals of the S =1 Ni^{II} ion which makes the O_2 binding unfavorable in the ^{2}**1a**$_{hs}$ state. The geometry around the Ni^{II} center is *SqP* in ^{2}**1a**$_{ls}$ but T_d in the ^{2}**1a**$_{hs}$ state. Thus, although ^{2}**1a**$_{ls}$ is assigned as the ground state, the calculated low energy of both the excited states (^{2}**1a**$_{hs}$ and ^{4}**1a**$_{hs}$ states) would suggest that both of these spin-states are accessible for reactivity. A large negative spin-density on the oxygen atoms was observed for ^{2}**1a**$_{hs}$. Furthermore, it involves a greater charge separation between the oxygen and the Ni^{II} sites compared to the ^{2}**1a**$_{ls}$ state. Thus, the electrophilic reactivity of nickel(II)-superoxo complex **1a**, can be attributed to the presence of a spin-polarized electronic structure. Thus, a two-state mechanism is proposed where the excited state ^{2}**1a**$_{hs}$ is possibly responsible for the electrophilic reactivity of the complex **1a**. The observed electrophilic reactivity of **1a** is most probably a result of the availability of two closely lying spin states, ^{2}**1a**$_{ls}$ GS and ^{2}**1a**$_{hs}$ ES,

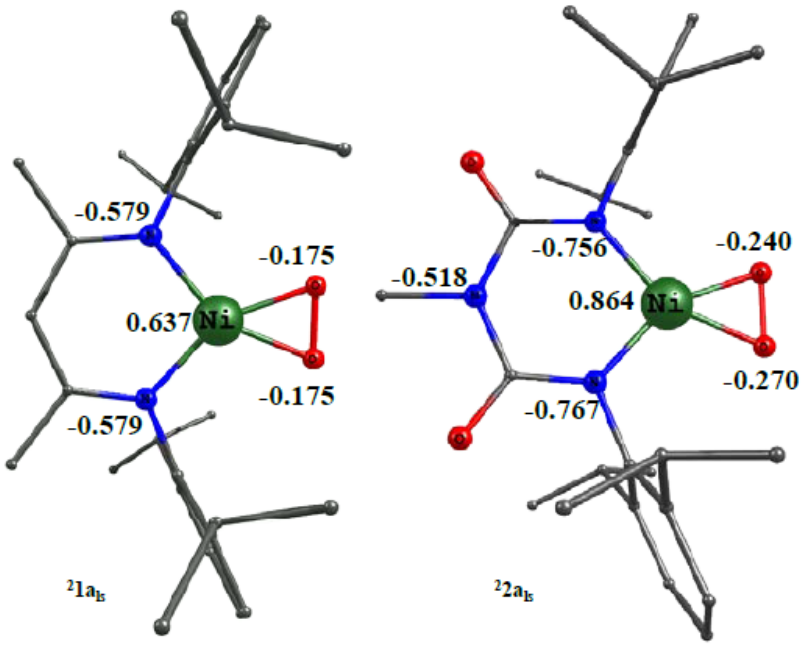

Figure 3.2.23: Optimized geometries of species ^{2}**1a**$_{ls}$ and ^{2}**2a**$_{ls}$ along with NPA computed atomic charges for selected atoms.

For monoanionic complex **2a**, the calculated ground state is ^{2}**2a**$_{ls}$, and the excited states are ^{2}**2a**$_{hs}$ and ^{4}**2a**$_{hs}$ (Figure 3.2.24). For the low spin ground state (^{2}**2a**$_{ls}$) the calculated Ni-O (1.88 Å) and Ni-N (1.86 Å), bond distances match well with the EXAFS data (Table 3.2.3). But the excited states are extremely high-lying in energy. The energies of the excited states are +63.2 and +74.8 kJmol^{-1} for the ^{2}**2a**$_{hs}$ and ^{4}**2a**$_{hs}$ states, respectively, relative to the ground ^{2}**2a**$_{ls}$ state. The very high energies of the excited states can be explained by the stronger electron donation from the dianionic biuret ligand **L,** which destabilizes the d_{x2-y2} and d_{z2} orbitals of the Ni^{II}-center and makes the spin-polarized ^{2}**2a**$_{hs}$ state extremely high-lying in energy. Due to its very

high energy, spin-polarized ^{2}**2a**$_{hs}$ state is not relevant for the reactivity of **2a**. Thus, in the absence of any low-lying excited states, the reactivity of **2a** likely occurs solely at the ground ^{2}**2a**$_{ls}$ state. From the natural population analysis, it is also evident that the oxygen atoms in the ^{2}**2a**$_{ls}$ state carry a higher negative charge than in the ^{2}**1a**$_{ls}$ state (Figure 3.2.23). These observations thus clearly explain the higher nucleophilicity of **2a** compared to **1a** in the presence of electrophiles.

DFT optimized spin densities for the species **1a** and **2a** are shown in table 3.2.4. The appearance of more intense broad absorptions band in the 800– 1100 nm region in the electronic spectra of **1a** (Figure 3.2.24) also suggests that the T_d Ni^{II}-hs state is more available in **1a** compared to *SqP* Ni^{II}-hs state in **2a.** These bands are presumably originating from the ligand–field (LF) transitions arising from a d^8-Ni^{II} center, which is expected to be spin and symmetry allowed (and hence more intense) in a T_d geometry and forbidden (with zero-intensity) in a pure *SqP* geometry.[20]

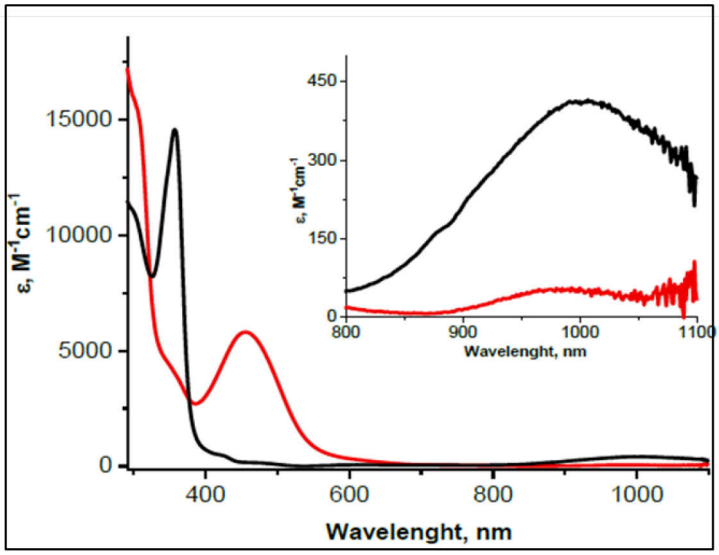

Figure 3.2.24: Comparison of the absorption spectra of **1a** (black) and **2a** (red). In the inset is shown the expansion of the 800-1100 nm region.

Table 3.2.3: DFT optimized structural parameters for the species **1a** and **2a**. The ground states are marked in bold.

	Ni-O1	Ni-O2	O1-O2	Ni-N1	Ni-N2
[(nacnac)$Ni^{II}O_2$] (**1**)					
^{4}**1a**$_{hs}$	1.996	1.995	1.322	1.955	1.917
^{2}**1a**$_{hs}$	1.995	2.013	1.325	1.963	1.912
^{2}**1a**$_{ls}$	**1.890**	**1.890**	**1.311**	**1.871**	**1.871**
Exp (XRD)[11]	1.817(2)	1.840(2)	1.347(2)	1.847(2)	1.849(2)
[(L)$Ni^{II}O_2$]$^-$ (**2**)					
^{4}**2a**$_{hs}$	1.890	2.751	1.310	1.911	1.911
^{2}**2a**$_{hs}$	1.826	2.765	1.312	1.906	1.906
^{2}**2a**$_{ls}$	**1.889**	**1.887**	**1.321**	**1.861**	**1.859**
Exp (EXAFS)	4 Ni-N/O @ 1.85 Å				

Table 3.2.4: DFT optimized spin densities for the species **1a** and **2a**.

	Ni	O1	O2	N1	N2
[(nacnac)$Ni^{II}O_2$] (**1**)					
^{4}**1a**$_{hs}$	1.357	0.666	0.667	0.148	0.109
^{2}**1a**$_{hs}$	1.434	-0.383	-0.359	0.156	0.11
^{2}**1a**$_{ls}$	-0.022	0.516	0.516	-0.006	-0.006
[(L)$Ni^{II}O_2$]$^-$ (**2**)					
^{4}**2a**$_{hs}$	1.387	0.558	0.718	0.128	1.128
^{2}**2a**$_{hs}$	1.367	-0.144	-0.557	0.132	0.132
^{2}**2a**$_{ls}$	0.012	0.498	0.497	-0.004	-0.004

3.3. Conclusions and Remarks:

A new nickel (II) dibromide complex (**M**) was synthesized from a new dianionic biuret ligand (**L**). The biuret ligand is structurally similar to its Nacnac analog (as shown before in Scheme 3.2.2). However, the electronic nature of these two ligands is different. The nacnac ligand is monoanionic whereas biuret is dianionic. A nickel(II)-superoxo intermediate (**2a**) was generated from **M,** using excess H_2O_2 in the presence of triethylamine (TEA). Complex **2a** was characterized using different spectroscopic techniques.

Complex **2a** shows unprecedented nucleophilic reactivity in contrast to the electrophilic reactivity of complex **1a** [**1a** = $Ni^{II}(O_2^{-\cdot})$(Nacnac)]. The contrasting reactivity pattern of the superoxido-nickel (II) intermediates cores of **1a** and **2a** is strongly dependent on subtle electronic changes**.** Such behavior of **1a** and **2a** can also be explained by the results of DFT calculations. Despite different charges, both the complexes **1a** and **2a** have identical ground states (GS) as predicted from DFT. Experimentally determined O-O vibrational energies, Ni-N/O bond distances, EPR *g*-tensors, and Ni *K*edge/pre-edge energies for **1a** and **2a** are also very similar. However, the only difference is the nature of the excited state (ES) in the two cases. The electrophilic nature of **1a** can be explained by the availability of two closely lying spin states, ^{2}**1a**$_{ls}$ GS and ^{2,4}**1a**$_{hs}$ ES, wherein the spin-polarized ^{2}**1a**$_{hs}$ state has a much lower reaction barrier than the ^{2}**1a**$_{ls}$ state. In contrast to **1a**, the excited states of complex **2a** are higher in energy and energetically not accessible for reactivity**.** The higher energy of the excited states in **2a** shuts down the electrophilic reactivity pathway completely. The single-state nucleophilic reactivity of **2a** solely arises from the strong electron donation of the dianionic biuret ligand on the ^{2}**2a**$_{ls}$ surface. The results presented here prove that changes in the electronic nature of the supporting ligand environment have an important impact on the reactivity of the superoxido-nickel (II) complexes. Taken together, this study therefore underlines the importance of minor electronic changes for governing the biologically relevant oxidation reactions.

3.4. References:

1. (a) E. I. Solomon, T. C. Brunold, M. I. Davis, J. N. Kemsley, S.- K. Lee, N. Lehnert, F. Neese, A. J. Skulan, Y.-S. Yang, J. Zhou, *Chem. Rev*. **2000**, *100*, 235. (b) M. Costas, M. P. Mehn, M. P. Jensen, L. Que. Jr., *Chem. Rev.* **2004**, *104*, 939.
2. (a) A. E. Shilov, G. B. Shul, G. B. Shul'pin, *Chem. Rev*. **1997**, *97*, 2879. (b) B. L. Conley, W. J. Tenn, K. J. H. Young, S. Ganesh, S. Meier, V. Ziatdinov, O. Mironov, J. Oxgaard, J. Gonzales, W. A. Goddard, R. A. Periana, *In Activation of Small Molecules:*

Organometallic and Bioinorganic Perspectives; W. B. Tolman, Ed.; *Wiley-VCH: Weinheim, Germany*, **2006**; pp 235.

3. (a) Y. Dai, P. C. Wensink, R. H. Abeles, *J. Biol. Chem.* **1999**, *274*, 1193. (b) V. Leclere, P. Boiron, R. Blondeau, *Curr. Microbiol*. **1999**, *39*, 365. (c) H. D. Youn, E. J. Kim, J. H. Roe, Y. C. Hah, S. O. Kang, *Biochem. J*. **1996**, *318*, 889. (d) B. Palenik, B. Brahamsha, F. W. Larimer, M. Land, L. Hauser, P. Chain, J. Lamerdin, W. Regala, E. E. Allen, J. McCarren, I. Paulsen, A. Dufresne, F. Partensky, E. A. Webb, J. Waterbury, *Nature.* ***2003***, *424*, 1037. (e) T. Corona and A. Company. *Chem. Eur. J*. **2016**, *22*, 13422.
4. (a) S. S. Stahl, *Angew. Chem. Int. Ed*. **2004**, *43*, 3400. (b) A. Heumann, K. J. Jens, M. Reglier, *Prog. Inorg. Chem.* **1994**, *42*, 483.
5. D. P. Barondeau, C. J. Kassmann, C. K. Bruns, J. A. Tainer, E. D. Getzoff, *Biochemistry.* **2004**, *43*, 8038.
6. J.-H. Jeoung, D. Nianios, S. Fetzner, H. Dobbek, *Angew. Chem. Int. Ed*. **2016**, *55*, 3281–3284; *Angew. Chem.* **2016**, *128*, 3339.
7. F. F. Pfaff, F. Heims, S. Kundu, S. Mebs, K. Ray, *Chem. Commun.* **2012,** *48*, 3730.
8. T. Corona, F. F. Pfaff, F. Acuna-Pares, A. Draksharapu, C. J. Whiteoak, V. Martin-Diaconescu, J. Lloret-Fillol, W. R. Browne, K. Ray, A. Company, *Chem. Eur. J*. **2015**, *21*, 15029.
9. (a) S. Yao, M. Driess, *Acc. Chem. Res*. **2012**, *45*, 276. (b) A. Bakac, *Coord. Chem. Rev*. **2006**, *250*, 2046. (c) M. Costas, M. P. Mehn, M. P. Jensen, L. Que, Jr., *Chem. Rev.* **2004**, *104*, 939. (d) C.-W. Chiang, S. T. Kleespies, H. D. Stout, K. K. Meier, P.-Y. Li, E. L. Bominaar, L. Que. Jr., E. Mgnck, W.-Z. Lee, *J. Am. Chem. Soc*. **2014,** *136*, 10846. (e) J. Shearer, R. C. Scarrow, J. A. Kovacs, *J. Am. Chem. Soc*. **2002**, *124*, 11709. (f) S. Hong, K. D. Sutherlin, J. Park, E. Kwon, M. A. Siegler, E. I. Solomon, W. Nam, *Nat. Commun*. **2014**, *5*, 5440. (g) J. Cho, J. Woo, W. Nam, *J. Am. Chem. Soc.* **2010**, *132*, 5958. (h) J. Cho, J. Woo, W. Nam, *J. Am. Chem. Soc.* **2012**, *134*, 11112. (i) T. Devi, Y.-M. Lee, W. Nam, S. Fukuzumi, *J. Am. Chem. Soc*. **2018**, *140*, 8372. (j) T. Devi, Y.-M. Lee, J. Jung, M. Sankaralingam, W. Nam, S. Fukuzumi, *Angew. Chem. Int. Ed.* **2017**, *56*, 3510.
10. (a) M. Costas, M. P. Mehn, M. P. Jensen, L. Que, Jr., *Chem. Rev*. **2004**, *104*, 939. (b) M. M. Abu-Omar, A. Loaiza, N. Hontzeas, *Chem. Rev*. **2005**, *105*, 2227. (c) R. P. Hausinger, *Crit. Rev. Biochem. Mol. Biol*. **2004**, *39*, 21.

11. (a) J. P. Klinman, *J. Biol. Chem*. **2006,** *281*, 3013. (b) S. C. Peck, W. A. van der Donk, *Curr. Opin. Chem. Biol*. **2013**, *17*, 580. (c) L. M. Mirica, J. P. Klinman, *Proc. Natl. Acad. Sci. USA.* **2008**, *105,* 1814. (d) J. M. Bollinger, J. C. Price, L. M. Hoffart, E. W. Barr, C. Krebs, *Eur. J. Inorg. Chem*. **2005,** 4245. (e) N. Lehnert, K. Fujisawa, E. I. Solomon, *Inorg. Chem*. **2003**, *42*, 469.
12. S. Kundu, E. Matito, S. Walleck, F. F. Pfaff, F. Heims, B. Rabay, J. M. Luis, A. Company, B. Braun, T. Glaser, K. Ray, *Chem. Eur. J*. **2012**, *18*, 2787.
13. P. Pirovano, A. M. Magherusan, C. McGlynn, A. Ure, A. Lynes, A. R. McDonald, *Angew. Chem. Int. Ed*. **2014**, *53,* 5946–5950; *Angew. Chem.* **2014**, *126*, 6056.
14. (a) J. Cho, R. Sarangi, J. Annaraj, S. Y. Kim, M. Kubo, T. Ogura, E. I. Solomon, W. Nam, *Nat. Chem*. **2009**, *1*, 568. (b) M. T. Kieber-Emmons, J. Annaraj, M. S. Seo, K. M. Van Heuvelen, T. Tosha, T. Kitagawa, T. C. Brunold, W. Nam, C. G. Riordan, *J. Am. Chem. Soc.* **2006**, *128*, 14230. (c) S. Yao, E. Bill, C. Milsmann, K. Wieghardt, M. Driess, *Angew. Chem. Int. Ed.* **2008**, *47*, 7110. (d) J. Cho, H. Y. Kang, L. V. Liu, R. Sarangi, E. I. Solomon, W. Nam, *Chem. Sci*. **2013**, *4*, 1502.
15. A. Company, S. Yao, K. Ray, M. Driess, *Chem. Eur. J.* **2010**, *16*, 9669.
16. B. Ramdhanie, J. Telser, A. Caneschi, L. N. Zakharov, A. L. Rheingold, D. P. Goldberg, *J. Am. Chem. Soc.* **2004**, *126*, 2515.
17. (a) M. T. Kieber-Emmons, C. G. Riordan, *Acc. Chem. Res*. **2007,** *40*, 618. (b) K. Fujita, R. Schenker, W. Gu, T. C. Brunold, S. P. Cramer, C. G. Riordan, *Inorg. Chem*. **2004**, *43*, 3324.
18. (a) J. Jašík, J. Žabka, J. Roithová, D. Gerlich, *Int. J. Mass Spectrom*. **2013**, 354, 204. (b) J. Jašík, R. Navrátil, I. Němec, J. Roithová, *J. Phys. Chem. A.* **2015**, *119*, 12648.
19. G. J. Colpas, M. J. Maroney, C. Bagyinka, M. Kumar, W. S.Willis, S. L. Suib, P. K. Mascharak, N. Baidya, *Inorg. Chem*. **1991**, *30*, 920.
20. C. A. L. Filgueiras, F. Carazza, *J. Chem. Educ*. **1980**, *57*, 826.

Chapter 4

Conclusions and Outlook

Selective functionalization of unactivated C−H bonds and dioxygen reduction reaction (ORR) are extremely important in the context of addressing various technological issues such as energy-crisis, synthesis of commercially important organic compounds, etc. The utilization of molecular O_2 as an abundant and environmentally benign oxidant is of great interest in the design of bioinspired synthetic oxidation catalysts. The catalytic four-electron reduction of O_2 to water has also merited increasing attention because of its relevance to fuel cell technology. Naturally occurring metalloenzymes activate dioxygen by employing cheap transition metals (*e.g.* iron, nickel, manganese, and copper) and exhibit diverse oxidative reactivities. Moreover, such reactions are carried out under ambient conditions with high efficiency and stereospecificity. Therefore, the isolation and characterization of the high-valent metal-dioxygen intermediates (such as metal-superoxo, -peroxo, -hydroperoxo, and -oxo) can provide a lot of useful information about the reaction mechanisms and is therefore helpful for the future design of more efficient catalysts.

This Thesis has explored the chemistry of different metal-oxygen intermediates ranging from bridging end-on μ-1,2-peroxo-dicobalt(III) species to nickel(II)-superoxo cores. Detailed spectroscopic and reactivity studies of the intermediates have been performed to reveal the correlations between their electronic structures and reactivity patterns. In my present thesis, I investigated the effect of the '*structure-activity relationship'* of different metal-dioxygen intermediates towards exogenous substrates. I also demonstrated the impact of suitable ligand design on the behavior of a given metal-dioxygen reactive system. The principal outcomes and prospects of this work are discussed below:

Chapter 2

In this chapter, the synthesis and characterization of a novel tetranuclear cobalt complex **Co$_4$L1** involving a nonheme ligand system, **L1,** supported on a stannoxane core (Sn_4O_2) are reported. Detailed spectroscopic and theoretical studies confirm the presence of an end-on μ-1,2-peroxo-dicobalt(III) species (**1**) as the active intermediate when **Co$_4$L1** reacts with dioxygen. The cobalt(II) centers in **Co$_4$L1** are in an S = 3/2 ground state with no interaction between them, whereas the end-on μ-1,2-peroxo-dicobalt(III) intermediate (**1**) is EPR silent. Spectroscopic characterization (together with theoretical studies) of **1** confirms the presence of an antiferromagnetically coupled μ-1,2-peroxodicobalt(III) cores in **1** with an S = 0 ground state. Furthermore, the formation of **1** depends on the temperatures.

The complex **Co4L1** acts as a unique catalyst for dioxygen reduction reaction (ORR), whose selectivity can be changed from a preferential $4e^-/4H^+$ dioxygen-reduction (to water) to a $2e^-/2H^+$ process (to hydrogen peroxide) only by increasing the temperature from −50 to 30°C. The reason why the same catalyst can behave differently towards ORR can be explained by the constraint provided by the stannoxane core that makes the O_2-binding to **Co4L1** an entropically unfavorable process. **Co4L1** is a better catalyst for the four-electron reduction of O_2, showing a turnover number TON_{2000s} of 28.7, which is three times larger than the TON_{2000s} for the two-electron reduction process. Experimental results confirmed that the catalytic efficiency of **Co4L1** depends on temperature.

Herein, we compare its dioxygen reduction ability with the previously reported hexanuclear cobalt complex **Co6L2.** The temperature dependence of the product selectivity of the catalytic dioxygen reduction is observed in **Co4L1,** similar to the previously reported **Co6L2**; however, some subtle differences are noted which can be attributed to the different nuclearity and Co–Co bond distances. In **Co6L2** all the six cobalt centers are equidistance from each other whereas in **Co4L1** only two of the four metal centers are close to each other. The four-electron reduction of O_2 to H_2O proceeds through a rate-determining PCET process at low temperature while the rate-determining step of the two-electron O_2 reduction proceeds through the PT process at a higher temperature. Detailed mechanistic investigation showed ~10 ^oC reduction in the transition temperature for **1** compared to **2** (end-on μ-1,2-peroxodicobalt(III) cores generated from **Co6L2**), which is also evident from the faster self-decay rate and lower ν_{Co-O} vibration energy in **1** relative to **2**.

The details about the kinetic behavior and the mechanistic insights into the oxidation of a wide range of substrates by the intermediate **1** and **2**, involving nonheme ligand systems (**L1** and **L2**), supported on stannoxane core (Sn_4O_2 and Sn_6O_6) were also evaluated. The intermediate **1** and **2**, generated at 25 °C from the reaction of **Co4L1** and **Co6L2** with O_2 **respectively**, are active both in nucleophilic as well as in electrophilic oxidative transformations. From the obtained KIE values and the $H_2{}^{18}O$ exchange experiments, it was determined that the electrophilic nature of both **1** and **2** is also attributable to the peroxo complex. Both the end-on μ-1,2-peroxodicobalt(III) complexes ($S = 0$) show an unprecedented electrophilic reactivity, in addition to the nucleophilic reactivity in oxidative deformylation of aldehydes. Details mechanistic studies were carried out to investigate the C-H and phenolic O-H bond activation mechanism. Positive deuterium kinetic isotope effects confirm about rate-limiting hydrogen atom transfer reaction in C-H and O-H bond activation process. Experimental

results suggest that **2** is a better electrophilic oxidant than **1**. Better cooperativity and higher constrain provided by the stannoxane core in **2** make it a better oxidant than **1**.

From these results, it is established that the multinuclear systems with an extensive cooperative effect between the metal centers have great potential in carrying out a variety of important transformations and show interesting and exceptional reactivity trends. In this respect, organooxotin clusters are particularly attractive because of their diverse structural arrangements, such as drum, O-capped, ladder, butterfly, cube, 1D, 2D, and 3D structures. There is a lot yet to be explored in the field of multinuclear complexes based on stannoxane ligands. This is a young field of research and more studies are necessary, with different metals such as copper, manganese, etc. Moreover, other types of multinuclear ligands, specifically without tin in their structures, could also lead to interesting results for the future design of more efficient catalysts in fuel cells.

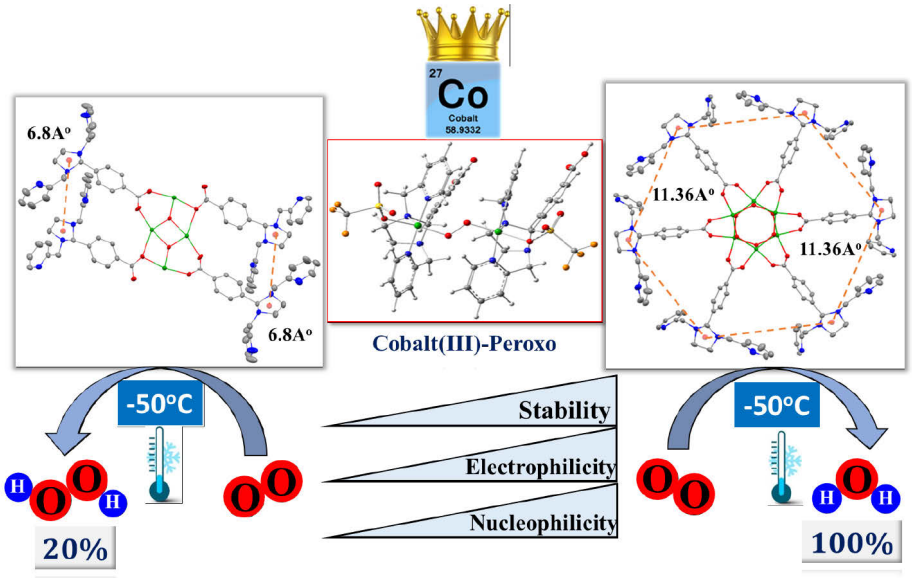

Chapter 3

This chapter describes the isolation, spectroscopic characterization, and unprecedented nucleophilic oxidative reactivity of a novel nickel(II)-superoxo intermediate (**2a**) bearing a dianionic biuret ligand (**L**). Although the biuret ligand is structurally similar to its Nacnac analog, the electronic nature of these two ligands is different. A new nickel (II) dibromide complex (**M**) was synthesized from the biuret ligand (**L**). Superoxido-nickel(II) intermediate (**2a**) was generated from nickel (II) dibromide complex (**M**), using excess H_2O_2 in the presence of triethylamine (TEA); which has been elucidated by X-ray absorption spectroscopy, IRPD, EPR, and DFT calculations. The O-O vibration in **2a** (980 cm^{-1}) appears at similar energy to

that of previously reported side-on superoxido–nickel(II) complex **1a** (971 cm^{-1}) [where **1a** = $Ni^{II}(O_2^{-\cdot})$(Nacnac)].

The newly synthesized nickel(II)-superoxo intermediate (**2a**) showed unprecedented nucleophilic reactivity in contrast to the electrophilic reactivity of **1a**. For the first time, it was possible to isolate a nucleophilic Ni(II)-superoxo species using the biuret ligand. A two-state reactivity (TSR) model has been proposed to explain the contrasting reactivity trends of **1a** versus **2a**. Two key factors were detected that might account for the contrasting reactivity of **2a** in comparison with **1a**:

(i) Dianionic biuret ligand is more electron-rich compared to the mono-anionic nacnac ligand. Therefore intermediate **1a** is a neutral species whereas **2a** is a monoanionic one.

(ii) Despite different charges, both complexes **1** and **2a** have identical ground states (GS) as predicted from DFT, however, the nature of the ES differs in the two cases. The electrophilic reactivity of **1a** arises due to the availability of two closely lying spin states, ^{2}**1a**$_{ls}$ GS and ^{2}**1a**$_{hs}$ ES. In contrast**,** the excited state (^{2}**2a**$_{hs}$) of **2a** is relatively higher in energy and not accessible for **2a,** which shuts down the electrophilic reactivity pathway. Strong electron donation by the dianionic biuret ligand (**L**) results in a single-state nucleophilic reactivity for **2a**, whereas higher availability of the T_d Ni^{II}-hs state in **1a** leads to the electrophilic reactivity.

The results obtained here underlines the importance of the subtle electronic charges in the reactivity pattern of the biologically relevant metal-dioxygen intermediate.

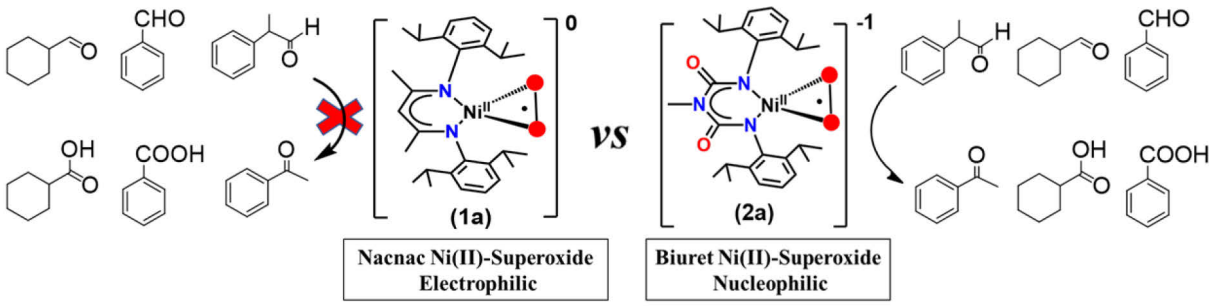

Chapter 5

Equipment and experimental work

5.1. General techniques and chemicals employed

Unless otherwise mentioned, all studies and measurements were performed at the Institut für Chemie, Humboldt-Universität zu Berlin. All chemicals were purchased from Sigma-Aldrich, Acros, ABCR, TCI, Ark Pharm, Roth and used without further purification unless required. Anhydrous solvents were purchased from Carl-Roth GmbH (≥ 99.5%, < 50 ppm H_2O) and degassed by a freeze-pump-thaw method prior to use.

Air and moisture sensitive compounds were prepared and handled under an inert atmosphere using standard Schlenk techniques or a glovebox OMNI-Lab 2 (VAC- Atmospheres) filled with N_2, with O_2 and moisture concentrations less than 1 ppm. Gases (N_2 and Ar) of quality 5.0 were used for this purpose and were purchased from Air-Liquide.

The glassware employed was cleaned in a KOH/isopropanol bath and then treated in an HCl bath for neutralization. The glassware was dried with a heat-gun under vacuum before each use.

5.2. Analytical techniques

All analytical samples of air- or water-sensitive compounds were prepared in the glove box under inert condition.

5.2.1. Elemental analysis

All elemental analyses were performed by the analytical service of the Institut für Chemie of the Humboldt Universität zu Berlin. Elemental analyses were performed with a EURO EA 3000 analyzer from the HEKA-tech. The values mentioned here are the averages of two independent measurements except for the sample containing Fluorine when only one measurement was performed.

5.2.2. NMR spectroscopy

All NMR spectroscopic measurements were routinely recorded either on a Bruker AV 400 NMR spectrometer or on a Bruker DPX 300 spectrometer at 27 °C. Samples were measured in NMR tubes with 5 mm of diameter. The chemical shifts (δ) values are expressed in ppm relative to the tetramethylsilane signal, whereas the residual proton signal of the deuterated solvent medium served as an internal standard [^{1}H-NMR: δ (ppm): $CDCl_3$ 7.26; CD_2Cl_2 5.30; $(CD_3)_2CO$ 2.10; CD_3CN 1.94]. The multiplicity of the signals are indicated as follows: s = singlet, d = doublet, t = triplet, m = multiplet.

5.2.3. Mass spectrometry

ESI-MS spectra of organic molecules and inorganic complexes in solution were recorded by using an Advion expression CMS spectrometer (in typical ionization mode); acetonitrile was

used as an eluent. For thermally unstable complexes, direct injection of the freshly thawed solutions was made. The analysis of the data was carried out with the ADVION DATA EXPRESS Version 6.0.11.3. Expected mass spectra (*i.e. m/z* values and isotopic distribution patterns) were calculated with the program Molecular Weight Calculator (Version 6.48.0.1, Author: Matthew Monroe).

5.2.4. Infrared spectroscopy (IR)

IR spectra were measured either from powdered samples using the ATR unit (diamond) or by dropping the sample solution on the dial-path unit connected to the Agilent-Cary 630 FTIR spectrometer. The intensities of the obtained vibrational bands here reported are abbreviated in the following way: s = strong, m = medium, w = weak, br = broad.

5.2.5. UV-vis absorption spectroscopy

The UV-vis absorption spectra were carried out with an Agilent 8453 diode array spectrometer connected to a stirrer and a cryostat from Unisoku Scientific Instruments, Japan. The temperature for the measurements was set with a cryostat USP-203-A from the company Unisocu Scientific Instruments. The software UV-visible Chemstation from the company Agilent was employed for the recording and workup of the spectra and kinetic data.

For a typical UV-Vis experiment, a stock solution with a known concentration of the complex was prepared in a glove box using anhydrous solvent; 2.0 mL of the stock solution was taken in a cuvette with a path length of 1 cm. The cuvette was closed tightly with a rubber septum inside the glovebox. The cuvette was then placed in the Unisoku cryostat connected to the UV-Vis spectrometer and the temperature of the cryostat was maintained to the specified temperature (as mentioned for the particular reaction). After attaining the thermal equilibrium, the solution of the next reactant (*i.e.* oxidant/substrate) in a minimum amount of the solvent was injected to the cuvette and the course of the reaction was monitored by the UV-Vis spectral changes.

The reported molar-extinction coefficient value (ε_{max}) corresponding to a particular absorption maximum (λ_{max}) is the average of several individual measurements. Half-life ($t_{1/2}$) of the complex/intermediate was determined from the time traces (absorbance *vs.* time plot) of the decay of its characteristic UV-vis band at a fixed temperature. The rate constants were determined from the decay kinetics of the characteristic absorption band in the presence of exogenous substrates.

5.2.6. Gas chromatography coupled to mass spectrometry (GC-MS)

The products formed after the oxidation of the various substrates were analyzed by GC-MS. GC analysis was carried out by using an AGILENT 7890B gas chromatograph (HP5 column, 30 m) with a flame-ionization detector. GC-MS was performed on an AGILENT 5977B spectrometer with a triple-axis detector. Before the analysis, the reaction mixture was passed through a silica-gel column using ethyl-acetate as an eluant to remove any metal complex. The resulting ethyl-acetate solutions were then analyzed with GC-MS. The products formed in the oxidation reactions were identified by comparing the retention times of the authentic compounds and the quantification of the products was done by using naphthalene as an internal standard.

5.2.7. Single-Crystal X-ray Structure Determination (XRD)

The crystal structure of the complex **M** (mentioned in chapter 3) was determined in collaboration with Prof. Matthias Driess and his working group. Each crystal was mounted on a glass capillary in perfluorinated oil and measured in a cold N_2 flow. The data of compound **M** was collected on an Oxford Diffraction SuperNova, Single source at offset, Atlas at 150 K (Cu-Kα radiation, λ = 1.54184 Å). The structures were solved by direct methods and refined on F2 with the SHELX-97 and Olex2 software package.[1] The positions of the H atoms were calculated and considered isotropically according to a riding model. CCDC 1832378 (**M**) contains the supplementary crystallographic data for this paper. These data can be obtained free of charge by contacting The Cambridge Crystallographic Data Centre, 12, Union Road, Cambridge CB2 1EZ, UK; fax: +441223 336033.

5.2.8. Electron paramagnetic resonance spectroscopy (EPR)

X-Band EPR spectra were recorded on a Bruker ELEXYS E580 X-band EPR spectrometer equipped with the Bruker ER4118X-MD5 probe head, and an Oxford Instruments CF935 helium flow cryostat using quartz tubes with 3 mm internal diameter. The freshly prepared samples were transferred to J. Young quartz EPR tubes and sealed. The solution in the tube was frozen in liquid nitrogen and kept frozen until measured. The measurements were performed in the following locations:

(a) Institut für Chemie of the Humboldt Universität zu Berlin

As mentioned previously in Chapter 2, the EPR spectra of the complex **Co_4L1 (**2 mM**)** was measured in acetone at 13.5 K. The spectrum was measured together with Beatrice Battistella

and Dr. Andrea Zehl. This spectrum was acquired at MWFQ = 9.354355 GHz, using a power of 2.00 mW and a field modulation amplitude of 5.002 G.

(b) Helmholtz-Zentrum Berlin für Materialien und Energie GmbH

The X-Band EPR spectra of the Ni^{II}-superoxo intermediate (**2a**), mentioned in chapter 3, was measured with Silvio Künstner. The spectrum was measured with the following parameters: Temperature 10 K, frequency 9.701858 GHz, modulation amplitude 1.0 mT, microwave power 0.015 mW, modulation frequency 100 kHz, the time constant 20.48 ms. The spectra were simulated using the function pepper for powder spectra of the Easy-spin software package[2] with anisotropic line widths (Gaussian line shapes).[2]

5.2.9. Resonance Raman (rR) spectroscopy

All rR measurements were performed in collaboration with the group of Prof. Dr. Peter Hildebrandt at the Technische-Universität Berlin. Resonance Raman spectra were measured by using a Horiba Jobin-Yvon LabRAM HR800 confocal Raman spectrometer. The power of the incident laser beam on the sample was in the range of 5 -30 mW. The scattered light was detected with a liquid-nitrogen-cooled SYMPHONY CCD detector.

Freshly prepared sample solutions were placed in NMR tubes with a diameter of 5 mm and frozen in liquid nitrogen. The samples were kept frozen until measured. The rR spectra were measured at low temperatures (-40 to -90 °C), which were controlled by a Bruker cryostat.

5.2.10. D_2-tagging IRPD spectroscopy:

The infrared photodissociation (IRPD) spectrum of deuterium-tagged anionic intermediate **2a** was acquired with the ISORI instrument.[3] The ions were generated by electrospray ionization (ESI) from 0.5 mM solution of **2a** (or ^{18}O-labeled **2a**) in acetonitrile and pre-trapped in a transfer quadrupole. The ionization conditions were -5 kV capillary voltage, 0 V metal capillary voltage, -115 V tube lens voltage, 150 °C metal capillary temperature, and 60 psi sheath gas pressure. In 3 s cycles, the complexes (**2a**) were extracted from the transfer quadrupole, mass-selected (m/z 525 and m/z 529 for ^{18}O labeled **2a**) by the next quadrupole, and guided with a quadrupole bender and an octopole to a cold trap operating at 3K. The helium buffer gas with 1 % deuterium served for trapping and cooling the ions and for forming the D_2-tagged complexes. The number of **D_2.2a** complexes (N) was counted by an ion detector after their mass-selection with a third quadrupole. The IRPD spectra are constructed as $(1 - N_{(\nu)}/N_0)$, where N_0 is the total number of **D_2.2a** and $N_{(\nu)}$ is the number of **D_2.2a** that remained after their irradiation in the trap.

5.2.11. X-ray absorption spectroscopy (XAS)

XAS experiments were carried out in two different places in collaboration with Dr. Erik R. Farquhar and Dr. Peter Hildebrandt.

at BESSY II, Helmholtz-Zentrum Berlin (HZB):

XAS measurements were conducted at the KMC3 beamline of the BESSY synchrotron at the Helmholtz-Zentrum Berlin (HZB) in collaboration with Prof. Dr. Holger Dau and Dr. Stefan Mebs (Freie Universität Berlin). The samples were disposed at ca. -60°C into cylindrical Teflon sample holders with thin walls of roughly 100 µm specifically designed for X-ray spectroscopy. The data were collected at 20 K in a liquid-helium cryostat in fluorescence detection mode using a 13 element ultra-low energy resolving Silicon drift detector (SDD) from Canberra. A relatively large sample was irradiated and in each scan different spots of the sample were exposed to the X-ray beam, thereby excluding any significant radiation-induced modification (radiation damage) of the investigated molecules. Over 25 spectra were averaged for each compound in order to improve the signal-to-noise ratio. Averaged spectra were background-corrected and normalized using in-house software. Subsequently, unfiltered *k*3-weighted spectra and phase functions from FEFF8.5[4] were used for least-squares curve-fitting of the EXAFS with in-house software and for calculation of Fourier-transforms representing *k*-values between 2 and 14 $Å^{-1}$. Data were multiplied by a fractional cosine window (10% at low and high *k*-side); the amplitude reduction factor S_0^2 was 0.95.[5] The structural models for the phase function computations were obtained by DFT optimization of the dimer structure (resembling **1**) at the UB3PW91/ 6-31+G*[6] level of theory (an effective core potential was used for Co[7]) applying Gaussian16[8].

at Brookhaven National Laboratory, Upton, NY, USA:

XAS data for **M** and **2a** was measured at beamline 4-1of the Stanford Synchrotron Radiation Lightsource (SLAC National Accelerator Laboratory, Menlo Park, CA; in collaboration with Dr. Erik Farquhar) with the storage ring operating at 3.0 GeV and 500 mA. A liquid-nitrogen cooled Si(220), phi = 0° double crystal monochromator was used for energy selection, and was detuned by ~50% for harmonic rejection 1000 eV above the Ni K-edge. Sample temperatures were maintained at 15K using closed-cycle liquid He cryostat. XAS spectra were collected as fluorescence excitation spectra using a 30-element solid-state germanium detector (Mirion), using the following parameters: 10 eV steps/1 sec. integration time in the pre-edge, 0.3 eV steps/2 sec. integration times in the edge, and 0.05*k* steps in the EXAFS, with integration time

increasing in a k^3-weighted fashion from 2 to 10 sec. over the energy range (k_{max} = 15.2k for **M** and 17.1k for **2a**). Total detector counts were maintained at <30 kHz, using a Soller slit assembly and 3μ cobalt oxide filter to reduce scatter. A Ni metal foil spectrum was recorded simultaneously for energy calibration, with the first inflection point of the reference foil edge set to 8333.0 eV. Tandem Mössbauer/XAS cups with a sample window of ~(6mm x 10mm) were used as sample cells. Multiple spots on each sample were exposed during data collection, and samples were monitored for photoreduction during data collection. No radiation damage was observed on the basis of the lack of any scan-to-scan red-shift in edge or pre-edge features. Averaging and normalization of XAS data was performed using Athena, while Artemis was employed for EXAFS analysis.[9]

Simple models of the structures of **2a** and **M** were constructed and used as FEFF6 input to identify significant single-scattering paths. For a given shell in all simulations, the coordination number 'n' was fixed, while 'r' and σ^2 were allowed to float. The amplitude reduction factor S_0^2 was fixed at 0.9, while the edge shift parameter ΔE0 was allowed to float at a single common value for all shells. The fit was evaluated in k^3-weighted R-space, and fit quality was judged by the reported R-factor. Significant fits are tabulated in Tables A3.2.1 and A3.2.2 in Appendices.

5.2.12. Density Functional Theory Calculations

Chapter 2:

To investigate the nature of **Co4L1**, DFT calculations on the same level of the theory have been conducted for six small model compounds, see Figure 2.2.13 in Chapter 2. Like for the calculation of the model **1**, the COSMO solvation model was used to mimic the acetone solvation[10]. The dispersion has been implemented by the empirical dispersion correction of Grimme[11]. After geometrical optimizations, normal mode analysis (frequency calculation) was carried out to check if the structures are local minima of the potential energy hypersurface. Model **1** (with one acetone and one triflate; Figure 2.2.13 in Chapter 2) exhibits one virtual vibration of -6.7 cm-1, which accords to a low-energy phononic-type of general motion and doesn't alter the structure/energy in any considerable fashion, so no efforts were made to reoptimize the structure. Model **2** shows three virtual vibrations at -49.4, -25.5, and -8.1 cm-1, all of which break the imposed Cs-symmetry. This model serves as a reference (effect of symmetry constraints) and wasn't expected to be the true structure of compound **Co4L1**. Models **3**-**6** are local minimum structures.

Chapter 3:

All the calculations have been performed using the Gaussian 09 suite of program.[12] The geometry optimizations were performed with B3LYP functional.[13] The B3LYP has a proven track record of predicting the structures and the energetics accurately for such metal-mediated catalytic reactions. LACVP basis set comprising LanL2DZ - Los Alamos effective core potential for Ni[14] and a 6–31G* basis set for the C, H, N, and O atoms[15] has been employed for geometry optimization, and the optimized geometries were then used to perform single-point energy calculations using a TZVP basis set on all atoms. Frequency calculations have been carried out to verify minima on the potential-energy surface (PES) and also to obtain free energy corrections. The quoted DFT energies are B3LYP energies incorporating Gibbs free energies correction at computed at the temperature of 298.15 K, unless otherwise mentioned. The fragment approach available in Gaussian 09 is employed to aid smooth convergence in the case of radical intermediates.

5.3. Synthesis of compounds and generation of the intermediates

Chapter 2

5.3.1. Synthesis of the Ligand L0

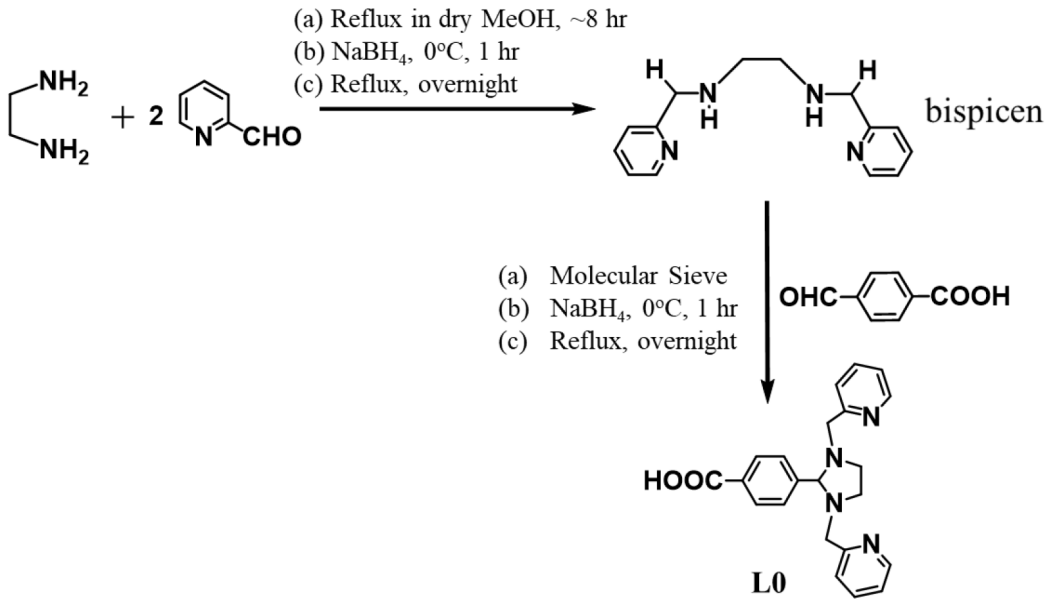

Scheme 5. 1.: Synthesis of the ligand **L0**.

The Ligand **L0** was prepared according to scheme 5.1.[16] N,N'-Bis(pyridin-2ylmethyl)-ethane-1,2-diamine (bispicen) was prepared according to the previously[17] reported method. 4-carboxybenzaldehyde (1.08 g, 7.18 mmol) was then added to a solution of bispicen (1.74 g, 7.18 mmol) in anhydrous diethyl ether (20 mL) and the reaction mixture was stirred overnight

at room temperature with a $CaCl_2$ protection tube. A white precipitate was obtained within an hour. The precipitate was filtered and washed repeatedly with diethyl ether until the residue was completely white. This white powder was then dried under high vacuum to remove any trace of moisture and stored inside a desiccator. The expected product was obtained as a white solid. Yield: 2.15 g (80.0%).

^{1}H NMR ($CDCl_3$, 400 MHz): δ (ppm) 8.48 (d, 2H, *H*-py), 7.93 (d, 2H, *H*-Ar), 7.65-7.58 (m, 4H, *H*-py), 7.33 (d, 2H, *H*-py), 7.15-7.12 (m, 2H, *H*-Ar), 4.078 (s, 1H, C*H*), 3.96 (d, 2H, CH_2-py), 3.51 (d, 2H, CH_2-py), 3.24 (q, 2H, CH_2-N), 2.72 (q, 2H, CH_2-N).
The resolution of 13C-NMR was poor due to the insolubility of **L1** in common organic solvents.
ESI-MS(+): *m/z* = 375.19 (*m/z calc*. for $[C_{22}H_{23}N_4O_2]^+$: 375.18). This *m/z* value corresponds to [M+1]+.
IR (KBr pellet): ($\tilde{\nu}$ in cm^{-1}) = 3509 br, 2916 m, 2799 s, 1693 s, 1599 s, 1474 m, 1429 m, 1420 m, 1342 m, 1313 m, 1284 s, 1213 w, 1155 m, 1118 m, 1098 m, 1013 s, 982 w, 854 m, 779 s, 704 m, 631 m.

5.3.2. Synthesis of the ligand L1

The ligand **L1** was synthesized following a previously reported procedure.[18] Di-*n*butyltin oxide, ^{n}Bu_2SnO (0.66 g, 2.67 mmol) was added to a suspension of 4-(1,3-bis(2-yridinylmethyl)-2-imidazolidinyl)benzoic acid **(L0)** (1.00 g, 2.67 mmol) in anhydrous toluene (80 mL) and the reaction mixture was refluxed at 120 - 130 ^{o}C with continuous removal of water by using a Dean-Stark apparatus. After ~7 hours, the reaction mixture was allowed to cool to room temperature and then filtered. The solvent from the filtrate was removed under reduced pressure. The expected product was recovered as a pale yellow solid. Yield: 1.47 g (90.1%).
Single crystals of **L1** suitable for X-ray crystallography were grown by slow evaporation of a concentrated solution of **L1** in toluene.

^{119}Sn NMR ($CDCl_3$, 150 MHz): δ (ppm) -210.82 (s) and -213.82 (s).
^{1}H NMR ($CDCl_3$, 400 MHz): δ (ppm) 8.48 (m, 8H, *H*-Ar), 8.04-7.93 (m, 8H, *H*-Ar), 7.75-7.62 (m, 16H, *H*-Ar), 7.15-6.98 (m, 16H, *H*-Ar), 4.15 (s, 4H, C*H*), 4.09-3.95 (m, 16H, CH_2-py), 3.51-3.28 (m, 16H, CH_2-N), 1.61-1.05 (m, 48H, CH_2), 0.92 (t, 24H, CH_3).
IR (KBr pellet): ($\tilde{\nu}$ in cm-1) = 3445 br, 3062 w, 3008 w, 2955 s, 2925 m, 2868 m, 2816 w, 1611 s, 1605s, 1593 s, 1569 s, 1546 s, 1475 m, 1432 s, 1403 s, 1340 s, 1290 m, 1157 m, 1129 m, 1081 w, 1018 s, 867 m, 783 s, 757 w, 710 m, 685 s.

5.3.3. Synthesis of the ligand L2

The ligand **L2** was synthesized following a previously reported procedure.[19] To a suspension of 4-(1,3-bis(2-pyridylmethyl)-2-imidazolidinyl)benzoic acid (1.03 g, 2.74 mmol) in anhydrous toluene (100 mL) was added n-butylstannoic acid (0.57 g, 2.74 mmol). The reaction mixture was then refluxed at 120 °C for 7 hours with continuous removal of H_2O by using a dean-Stark apparatus. After this time, the reaction mixture was allowed to cool down to room temperature and then filtered. The solvent from the filtrate was removed under reduced pressure. **L2** was obtained as a yellow solid. Yield: 1.24 g (0.36 mmol, 80%).

^{1}H NMR ($CDCl_3$, 400 MHz): δ (ppm) 0.85 (t, 36H, C*H*$_3$), 1.01-1.77 (m, 72H, C*H*$_2$), 2.88-3.51 (m, 24H, CH_2-N), 3.95 (d, 12H, C*H*$_2$-py), 4.25 (s, 6H, C*H*), 6.90-7.09 (m, 12H, *H*-Ar), 7.30-7.58 (m, 48H, *H*-Ar), 7.85-8.02 (m, 12H, *H*-Ar), 8.16 (m, 12H, *H*-Ar), 8.35 (m, 12H, *H*-Ar).
^{119}Sn NMR ($CDCl_3$, 150 MHz): δ (ppm) -482.47 (s).
IR, (KBr pellet): $\tilde{\nu}$ (cm^{-1}) 3447 (br), 3061 (w), 2953 (m), 2927 (m), 1703 (w), 1604 (s), 1590 (s), 1561 (m), 1529 (s), 1445 (m), 1413 (s), 1292 (m), 1148 (m), 1018 (m), 865 (m), 779 (m), 751 (w), 682 (s).

5.3.4. Synthesis of the ligand LE

4′-formyl-biphenyl-4-carboxylic acid (3.20 g, 7.18 mmol) was added to a solution of bispicen (1.74 g, 7.18 mmol) in anhydrous methanol (50 mL) and the reaction mixture was stirred overnight at room temperature under argon atmosphere. A white precipitate was obtained within fes hours. The precipitate was filtered and washed repeatedly with diethyl ether until the residue was completely white. This white powder was then dried under high vacuum. The expected product was obtained as a white solid.
^{1}H NMR ($CDCl_3$, 400 MHz): δ (ppm) 8.48 (d, 2H, *H*-py), 7.93 (d, 2H, *H*-Ar), 7.65-7.58 (m, 4H, *H*-py), 7.33 (d, 2H, *H*-py), 7.15-7.12 (m, 2H, *H*-Ar), 4.078 (s, 1H, C*H*), 3.96 (d, 2H, C*H*$_2$-py), 3.51 (d, 2H, C*H*$_2$-py), 3.24 (q, 2H, C*H*$_2$-N), 2.72 (q, 2H, C*H*$_2$-N).
ESI-MS(+): *m/z* = 451.20 (*m/z calc*. for $[C_{28}H_{27}N_4O_2]^+$: 450.21). This *m/z* value corresponds to $[M+H]^+$.

Elemental Analysis $C_{28}H_{26}N_4O_2$ Calculated (%): C, 74.65; H, 5.82; N, 12.44; O, 7.10. Found (%): C, 74.51; H, 5.75; N, 12.76.

5.3.5. Synthesis of the complex Co$_4$L1:

A solution of **L1** (0.50 g, 0.2 mmol) in anhydrous acetone (2 mL) was added to a suspension of $Co^{II}(OTf)_2$ (0.290 g, 0.8 mmol) in anhydrous acetone (4 mL). The light orange reaction mixture

was stirred in anhydrous conditions, under nitrogen at room temperature for 24 hours. The solution was then filtered. After the addition of 40 mL of anhydrous *n*-hexane to the filtrate, **Co_4L1** precipitated as a dark-yellow powder. The remaining solvent was removed by decantation and **Co_4L1** was dried in high-vacuum overnight.

Elemental analysis: $C_{128}H_{160}Co_4F_{24}N_{16}O_{34}S_8Sn_4$ Calculated (%): C, 39.52; H, 4.15; N, 5.76. Found (%) C, 38.82; H, 4.35; N, 5.56

IR (KBr pellet): $\tilde{\nu}$ (cm^{-1}) 3265 br, 3050 w, 2958 s, 2923 s, 2856 s, 2323 s, 2093 s, 1705 s, 1625 s, 1615 s, 1605 s, 1593 m, 1572 m, 1549 m, 1463 s, 1404 s, 1378 s, 1344 m, 1281 w, 1259 s, 1225 s, 1158 s, 1080 s, 1032 s, 871 s, 797 s, 752 w, 700 m, 685 s, 668 s.

X-band EPR: effective $g'_{\perp} = 4.01$ and $g'_{\parallel} \approx 2.0$

5.3.6. Synthesis of the complex Co_6L2:

A solution of ligand **L2** (0.40 g, 0.12 mmol) in anhydrous acetone (2 mL) was added to a suspension of $Co^{II}(OTf)_2$ (0.49 g, 1.3 mmol) in anhydrous acetone (2 mL). The orange-pink reaction mixture was stirred in anhydrous conditions at room temperature for 24 hours. The solution was then filtered. After the addition of 50 mL of anhydrous *n*-hexane to the filtrate, complex **Co_6L2** precipitated as a light-orange powder. The remaining solvent was removed by decantation and **Co_6L2** was dried in vacuum overnight.

Elemental analysis: $C_{168}H_{180}N_{24}F_{36}O_{54}S_{12}Sn_6Co_6$; Calculated (%): C, 36.42; H, 3.38; N, 6.07.

Found (%): C, 35.51; H, 3.64; N, 5.52.

IR (KBr pellet): $\tilde{\nu}$ (cm^{-1}) 3062 w, 2955 m, 2907 w, 1702 m, 1626 s, 1607 s, 1595 m, 1575 s, 1565 m, 1545 m, 1414 s, 1291 m, 1274 m, 1233 s, 1194 m, 1159 s, 1029 s, 1018 m, 972 w, 881 w, 865 w, 811 w, 769 m, 682 s, 668 m.

X-band EPR: effective $g'_{\perp} = 4.2$ and $g'_{\parallel} \approx 2.1$

5.3.7. Generation of the intermediate 1

Under inert conditions, a pale yellow solution of the complex **Co_4L1** in anhydrous acetone (0.5 mM, 2 mL) was kept at -50 °C. Anhydrous O_2 was then bubbled into the solution. The formation of a deep orange intermediate was monitored following the growth of the 464 nm band in the UV-vis spectrum.

UV-vis (acetone, -50 °C): λ_{max} (ε_{max}) 464 nm (12,232 $M^{-1}cm^{-1}$).

X-band EPR: Silent

5.3.8. Generation of the intermediate 2

The intermediate **2** was generated following a previous report.[19] Under inert conditions, a pale orange solution of the complex **1** in anhydrous acetone (1 mM, 2 mL) was kept at -50 °C. Anhydrous O_2 was then bubbled into the solution. The formation of a deep orange intermediate was monitored following the growth of the 470 nm band in the UV-vis spectrum.

UV-vis (acetone, -50 °C): λ_{max} (ε_{max}) 470 nm (28,000 $M^{-1}cm^{-1}$).

X-band EPR: Silent

Chapter 3

5.3.9. Synthesis of the diisopropylphenyl biuret ligand LH_2

To a solution of 2,6-diisopropyl aniline (2.42 mL; 12.82 mmol; 1 eqv.) in 30 mL of dry THF was added triethylamine (1.96 mL; 14.11 mmol; 2.2 eqv.) and the mixture was stirred at 0 °C for 5 minutes. To this resultant solution mixture, was added, a solution of dichloformyl methylamine (0.715 mL; 6.41 mmol; 0.5 eqv.; density = 1.40 g/mL) in 30 mL of dry THF, dropwise under stirring condition at 0 °C, over a time period of 20 minutes. The mixture was allowed to stir overnight at room temperature. Precipitation of the trimethylamine salt was observed over the reaction time period. The salt precipitate was filtered off through celite using a frit funnel. Solvent was evaporated using a rotary evaporator and the solid residue was washed with hexane (3x20 mL) to get rid of any unreacted 2,6 diisopropyl aniline. Finally, the desired compound (2.3 gm; 82%) was obtained by flash column chromatography (15% EtOAc: Hexane; R_f = 0.7).

^{1}H NMR (400 MHz, benzene-d_6,25 °C): δ (ppm) 8.43 (s, 2H; NH), 7.24-7.07 (m, 6H; Ar), 3.18 (septet, j = 7 Hz, 4H; isopropyl methine), 2.87 (s, 3H; Me), 1.20 (s, 24H; Me).

Elemental analysis: $C_{27}H_{39}N_3O_2$; Calculated (%): C, 74.10; H, 8.98; N, 9.60. Found(%): C, 73.95; H, 9.15; N, 9.38.

IR (ATR-Diamond): $\tilde{\nu}$ (cm^{-1}) 3300 (N-H), 2962, 2916, 2868, 1687 (C=O), 1643 (C=O), 1589, 1533, 1471, 1422, 1381, 1361, 1294, 1256, 1211, 1166, 1130, 1003, 936, 800, 776, 744, 722, 676 and 602.

ESI-MS(+): *m/z* (found) = 438.3117 (*m/z calc*. for $[C_{27}H_{40}N_3O_2]^+$: 438.3121). This *m/z* value corresponds to $[M+H]^+$.

5.3.10. Synthesis of the Nickel(II)Br$_2$ complex (M)

To a cooled (-20 °C) solution of **LH$_2$** (200 mg; 0.457 mmol; 1 eqv.) in 20 mL of dry THF was added n-Butyl lithium (2.5 M in hexane) (0.365 mL; 0.914 mmol; 2 eqv.) and stirred for 2 hrs under dry N_2. The cooling bath was removed and the reaction mixture was allowed to stir for additional 4 hrs at room temperature. Anhydrous $NiBr_2(thf)_{1.5}$ (102 mg; 0.466 mmol; 1.02 eqv) was added to the reaction mixture and stirred overnight at RT to give a dark blue colored solution. The solvent was pumped off and the residue was dissolved in 10 mL of THF and filtered through a sintered funnel. The volume was reduced to 5 mL and the desired compound was recrystallized (yield; 62%) from dry THF as dark blue crystals of **M**.

^{1}H NMR (400 MHz, ACN-d_3, 25 °C): δ (ppm) 38.13, 32.07, 26.84, 11.26, 9.19, 7.27, 5.59, 3.74, 2.87, 1.93, 1.23, -26.52.

Elemental analysis: $C_{39}H_{61}Br_2Li_2N_3NiO_5$ (**M** – 3 times THF); Calculated (%): C, 52.97; H, 6.95; N, 4.75. Found(%): C, 52.13; H, 7.30; N, 4.92.

IR (ATR-Diamond): $\tilde{\nu}$ (cm^{-1}) 2958, 2865, 1600 (C=O), 1576 (C=O), 1465, 1437, 1379, 1303, 1254, 1045, 889, 800, 777, 750 and 627.

UV-vis (CH_3CN; 25 °C): λ_{max} (ε_{max}) 356 nm (7770 M^{-1}cm^{-1}), 480 nm (680 M^{-1}cm^{-1}), 558 nm (755 M^{-1}cm^{-1}) and 830 nm (70 M^{-1}cm^{-1}).

5.3.11. Generation of the intermediate 2a

In a typical experiment, 2 mL of a 1 mM solution of $[Li(thf)_3]_2[(biuret)Ni^{II}Br_2]$ (**M**) in MeCN were placed in a 1 cm path-length cuvette. The quartz cell was placed in the Unisoku cryostat of the UV−Vis absorption spectrophotometer. UV−Vis absorption spectrum of the starting complex was recorded at 25ºC. Then, a solution of H_2O_2 in MeCN was added (5 equiv) followed by a solution of triethylamine (Et_3N) in MeCN (5 equiv). The formation of a yellow-orange species was monitored following the growth of the 455 nm band in the UV-vis spectrum.

The formation of one band at λ_{max} = 455 nm (ε = 5900 M^{-1} cm^{-1}) was observed with a shoulder 300 nm. The formation of **2a** reached a maximum within 800 sec.

UV-vis (CH_3CN; 25 °C): λ_{max} (ε_{max}) 455 (5900 M^{-1}cm^{-1})

X-band EPR (CH_3CN; 10K): g_x = 2.21, g_y = 2.17, g_z = 2.06.

ESI-MS (+) (in CH_3CN): *m/z* = 539.25 (for ^{16}O sample), 543.26 (for ^{18}O labeled sample) (*m/z calc*. for $[C_{27}H_{37}Li_2N_3NiO_4]^+$: 539.25).

5.4. Reactivity Studies

5.4.1. Determination of k2 by time-resolved UV-Vis spectroscopy.

The reactivity studies of the complexes/intermediates were performed at a specified temperature (as mentioned in the respective chapters) under an inert atmosphere. Upon addition of exogenous substrates in large excess (>50 eqv.) to the solution of preformed complexes/intermediates, the decay profiles of the characteristic absorption bands were followed by a time-resolved UV-Vis-spectrometer. Pseudo-first order fitting to the resultant decay curves corresponding to the characteristic absorption features afforded pseudo-first-order rate constants (k_{obs}), which were found to be linearly increasing with the increment of substrate concentrations. The slope of the k_{obs} versus
substrate concentration fitting plot provided the second-order rate constants (k_2) at the specific temperature.

Rate = k_2 [Substrate][Complex]

when, [Substrate] >> [Complex], [Substrate] ≈ constant;

Rate = k_{obs} [Complex] and k_{obs} = k_2 [Substrate]

Product Analysis. Unless otherwise mentioned, the substrate solution was injected to the preformed solution of the intermediate in a cuvette. Then the progress of the reaction was followed by a time-resolved UV-Vis spectrometer. Finally, the crude reaction mixture was analyzed for the identification of the product(s). For all substrates, the quantitative product analyses were done by GC-MS. In addition, the crude reaction mixtures prepared in deuterated solvent were also analyzed by ^{1}H-NMR. Either biphenyl or 1,3,5-trimethoxybenzene was used as an internal standard. All the reported yields are the average of at least three independent measurements. In the case of all substrates, blank reactions (*i.e.* the reactivity of substrate with oxidant in absence of complex) were verified under identical experimental conditions. Phenoxyl radicals were identified and quantified by EPR spectroscopy at 77 K.

Chapter 2

5.4.2. Reaction of intermediates 1 and 2 with substrates:

A solution of cobalt(II) complex (**Co$_4$L1** or **Co$_6$L2**) in anhydrous dichloromethane (2 mL) was prepared in a glove box and taken in a cuvette with a path length of 1 cm, sealed with an airtight rubber septum. The cuvette was then placed in a Unisoku cryostat connected to the UV-vis spectrometer and the temperature of the cryostat was maintained at -50 °C. After attaining the thermal equilibrium, 0.1 mL of an oxygen saturated acetone solution (11 mM; final

concentration 0.55 mM) was injected into the cuvette using an airtight syringe under argon atmosphere. Intermediate (**1** or **2**) starts forming immediately after the addition of O_2 into the solution of cobalt(II) complex. Formation of the intermediate was monitored by following the rise in the respective absorbance band in the UV-vis spectra at -50 ^oC. Argon was then bubbled into the solution (through the septum) with an outlet for 3-4 mins, in order to remove the excess O_2 from the solution completely. There was no change in absorption after bubbling argon. An excess amount of substrate (in 0.1 mL DCM or acetone solution) was then injected into the reaction mixture at -50 ^oC and the temperature was quickly raised up to +25 ^0C. The decay of the band at 464 nm for **1** and 470 nm for **2** was monitored and fitted to a pseudo-first-order rate, from which k_{obs} was determined. The pseudo-first-order fitting of the decay curves yielded the rate constants (k_{obs}) which were found to be linearly increasing with the increment of substrate concentrations. The slope of the rate constant (k_{obs}) vs substrate concentration fitting plot provided the second-order rate constants (k_2).

For 18-Oxygen labeling experiment, $^{18}O_2$ saturated acetone solution was used to generate the intermediates **1** and **2.**

5.4.3. Product analysis by the intermediate 2

Table 5.1.*: Substrates used for testing the reactivity of the intermediate **2** and analyses of products.*

Substrates	Product (% of yield)	Analyzed by**
Ph_3P	Triphenyl phosphine oxide (38%)	GC-MS
Xanthene	Xanthone (36%)	GC-MS
2,6-DTBP	2,6-di-tert-butyl-1,4-benzoquinone (31%) and 3,3',5,5'-Tetra-*tert*-butyl-4,4'-diphenoquinone (30%)	GC-MS
2,4,6-TTBP	2,6-di-tert-butyl-1,4-benzoquinone (42%) and 3,3',5,5'-Tetra-*tert*-butyl-4,4'-diphenoquinone (35%)	GC-MS
4-OMe-2,6-DTBP	2,6-di-tert-butyl-1,4-benzoquinone (28%)	GC-MS
4-Methoxyphenol	1,4-benzoquinone (33%)	GC-MS

*** The reaction mixture was passed through silica layer to remove the paramagnetic metal-complexes prior to the GC-MS measurements.*

5.4.3a. Detection of formaldehyde generated in the reaction of 2 with 4-OMe-2,6-DTBP

The formation of formaldehyde during the reaction of intermediate **2** with 4-OMe-2,6-DTBP was detected by the aqueous-based Nash assay.[21] The Nash reagent was prepared by dissolving

7.5 g of ammonium acetate, 100 µL of 2,4-pentadione, and 150 µL of acetic anhydride in 25 mL of water. A solution of **Co_6L2** (1 mM) in anhydrous acetone (0.5 mL) was prepared in a glove box and taken in a cuvette with a path length of 0.5 cm. The cuvette was then placed in a Unisoku cryostat connected to the UV-vis spectrometer and the temperature of the cryostat was maintained at -50 °C. After attaining the thermal equilibrium, pure oxygen gas was bubbled into the solution, through the septum, with an outlet. Intermediate **2** starts forming immediately after the addition of O_2 into the solution of **Co_6L2**; approximately 300 seconds were necessary for the complete formation of **2**. Argon was then bubbled into the solution (through the septum) with an outlet for 3-4 mins, in order to remove the excess O_2 from the solution completely. The temperature was then raised to 25 ºC. An acetone solution of 4-Ome-2,6-DTBP (20 mg in 0.2 mL acetone) was then added into the solution. The disappearance of the characteristic absorption band at 470 nm with a pseudo-first-order decay profile was observed. Wait for 2.5 hours to complete the reaction. 0.2 mL of this reaction mixture was then added to a vial containing 1.5 mL of the Nash reagent cocktail. The reaction mixture was then heated to 70 °C for 15 min and then taken in a cuvette with a path length of 0.5 cm. Formation of the absorbance at 413 nm was recorded, which confirms the presence of formaldehyde in the reaction mixture.

Chapter 3

5.4.4. Reaction of intermediate 2a with substrates

Reactivity studies of **2a** were done at 25°C under an inert atmosphere, by injecting the CH_3CN solutions of the substrates to a preformed solution of **2a** in CH_3CN. The pseudo-first-order decay of the 455 nm band was monitored by acquiring a UV-Vis spectrum every second. The pseudo-first-order fitting of the decay curves yielded the rate constant (k_{obs}) (Figure 3.2.15; chapter 3), which were found to be linearly increasing with the increment of the substrate concentrations. The slope of the rate constant (k_{obs}) *vs* substrate concentration plot provided the second-order rate constant (k_2) values. Similarly, reactions were carried out with differently para-substituted benzaldehydes to obtain the Hammet plot (Figure 3.2.18; chapter 3).

For product analysis, a calculated amount of the substrate (1-2 equivalents) in 0.1 mL CH3CN was added to the preformed solutions of **2a** in CH_3CN at 25°C and left for 1 hour at 25°C. After adding 0.4 equivalent of 1,3,5-trimethoxybenzene as an internal standard, the resultant solutions were filtered through silica and diluted with 1 mL ethyl acetate. After evaporation of the solvent, the residue was dissolved in CD_3CN and analyzed for products by ^{1}H-NMR. The chemical shifts are reported in ppm relative to the residual solvent signal. Quantification was performed by comparing the intensity of the product signals relative to that of the standard.

5.4.5. Product Analysis by the intermediate 2a

Table 5.2*.: Substrates used for testing the reactivity of the intermediate* ***2a*** *and analyses of products.*

Substrates	Product (% of yield)	Analyzed by**
2-PPA	Acetophenone (74%)	^{1}H-NMR
CCA	Cyclohexane carboxylic acid (54%)	^{1}H-NMR

*** The reaction mixture was passed through silica layer to remove the paramagnetic metal-complexes before the NMR measurements.*

5.5. References

1. (a) G. Sheldrick, *Acta Cryst. C* **2015**, *71*, 3. (b) G. Sheldrick, *Acta Cryst. A* **2015**, *71*, 3.

2. S.Stoll, A. Schweiger, *Journal of Magnetic Resonance,* 178, **2006,** 42.

3. (a) J. Jašík, J. Žabka, J. Roithová, D. Gerlich, Int. *J. Mass Spectrom*. **2013**, 354, 204. (b) J. Jašík, R. Navrátil, I. Němec, J. Roithová, *J. Phys. Chem. A* **2015**, *119*, 12648.

4. A.L. Ankudinov, B. Ravel, J.J. Rehr, S.D.Conradson, *Phys. Rev. B.,* 1998, **58**, 7565.

5. H. Dau, P. Liebisch, M. Haumann, *Anal. Bioanal. Chem.***, 2003**, *376*, 562.

6. (a) A.D. Becke, *J. Chem. Phys*., **1993**, *98*, 5648–5652. (b) J.P. Perdew, J.A. Chevary, S.H. Vosko, K.A. Jackson, M.R. Pederson, D.J. Singh, C. Fiolhais, *Phys. Rev. B.,* **1992**, *46,* 6671.

7. (a) M. Dolg, U. Wedig, H. Stoll, H. Preuss, *J. Chem. Phys.* **1987,** *86*, 866. (b) J.M.L. Martin, A. Sundermann, *J. Chem. Phys.* **2001,** *114*, 3408.

8. Gaussian 16, Revision C.01, M. J. Frisch, *et al.* Gaussian, Inc., Wallingford CT, **2016**.

9. B. Ravel, M. Newville, *J. Synchrotron Rad.* **2005**, *12*, 537.

10. A. Klamt, G. Schüürmann, *J. Chem. Soc., Perkin Trans 2.,* **1993**, *5*, 799-805.

11. S. Grimme, J. Anthony, S. Ehrlich, H. Krieg, *J. Chem. Phys.* **2010**, *132*, 154104.

12. M. J. T. Frisch, G. W.; Schlegel, H. B.; Scuseria, G. E.; Robb, M. A.; Cheeseman, J. R.; Scalmani, G.; Barone, V.; Mennucci, B.; Petersson, G. A.; Nakatsuji, H.; Caricato, M.; Li, X.; Hratchian, H. P.; Izmaylov, A. F.; Bloino, J.; Zheng, G.; Sonnenberg, J. L.; Hada, M.; Ehara, M.; Toyota, K.; Fukuda, R.; Hasegawa, J.; Ishida, M.; Nakajima, T.; Honda, Y.; Kitao, O.; Nakai, H.; Vreven, T.; Montgomery, J. A., Jr.; Peralta, J. E.; Ogliaro, F.; Bearpark, M.; Heyd, J. J.; Brothers, E.; Kudin, K. N.; Staroverov, V. N.; Kobayashi, R.; Normand, J.; Raghavachari, K.; Rendell, A.; Burant, J. C.; Iyengar, S. S.; Tomasi, J.; Cossi, M.; Rega, N.; Millam, N. J.; Klene, M.; Knox, J. E.; Cross, J. B.; Bakken, V.; Adamo, C.; Jaramillo, J.; Gomperts, R.;

Stratmann, R. E.; Yazyev, O.; Austin, A. J.; Cammi, R.; Pomelli, C.; Ochterski, J. W.; Martin, R. L.; Morokuma, K.; Zakrzewski, V. G.; Voth, G. A.; Salvador, P.; Dannenberg, J. J.; Dapprich, S.; Daniels, A. D.; Farkas, Ö.; Foresman, J. B.; Ortiz, J. V.; Cioslowski, J.; Fox, D. J., *Gaussian, Inc. Wallingford CT* **2009**.

13. (a) C. Lee, W. Yang, R. G. Parr, *Phys. Rev. B.* **1988**, *37*, 785. (b) A. D. Becke, *J. Chem. Phys.* **1993**, *98*, 5648. (c) P. Stephens, F. Devlin, C. Chabalowski, M. J. Frisch, *The Journal of Physical Chemistry* **1994**, *98*, 11623.

14. (a) P. J. Hay, W. R. Wadt, *J. Chem. Phys.* **1985**, *82*, 299. (b) P. J. Hay, W. R. Wadt, *J. Chem. Phys.* **1985**, *82*, 270. (c) W. R. Wadt, P. J. Hay, *J. Chem. Phys.* **1985**, *82*, 284. (d) R. Kumar, M. Katari, A. Choudhary, G. Rajaraman, P. Ghosh, *Inorg. Chem.* **2017**, *56*, 14859.

15. (a) R. Ditchfield, W. J. Hehre, J. A. Pople, *J. Chem. Phys.* **1971**, *54*, 724. (b) W. J. Hehre, L. Radom, P. R. Schleyer, J. A. Pople, *Ab Initio Molecular Orbital Theory*, Wiley: New York, **1986**.

16. S. Kundu, E. Matito, S. Walleck, F. F. Pfaff, F. Heims, B. Rábay, J. M. Luis, A. Company, B. Braun, T. Glaser, K. Ray., *Chem.- Eur. J.* **2012**, *18*, 2787.

17. P. Mialane, A. Nivorojkine, G. Pratviel, L. Az8ma, M. Slany, F. Godde, A. Simaan, F. Banse, T. Kargar-Grisel, G. Bouchoux, et al., *Inorg. Chem*. **1999**, *38*, 1085.

18. S. Kundu, *PhD Thesis: Synthesis, Spectroscopic Characterization and Reactivity of the High-Valent Metal-Oxo/Imido Cores of the Late Transition Metals*, Humboldt-Universität Zu Berlin, Berlin, **2013**.

19. I. M. Pérez, S. Kundu, A. Chandra, K. E. Craigo, P. Chernev, U. Kuhlmann, H. Dau, P. Hildebrandt, C. Greco, C. Van Stappen, N. Lehnert and K. Ray, *J. Am. Chem. Soc*. **2017**, *139*, 15033–15042.

20. (a) J. England, Y. Guo, K. M. Van Heuvelen, M. A. Cranswick, G. T. Rohde, E. L. Bominaar, E. Mgnck, L. Que, Jr., *J. Am. Chem. Soc.* **2011**, *133*, 11880. (b) S. Herres-Pawlis, A. Neuba, O. Seewald, T. Seshadri, H. Egold, U. Flörke, G. Henkel, *Eur. J. Org. Chem.* **2005**, *2005*, 4879.

21. T. Nash, *Biochem. J.* **1953,** *55*, 416−421.

Appendices

A1. List of the ligands and complexes used for the studies

A2. List of substrates used for reactivity studies

A3. Tables for EXAFS fitting analyses

A4. Crystallographic data

A5. GC-MS figures

A6. Lists of abbreviations

A7. Declaration

A8. Publications and Presentations

A1. List of the ligands and complexes used for the studies

A1.1 Ligands:

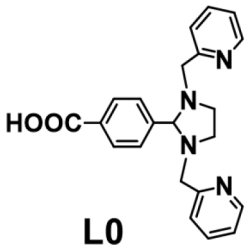

L0

(For details see Chapter 2)

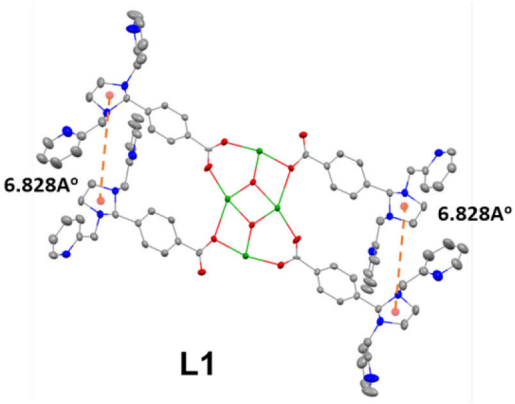

L1

(For details see Chapter 2)

Hydrogen atoms and the *n*-butyl (^{n}Bu-) groups on the tin atoms have been omitted for clarity.

Color code: nitrogen-blue; carbon-grey; oxygen-red; tin-green.

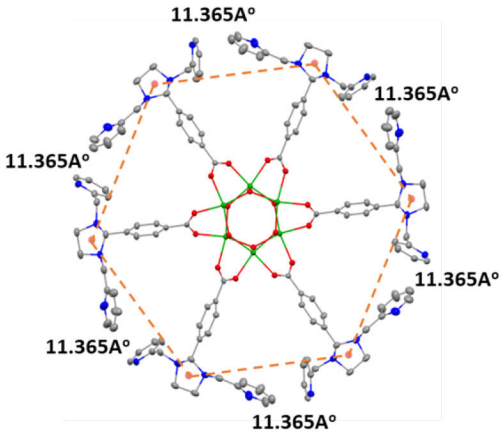

L2

(For details see Chapter 2)

Hydrogen atoms and the *n*-butyl (^{n}Bu-) groups on the tin atoms have been omitted for clarity. Color code: nitrogen-blue; carbon-grey; oxygen-red; tin-green.

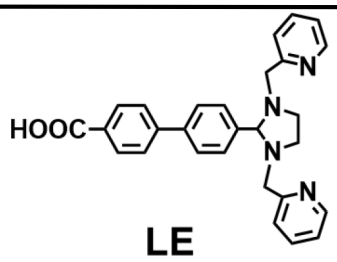

LE

(For details see Chapter 2)

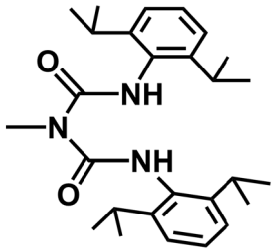

LH_2

(For details see Chapter 3)

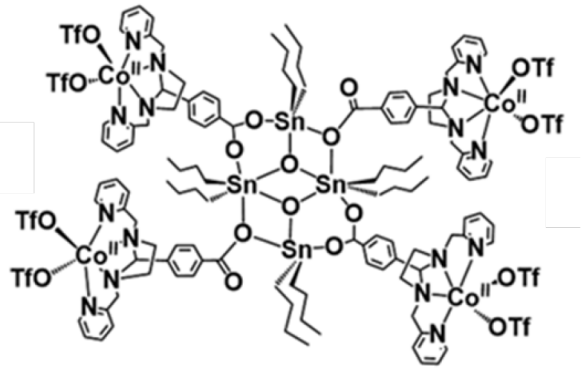

Co_4L1

(For details see Chapter 2)

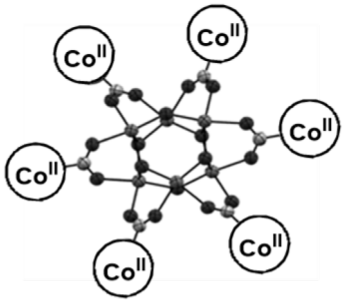

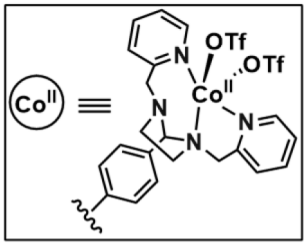

Co_6L2

(For details see Chapter 2)

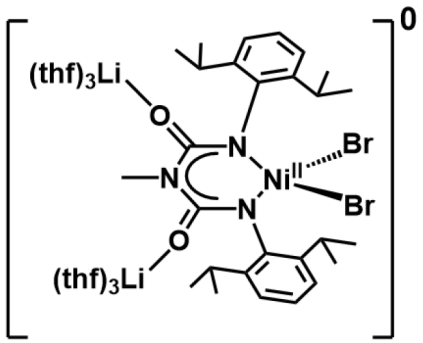

M

(For details see Chapter 3)

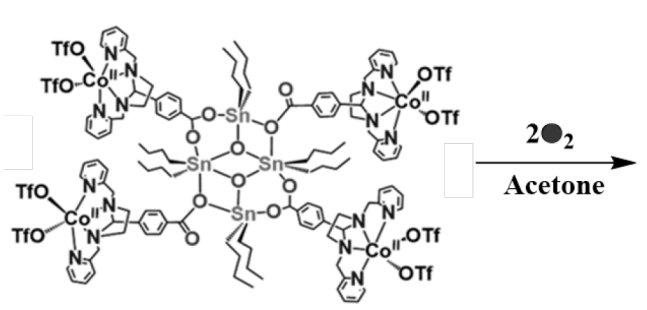

Co_4L1

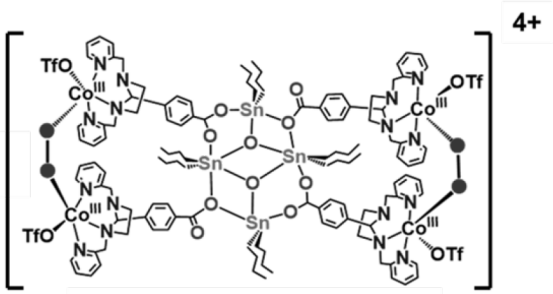

End on Peroxo Complex (1)

(For details see Chapter 2)

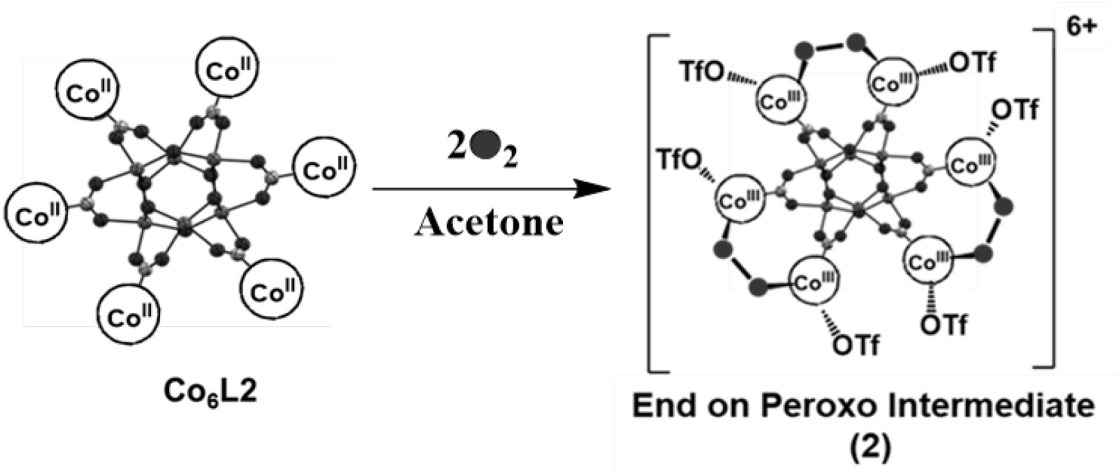

(For details see Chapter 2)

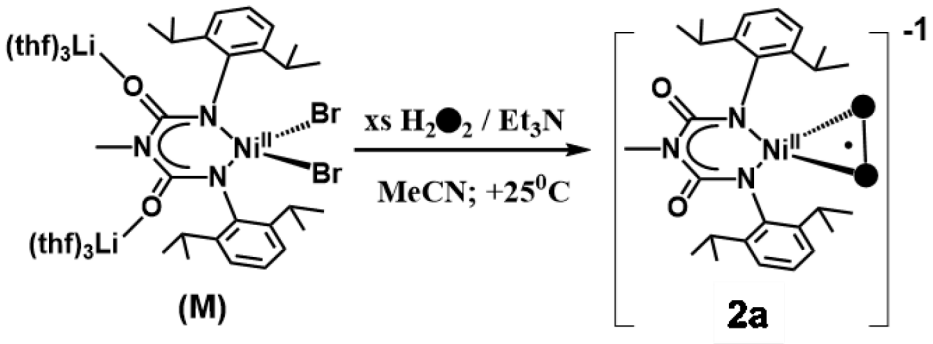

(For details see Chapter 3)

A2. List of substrates used for reactivity studies

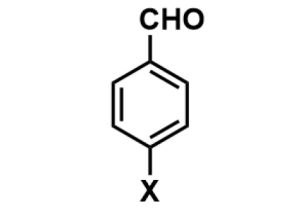

X = Cl, H, Me, OMe

***p*-*X*-Benzaldehyde**

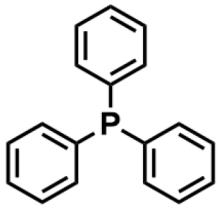

Triphenyl phosphine

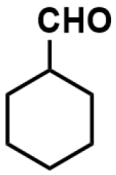

CCA

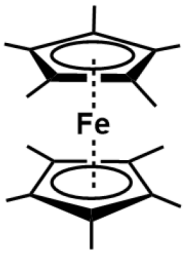

$Me_{10}Fc$

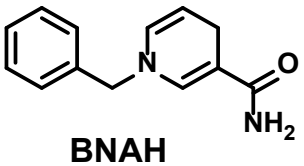

BNAH

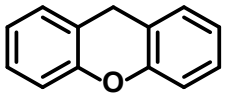

Xanthene

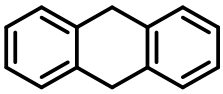

DHA

1,4-CHD

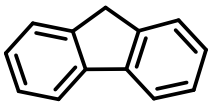

Fluorene

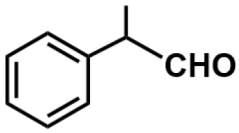

2-PPA

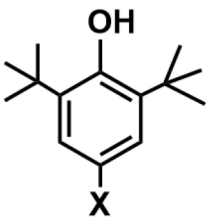

X = H, ^{t}Bu, OMe, Br

***p*-*X*-2,6-DTBP**

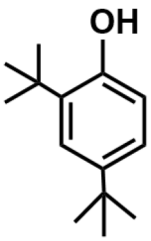

2,4-DTBP

***p*-*X*-PhOH**

A3. Tables for EXAFS fitting analyses

Chapter 3

***Table A3.2.1**: Selected EXAFS fits of **M**.*[a]

	Ni-N/O			Ni-Br			Ni···C					
fit	**n**	**r**	**σ^2**	**n**	**r**	**σ^2**	**n**	**r**	**σ^2**	**ΔE_0**	**red χ^2**	**R**
1				2	2.42	4.4				2.90	376.3	0.2677
2	2	1.93	-0.1							-3.52	975.2	0.6939
3	3	1.92	2.4							-5.88	1038.8	0.7391
4	4	1.92	5.1							-7.81	1105.1	0.7863
5	*2*	*1.93*	*1.0*	*2*	*2.40*	*4.7*				*-1.47*	*26.7*	*0.0141*
6	1	1.94	-2.4	3	2.42	7.1				1.97	91.3	0.0482
7	3	1.93	4.3	1	2.39	1.4				-4.17	48.4	0.0255
8	2	1.93	0.9	2	2.40	4.7				-1.45	95.6	0.0833
9	2	1.93	1.1	2	2.40	4.6	4	2.93	1.7	-1.97	76.5	0.0539
10	***2***	***1.93***	***0.9***	***2***	***2.40***	***4.7***	***4*** ***4***	***2.94*** ***3.24***	***2.9*** ***2.5***	***-1.88***	***41.1***	***0.0221***
Exp(XRD)		***1.953(4)*** ***1.959(4)***			***2.4102(10)*** ***2.4018(11)***							

[a] Fitting range was k = 2.0-14.0 Å-1 (resolution = 0.13 Å) with back transform ranges of 1-2.45 Å for fits 1-7, and 1-3.05 Å for fits 8-10. r is in units of Å; σ^2 is in units of 10-3 Å; ΔE_0 is in units of eV; R represents the fractional mis-fit of the data, while red. χ^2 is the χ^2 fitting metric normalized by the number of independent data points in a given fit.

***Table A3.2.2**: Selected EXAFS fits of **2a**.*[a]

	Ni-N/O			Ni···C			Ni···C					
fit	**n**	**r**	**σ^2**	**n**	**r**	**σ^2**	**n**	**r**	**σ^2**	**ΔE_0**	**red χ^2**	**R**
1	3	1.86	1.3							-5.63	40.2	0.0197
2	*4*	*1.85*	*2.4*							*-7.00*	*36.3*	*0.0178*
3	5	1.85	3.5							-8.40	120.8	0.0591
4	4	1.85	2.4							-6.96	47.4	0.0619
5	4	1.85	2.4				4	3.18	5.6	-7.25	47.7	0.0535
6	4	1.85	2.4	2	2.83	2.7				-6.62	39.7	0.0445
7	4	1.85	2.4	4	2.83	7.5				-6.98	50.6	0.0567
8	***4***	***1.85***	***2.4***	***4***	***2.85***	***6.9***	***4***	***3.16***	***4.8***	***-6.79***	***28.8***	***0.0270***

[a] Fitting range was k = 2.0-16.0 Å-1 (resolution = 0.11 Å) with back transform ranges of 1-1.95 Å for fits 1-3 and 1-2.95 Å for fits 4-8. r is in units of Å; σ^2 is in units of 10-3 Å; ΔE_0 is in units of eV; R represents the fractional mis-fit of the data, while red. χ^2 is the χ^2 fitting metric normalized by the number of independent data points in a given fit.

A4. Crystallographic data

Chapter 3

	Complex M
Empirical formula	$C_{59}H_{101}Br_2Li_2N_3NiO_{10}$
Formula mass	1244.83
Crystal habit, color	clear dark blue
Crystal shape	plate
Crystal dim. (mm)	0.17×0.14×0.04
Crystal System	triclinic
Space group	P-1
a [Å]	12.6562(9)
b [Å]	12.8089(8)
c [Å]	23.1091(17)
α [°]	96.087(6)
β [°]	90.017(6)
γ [°]	116.311(7)
V [Å^3]	3334.5(4)
Z	2
T [K]	149.97(10)
D [g cm^{-1}]	1.240
GooF	1.018
μ [mm^{-1}]	2.237
Refl. measured	22869
R_{int}	0.0646
Parameters refined	769
wR_2 (all data) wR_2	0.2314 0.1922
R_1(all data) R_1	0.1089 0.0728

A5. GC-MS figures

Chapter 2

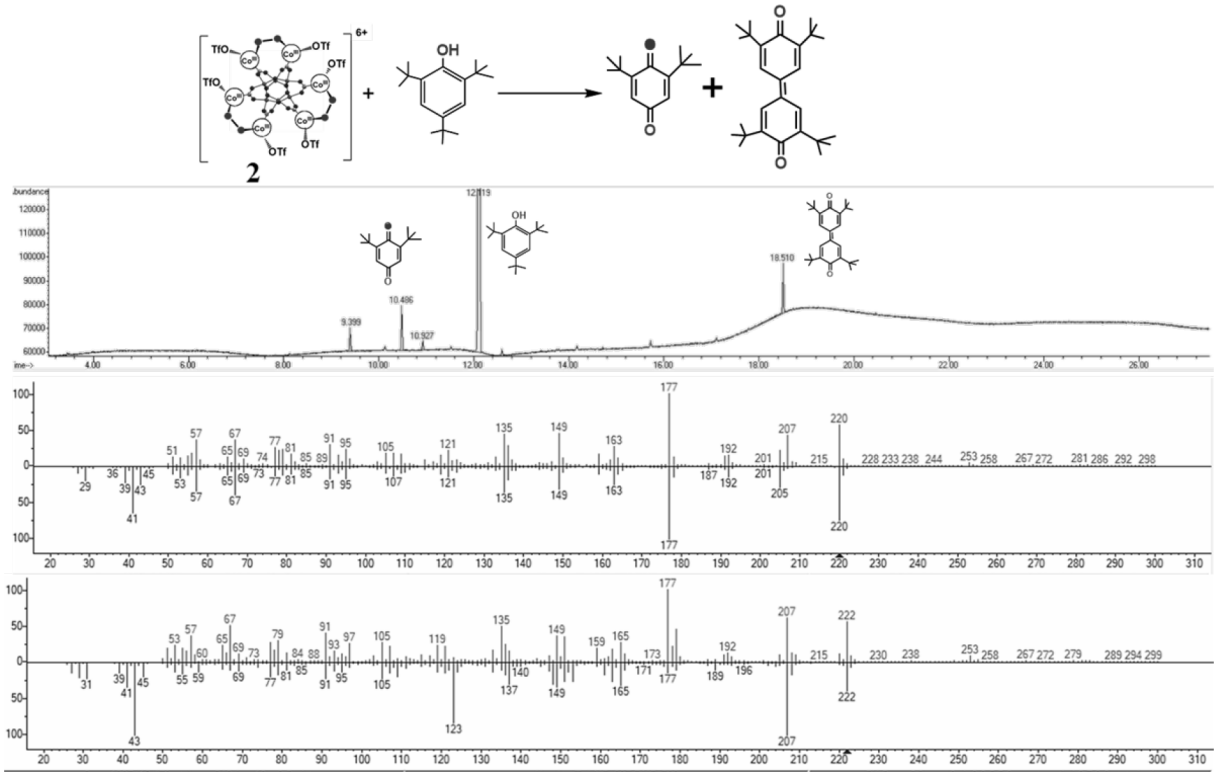

Figure A5.1: GC flame ionization detection spectrum for the reaction of the intermediate **2** with 2,4,6-trii-tert-butylphenole showing the formation of the corresponding products (determined by comparison to an internal biphenyl standard) (top) and the mass spectrum at 10.486 minutes compared to the bibliographical reported mass spectrum of 2,6-di-tert-butylcyclohexa-2,5-diene-1,4-dione (middle). The mass spectrum at 10.485 minutes compared to the bibliographical reported mass spectrum of 2,6-di-tert-butylcyclohexa-2,5-diene-1,4-dione identifying a mass shift of two units due to ^{18}O-labeling (bottom).

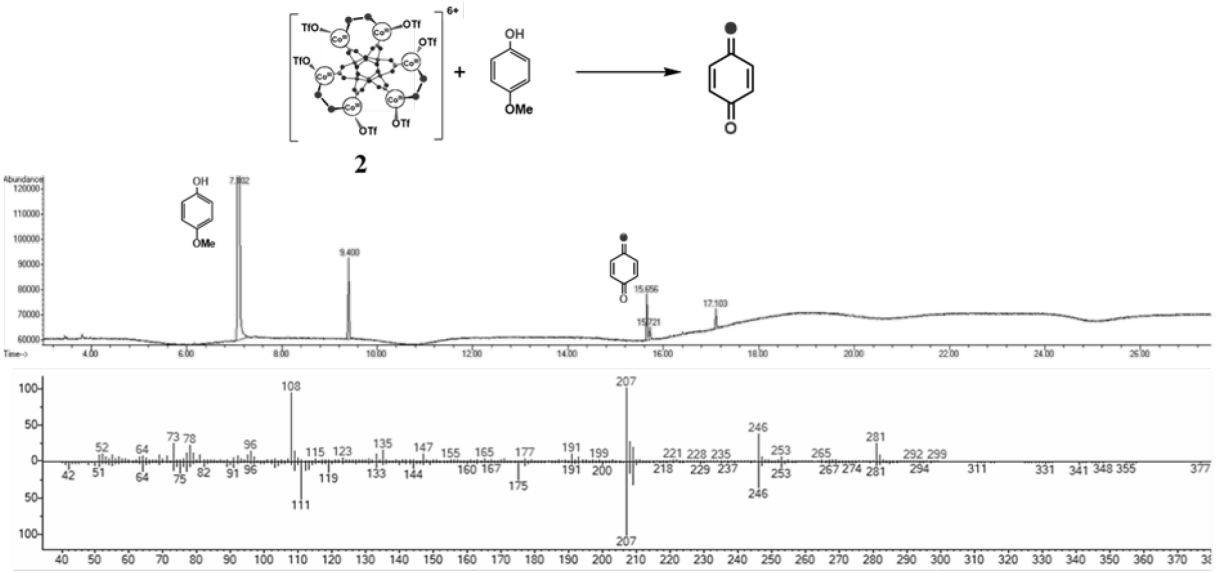

Figure A5.2: GC flame ionization detection spectrum for the reaction of the intermediate **2** with 4-methoxy phenol showing the formation of the corresponding products (determined by comparison to an internal biphenyl standard) (top) and the mass spectrum at 15.67 minutes compared to the bibliographical reported mass spectrum of 1,4-Benzoquinone (bottom).

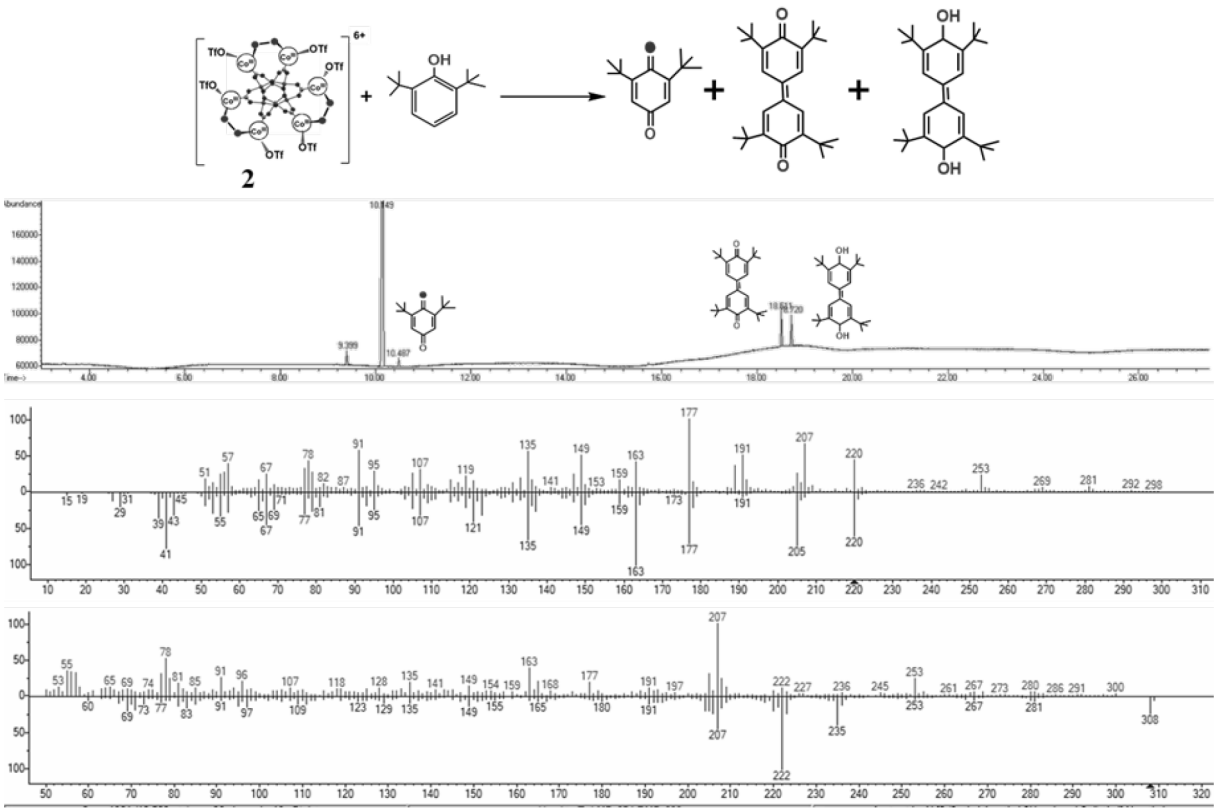

Figure A5.3: GC flame ionization detection spectrum for the reaction of the intermediate **2** with 2,6-di-tert-butylphenole showing the formation of the corresponding products (determined by comparison to an internal biphenyl standard) (top) and the mass spectrum at 10.486 minutes compared to the bibliographical reported mass spectrum of 2,6-di-tert-butyl-1,4-benzoquinone (middle). The mass spectrum at 10.487 minutes compared to the bibliographical reported mass spectrum of 2,6-di-tert-butyl-1,4-benzoquinone identifying a mass shift of two units due to ^{18}O-labeling (bottom).

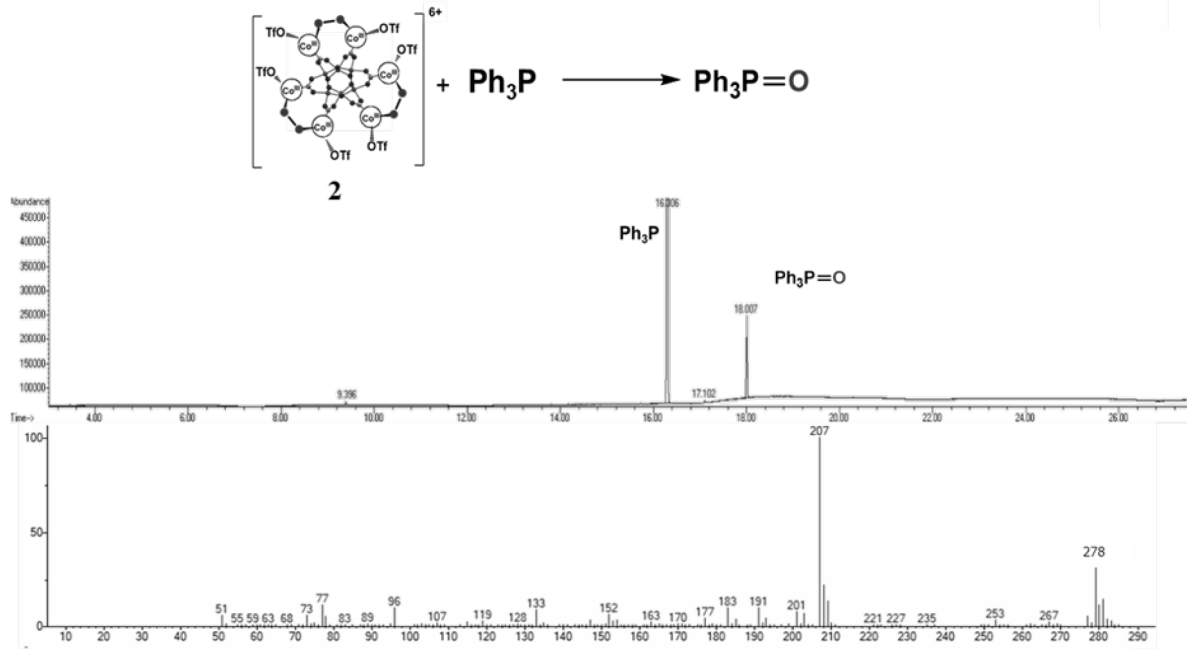

Figure A5.4: GC flame ionization detection spectrum for the reaction of the intermediate **2** with triphenyl phosphine showing the formation of the corresponding products (determined by comparison to an internal biphenyl standard) (top) and the mass spectrum at 18.07 minutes compared to the bibliographical reported mass spectrum of triphenylphosphine oxide (bottom).

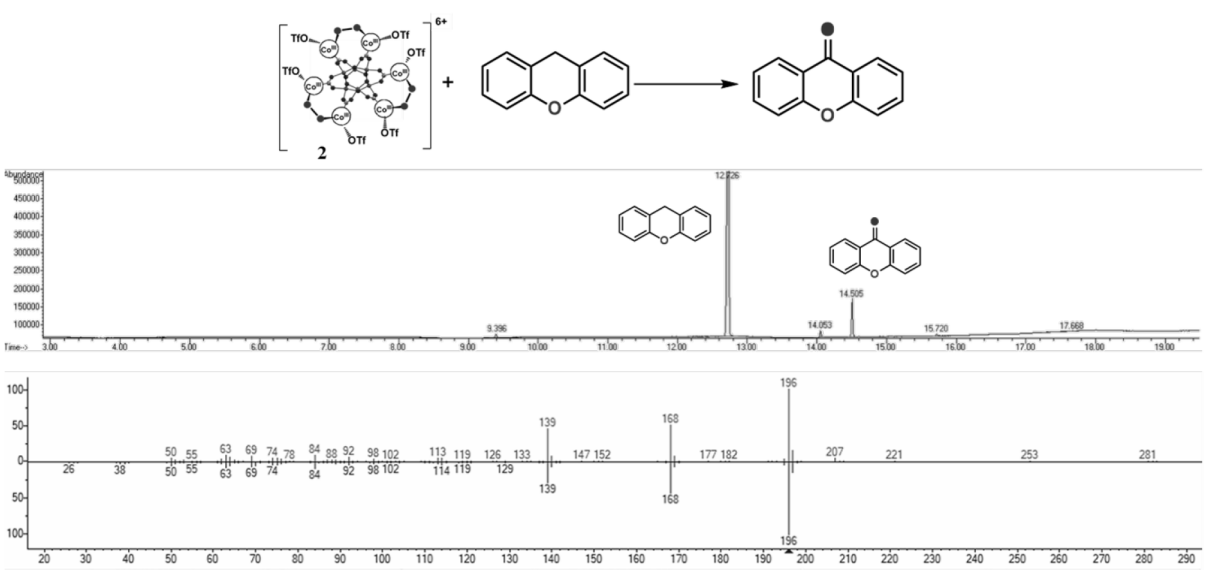

Figure A5.5: GC flame ionization detection spectrum for the reaction of the intermediate **2** with xanthene showing the formation of xanthone (determined by comparison to an internal biphenyl standard) (top) and the mass spectrum at 14.50 minutes compared to the bibliographical reported mass spectrum of xanthone (bottom).

A6. List of Abbreviations

Techniques and technical terms

ATP	Adenosine triphosphate
Asp	Aspartic acid
B	Magnetic field
BDE	Bond disociation energy
Calc.	Calculated
CT	Charge transfer
Cys	Cysteine
DFT	Density functional theory
e^-	Electron
EA	Elemental analysis
EPR	Electron paramagnetic resonance
eqv.	Equivalents
ESI	Electrospray ionization
EXAFS	Extended X-ray absorption fine structure
Exp.	Experimental
GC	Gas chromatography
HAA	Hydrogen atom abstraction
HAT	Hydrogen atom transfer
k_{obs}	Pseudo-first order rate constant
k_2	Second order rate constant
KIE	Kinetic isotope effect
MS	Mass spectroscopy
m/z	Mass per charge
$[M]^+$	Molecular ion peak
NMR	Nuclear magnetic resonance
PCET	Proton coupled electron transfer
rR	Resonance Raman
S	Electron spin
SCE	Saturated Calomel Electrode
Sim.	Simulated
UV-vis	Ultraviolet-visible
XAS	X-ray absorption spectroscopy
XANES	X-ray absorption near edge spectroscopy

Units

Å	Angstrom (10^{-10} m)
cm	Centimeter
°C	Degree Celsius
G	Gauss
Hz	Hertz
K	Kelvin
Kcal	kilo calories
mg	Milligram (10^{-3} g)
Min	Minute
mL	Milliliter (10^{-3} L)
mM	Millimolar (10^{-3} M)
mm	Millimeter (10^{-9} m)
S	Second

T	Tesla
W	Watt

Latin expressions

ca.	Around
et al.	and coworkers
in situ	In the original place
tert-	Tertiary
via	By means of
vs.	Versus, against

Symbols

δ	Chemical shift (ppm)
δ’	Isomer shift (mm/s)
ΔE_Q	Quadrupole splitting (mm/s)
ε	Extinction coefficient ($M^{-1}cm^{-1}$)
λ	Wavelength (nm)
ν	Wavenumber (cm^{-1})

Chemicals

AcO	Acetate
BNAH	1-benzyl-1,4-dihydronicotinamide
CHD	Cyclohexadiene
CCA	cyclohexane carboxaldehyde
DHA	Dihydroanthracene
Fc	Ferrocene
Me10Fe	Decamethylferrocene
Fc^+	Ferrocenium
$Me10Fc^+$	Decamethylferrocenium
-OTf	Triflate (trifluoromethane sulfonate)
TFA	Trifluoroacetic acid
DTBP	di-*tert*-butylphenol
DCM	dichloromethane

A7. Declaration

I declare that I have completed the thesis independently, using only the aids and tools specified. I have not applied for a doctor's degree in the doctoral subject elsewhere and do not hold a corresponding doctor's degree. I have taken due note of the Faculty of Mathematics and Natural Sciences Ph.D. Regulations, published in the Official Gazette of Humboldt-Universität zu Berlin no. 42/2018 on 11/07/2018.

I declare that the written and electronic version of the dissertation written by me in the University Library agrees with the accepted dissertation.

Anirban Chandra Berlin, den

A8. Publications and Presentations

A.8.1. Publications

Publications relevant to the work presented in the thesis:

(1). **Anirban Chandra,** Stefan Mebs, Subrata Kundu, Uwe Kuhlmann, Peter Hildebrandt, Holger Dau and Kallol Ray.

"Catalytic dioxygen reduction mediated by a tetranuclear cobalt complex supported on a stannoxane core.'' ***Dalton Transactions*.**, 2020, 49, 6065-6073. DOI: 10.1039/D0DT00475H

(2). Chakadola Panda[§], **Anirban Chandra**[§], Teresa Corona, Erik Andris, Bhawana Pandey, Somenath Garai, Nils Lindenmaier, Silvio Künstner, Erik R. Farquhar, Jana Roithov, Gopalan Rajaraman, Matthias Driess, and Kallol Ray. **(§ = Equivalent Contribution)**

"Nucleophilic vs. Electrophilic Reactivity of Bioinspired Superoxido Nickel (II) Complexes''. Angew. Chem. Int. Ed., 2018*, 57*, 14883-14887. DOI: 10.1002/anie.201808085

(3). Ines Monte-Pe´rez, Subrata Kundu, **Anirban Chandra**, Kathryn E. Craigo, Petko Chernev, Uwe Kuhlmann, Holger Dau, Peter Hildebrandt, Claudio Greco, Casey Van Stappen, Nicolai Lehnert, and Kallol Ray.

"Temperature Dependence of the Catalytic Two- versus Four Electron Reduction of Dioxygen by a Hexanuclear Cobalt Complex." *J. Am. Chem. Soc.,* 2017, 139, 42, 15033-15042. DOI: 10.1021/jacs.7b07127

(4). Xue-Peng Zhang, **Anirban Chandra**, Yong-Min Lee, Rui Cao, Kallol Ray, and Wonwoo Nam.

"Transition-Metal-Mediated O–O Bond Formation and Activation in Chemistry and Biology.'' Manuscript Submitted to *Chemical Society Reviews*. (Manuscript ID: CS-VPT-11-2020-00145)

Other publications:

(5) Deesha D. Malik, **Anirban Chandra**, Mi Sook Seo, Yong-Min Lee, Stefan Mebs, Anil Kumar Vardhaman, Holger Dau, Kallol Ray, and Wonwoo Nam

"Formation of a Cobalt (IV)-Oxo Complex by Dioxygen Activation at a Mononuclear Nonheme Cobalt (II) Center.'' Manuscript Submitted to *Chemical Science*. (Manuscript ID: SC-EDG-05-2020-002723).

A.8.2. Presentations

- ECOST-BIO Final Meeting Berlin; Seestrasse 39, 15537 Erkner, Germay; 9-11th April, 2018.
  Role: *Organizing Volunteer*
- Niedersächsisches Katalyse Symposium (NIKAS) 2018; Georg-August-Universität Göttingen, Germany; 19-20th September 2018.
  Role: Poster presentation
- 13. KCT-Koordinationschemie-Treffen, PotsdamUniversität Potsdam, 14476 Potsdam, Germany; 05-07 th March 2017
  Role: Oral Presentation